Iterative Learning Control of Hysteresis in Piezo-based Nano-positioners: Theory and Application in Atomic Force Microscopes

Kam K. Leang

A dissertation submitted in partial fulfillment of
the requirements for the degree of

Doctor of Philosophy

University of Washington

2004

Program Authorized to Offer Degree: Mechanical Engineering

University of Washington

Graduate School

This is to certify that I have examined this copy of a doctoral dissertation by

Kam K. Leang

and have found that it is complete and satisfactory in all respects,
and that any and all revisions required by the final
examining committee have been made.

Chair of Supervisory Committee:

_____

Santosh Devasia

Reading Committee:

_____

Martin C. Berg

_____

Santosh Devasia

_____

Brian C. Fabien

_____

Rolf T. Rysdyk

Date: _____

University of Washington

Abstract

Iterative Learning Control of Hysteresis in Piezo-based Nano-positioners:
Theory and Application in Atomic Force Microscopes

by Kam K. Leang

Chair of Supervisory Committee:

Associate Professor Santosh Devasia
Mechanical Engineering

Atomic force microscopy (AFM)-based systems are the key enabling tools in emerging nanotechnologies, such as high-density data storage devices, semiconductor lithography, and nanosurgery. By using piezo-based positioners (actuators), the AFM-probe tip can be moved relative to the sample surface for observing, manipulating, and fabricating objects at nanometer scale. However, a critical problem in AFM is nano-precision control of the piezo positioner. In particular, hysteresis (as well as creep and vibration) in piezos makes precise positioning a challenge and the relatively large tracking error due to hysteresis, which is substantially larger than 100 nm, is not sufficient for emerging nanoscale applications. This thesis solves an iterative learning control (ILC) problem for hysteretic systems to achieve nano-precision positioning. Specifically, an ILC algorithm is proposed and applied to compensate for hysteresis-caused positioning error in piezo-based systems, such as AFMs, and a proof of convergence, based on the Preisach hysteresis model, is presented. Moreover, the required number of iterations to achieve a desired tracking precision is quantified, and the method is experimentally evaluated on a commercial AFM system. Results show that the proposed ILC algorithm reduces the tracking error to the noise level of the sensor measurement.

TABLE OF CONTENTS

LIST OF FIGURES

viii

LIST OF TABLES

ACKNOWLEDGMENTS

DEDICATION

In loving memory of my mother, Ngor Lay Leang,

May 10, 1949 – August 15, 2004.

Chapter 1

INTRODUCTION

This thesis solves an iterative learning control (ILC) problem for hysteretic systems, such as piezo-based nano-positioners. The objective of this work is to achieve nano(high)-precision control by compensating for hysteresis effect. It is noted that piezo positioner-based devices, such as atomic force microscopes (AFMs), are used in emerging nanotechnologies for creating, manipulating and investigating objects down at the atomic scale [1]. However, loss in precision due to the effect of hysteresis (as well as creep and vibration) limit the performance of piezo-based devices [2]. Currently, feedback and model-based feedforward control can minimize the tracking error to 2-5% of the displacement range [3, 4, 5]. However, even at this level of precision relatively large error remains. For example, 2% error over a scan range of 50 micrometers leaves 1 micrometer (1000 nanometers) of error, which is not sufficient for nanoscale applications that require less than 100 nm precision, for example, nanofabrication and nanosurgery. Therefore, the critical need to achieve nano-precision positioning motivates the effort to correct for positioning errors due to hysteresis (as well as creep and vibration effects).

Specifically, this thesis proves convergence of an ILC algorithm for hysteretic systems. In the analysis, the Presiach hysteresis model is used to characterize the hysteresis behavior and the properties of the model are exploited to solve the convergence problem. It is noted that because of the multivalued input-output behavior or branching effects associated with the nature of hysteresis, the convergence problem is challenging and difficult to solve. However, a solution is found by restricting the system's input-output behavior to belong on a single branch. And by proving convergence, the number of iterations required to achieve a desired tracking precision is quantified in terms of the model parameters. Additionally, the method

is applied to an AFM system and experimental results show that the proposed ILC method reduces the tracking error to the noise level of the sensor measurement.

In addition to ILC, this thesis investigates the use of integrated feedback and feedforward control to minimize the three effects of creep, hysteresis and vibration in piezo positioners. The motivation to integrate feedback and feedforward control is to enhance performance of the control system by combining the advantages of both feedback and feedforward techniques. For instance, high-gain feedback control is used to compensate for creep and hysteresis effects, and it provides robustness to parameter variation [6]. On the other hand, feedforward control is used to improve the bandwidth of the system by compensating for vibration effect.

The work in this dissertation is important for two main reasons. First, the results can be used in the design of critical emerging high-precision technologies for scientific studies and commercial applications. Some examples of such technologies include scanning probe microscopy-based nanotechnologies for studying cells [7] and atoms [8], and nanolithography-based tools for semiconductor manufacturing [9, 10, 11]. Second, the results will contribute to the greater understanding of hysteretic systems and piezo positioners. The effect of hysteresis not only appears in piezo-based systems, but also in biology (*e.g.*, the Lotka-Volterra model for predator-prey interaction [12]) and economics (*e.g.*, the unemployment rate [13]), to name a few.

1.1 Thesis Goals

This thesis encompasses two main goals, with the second goal being the main focus of this thesis. The first goal is compensating for the effects of creep, hysteresis and vibration effects in piezos using an integrated feedback and feedforward controller. Specifically, feedback control is used to account for creep and hysteresis effects. Then, inversion-based feedforward input is integrated with the feedback controlled system to compensate for vibration effects [14]. The advantage of using feedback is that it eliminates the need to model the complicated creep and hysteresis behaviors. Furthermore, the feedback controller provides robustness with respect to parameter variation, such as the effects of temperature [15]. By integrating

inversion-based feedforward control – a technique also applicable to nonminimum phase systems [16] – the scanning speed of piezo positioners is improved significantly.

The second goal of this thesis is solving an ILC problem for hysteretic systems; this is the main focus of the thesis and the objective is to iteratively find feedforward input to compensate for hysteresis to achieve nano-precision positioning. An ILC problem is solved by proving convergence of a propose ILC algorithm for Preisach-type hysteretic systems. Briefly, the ILC methodology is based on the observation that, for some systems, information about its repetitive behavior can be used to improve its performance [17]. An ILC problem is solved by characterizing the hysteresis behavior using the Preisach model. The Preisach model captures the rate-independent hysteresis effect; the model has successfully modeled piezoactuator systems, and its generality will allow the proposed ILC technique to be extended to other similar hysteretic systems [18]. Based on the properties of the Preisach hysteresis model, we show that precision-output tracking can be achieved. Additionally, we investigate the rate of convergence for the ILC approach; the rate of convergence can be used to quantify the performance of the proposed ILC design. Furthermore, we quantify the tracking error with respect to the iteration number. Finally, the ILC approach was experimentally evaluated on a commercial atomic force microscope system and results demonstrate that the tracking error reduces to the noise level of the sensor measurement.

1.2   Outline

This dissertation is organized as follows. Chapter 2 provides a background on piezo-based positioners and the principle of the piezoelectric effect, the method by which electrical energy is transformed into mechanical energy and vice versa. Additionally, the relevant applications of piezo-based positioners are presented, as well as a detailed discussion of the main challenges associated with high-precision control of piezos, namely, the effects of creep, hysteresis, and vibration.

Chapter 3 discusses the work of the first goal of the thesis, that is, compensating for creep, hysteresis and vibration using an integrated feedback and feedforward approach. The basis of the approach is to use feedback control to compensate for creep and hysteresis ef-

fects and then to integrate this technique with model-based feedforward control to account for vibration. The integrated controller eliminates the need to model the complicated creep and hysteresis behaviors to achieve high-precision positioning. At the end of this chapter, experimental results are presented that show over an order of magnitude reduction in tracking error compared to the uncompensated case.

The second (and main) goal of this thesis, *i.e.*, solving an ILC problem for hysteretic systems, begins with an introduction of the Preisach hysteresis model in Chapter 4. In this chapter, relevant properties of the model in the context of this work are discussed. Afterwards, an ILC problem is formulated and solved in Chapter 5. Chapter 6 discusses the implementation of the ILC approach and the experimental results. Finally, concluding remarks and a discussion of future work follow in Chapters 7 and 8, respectively. Appendices, which document circuit diagrams, miscellaneous analysis, and example `C` and `MATLAB` programs are found at the end of this dissertation.

Chapter 2

PIEZO-BASED NANO-POSITIONERS

This chapter provides a background on piezo-based nano-positioners. The first section discusses the piezoelectric effect in crystals, the mechanism which transforms mechanical energy to electrical energy, and vice versa. The second section provides an overview of the applications for piezoelectric materials. In particular, the discussion focuses on the popular lead-zirconate-titanate ferroelectric-ceramic material and its application in emerging scanning probe microscopy-based nanotechnologies, such as atomic force microscopes. Finally, the last section presents a detailed discussion of the main challenges that arise when piezo-based positioners are used for high-precision positioning, namely, the loss in positioning precision due to the effects of creep, hysteresis and vibration. It is noted that overcoming these challenges is the focus of this thesis.

2.1 The Piezoelectric Effect

In 1784, Charles Coulomb conjectured that electricity might be produced by pressure [19]; however, no conclusive experiments were performed to validate the claim, until the year 1880, when Pierre and Jacques Curie[1] discovered that certain crystals (such as quartz, sodium chlorate, boracite, cane sugar, and Rochelle salt) when subjected to mechanical stress produce electric charge (see timeline in Fig. 2.1). One year later, the French physicist Lippmann predicted, based on thermodynamic analysis, the converse effect: strain as a result of an applied voltage. That same year the Curie brothers verified Lippmann's prediction [21]. Subsequently, the discovery was named the *piezoelectric* effect from the Greek word *piezein*, meaning to press or squeeze, and the Curie Brothers were created with the discovery [22, 19].

---

[1]Pierre Curie was born in 1859 and died of an accident with a horse carriage in 1906. Jacques was born in 1855 and lived till 1941. The discovery of the piezoelectric effect was made in Jacques' laboratory [20].
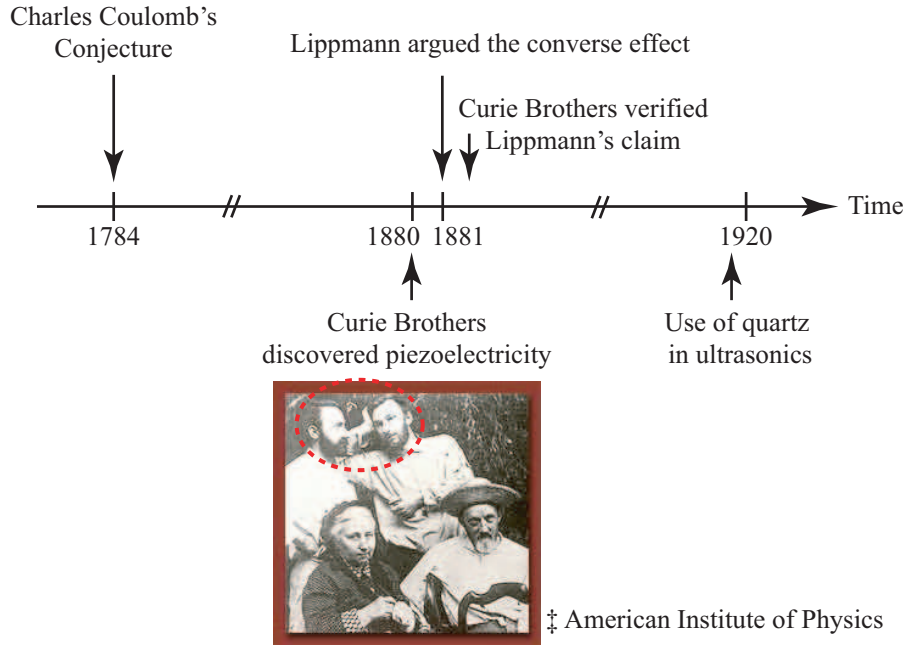
Figure 2.1: Piezoelectricity timeline [22].

Figure 2.2 shows a simplified two-dimensional model representing the piezoelectric effect for quartz crystal. Lord Kelvin conceived the model in 1893 to explain the piezoelectric effect [21, 19]. The piezoelectric effect is based on the unique characteristic of certain crystalline lattices to deform under pressure, and as a result, the centers of gravity of the positive and negative charges separate, creating a dipole moment (product of charge value and their separation). The resulting dipole moment induces an electric charge which can be measured across the surface of the material. Conversely, an applied voltage induces a mechanical strain in the crystalline lattice [21]. The circles in Fig. 2.2 represent positive (silicon) and negative ions (oxygen pair) of the unit cell of quartz, where the small solid circle represents the center of gravity for the positively charged ions and the small open circle represents the center of gravity for the negatively charged ions. In Fig. 2.2(a), the centers of gravity for both positive and negative ions coincide in the equilibrium state, therefore yielding no dipole moment. On the other hand, as the crystal is compressed by mechanical
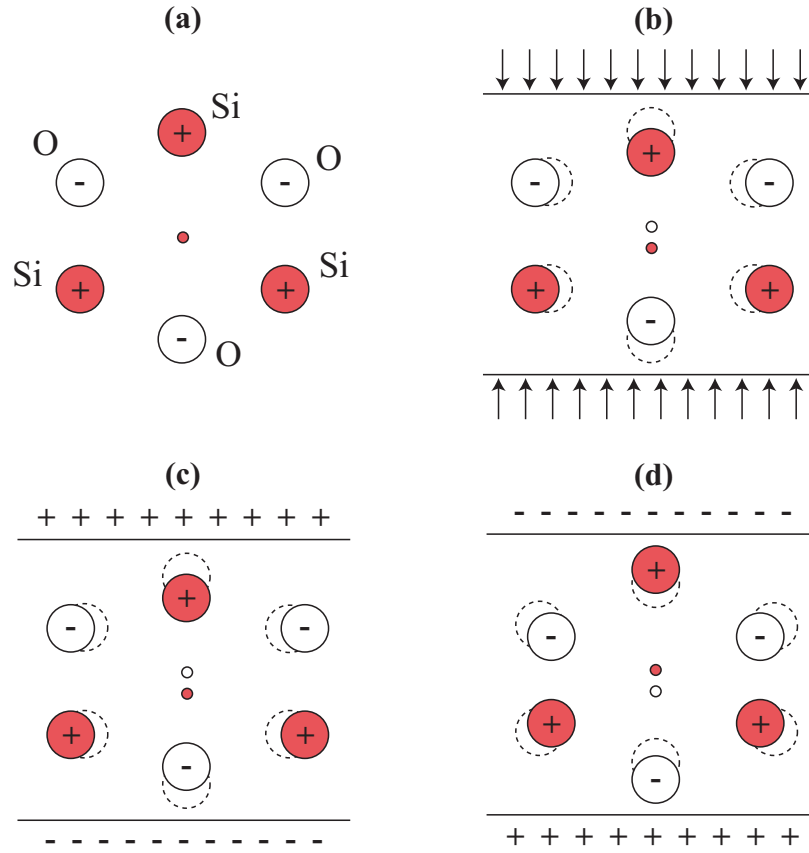
Figure 2.2: A two-dimensional model of a unit cell for a quartz crystal illustrating the piezoelectric effect. This model was first conceived by Lord Kelvin in 1893 [21]. The large solid circles represent positively charged ions and the small solid circle represents their center of gravity. Likewise, large open circles represent negatively charged ions, and their center of gravity is represented by the small open circle. (a) The equilibrium state where there is no net dipole moment, *i.e.*, the centers of gravity for positive and negative ions coincide; (b) mechanical stress induces an electric dipole – separation of centers of gravity for positive and negative ions; (c) and (d) an applied field produces mechanical strain. (Figure is based on reference [21].)

pressure, a relative displacement of the centers of gravity between the positive and negative ions induces a dipole moment as illustrated in Fig. 2.2(b). Consequently, an electric potential develops along the axis of polarization; the electric potential can be measured across the surface of the crystal. Likewise, by applying a voltage across the crystal the converse effect, mechanical strain induced by an electric potential, is achieved as illustrated in Figs. 2.2(c) and (d). For example, Fig. 2.2(c) shows two electrodes of opposite sign, one applied to the top and the other applied to the bottom of the unit cell. As the applied field increases, it causes the corresponding ions to move in a favorable direction, consequently inducing deformation in the crystal lattice and mechanical strain is achieved [23]. By reversing the sign of the electrodes, strain in the opposite direction is achieved as depicted in Fig. 2.2(d).

Interestingly, the piezoelectric effect only occurs in crystals with no center of symmetry. Of the 32 possible classes of crystals, 20 are piezoelectric and 12 are not; therefore, this effect depends on the type of symmetry existing in the crystal. According to Ballato [19], substances such as bone, wood, and ice exhibit the piezoelectric effect due to the asymmetric nature of the molecules that make up the material.

2.1.1 Ferroelectric Materials

Piezoelectric materials, either by mechanical stress or applied voltage, produce electric dipoles. Materials which exhibit a spontaneous polarization (*i.e.*, electric dipoles) in the absence of an applied stress or electric field are referred to as ferroelectrics[2]. All ferroelectrics exhibit the piezoelectric effect; however, the converse is not necessarily true. For example, quartz exhibits the piezoelectric effect, but the crystal structure does not yield a spontaneous polarization, *i.e.*, no net dipole moment in its equilibrium state because the centers of gravity for the positive and negative ions coincide as shown in Fig. 2.2(a). On the other hand, the microscopic crystallites of lead-zirconate-titanate ($Pb(Ti,Zr)O_3$, PZT) exhibit a spontaneous polarization due to the arrangements of atoms within the unit cell at room temperature. But when manufactured, the random orientations of the crystallites in this ferroelectric material produce no net effect when mechanically stressed or when voltage

---

[2]Ferroelectricity was discovered in the late 1940s [24, 25]. We note that all ferroelectrics are piezoelectric, but not all piezoelectrics are ferroelectric.

is applied. However, through a process called *poling*, the material can be made to exhibit considerable piezoelectric effect. Basically, the poling processes forces the dipoles in the material to align in a favorable direction. The poling process involves heating the material near its Curie temperature, typically between $100°$ and $300°$ C, then applying a strong electric field while cooling the material. The heating process allows movement of the individual crystallites and the application of a strong electric field causes the dipoles to align with the field in favor of a net effect [24, 25]. As the field is maintained during the cooling process, the majority of the dipoles maintain their alignment. After poling, the ferroelectric PZT material exhibits considerable piezoelectric effect. Such materials are exploited in numerous actuator and sensor applications, and PZT ceramics are the most widely used piezoelectric materials. Additionally, PZT ceramics are manufactured into a wide variety of shapes and sizes, from tube-shaped actuators, as shown in Fig. 2.4, to the stacked configuration. Although barium titanate ($BaTiO_3$) was the first ferroelectric material used for piezo-based applications in the 1950s, PZT ceramic has since then replaced barium titanate because PZT exhibits nearly twice the piezoelectric effect [22, 24, 25, 26].

2.2 Applications of Piezoelectric Materials

2.2.1 Early Uses of Piezoelectric Materials

Since the discovery of the piezoelectric effect, countless applications have emerged for materials that exhibit this behavior. Piezoelectric materials (or piezos) were first used in underwater acoustics, as an ultrasonic submarine detector, a device developed at the end of World War I by Langevin [19]. Back then, Langevin achieved the goal of emitting a high frequency "chirp" underwater and measuring depth by timing the return echo.

In the 1920s, the primary use of piezoelectric crystals (namely quartz and Rochelle salt) were for resonators (oscillators), stabilizers and filters. For instance, resonators were common in radio broadcasting applications [21]. Additionally, composite resonators were constructed for use as a tool to study and determine the coefficients of various solids [22]. Also, piezo resonators, such as the vibrating quartz plate, replaced the swinging pendulum of clocks [27]. The frequency of oscillation of a quartz resonator is extremely stable against

changes in temperature. According to Cady [22], such timepieces are more constant than the best astronomical clocks.

A common household device that exploits the piezoelectric effect is the ignitor found in gas stoves and pocket lighters. A high-voltage spark is generated by striking a piezoelectric material (such as quartz) with a spring-loaded impact hammer; the spark ignites the fuel. Such a device was first developed in Japan in the 1965; however, the idea of using high-voltage to ignite fuel dates back to 1951 in the United States, according to reference [28]. Piezo-based ignitors are common and their use even extends to specialized high-altitude climbing and mountaineering cooking stoves as shown in Fig. 2.3. In the figure, a spark, which ignites the fuel, is generated by pressing a small button on the device as indicated. The use of such ignitors eliminate the need to carry matches or pocket lighters.

Figure 2.3: A specialized cooking stove for high-altitude climbing and mountaineering that uses a piezo-based ignitor to light the fuel. A high-voltage spark is generated by pressing a button to trigger an impact hammer. The hammer strikes a piezoelectric material (such as quartz) to generate a high-voltage spark, which lights the fuel. (Photo by Kam K. Leang; climber: Chris Cass; location: The Mount Spickard and Redoubt Group, North Cascades, WA.)

2.2.2   Actuators and Sensors

Piezoelectric-ceramic materials, such as PZT, with their ability to change shape under the application of an electric field, as well as generate electric charge under applied mechanical stress, have been exploited in various actuator and sensor technologies [29]. For instance, piezoceramics are currently manufactured in a variety of configurations, such as the tube-shaped geometry shown in Fig. 2.4, for use as a positioner (or actuator). In the figure, the outer and inner electrodes are sectored into four equal and isolated quadrants. Depending on how the voltage is applied to the electrodes, displacement in the three coordinate axes (x, y and z) can be achieved. Typically, either an optical, strain or capacitive sensor is used to infer the displacement of the piezo positioner [30]. By applying a voltage, the change in volume associated with each sectored region of the tube causes it to displace, where a lateral displacement (along the x- or y-axis) is created by an asymmetrical change in volume between opposing sectors, for example. Also shown in the figure is a continuous electrode at one end of the tube. When voltage is applied to this electrode, expansion or contraction along the axial (z-axis) direction is achieved. Furthermore, when mechanical stress is applied to the tube-shaped actuator, an electric potential can be measured across certain electrodes; therefore, the actuator can function as a sensor.

The relationship between the applied input voltage and static (and/or dynamic) displacement of the device has been extensively studied to aid in designing piezo-based systems. For example, Locatelli [31] introduced a simple deflection equation for a tube-shaped piezo positioner similar to the one shown in Fig. 2.4. Likewise, Chen [32, 33] derived a deflection equation for a quarter-sectored piezo-tube actuator using the theory of elasticity. In both cases, the deflection was found to be proportional to the applied input voltage and experiments were performed to validate the claim. In their work, good agreement was found; however, the analysis did not incorporate the effects of creep and hysteresis. (Both of these effects are discussed in the next section.) In general, the constitutive equations relating the induced strain (or displacement) and electric field (or applied input voltage) can easily be obtained; but the coupling effects (piezoelectric and electrostrictive coefficients) depend on impurities in the material, as well as many other factors [34].
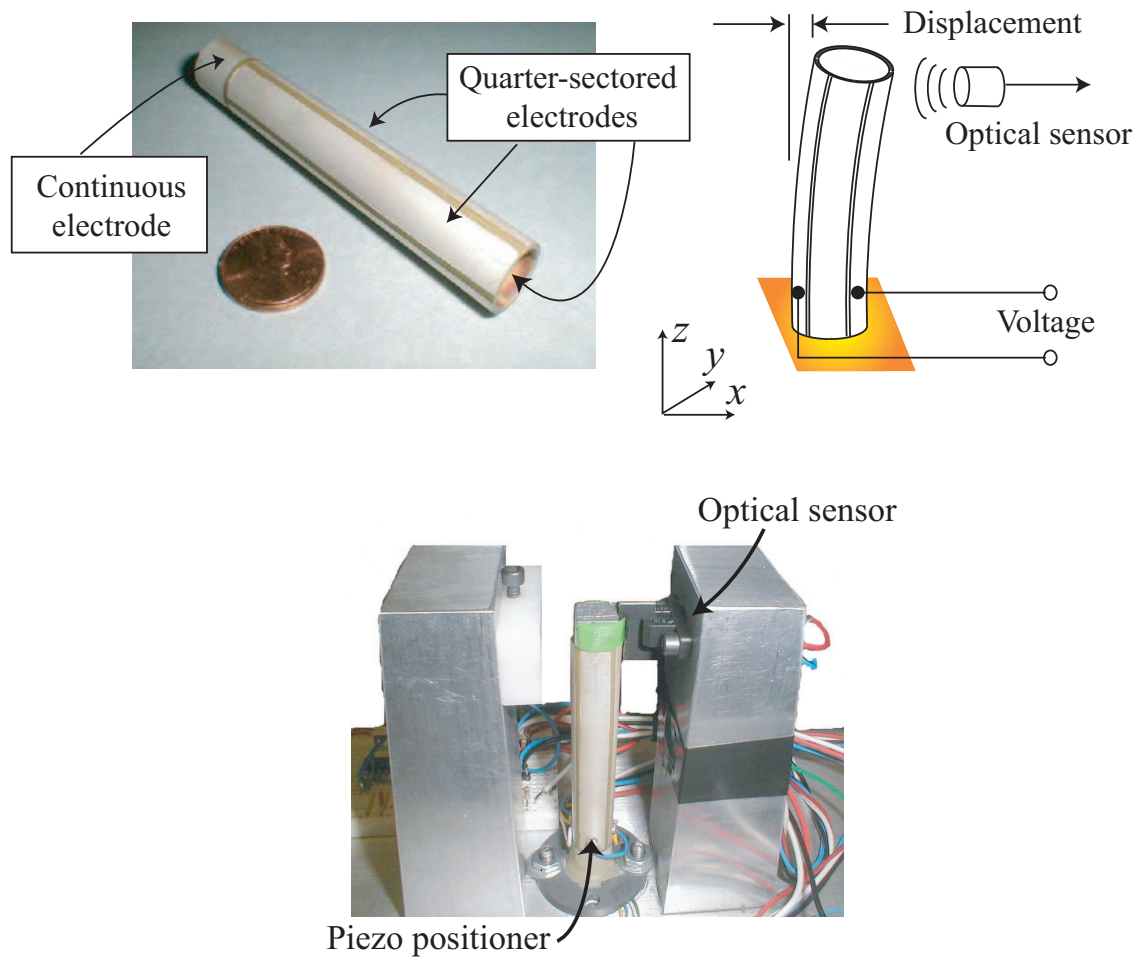
Figure 2.4: A typical tube-shaped piezo positioner consisting of a lower, continuous electrode (for generating axial motion) and quarter-sectored electrodes (for generating axial and lateral motions). Depending on how the voltage is applied to the electrodes, displacement in the three coordinate axes (x, y and z) can be achieved. Typically, an optical sensor is used to infer the displacement of the piezo positioner [30].

Piezo-based actuators can position with sub-angstrom level resolution. Because of their ability for fine movements, piezos are used in applications such computer hard disk drives for positioning a read/write head [35, 36, 37, 38]. Similarly, piezo positioners are exploited in micro-machining for the positioning of cutting tools [39] and they are used in ink jet printers [40]. Also, piezo-based positioners are used for mask alignment in imprint lithography [41, 10]. In the field of optics, there are piezo-driven deformable mirrors [42, 43]. Piezos are used for metrological purposes [44, 45], too, for example, to measure the line widths of photomasks in the microelectronics industry [46] and for accurate pitch measurements [47]. They have been used to actively suppress vibration in structures [48], as well as in the design of micropumps for fluid microsystems [49]. Additionally, their fast response makes them ideal for high-speed solution switching in bioengineering applications [50]. Piezo materials are widely used in ultrasonics; for instance, Haake and Dual [51] used a thin piezoelectric layer to generate ultrasonic standing waves to manipulate small particles by node position control. Likewise, Kurosawa *et al.* [52] developed a similar ultrasonic motor. In the biomedical field, piezo-based ultrasonics are used for hyperthermia treatment of cancerous tumors [53, 54]. By using a bimorph design, grasping tools for minimally invasive surgery have been designed [55, 56]. The design consists of two piezoelectric bimorph actuators configured for holding and gripping a cutting tool. The fine movements of the piezo tool allow for precise surgical operations which exceeds the capabilities of the human hand. With the recent advancement in plasma-discharge jet [57] and femtosecond laser technologies [58], piezo-based positioners, such as ultra-precision stepping positioners [59], can be used to move these highly-precise cutting tools for nanofabrication and nanosurgery.

As previously mentioned, piezoelectric materials can be made into sensors. For example, by exploiting the piezoelectric effect, piezo-based force and pressure sensors have been designed [60]. Likewise, piezo-sensors have been used to measure electronic properties of semiconductor devices via the application of stress [61]. A list of other types of piezo-based sensors, as well as other piezo-based actuator applications, can be found in references [19] and [62]. Now we turn our attention to emerging piezo-based scanning probe microscopy-based nanotechnologies.

2.2.3 Scanning Probe Microscopy-based Applications

Although piezo-based positioners are widely used in various high-precision applications, one of their most significant contributions is in emerging scanning probe microscopy (SPM)-based nanotechnologies. In 1982, a group of researchers at the IBM research lab exploited the positioning capabilities of a piezoactuator for imaging atoms in a scanning tunneling microscope (STM) [63, 64]. Since then, the piezoactuator has been the workhorse of emerging SPM-based systems for studying, manipulating and creating objects at the nanoscale [65, 1, 66].

Figure 2.5 shows an example SPM, specifically it's an atomic force microscope (AFM) imaging system [67, 64, 65]. The conceptual diagram of the AFM is depicted in Fig. 2.5(a) and the basic block diagram of the system is shown in Fig. 2.5(c). Like all SPMs, the AFM consists of a piezo-scanning device. The function of the piezo-scanner is to position a sample relative to a cantilever and probe tip along the x-, y-, and z-axis as shown in Fig. 2.5. The AFM obtains an image of the sample topology by moving a probe tip over a sample surface and simultaneously recording the surface "contours" similar to a stylus profilometer. For instance, scanning is performed parallel to the sample surface (along the x- and y-axis), *e.g.*, see the scanning trajectories shown in Fig. 2.6. As the sample is scanned relative to the probe tip, surface contours deflect the cantilever beam perpendicular (z-axis) to the sample surface. The deflection of the cantilever beam is measured by an optical sensor and a z-axis feedback controller is used to maintain appropriate tip-to-sample separation for *contact* and *non-contact* mode operations [68]. The output of the optical sensor, a signal proportional to the height of the tip from the sample surface in the z-direction, is used to construct an image of the topology of the sample surface [67].

One distinct advantage of the AFM compared the STM is the sample can be nonconductive. Therefore, the AFM can be used to image living biological samples, such as cells [69, 70, 71, 72, 73] and DNA [74, 75, 76]. The AFM can also be used for measuring the properties of materials and biological samples [77, 78, 79]. Additionally, AFMs can be used to manipulate nano-sized features and cells [80]. Similar to STMs, AFMs can be used for nanofabrication and even designing high-density data storage devices [81, 82, 83, 84, 85].

Detector

Optical sensor

Cantilever and
probe tip

Sample

Piezo positioner

(a)

Probe Tip

Sample

Piezo-tube
Actuator

z

y

x

(b)

Optical
Deflection Sensor

z

z-axis
Feedback
Controller

Image

Cantilever Beam
and Probe Tip

Sample

u_z

z

x PZT

y

u_x

u_y

x, y-axis
Scanner Control

x, y

z

x

y
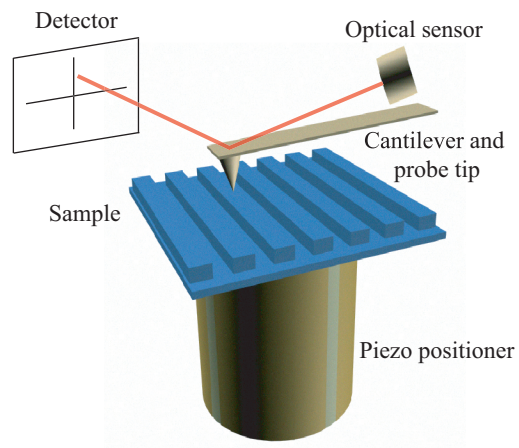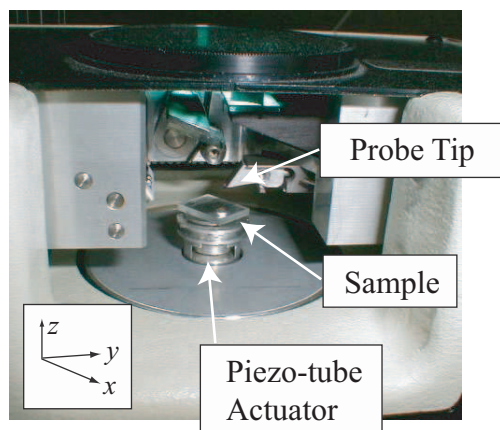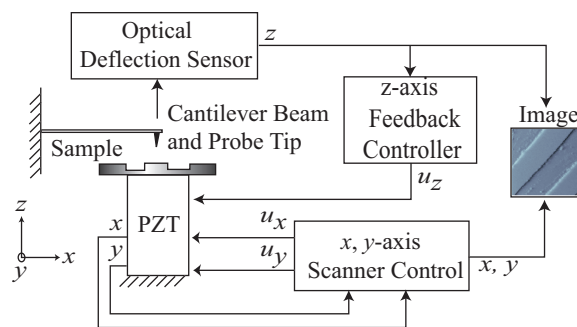
(c)

Figure 2.5: The AFM system. (a) Conceptual diagram of the AFM; (b) photograph of an experimental AFM system; and (c) block diagram of the AFM system.
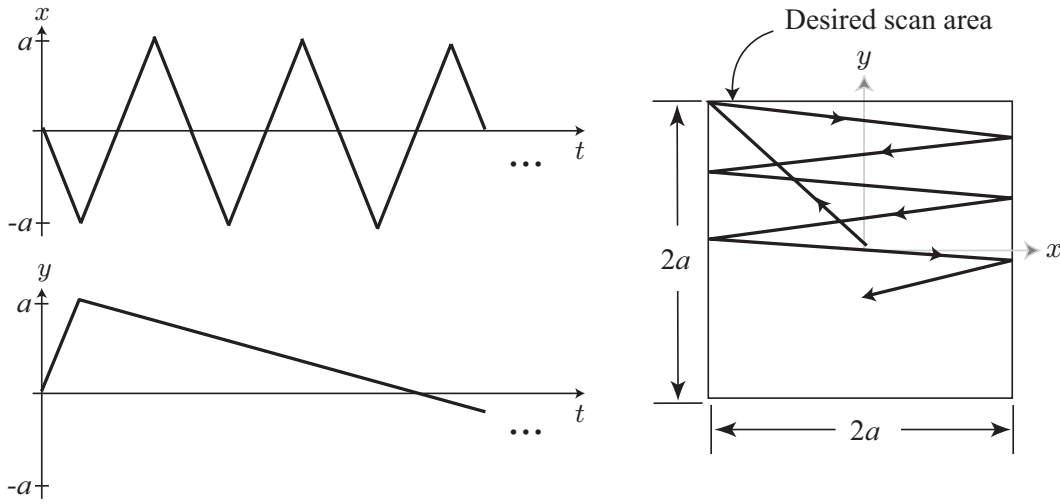
Figure 2.6: A typical raster pattern used for AFM imaging [2].

2.3   Challenges in High-precision Positioning

Piezo-based positioners are the preferred workhorse of current micro- and nano-positioning technologies because of their ability to displace with sub-nanometer level precision [29]. Additionally, they are fast (*i.e.*, high-bandwidth response), consume very little power, possess no movable parts to cause wear and tear, and they lack backlash. In spite of their advantages, however, the performance of piezos are limited by three major effects: creep, hysteresis, and vibration. These three effects are discussed in the following.

2.3.1   Creep

Creep (or drift) leads to significant error when positioning over extended periods of time (*e.g.*, during slow-speed scanning operations) [86, 87, 88]. In mechanics, creep is a rate-dependent deformation of the material when subjected to a constant load or stress [23]. Similarly, creep in piezoelectric materials is a rate-dependent deformation due to a constant electric field. Creep manifests itself as the remnant polarization slowly increases after the onset of a constant field. Figure 2.7 shows the effect of creep in the positioning of an experimental piezoactuator. The actuator is commanded to a reference position, say 25 μm,
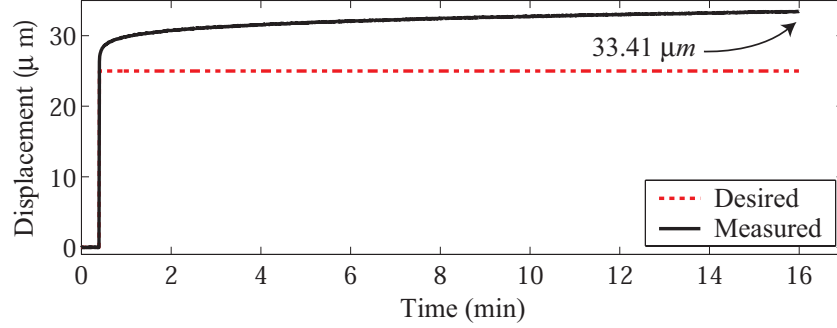
Figure 2.7: The effects of creep in the output displacement measured over a period of 15 minutes.

but after a period of 15 minutes, the actuator's position creeps to a new position of 33.41 μm. As a result, the error due to creep is 24.44% of the total displacement range.

One method to avoid creep is to operate fast enough so that the creep effect becomes negligible [2]; however, such effort prevents the use of piezo positioners in slow and static applications. For example, because of drift, it is difficult to precisely fabricate nanofeatures using AFMs when the process time-scale is on the order of minutes, *e.g.*, see [86]. Methods to compensate for creep have been well studied in the past and some examples include the use of feedback control, *e.g.*, [3, 89, 90, 4], and model-based feedforward control, *e.g.*, [88, 91, 92, 2, 93, 94]. A more detailed discussion of the advantages and disadvantages of these approaches will be presented in subsequent chapters.

2.3.2 Hysteresis

Hysteresis, a nonlinear behavior between the applied electric field and the mechanical displacement of the piezoactuator [95, 96], leads to loss in positioning precision when operating over relatively long-range displacements [3]. The term hysteresis comes from the Greek word "to be late" or "come behind" and the term was first coined for application in 1881 by physicist Ewing when he was studying magnetization. Interestingly, in the year 1881 the Curie Brothers were credited with the discovery of the piezoelectric effect. Hysteresis is often referred to as a lag in the response. An interesting writing on the history of hysteresis can be

gleaned from reference [13], which describes other systems which exhibit this behavior. The mechanism responsible for hysteresis in piezoactuators is be better understood by considering the domain wall analogy for describing hysteresis in magnetic materials [96, 95, 97]. For example, magnetic materials consist of tiny elementary magnetic dipoles. These particles align to an applied field. The analogy to this in piezoelectric materials is the unit cell of the crystal which exhibits an electric dipole. The term *domains of polarization* refers to regions of similarly-oriented dipoles, that is, a relatively large region of connected unit cells having similarly-oriented net polarization. The imaginary boundary which separates these regions are referred to as *domain walls*. These boundaries grow or shrink depending on the nature of the applied field. For the simple case, an isolated elementary dipole subjected to an applied field will orient itself to the field instantaneously, and therefore displays no hysteresis. However, hysteresis is said to arise due to "internal forces", which causes the dipoles to exhibit a preference for their orientation, and hence the motion of the domain walls are retarded by such forces. These internal forces are attributed to material defects and internal friction between dipoles and the domain walls. Even though the domain wall analogy was conceived for magnetic materials, it can easily be extended to materials which consist of elementary dipole-like particles, such as piezoelectric materials. Additionally, hysteresis "remembers" the effect of the past, which further complicates the problem in terms of precision control (see Chapter 4).

Figures 2.8(a) and (b) shows the effect of hysteresis in an experimental piezo-based system. In Fig. 2.8(c), the curve depicts the nonlinear relationship between the output displacement and applied input voltage (hysteresis curve). This nonlinear effect leads to distortion in scanning probe microscopy (SPM)-based imaging as shown in Fig. 2.8(d). Although the actual features are oriented in a parallel fashion, hysteresis causes the features to appear curved. More specifically, the distortion is caused by plotting the information collected about the sample topology with respect to the desired position of the probe. Because of hysteresis, the probe does not achieve the desired position, therefore leading to the distorted image. Hysteresis can be avoided by operating in the linear range, *i.e.*, over short range displacements; however, this limits the achievable positioning range.
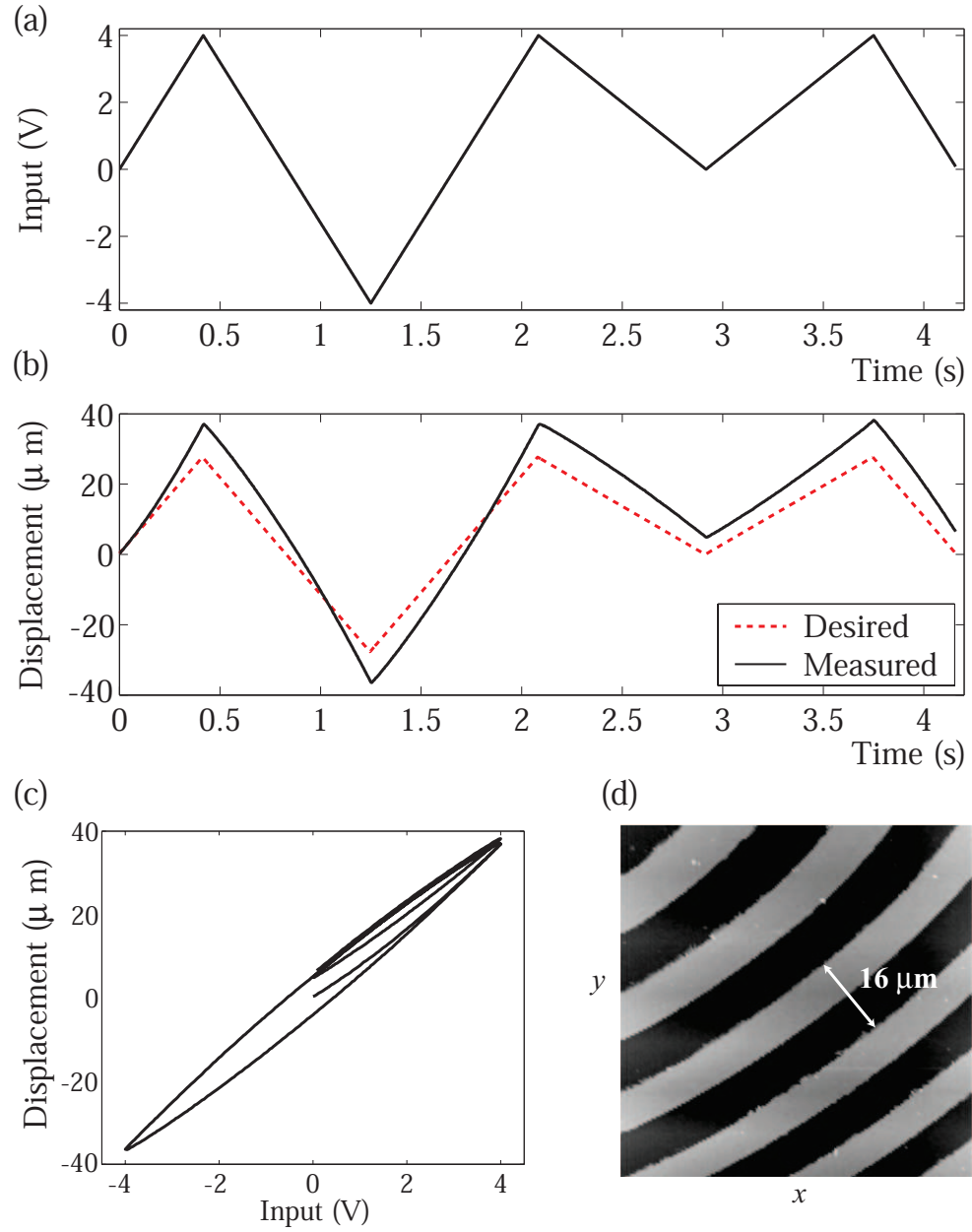
Figure 2.8: The effects of hysteresis: (a) applied input versus time, (b) resulting output displacement versus time, (c) displacement versus input curve (hysteresis curve) and (b) distortion in AFM imaging of 16-μm pitch encoder gratings due to hysteresis effect. The actual features are parallel.

2.3.3 Vibration

Vibration effect limits the operating bandwidth of piezo-based positioning systems. The effect is caused by command signals exciting the flexible modes of a system [2]. For example, the frequency response of a piezo-based positioner typically reveals sharp resonant peaks. These resonant peaks can easily be excited by certain command signals applied to control the positioner. Figures 2.9(a) and (b) clearly illustrate the effect of vibration, where significant tracking error can be observed in the displacement versus time response (Fig. 2.9(a)). When the piezoactuator is scanned at high frequencies relative to the first resonant-vibrational frequency of the positioner, movement-induced vibration leads to significant positioning error [98, 99]. Such effects cause distortion in the SPM-based imaging, for example the rippling effect in the image of Fig. 2.9(b).

Typically, scan rates (*i.e.*, scan frequencies) are restricted to less than $1/10^{th}$ to $1/100^{th}$ of the first resonant frequency, thus limiting the bandwidth of piezo-based systems because the achievable scan rate is lower for increased resolution in positioning. However, higher operating speed can be achieved by using *stiffer* piezoactuators with higher resonant frequencies, for example, Ando *et al.* [100] used a *stiff* piezo with a resonant frequency of $260 \ kHz$ in an AFM to image biological macromolecules in action. Additionally, Sulchek *et*
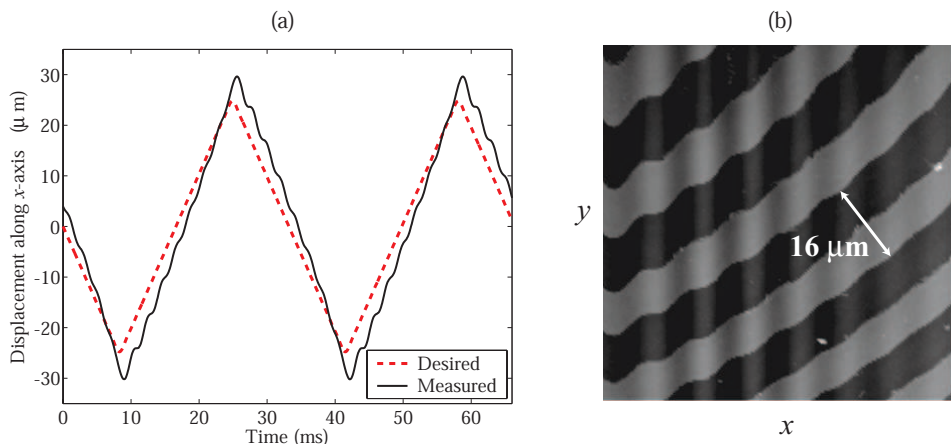
Figure 2.9: The effects of vibration (and hysteresis) scanning at 30 Hz: (a) displacement versus time response, and (b) distorted AFM image, but actual features are parallel.

al. [101] considered the use of high-bandwidth piezos for high-speed AFM imaging. But in general these stiff piezos have shorter effective displacement ranges. Therefore, the use of stiffer piezos to increase bandwidth also leads to reduction of positioning range. An alternative for improving the throughput of AFM-based systems is to operate multiple probes in parallel [102, 103, 104, 105, 106]. However, movement-induced vibration caused by the dominant resonant peak still limits the achievable scanning speed [105, 101].

In summary, creep, hysteresis and vibration effects significantly limit the performance and application of piezo-based positioning systems [86]. This thesis addresses the issue of improving the performance of piezo-positioners by compensating for these effects.

2.4   Summary

This chapter introduced the piezoelectric effect, the fundamental mechanism that transforms mechanical energy to electrical energy, and vice versa. A discussion of various applications of the piezoactuator was presented and the three adverse effects of creep, hysteresis, and vibration were discussed in detail. We conclude that these effects lead to significant loss in positioning precision. Furthermore, it is noted that the focus of this dissertation is to compensate for the effects of creep, hysteresis and vibration to achieve high-precision positioning. In the next chapter, we will discuss integrating feedback and model-based feedforward control to compensate for creep, hysteresis and vibration effects. Afterwards, we will focus on an iterative learning control approach to compensate for hysteresis.

Chapter 3

DECOUPLED FEEDBACK/FEEDFORWARD COMPENSATION OF CREEP, HYSTERESIS AND VIBRATION IN PIEZOACTUATORS

This chapter describes a decoupled feedback/feedforward control approach to compensate for creep, hysteresis and vibration in piezo positioners. The objective is to achieve high-precision positioning by decoupling the control of creep and hysteresis from the control of vibration. For instance, a high-gain feedback controller is designed to compensate for creep and hysteresis. Compared to traditional model-based feedforward techniques, feedback control avoids the use of complicated creep and hysteresis models. Then, a feedforward controller is designed and augmented to the feedback controlled system to account for vibration.

The first section of this chapter is a review of current compensation techniques, their advantages and disadvantages. Section 3.2 describes the experimental piezo-positioning system and the process by which the linear vibrational dynamics model (used to find feedforward inputs to compensate for vibration) was obtained. In Section 3.3, the design of the high-gain feedback controller is presented, followed by a discussion of the inversion-based feedforward approach in Section 3.4. Finally, experimental results and a discussion are presented in Section 3.5, and a summary follows in Section 3.6.

3.1 Introduction and Motivation

In the past, numerous studies have been done to develop techniques to compensate for the effects of creep, hysteresis, and vibration in piezo systems. In general, these techniques can be categorized as either feedback control or model-based feedforward control, each with its advantages and disadvantages. For example, feedback control schemes such as proportional-integral-derivative (PID) [3], state-feedback [39], and H_∞ control [107, 4] have demonstrated

substantial reduction of positioning errors due to creep and hysteresis. The advantages of feedback control include: (i) the ability to handle modeling errors and (ii) it is robust with respect to parameter variation due to aging effects [108] and environmental changes, such as temperature changes [15]. Although feedback control reduces positioning errors, the low gain margin in piezo positioners tend to limit the achievable performance, *i.e.*, high feedback gain tends to destabilize the system [3, 109]. In particular, low structural damping in piezo positioners results in high quality factor Q_f (*i.e.*, sharp resonant peak) which gives rise to low gain margin. In practice, a compromise is sought between performance and instability; feedback gains (such as proportional, derivative, and integral terms) are adjusted to improve performance without instability (*e.g.*, in references [68, 110, 89, 89]). Moreover, feedback-based approaches have had limited success in compensating for dynamics effects [3].

To overcome some of the performance limitations inherent in feedback control (*e.g.*, limited dynamic compensation due to low gain margin), model-based feedforward input has been used to compensate for creep and hysteresis effects [111, 112, 91, 113, 114, 94]. The feedforward input is found by carefully modeling the complicated creep and hysteresis behaviors. Many model-based approaches have been considered, for instance, Smith *et al.* [115] developed a hysteresis model based on energy methods and then used the model for the design of an inverse compensator. Additionally, vibration compensation can be achieved using a model-based feedforward approach [116, 99, 117], as well as accounting for the other two effects (creep and hysteresis), *e.g.*, in reference [2]. However, a major disadvantage of using model-based feedforward approaches to compensate for creep and hysteresis is that these effects are difficult to model accurately and the approach is prone to errors. Furthermore, model-based approaches can be computationally cumbersome to implement.

The contribution of this chapter is developing a decoupled feedback/feedforward approach to compensate for creep, hysteresis and vibration. The approach integrates the advantages of existing feedback techniques, and improves the operating speed by the addition of feedforward input to compensate for the vibrational dynamics. Specifically, high-gain feedback control is used to compensate for the effects of creep and hysteresis. The feedback approach, compared to model-based feedforward techniques, avoids the need to model the

complicated creep and hysteresis behaviors. However, because piezos tend to be *flexible, i.e.,* they have sharp resonant peaks which lead to low gain margin, high-gain feedback control is achieved by modifying the sharp resonant peak of the system with a notch filter [39, 38] — experimental results are presented to show that this approach can lead to a substantial increase in the measured gain margin (the gain margin was increased from -17.05 dB to 30.86 dB for our experimental system). Experimental results are also presented to show that a high-gain feedback controller can then be designed to compensate for errors caused by creep and hysteresis effects.

Next, the performance of the proposed feedback controller is further improved by adding feedforward input obtained through a model-based approach [118]. Such feedback/feedforward integration does not limit the choices of the feedback approach, that is, the model-based feedforward technique can be used with any of the existing or emerging feedback approaches. Moreover, the integrated approach provides robustness to parameter variation and simplifies the computation of the feedforward input by avoiding the modeling of the creep and hysteresis behaviors. The block diagram of the proposed decoupled feedback/feedforward approach to control piezo-positioners is shown in Fig. 3.1.
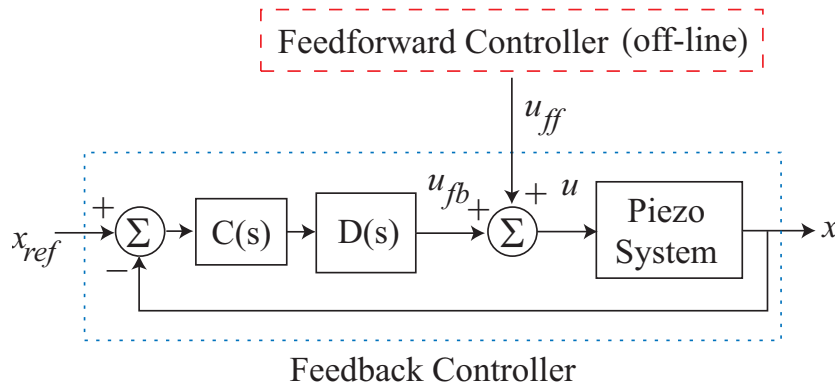
Figure 3.1: Block diagram of control system where u_{ff} and u_{fb} are the feedforward and feedback inputs, respectively; u is the input to the system; $C(s)$ is the feedback controller; $D(s)$ is the notch filter for improving gain margin (discussed later in Section 3.3); x_{ref} is the reference trajectory to the feedback system; x is the actual system output.

At the end of this chapter, the decoupled feedback/feedforward is applied to an experimental piezo-positioning system. Results are presented to show that the proposed approach leads to precision piezo-based positioning over extended periods of time (creep compensation), long ranges (hysteresis compensation) and at high scan rates (vibration compensation).

3.2 The Experimental Piezo-positioning System: Modeling the Vibrational Dynamics

This section describes the experimental piezo-positioning system and the vibrational-dynamics model. The experimental system studied in this article is a sectored piezoelectric-tube (lead-zirconate-titanate, PZT) actuator used, for example, in scanning-probe-microscopy applications [1]. The linear vibrational dynamics model of the piezo-positioning system was obtained using a black-box identification technique, where the model was found by curve fitting the system's measured frequency response. The frequency response was measured using a commercially available dynamic signal analyzer (DSA)[1]. A sinusoidal input voltage, u, generated by the DSA was applied to the piezo-positioning system. The resulting lateral displacement of the piezoactuator (in the x-direction) was measured by an optical sensor (which has a static gain of 20 $\mu m/V$) and fed back to the DSA to construct the frequency response curve shown in Fig. 3.2 (solid line). The frequency response was measured over a displacement range of ± 2.00 μm, which is approximately 5% of the maximum output range, where hysteresis is negligible. In addition, the frequency response was measured over a relatively high frequency range (1 Hz - 2 kHz) so that the effect of creep is small.

A linear vibrational-dynamics model, represented as a transfer function in the Laplace domain, relating the input voltage, u, to the sensor output, $\hat{x}$, of the piezo-positioning system, was curve-fitted to the measured frequency response. The model was found to be

$$\hat{G}(s) = \frac{\hat{x}(s)}{u(s)} = k_0 \frac{\prod_{m=1}^{2}(s - 2\pi z_m)}{\prod_{n=1}^{6}(s - 2\pi p_n)} \left(\frac{V}{V}\right), \tag{3.1}$$

where $k_0 = 7.20 \times 10^{13}$ is the nominal system (model) gain factor (*i.e.*, measured over the
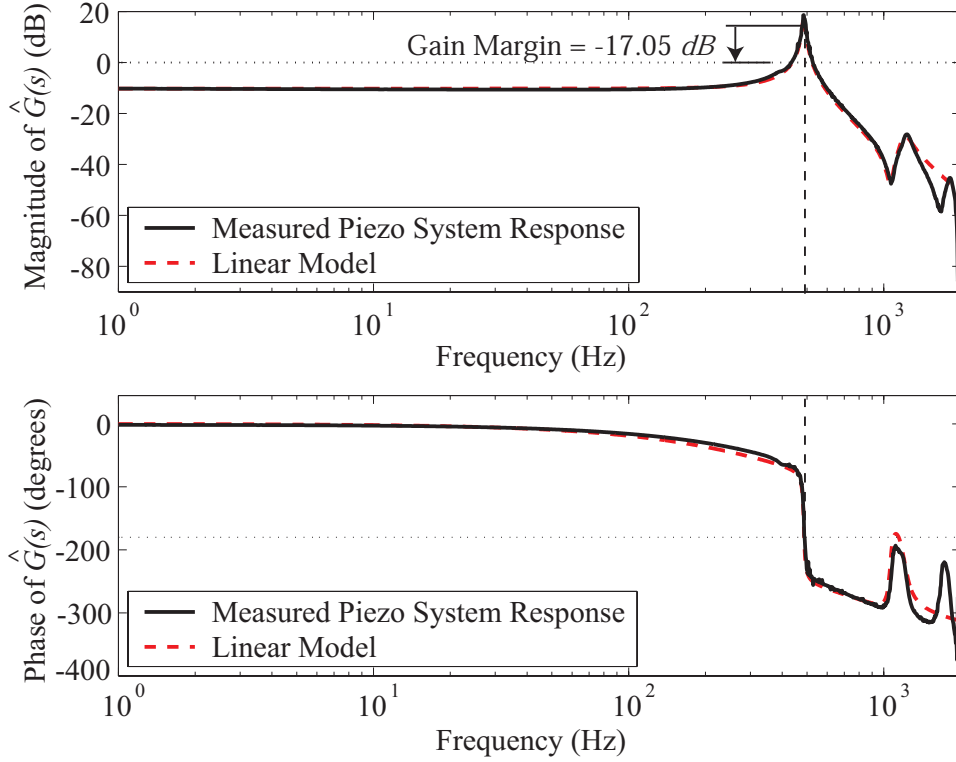
Figure 3.2: Frequency response of the experimental piezoactuator system measured over small displacements (± 2 μm): measured (solid line) and linear model (dashed line).

± 2.00 μm range), and the zeros (z_m, for $m = 1, 2$) and poles (p_n, for $n = 1, \cdots, 6$) of the model are presented in Table 3.1. The units of the transfer function $\hat{G}(s)$ can be expressed in actual displacement units ($\mu m/V$) by multiplying with the static sensor gain of 20 $\mu m/V$, i.e., $G(s) = 20\hat{G}(s)$ ($\mu m/V$). The linear single-input single-output (SISO) model (shown as a dashed line in Fig. 3.2) is a good fit of the measured system response up to approximately 1.5 kHz [118].

Remark 1 *The sharp resonant peak at 486 Hz limits scanning to very low frequencies — typically 10–100 times lower than the first resonant frequency during high-precision applications. Therefore, open-loop scanning is limited to less than 5 Hz for avoiding significant vibration effect.*

Table 3.1: Zeros and poles of piezo-positioning system.

m, n	Zeros, z_m (Hz)	Poles, p_n (Hz)
1	-25 + j1059	-411
2	-25 - j1059	-5 + j486
3	—	-5 - j486
4	—	-70 + j1200
5	—	-70 - j1200
6	—	-1200

3.3 Creep and Hysteresis Compensation: High-gain Feedback Control

3.3.1 Improving the gain margin

Positioning errors in piezos can be reduced with the use of feedback control; however, a problem with using feedback-based approaches is the low-gain margin inherent in piezo systems. In particular, piezos ten to have low structural dampening (*i.e.*, high quality factor Q_f or sharp resonant peak) which causes to low gain margin. For example, the experimental piezo-positioning system has a measured gain margin of -17.05 dB (see Fig. 3.3). This means that with a proportional feedback controller, the proportional gain is restricted to be less than 0.14 for stability of the closed loop system; such low-gain feedback controllers do not lead to significant improvement in the tracking response when compared to the open-loop system.

To enable the use of high-gain feedback control, the gain margin was increased by modifying the sharp resonant peak of the open-loop system with a notch filter cascaded with the piezo-positioning system as shown in Fig. 3.1 [39, 38]. The notch filter was chosen as:

$$D(s) = k_D \frac{(s - 2\pi z_1)(s - 2\pi z_2)}{(s - 2\pi p_1)(s - 2\pi p_2)} \left(\frac{V}{V} \right),$$ (3.2)

where $k_D = 2.22$, $z_1 = -5 + j475$ Hz, $z_2 = -5 - j475$ Hz, $p_1 = -100$ Hz, and $p_2 = -5000$ Hz. In the design of the notch filter $D(s)$, the zeros were chosen to cancel the effects of

the dominant resonant peak of the piezoactuator (at 486 Hz); they were placed at 475 Hz to achieve high gain margin for the composite system despite small changes in the location of the resonant frequency of the open-loop system. Moreover, the poles were added to the notch filter for attenuating high frequency noise. The notch filter was realized using analog op-amp circuits (*e.g.*, see [119], pp. 394-399 and Appendix B for more details) and its measured frequency response is shown by the dotted line in Fig. 3.3, together with the superimposed frequency response of the original system (dashed line) for comparing the old and new gain margins. The frequency response of the composite system (solid line in Fig. 3.3) shows that the effect of the sharp resonant peak is significantly reduced, and the gain margin was increased to 30.86 dB.

3.3.2   High-gain Feedback Control

A *proportional-plus-derivative* (PD) high-gain feedback controller of the form:

$$C(s) = K_p + K_d \frac{\sigma^2 s}{(s+\sigma)^2} \quad \left(\frac{V}{V}\right), \tag{3.3}$$

was used to compensate for the effects of creep and hysteresis, and was implemented using analog op-amp circuits (*e.g.*, see Fig. 3.1 and Appendix B). The two-poles in the derivative term (at 5000 Hz, *i.e.*, $\sigma = 3.14 \times 10^4$ rad/s) attenuates high frequency noise that will otherwise be amplified by differentiating the error signal. The feedback gains (K_p and K_d) were tuned experimentally (*e.g.*, see [120], Section 4.5); the controller gains were chosen to be $K_p = 20$ and $K_d = 6.56 \times 10^{-3}$. With these controller gains, the settling time for the output response (to 2% error of the final value for a step input) was reduced significantly from 100 ms (open-loop case) to 6 ms (closed-loop case) as shown in Fig. 3.4.

3.4   Vibration Compensation: Inversion-based Feedforward Control

Tracking error due to vibration can be reduced by exploiting the known dynamics of the piezo-positioning system. An inversion-based approach was considered for finding feedforward inputs that compensate for the vibrational dynamics during high-speed positioning [14, 16, 121, 122, 117]. The linear vibrational dynamics model $G(j\omega)$ of the piezo-positioner
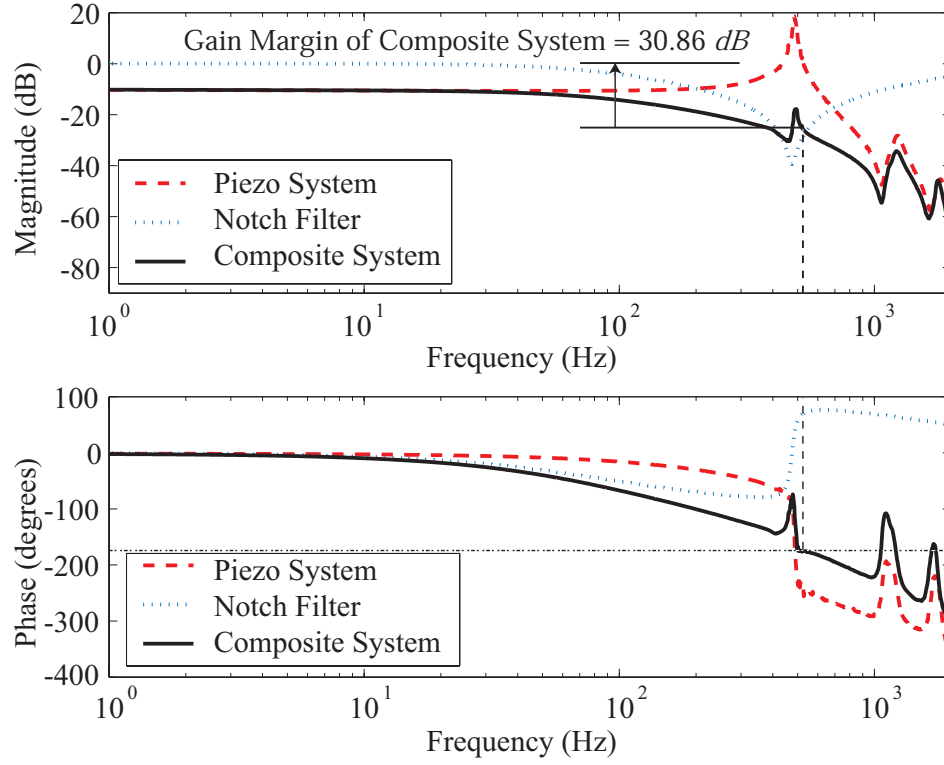
Figure 3.3: Measured frequency response of the experimental piezoactuator system (dashed line), the notch filter (dotted line), and the notch filter cascaded with the experimental system (solid line). The measured gain margin of the original system is -17.05 dB, whereas the gain margin of the composite system is 30.86 dB.
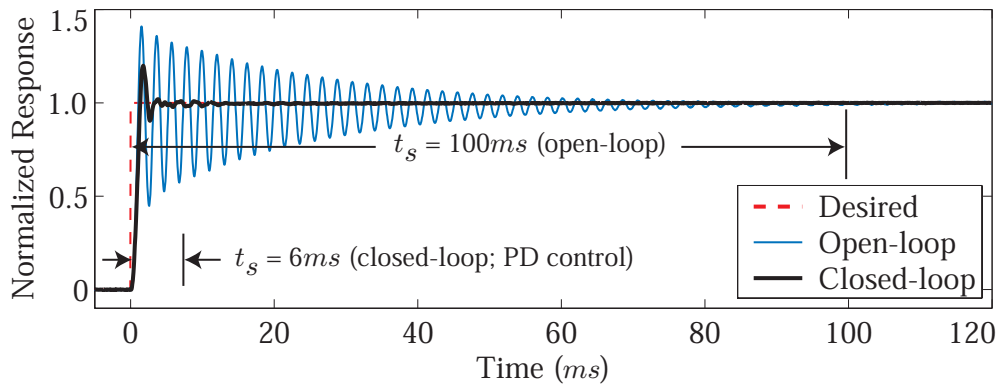
Figure 3.4: Step response comparing 2% settling time between open-loop (without notch filter) and closed-loop performance. Desired displacement is 25 μm.

was inverted to find such feedforward inputs. Two methods of model-based dynamic compensation were considered for the design of the feedforward controller: (i) the exact and (ii) the optimal inversion method. In the first method, for a SISO system, the feedforward input is given by

$$u_{ff}(j\omega) = G^{-1}(j\omega)x_d(j\omega), \tag{3.4}$$

where $G^{-1}(j\omega)$ is the inverse of the system and $x_d(j\omega)$ is the desired trajectory. In Eq. (3.4), the Laplace transform of each term has been converted into the frequency domain by replacing s with the complex frequency $j\omega$. If the system is nonminimum phase (*i.e.*, $G(j\omega)$ has right-half-plane zeros), the feedforward input is noncausal, but can be computed as described in reference [123]. This Fourier-based inversion approach (described in detail in references [14, 16]) finds the feedforward input required to track the desired trajectory x_d.

However, the input generated by exact inversion (Eq. (3.4)) can be excessively large for tracking certain output trajectories, especially for trajectories containing frequency components near *lightly-damped* system zeros. These large command signals can saturate the system's actuators, and in the case of piezos, they can depolarize them. Additionally, for system models with a high degree of uncertainty over a particular frequency range, exact inversion can result in poor performance irrespective of the type of feedback controller being used [118]. Therefore, an optimal inversion approach [121] was also considered in the design of feedforward input that trade-off tracking precision with other goals such as reduction of input energy. In particular, the optimal inversion approach finds feedforward input that minimize the cost functional given by:

$$J(u) = \int_{-\infty}^{+\infty} \{u^*(j\omega)R(j\omega)u(j\omega) + [x_d(j\omega) - x(j\omega)]^* \\ \times Q(j\omega)[x_d(j\omega) - x(j\omega)]\}d\omega, \tag{3.5}$$

where each term is expressed in the frequency domain. The superscript "*" denotes complex conjugate transpose. The cost criterion J is a design tool for trading off tracking precision with reduction of input energy by varying the relative weights between Q and R. These parameters represent frequency dependent real-valued weightings and should not be simultaneously zero at any frequency. For instance, by increasing R relative to Q, input magnitude (energy) is reduced at the cost of tracking precision. Conversely, tracking error

is minimized by increasing Q relative to R. We point out two extreme cases for the choice of Q and R. First, if the weight on the tracking error is zero (*i.e.*, $Q = 0$) and R nonzero, then not tracking the desired trajectory x_d would be the best approach. In the second case, if $R = 0$ and Q nonzero, then exact tracking is achieved, *i.e.*, $x = x_d$. The solution (input that minimizes J subject to weightings Q and R) of the optimal inversion approach is given by [121]

$$
\begin{aligned}
u_{opt}(j\omega) &= \left[\frac{G^*(j\omega)Q(j\omega)}{R(j\omega) + G^*(j\omega)Q(j\omega)G(j\omega)} \right] x_d(j\omega), \\
&\triangleq G_{opt}(j\omega)x_d(j\omega).
\end{aligned}
\tag{3.6}
$$

By applying $u_{opt}(j\omega)$, it causes the system to track of the modified desired trajectory, *i.e.*,

$$
\begin{aligned}
x_{opt}(j\omega) &= G(j\omega)u_{opt}(j\omega), \\
&= G(j\omega)G_{opt}(j\omega)x_d(j\omega), \\
&\triangleq G_f(j\omega)x_d(j\omega).
\end{aligned}
\tag{3.7}
$$

In Eq. (3.7), $G_f(j\omega)$ is a filter that modifies the desired trajectory $x_d(j\omega)$ based on the R and Q weightings. When the optimal inversion approach is integrated to a feedback controlled system, the modified trajectory x_{opt} is used as the reference trajectory to the feedback system (*i.e.*, $x_{ref} = x_{opt}$ in Fig. 3.1). For a discussion of trade-offs and design related issues using this technique, for example, see references [122, 118].

3.5 *Experimental Results and Discussion*

In this section, experimental results are presented to demonstrate the efficacy of the decoupled and integrated feedback and feedforward approach. First, we demonstrate creep and hysteresis compensation using the proposed high-gain *proportional-plus-derivative* feedback controller for scanning at slow rates ($\leq 1\ Hz$). Then, we demonstrate that the output tracking performance at high speeds (for the feedback system) can be significantly improved by integrating feedforward inputs (computed using the two inversion methods presented). Also a discussion of the results is included.

3.5.1 High-gain Feedback Control

Creep Compensation

Experiments were performed to demonstrate creep compensation using the proposed high-gain feedback controller. Figure 3.5 shows a step response measured over a period of 15 minutes. The sampling period during measurement was 250 ms, too slow to capture the initial dynamic response of the system [88], but adequate for capturing the slow creep behavior as depicted in Fig. 3.5. Two cases were compared: (i) without high-gain feedback compensation (dashed line), and (ii) with high-gain feedback compensation (solid line). The desired output displacement for both cases is 25.00 μm (dotted line). For the feedback system, to achieve the desired output range, the applied reference trajectory was the desired trajectory scaled by the measured static gain of closed-loop system, *i.e.*, $x_{ref} = 1.14x_d$. This scaling by the static gain is used for all experiments that involved only feedback control. Without feedback compensation (case (i)) the output creeps to 33.41 μm after 15 minutes, and the maximum positioning error as a percentage of the step range (25 μm) is $e_{max} = 33.64\%$, defined as

$$e_{max}(\%) = \max \left| \frac{x_d - x}{\max(x_d) - \min(x_d)} \right| \times 100\%, \tag{3.8}$$

where x_d and x are the desired and measured displacements in μm, respectively. In contrast, the displacement measured after 15 minutes with high-gain feedback compensation (case (ii), solid line) is 25.37 μm, resulting in the maximum positioning error $e_{max} = 1.48\%$, a reduction by over 95% compared to the open-loop case.

Hysteresis Compensation

Without compensation (open-loop), the effect of hysteresis is significant as noted by the difference between the desired and measured response (see Fig. 3.6(a)). In Fig. 3.6(b) (hysteresis curve), the measured displacement x is plotted versus the desired displacement x_d, which clearly shows the distortion due to hysteresis. Without compensation the maximum positioning error is $e_{max} = 18.08\%$ (Eq. (3.8)). Hysteresis can also cause the output-to-input ratio to vary with displacement range (or equivalently, with the amplitude of the
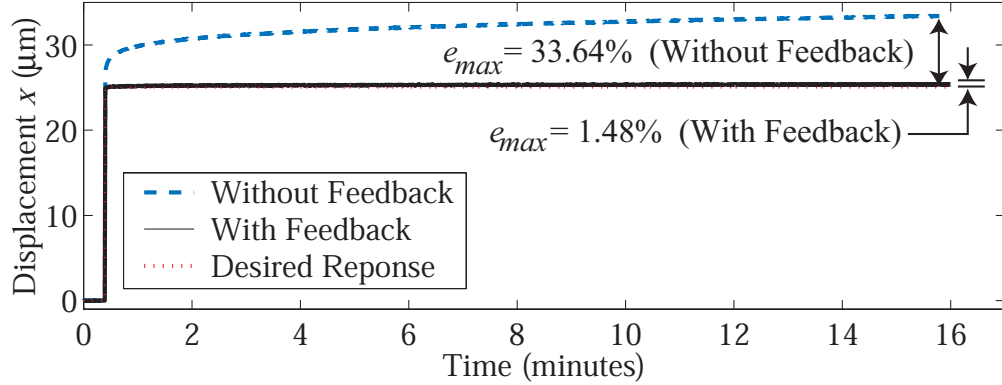
Figure 3.5: Experimental results: creep compensation using high-gain feedback control. Dashed line is without compensation, solid line is with compensation, and dotted line is the desired response.

applied electric field). In terms of the model (Eq. (3.1)), this behavior can be attributed to the open-loop gain factor k changing, or the effective sensitivity of the piezo-positioner changing (*e.g.*, [3, 98, 87]). More specifically, the variation in the system's gain factor is observed by the change in slope of each individual hysteresis loop, *i.e.*, the slope of the line connecting the turning points of each loop shown in Fig. 3.6(b). Graphically, this variation is represented in Fig. 3.6(c), a plot of the gain factor k (nondimensionalized with respect to the nominal gain factor $k_0 = 7.20 \times 10^{13}$, Eq. (3.1)) versus the desired displacement amplitude. In Fig. 3.6(c), k increases by as much as 37% over 25 μm displacement range. *The gain factor can also be affected by temperature* [15]. We show next that high-gain feedback control minimizes the effects of hysteresis and the variation in the gain factor in the closed-loop system.

Experiments were performed to demonstrate hysteresis compensation using the proposed feedback controller and results are shown in Fig. 3.7. Figure 3.7(a) shows the time response of the closed-loop system for scanning at 1 Hz—slow enough that dynamics effects are negligible and fast enough that creep effects are small. The maximum scan range is 50.00 μm (*i.e.*, [-25.00, 25.00] μm). In Fig. 3.7(b) (hysteresis curve), the measured displacement x is plotted versus the reference (desired) displacement x_{ref} for the feedback controlled system.
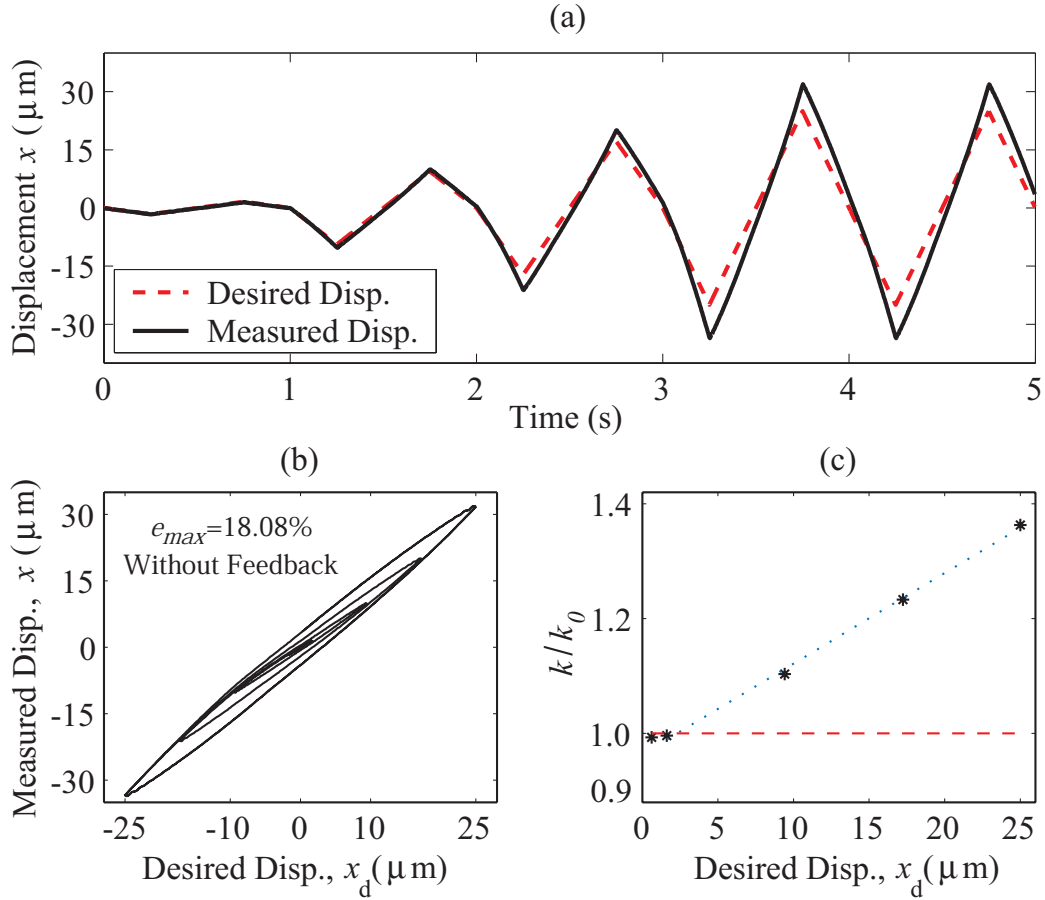
Figure 3.6: Hysteresis effect and variation in the output-to-input ratio (the system gain factor) in the experimental piezo-positioning system (scanning at $1\ Hz$): (a) displacement versus time, (b) hysteresis curves, and (c) variation in system gain factor versus desired displacement.
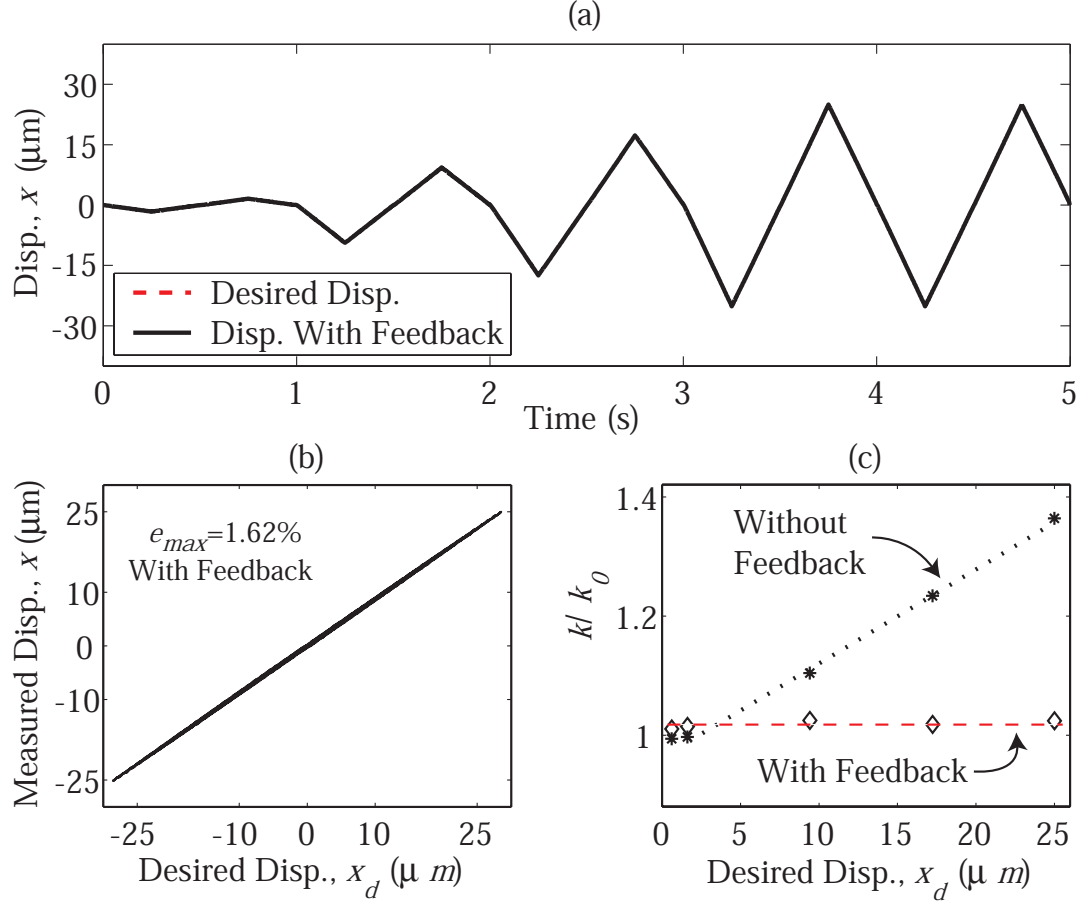
Figure 3.7: Experimental results: hysteresis compensation using high-gain feedback control; (a) displacement versus time of high-gain feedback system, (b) closed-loop hysteresis curves, and (c) comparison of the variation in the open-loop and closed-loop system gain factor.

By applying high-gain feedback control, positioning error due to hysteresis was significantly reduced, resulting in the maximum positioning error $e_{max} = 1.62\%$, a reduction by over 91% compared to the uncompensated case (Figs. 3.6(a) and (b)). Also, the hysteresis reduction lead to a smaller closed-loop gain factor variation (*e.g.*, the closed-loop transfer function gain factor increases by only 1.3% over 25 μm displacement range as shown in Fig. 3.7(c)) and feedback control provides robustness to such variations. We note that further performance improvements can be achieved provided larger feedback gains can be used; however, the possible improvement was limited by the gain margin of the system (30.86 dB).

High-speed Scanning Using Feedback

The performance of the feedback controller was evaluated for high-speed tracking of a sinusoidal reference trajectory over 50.00 μm displacement range. Figure 3.8 compares the tracking for 1, 50, 100, and 140 Hz scan rates and Table 3.2 lists the corresponding maximum tracking error e_{max} and root-mean-square error e_{rms} as a percentage of the total displacement range (50.00 μm). For scanning at 1 Hz, the maximum error is $e_{max} = 1.59\%$ (Eq. 3.8) and the root-mean-square error is $e_{rms} = 0.95\%$, defined as

$$e_{rms}(\%) = \left(\frac{\sqrt{\frac{1}{T} \int_0^T e^2(t)dt}}{\max(x_d) - \min(x_d)} \right) \times 100\%, \tag{3.9}$$

where T is the scanning period (*e.g.*, scanning at 1 Hz, $T = 1$ s), and $e(t) = x_d(t) - x(t)$ is the tracking error. Overall, the experimental results show that feedback control achieves good tracking (*i.e.*, $e_{max} \leq 5\%$) over moderate scan rates (< 50 Hz). However, at high speeds, the effect of dynamics becomes significant, where phase lag and vibration in the output contribute greatly to the tracking error and this leads to distortion in piezo-positioning. Tracking error as much as 16.90% is observed for scanning at 140 Hz. At higher scan rates (> 140 Hz in the experimental system), the unacceptably large error causes the feedback controller to saturate (*i.e.*, the magnitude of the output of the op-amp circuit exceeds 10 V). As creep and hysteresis effects are minimized, experimental results show that compensation of vibrational dynamics at high speeds is not effective using feedback control. However, we demonstrate next that adding feedforward inputs can significantly improve the performance of the feedback-controlled system.

3.5.2 Integrated Feedback and Feedforward Control: Vibrational Dynamics Compensation at High Speeds

In the first experiment, feedforward input computed off-line using the exact inversion approach (Eq. (3.4)) is integrated to the high-gain feedback system for tracking a sinusoidal reference trajectory (see Fig. 3.1). In the second experiment, the optimal inversion method is applied for tracking a more general (triangular) output trajectory. Both experiments
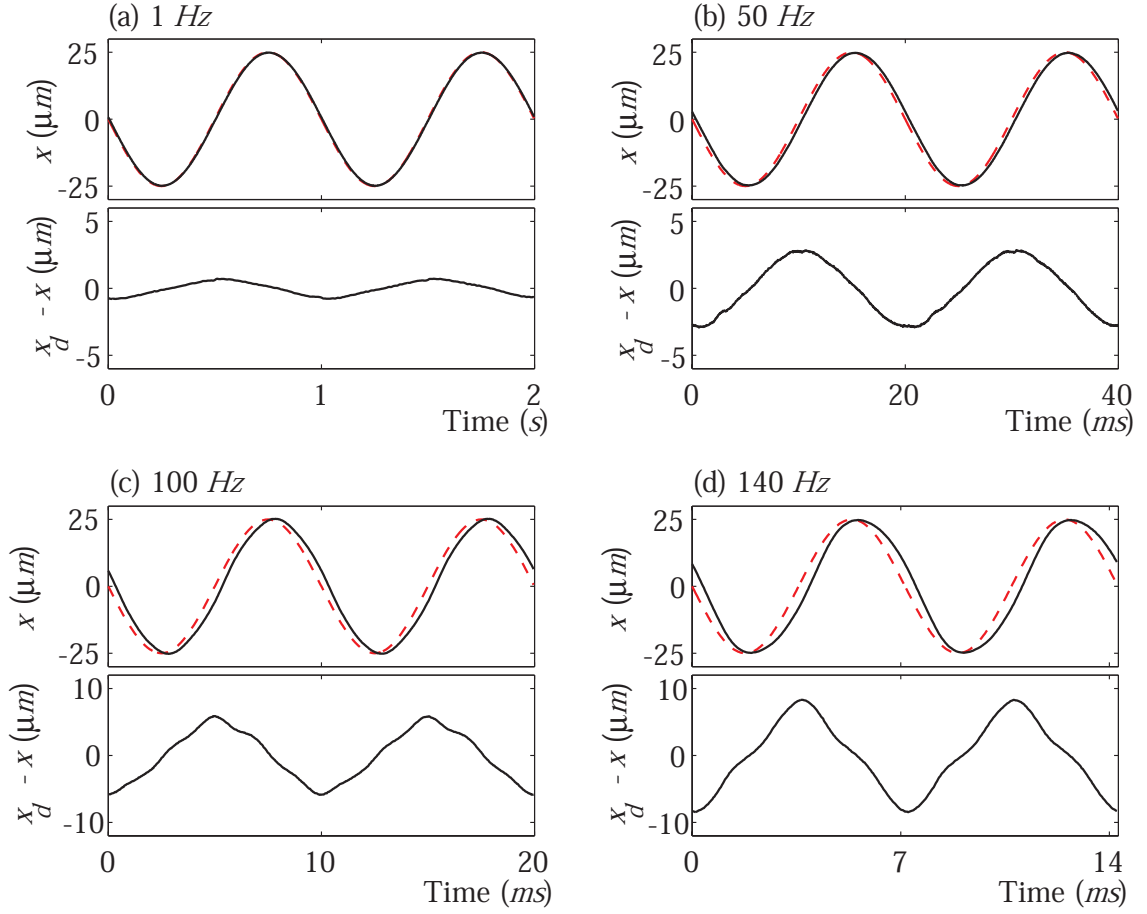
Figure 3.8: Experimental results: Tracking of sinusoidal reference trajectory using high-gain feedback control. Scan rates: (a) 1 *Hz*, (b) 50 *Hz*, (c) 100 *Hz*, and (d) 140 *Hz* (beyond this frequency, PD controller output saturates). Solid line is the measured response and dotted line is the desired trajectory.

Table 3.2: Tracking performance for sinusoidal reference trajectory using high-gain feedback control. Values reported as percentage of total output range (50.00 μm).

Scan Rate (Hz)	e_{max} (%)	e_{rms} (%)
1	1.59	0.95
50	5.79	3.93
100	11.72	7.40
140	16.90	10.38

illustrate that substantial improvement in output tracking performance can be achieved by integrating feedback and inversion-based dynamic feedforward input.

Results for the first experiment are shown in Fig. 3.9, which illustrate the tracking performance of a sinusoidal trajectory using feedback integrated with exact inversion feedforward control. The scan range for the experiment is 50.00 μm. Table 3.3 lists the associated performance measures, e_{max} and e_{rms}, for 140, 200, 300 and 450 Hz scan rates. The initial scan rate of 140 Hz (Fig. 3.9(a)) was chosen because it was the limit of the feedback only case (Fig. 3.8(d)). The feedforward input was computed using the exact inverse of $G(j\omega)$ (Eq. (3.4)) and augmented to the feedback input (i.e., the input to the piezo system is $u = u_{fb} + u_{ff}$, Fig. 3.1). The reference trajectory to the feedback system is the desired trajectory, i.e., $x_{ref} = x_d$. The experimental results confirm that integrating dynamic-inversion feedforward inputs significantly reduces the maximum and root-mean-square of the tracking error. For example, scanning at 140 Hz using the integrated approach reduces e_{max} and e_{rms} by 78.52% and 82.66%, respectively, compared to using only feedback compensation for scanning at the same rate (Fig. 3.8(d) and Table 3.2). As shown, the integrated feedback/feedforward approach achieves good tracking (i.e., $e_{max} \leq 5\%$) beyond 300 Hz, an improvement by over six-times compared to using only feedback control. Furthermore, the bandwidth of the integrated scheme is improved to 450 Hz, i.e., the controller saturates beyond this frequency. The improvement is substantial compared to the 140 Hz limit for the feedback only case. In addition, the experimental results show that the integrated approach maintains precision positioning over a wider range of scan rates; the high-gain feedback control accounts for creep and hysteresis effects, while the inversion feedforward input compensates for vibrational dynamics effects at high speeds.

Finally, in the second experiment, the optimal inversion approach was integrated with the feedback system to demonstrate tracking of a more general (triangular) trajectory. The results of the second experiment are shown in Fig. 3.10 and Table 3.4. We compare the performance of the integrated feedback/feedforward approach to the proposed high-gain feedback controller and the scan range for the experiment is 50.00 μm. For the integrated feedback/feedforward scheme, the optimal input u_{opt} tracks the modified desired trajectory x_{opt}, and thus the reference trajectory to the feedback system is $x_{ref} = x_{opt}$; for the feedback
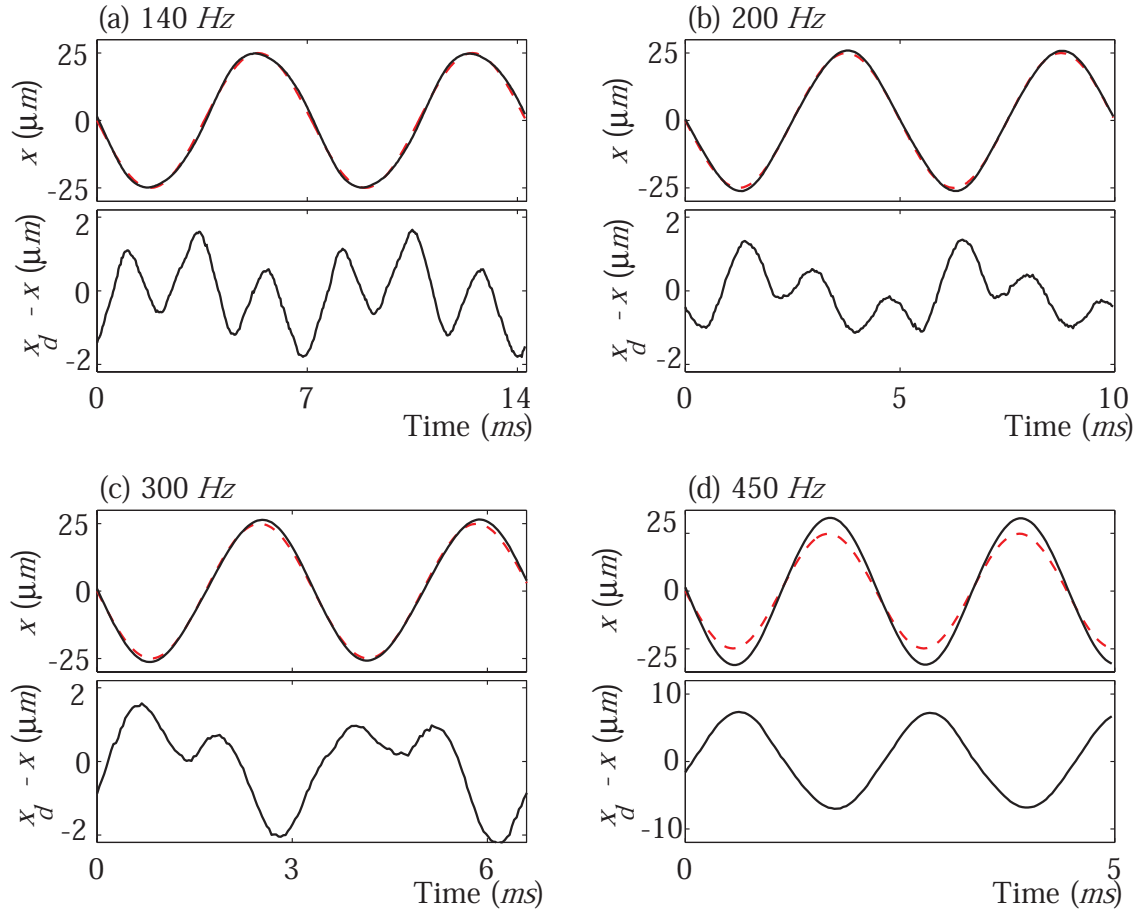
Figure 3.9: Experimental results: tracking of sinusoidal reference trajectory using integrated feedback and exact inversion feedforward control. Scan rates: (a) 140 Hz, (b) 200 Hz, (c) 300 Hz, and (d) 400 Hz. Solid line is measured response and dotted line is desired trajectory.

Table 3.3: Tracking performance for sinusoidal reference trajectory using integrated feedback and exact inversion feedforward control. Values reported as percentage of total output range (50.00 μm).

Scan Rate (Hz)	e_{max} (%)	e_{rms} (%)
140	3.63	1.80
200	2.72	1.39
300	4.88	2.32
450	14.81	10.15
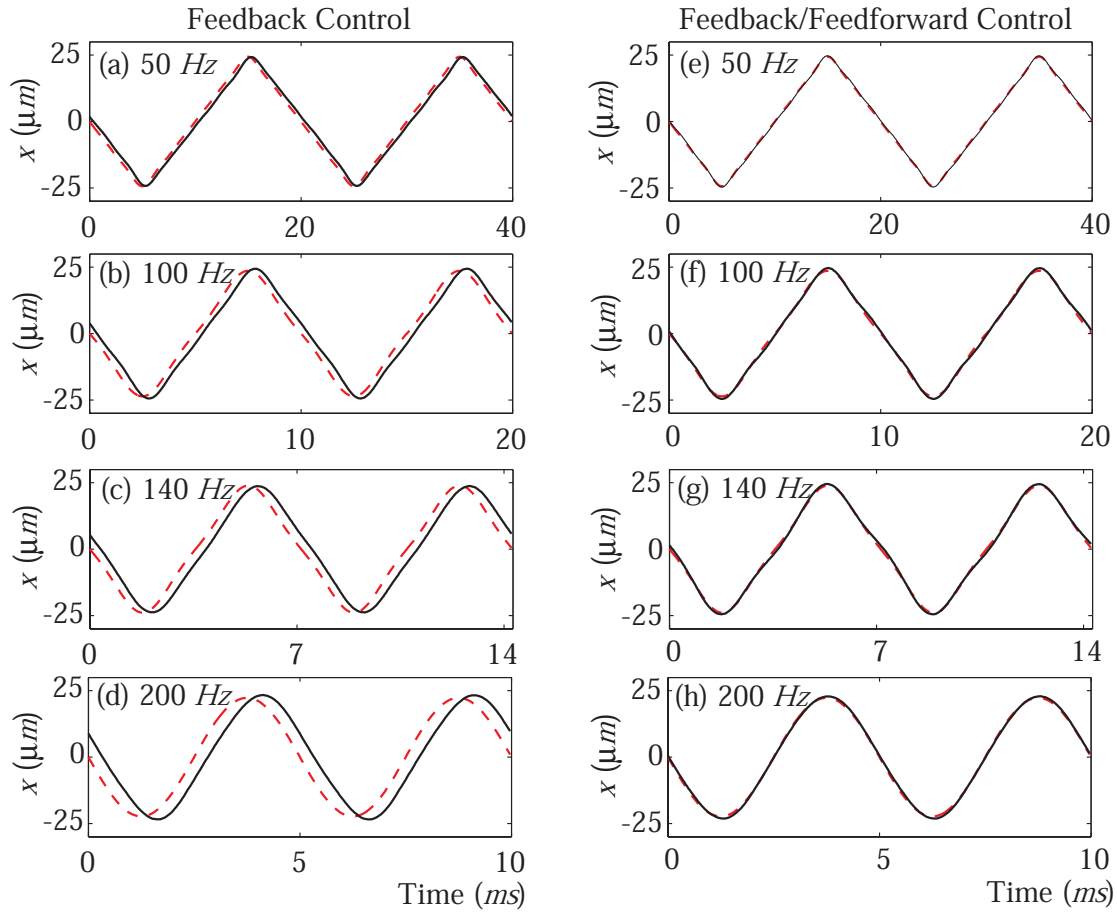
Figure 3.10: Experimental results: tracking of triangular reference trajectory. (a)–(d) Feedback control. (e)–(h) Feedback and optimal inversion feedforward control. Optimal weightings were chosen as $Q = 1$ and $R = 0$ for $\omega \leq 450\,Hz$, and $Q = 0$ and $R = 1$ for $\omega > 450\,Hz$. Solid line is the measured response and dotted line is the desired trajectory.

Table 3.4: Tracking performance for triangular reference trajectory using integrated feedback and optimal inversion feedforward control. Values reported as percentage of total output range (50.00 μm).

Scan Rate (Hz)	Feedback		Integrated Feedback/Feedforward	
	e_{max} (%)	e_{rms} (%)	e_{max} (%)	e_{rms} (%)
50	4.37	3.58	1.54	0.74
100	9.49	6.79	2.95	1.39
140	12.11	9.33	2.94	1.42
200	18.15	13.69	2.03	1.18

only case, we chose $x_{ref} = 1.14 x_{opt}$ (scaled by the DC gain of the closed-loop system). The weightings of the optimal inversion controller were chosen to give up tracking of all frequency components beyond 450 Hz (to avoid saturation). In particular, the weightings are $Q = 1$ and $R = 0$ for $\omega \leq 450 \ Hz$, and $Q = 0$ and $R = 1$ for $\omega > 450 \ Hz$.

The integrated feedback and optimal inversion feedforward approach substantially reduces positioning errors compared to just using feedback control for tracking a triangular trajectory as illustrated in Fig. 3.10 and Table 3.4. Good tracking (i.e., $e_{max} \leq 5\%$) is achieved even at the 200 Hz scan rate. Furthermore, the maximum and root-mean-square of the tracking error were reduced by over 88% and 91% at this scan rate compared to using only feedback control.

In summary, the experimental results show that the proposed decoupled feedback/ feedforward approach significantly improves tracking performance of an experimental piezo-positioning system. In particular, by achieving relatively high gain (by cascading a notch filter to improve the gain margin of the system), a feedback controller can be designed to account for creep and hysteresis effects without modeling such complicated behaviors. Additionally, the feedback controller is robust to parameter variation (e.g., such as change in the system's gain factor). Although feedback control can account for creep and hysteresis effects, it provides limited dynamic compensation at high scan rates. However, the per-

formance of such systems can be improved substantially by integrating feedforward inputs. Specifically, the inversion-based approach significantly improves the positioning precision at high scan rates as well as increase the system's bandwidth. Therefore, the integrated approach provides a means of achieving precise positioning over a wider range of scan rates and displacements.

3.6 Summary

We proposed a decoupled feedback/feedforward approach to compensate for the effects of creep, hysteresis and vibration for piezoactuators. By achieving relatively high gain (by cascading a notch filter to improve the gain margin of the system), a feedback controller can be designed to account for creep and hysteresis effects without modeling such complicated behaviors. Vibration compensation was achieved by integrating feedforward inputs computed using the inversion-based approach. Experimental results demonstrate a significant performance increase for an experimental piezo-positioning system over extended periods of time, long ranges and high scan rates. In the remaining chapters of this dissertation, we will apply iterative learning control to further improve the tracking precision. In particular, the method will be developed for hysteretic systems.

Chapter 4

THE PREISACH HYSTERESIS MODEL

This chapter focuses on the Presiach hysteresis model. The properties of the model will be used in the following chapter to develop and analyze an iterative learning control scheme to compensate for hysteresis. The first section of this chapter describes the modeling of piezo-based positioning systems as a cascade two sub-systems: (i) a rate-independent nonlinear element that represents the hysteresis behavior and (ii) a linear time-invariant dynamic block that captures the creep and vibration effects. Then, subsequent sections describe in detail the Preisach hysteresis model and its properties in the context of the study in this dissertation.

4.1 Modeling Piezo-based Positioners

Piezo dynamics consists of hysteresis, creep and vibration effects [2]. To accurately model a piezo-based system requires consideration of all three effects. To this end, we consider a widely used model structure which involves cascading a nonlinear element (NLE), representing the hysteresis behavior, with a linear time-invariant (LTI) dynamic block, which captures the creep and vibration effects, as shown in Fig. 4.1 [124, 2, 125]. Such a model structure, where a nonlinear element precedes (and is in series with) a LTI system, is known as a Hammerstein-based model. Hammerstein-based dynamic models have been used to characterize nonlinear chemical processes [126] and hysteresis behavior [124], for example. The structure of the model is justified by observing that the physical mechanisms of hysteresis behavior in piezos is attributed to domain wall interaction, a phenomenon that leads to nonlinear electromechanical coupling [127, 128, 129, 97]. For instance, the induced strain in a piezoactuator is a nonlinear function of the applied electric field (denoted by u); and as a result, the effect of hysteresis can be regarded as an input nonlinearity. On the other hand, it has been shown that the relationship between the induced strain and mechanical
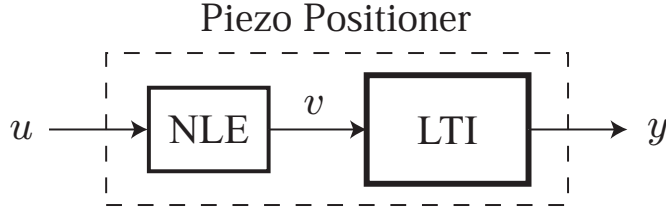
Piezo Positioner

Figure 4.1: The model of piezoelectric positioners. The applied electric field is denoted by u, which is mapped to v by a rate-independent nonlinear element (NLE), and the signal v becomes the input to the linear time-invariant dynamic block (LTI), which has output y.

displacement behaves linearly [130, 131]. Therefore, the input-to-output behavior of piezo-based systems can be modeled by combining a rate-independent nonlinear element in series with a linear time-invariant dynamic block as shown in Fig. 4.1. In this representation, the rate-independent nonlinear element maps the input u to v and then v becomes the input to the LTI block with output y (see Fig. 4.1). More specifically, the complete model is given by

$$y(t) = G(v(t)); \qquad v(t) = \mathcal{H}[u](t), \tag{4.1}$$

where $\mathcal{H}$ represents the rate-independent[1] hysteresis behavior, G is a linear mapping from v to y and u is the input to the system. The above representation has been exploited in the past for position control [2, 125]. In the next section, we describe the Preisach model, the rate-independent nonlinear element $\mathcal{H}$, in more detail.

We note that for the model depicted in Fig. 4.1, given a desired trajectory y_d, the system inversion technique [14, 16] can be used to find input to achieve y_d. Therefore, in the remainder of this dissertation, we focus on the hysteresis behavior $\mathcal{H}$ and consider the objective of iteratively finding a feedforward input to track a desired trajectory v_d. At the end of this dissertation, we discuss future work (see Chapter 8) to extend the iterative learning control method to include the LTI dynamics.

---

[1]A formal definition of rate independence is discussed in reference [18], Section 2.2.

4.2   The Preisach Hysteresis Model and the Preisach Plane

In 1935, Ferenc Preisach[2], through his studies of magnetic materials, developed an interesting model to describe hysteresis [133]. Although it was originally developed to model the hysteresis in magnetic materials, the Preisach model has been successfully applied to model the hysteresis behavior in piezoelectric materials (*e.g.*, see references [134, 135, 113, 136, 137]), as well as many other hysteretic systems such as shape memory alloys [138, 139] and magnetostrictive actuators [140]. Additionally, the unique structure of Preisach's model motivated further abstraction of the model to more general hysteresis operators by Krasnosel'skii and Pokrovskii [141], the properties of which have been studied extensively in the past, for example, in the collection edited by Visintin [142] and in the work of Brokate and Sprekels [18]. However, one drawback of this generalization is that the parameters of the model are difficult to associate with physical systems. On the other hand, the generality of the model extends its usefulness to a broad spectrum of systems. Therefore, the results of this thesis will be valid for systems with hysteresis behavior that fit the Preisach model description.

In the Preisach model, the individual dipoles in the magnetic (or piezoelectric) material are modeled by elementary relays as shown in Fig. 4.2(a). Each relay can assume a value of $+1$ or -1 depending on the current and future values of the input u (*e.g.*, applied voltage). More formally, the relay operator $\mathcal{R} : \mathbb{R} \to \{-1, +1\}$ is defined as [143]:

$$\mathcal{R}_{\alpha,\beta}[u](t) = \begin{cases} +1 & u(t) > \alpha, \\ -1 & u(t) < \beta, \\ \text{unchanged} & \beta \leq u(t) \leq \alpha, \end{cases} \quad (4.2)$$

where the input $u \in \mathbb{R}$. For each relay $\mathcal{R}$, there is a unique pair of "up" and "down" switching values (α, β) associated with it, such that $\alpha \geq \beta$. In Fig. 4.2(a), the horizontal segment is reversible; however, the vertical segments can only be traversed in one direction. Relays with $\alpha = \beta$ are called degenerate, and the associated vertical segments can be traversed in both directions. The elementary relay operator is considered to exhibit local

---

[2]Very little is known about Ferenc Preisach. In fact, most do not know his first name. In honor of his contributions in the area of hysteresis modeling, Vajda and Torre published a short history of Ferenc Preisach in the March 1995 issue of the IEEE Transactions on Magnetics [132].
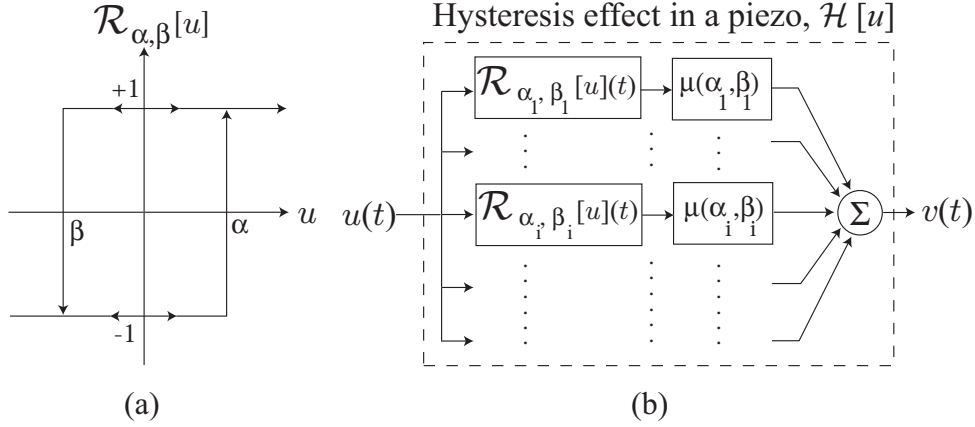
Figure 4.2: (a) The elementary relay (Preisach hysteron) with switching values $\alpha \geq \beta$, and (b) the model of hysteresis in a piezo positioner, where the output $v(t)$ is the sum of weighted hysterons.

memory [143]; that is, the output of the relay for $t \geq t_0$ can be uniquely determined by knowing the output $v(t)$ at the current time t_0 and the input $u(t)$ for $t \geq t_0$. In piezoelectric materials, the relays $\mathcal{R}_{\alpha,\beta}$ can represent individual electric dipoles and the two states, ± 1, model the possible orientation of the dipole, for example. In addition, the behavior of these relays, and hence the Preisach model, is only defined for continuous inputs u.

By modeling the behavior of individual dipoles as elementary relays, Ferenc Preisach then assumed that the output v is the weighted sum of an infinite number of relays as illustrated in Fig. 4.2(b). Thus, the output v is expressed as:

$$v(t) = \mathcal{H}[u](t) = \iint_{\alpha \geq \beta} \mu(\alpha,\ \beta)\mathcal{R}_{\alpha,\beta}[u](t)d\alpha d\beta, \tag{4.3}$$

where $\mu : \mathbb{R} \times \mathbb{R} \to \mathbb{R}$ is the weighting associated with each relay $\mathcal{R}_{\alpha,\beta}$, otherwise known as the Preisach weighting function [143, 18].

The collection of all possible "up" and "down" switching pairs (α, β) make up the Preisach plane $\mathbf{P}$, defined as

$$\mathbf{P} \triangleq \{(\alpha, \beta) \in \mathbb{R} \times \mathbb{R} | \alpha \geq \beta\}. \tag{4.4}$$

However, the boundary of the Preisach plane for physical systems is limited by the restrictions on the input u, for instance $u \in [\underline{u}, \bar{u}]$. It is quite possible that relays outside of this boundary may never be exercised. For hysteresis with closed major loops, the behavior is bounded by $[\underline{u}, \bar{u}]$. The hysteresis behavior outside of $[\underline{u}, \bar{u}]$ are fully reversible, therefore only degenerate relays can contribute to the output. Taking this restriction into consideration, and for convenience, the Presiach plane $\mathbf{P}$ is redefined as

$$\mathbf{P} \triangleq \{(\alpha, \beta) | \alpha \geq \beta; \underline{u} \leq \alpha; \beta \leq \bar{u}\}. \tag{4.5}$$

The behavior of the model in this restricted plane produces closed major hysteresis loops. In the remaining when points (α, β) are considered to be outside of $\mathbf{P}$, they will be stated explicitly. Furthermore, we emphasize that every point (α, β) in the Preisach plane $\mathbf{P}$ is associated with a unique relay $\mathcal{R}_{\alpha,\beta}$. It will be shown in the following that the Preisach plane provides a convenient way of keeping track of the state of relays $\mathcal{R}_{\alpha,\beta}$ as the input u varies.

4.2.1   The Geometric Interpretation of the Presiach Plane

The geometric interpretation of the Preisach model provides interesting insight. For example, to illustrate this consider the right triangle $\mathbf{P}$ shown in Fig. 4.3(a). This triangular region is the restricted Preisach plane $\mathbf{P}$. The hypotenuse of the triangle is the line $\alpha = \beta$ and the vertex of the right angle is the point $(\underline{u}, \bar{u})$. As previously stated, the values $\underline{u}$ and $\bar{u}$ relate to the limits of the input u, that is, $u \in [\underline{u}, \bar{u}]$. Now, assume that the input $u(t)$ at some time t_0 is below $\underline{u}$. Then, all relays $\mathcal{R}_{\alpha,\beta}$ with α and β values below $\underline{u}$ are in the -1 state. This is depicted in Fig. 4.3(a) by the open right triangle. In this situation, the system is said to be in the state of "negative saturation", *i.e.*, every relay in the right triangular region $\mathbf{P}$ is in the "down" or -1 state.

Next, assume that the input $u(t)$ is monotonically increased to a value u_1 at time t_1. As the input increases, relays with α value below the current input value $u(t)$ are switched "up" such that their outputs are $+1$. Geometrically, the relays in the $+1$ state lie below the horizontal line depicted in Fig. 4.3(b), *i.e.*, the shaded region represents the relays that
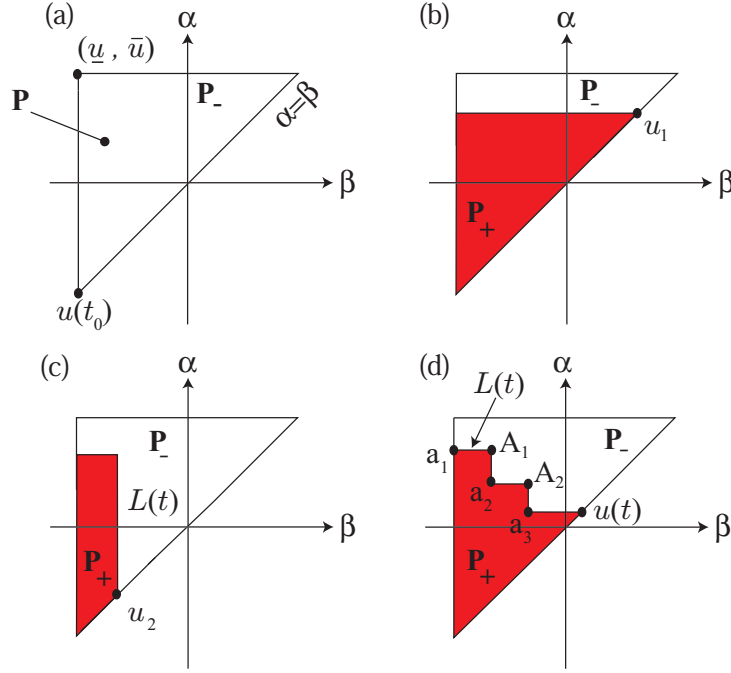
Figure 4.3: The Preisach plane and its behavior with respect to the input u.

have switched "up". Then, the right triangle region $\mathbf{P}$ is subdivided into two sets:

$$\mathbf{P}_+(t) \triangleq \{(\alpha, \beta) \in \mathbf{P} \; : \; \text{output } \mathcal{R}_{\alpha,\beta}[u](t) = +1\}, \tag{4.6}$$

$$\mathbf{P}_-(t) \triangleq \{(\alpha, \beta) \in \mathbf{P} \; : \; \text{output } \mathcal{R}_{\alpha,\beta}[u](t) = -1\}, \tag{4.7}$$

with $\mathbf{P} = \mathbf{P}_+(t) \cup \mathbf{P}_-(t)$. These two sets are connected. Furthermore, we note that as the input increases, the horizontal line $\alpha = u(t)$ sweeps upward, switching relays with α value less than the current input $u(t)$ to the $+1$ state.

Now, we assume that the input $u(t)$ is monotonically decreased to some value u_2 at time t_2. As the input decreases, relays with β value greater than the current input value $u(t)$ are switched "down" such that their outputs are -1. Geometrically, the relays that are in the -1 state lie to the right of the vertical line shown in Fig. 4.3(c). It is easy to see that the Preisach plane at time t is subdivided into the two sets: $\mathbf{P}_+(t)$ and $\mathbf{P}_-(t)$, as described above. In addition, as the input decreases, the vertical line shown in Fig. 4.3(c) sweeps vertically from right to left.

The interface that separates the two sets $\mathbf{P}_+(t)$ and $\mathbf{P}_-(t)$ is denoted by $L(t)$. In fact, as the input increases and decreases monotonically, additional horizontal and vertical links are added to the interface $L(t)$ as shown in Fig. 4.3(d). Therefore, at any instant of time t, the Preisach plane $\mathbf{P}$ is subdivided into two sets: $\mathbf{P}_+(t)$ and $\mathbf{P}_-(t)$, such that $\mathbf{P} = \mathbf{P}_+(t) \cup \mathbf{P}_-(t)$ and the interface $L(t)$ separates the two sets. In his work, Mayergoyz [143] emphasized that the links of $L(t)$ may not necessarily be segments of lines parallel to the coordinate axes. In addition, different weighting functions $\mu_+(\alpha, \beta)$ and $\mu_-(\alpha, \beta)$ can be defined on the positive and negative sets, respectively. However, in the context of this work, we adopt the traditional Preisach model, *i.e.*, the links of $L(t)$ are segments of lines parallel to the coordinate axes and a single weighting function $\mu(\alpha, \beta)$ is assumed over the Presiach plane $\mathbf{P}$. The properties of $\mu(\alpha, \beta)$ is addressed in subsequent sections.

From the geometric perspective of the Preisach model, we conclude that the output $v(t)$ can be expressed in terms of the two sets $\mathbf{P}_+(t)$ and $\mathbf{P}_-(t)$ as,

$$v(t) = \iint_{\mathbf{P}_+(t)} \mu(\alpha,\ \beta)d\alpha d\beta - \iint_{\mathbf{P}_-(t)} \mu(\alpha,\ \beta)d\alpha d\beta. \tag{4.8}$$

Furthermore, considering that $\mathbf{P} = \mathbf{P}_+(t) \cup \mathbf{P}_-(t)$, we obtain

$$
\begin{aligned}
v(t) &= \iint_{\mathbf{P}_+(t)} \mu(\alpha,\ \beta)d\alpha d\beta - \iint_{\mathbf{P}_-(t)} \mu(\alpha,\ \beta)d\alpha d\beta, \\
&= \iint_{\mathbf{P}_+(t)} \mu(\alpha,\ \beta)d\alpha d\beta - \left(\iint_{\mathbf{P}} \mu(\alpha,\ \beta)d\alpha d\beta - \iint_{\mathbf{P}_+(t)} \mu(\alpha,\ \beta)d\alpha d\beta \right), \\
v(t) &= 2 \iint_{\mathbf{P}_+(t)} \mu(\alpha,\ \beta)d\alpha d\beta - \iint_{\mathbf{P}} \mu(\alpha,\ \beta)d\alpha d\beta. \tag{4.9}
\end{aligned}
$$

Now we are ready to state some of the properties of the Preisach model.

4.3 Properties of the Preisach Model

The following properties of the Preisach model will be used in the remainder of this dissertation. We begin with some geometric properties and point out that a detailed discussion of the Preisach model can be found in references [143, 18].

4.3.1 The Wiping-out Property

Mayergoyz [143] presented a representation theorem which states that the wiping-out property and the congruency property constitute the necessary and sufficient conditions for a hysteresis nonlinearity to be represented by the Preisach model. Furthermore, the model is defined over the set of continuous piecewise monotonic inputs. In the following, the wiping-out and the congruency properties are discussed.

The wiping-out property simply states how the interface $L(t)$ evolves as the input u is varied. As previously mentioned, the interface $L(t)$ stores the effect of past input history (extremum), *i.e.*, the Preisach model has the ability of memory storage. To make this more precise, consider the following definition:

Definition 1 (Global Maximum and Minimum) *Consider an input $u(t)$ defined over the time interval $t_0 \le t \le t'$. Assume that at the initial time t_0 the input value $u(t_0)$ was below $\underline{u}$ (e.g., input that achieves full negative saturation). Then, the alternating series of global maximum M_j and global minimum m_j points are defined as:*

$$M_j = \max_{[t_{j-1}^-,t']} u(t); \quad u(t_j^+) = M_j,$$

$$m_j = \min_{[t_j^+,t']} u(t); \quad u(t_j^-) = m_j,$$

for $j = 1, 2, 3, \cdots, q$, where $q \in \mathbb{N}$, and $\mathbb{N}$ is the set of all positive integers.

To better illustrate this definition, consider the input versus time curve shown in Fig. 4.4. The global maximum M_j and global minimum m_j, as defined above, are indicated on the curve in Fig. 4.4.

Property 1 (The Wiping-Out Property) *The Preisach model only accumulates the alternating series of global maximum M_j and global minimum m_j established by Definition 1. Intermediate input extrema are erased.*

The wiping-out property is illustrated in Fig. 4.5. The figure shows how intermediate input extrema are erased as the input varies and how the interface $L(t)$ captures the global maximum and minimum points.
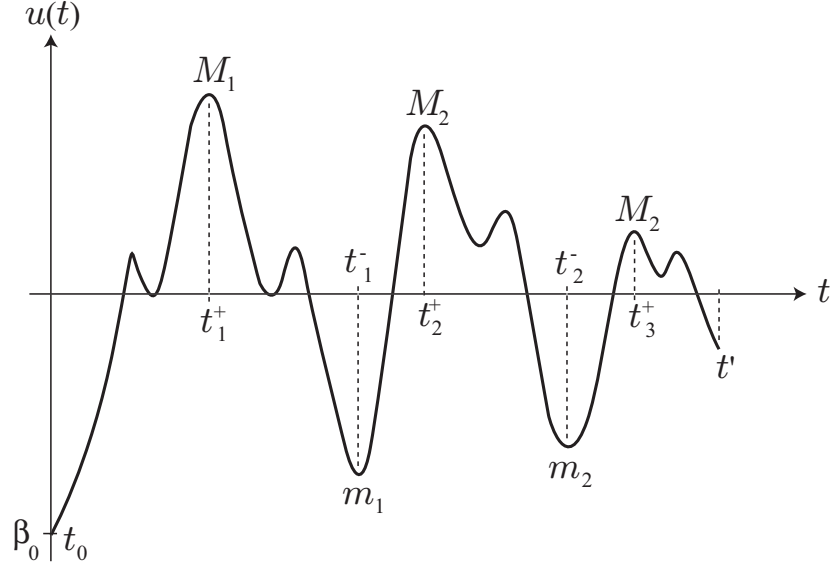
Figure 4.4: Input $u(t)$ and the global maximum and global minimum points.

The coordinates of the vertices for the staircase interface $L(t)$ (as shown in Fig. 4.3(d) and Fig. 4.5) are given by

$$a_0 = (\beta_0, M_1),$$

$$A_i = (m_i, M_i) \quad \text{for} \quad i = 1, 2, \cdots, q,$$

$$a_i = (m_i, M_{i+1}) \quad \text{for} \quad i = 1, 2, \cdots, r.$$

4.3.2 The Congruency Property

The congruency property simply states that the output variation for two inputs $u_1(t)$ and $u_2(t)$ that vary between two consecutive extremum values $[u_a, u_b] \subset [\underline{u}, \bar{u}]$ are the same. The following proposition makes this property more clear.

Proposition 1 (Output Variation) *A monotonic change in input which causes the boundary to sweep out an area $\boldsymbol{\Omega}$ from t_1 to time t_2 results in an output variation [139]*

$$v(t_2) - v(t_1) = 2sgn[u(t_2) - u(t_1)] \iint\limits_{\Omega} \mu(\alpha, \beta)d\alpha d\beta. \tag{4.10}$$

52
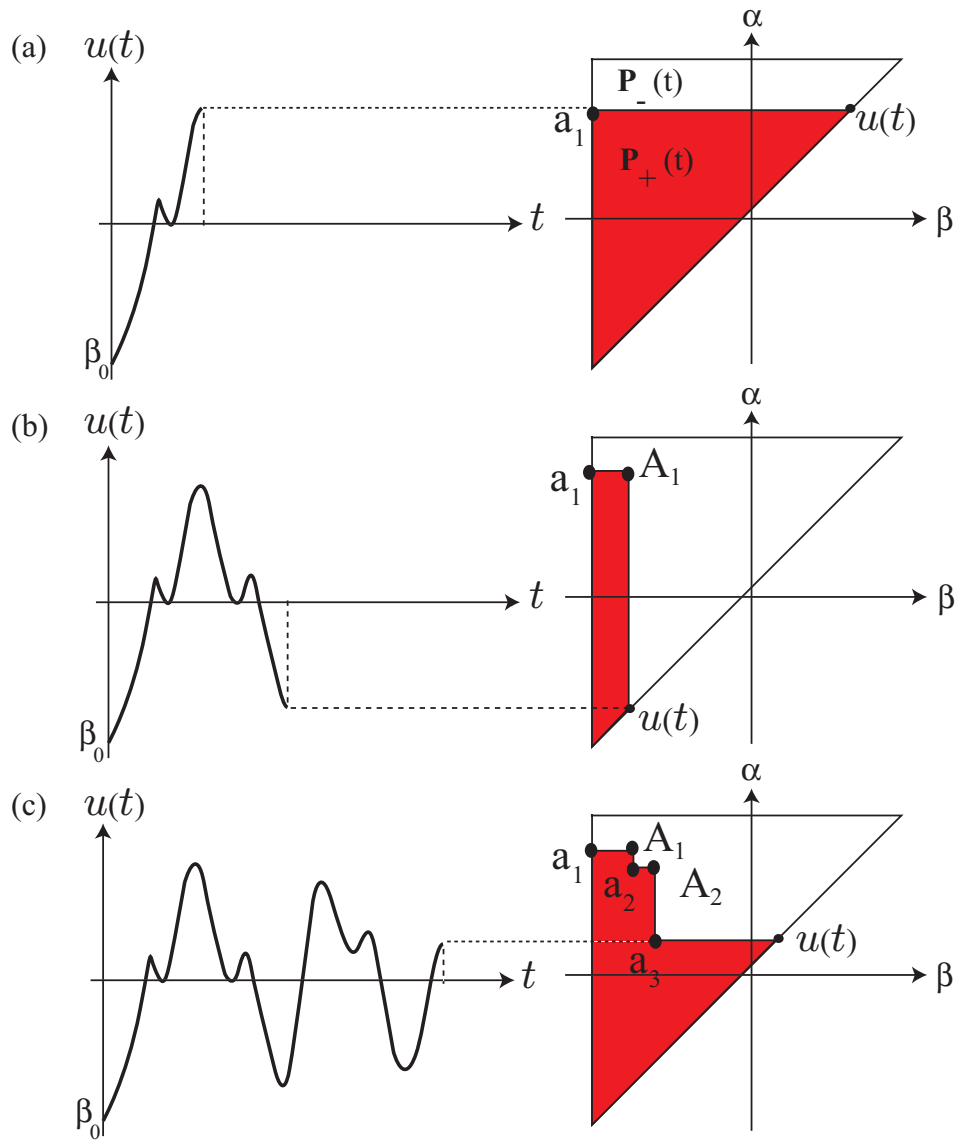
Figure 4.5: The wiping out property.

Proof

Consider the case for monotonically increasing $u(t)$ from time t_1 to t_2. As the input $u(t)$ increases from time t_1 to t_2, the area $\boldsymbol{\Omega}$ is swept out (see Fig. 4.6). Then, the output at t_1 and t_2 can be written as (from Eq. (4.9))

$$v(t_1) \quad = \quad 2 \iint\limits_{\mathbf{P}_+(t_1)} \mu(\alpha,\ \beta) d\alpha d\beta - \iint\limits_{\mathbf{P}} \mu(\alpha,\ \beta) d\alpha d\beta, \tag{4.11}$$

$$v(t_2) \quad = \quad 2 \iint\limits_{\mathbf{P}_+(t_2)} \mu(\alpha,\ \beta) d\alpha d\beta - \iint\limits_{\mathbf{P}} \mu(\alpha,\ \beta) d\alpha d\beta. \tag{4.12}$$

Subtracting $v(t_1)$ from $v(t_2)$, we obtain

$$v(t_2) - v(t_1) \quad = \quad 2 \iint\limits_{\mathbf{P}_+(t_2)} \mu(\alpha,\ \beta) d\alpha d\beta - 2 \iint\limits_{\mathbf{P}_+(t_1)} \mu(\alpha,\ \beta) d\alpha d\beta. \tag{4.13}$$

Now, considering that $\mathbf{P}_+(t_2) = \mathbf{P}_+(t_1) \cup \boldsymbol{\Omega}$, we conclude

$$v(t_2) - v(t_1) \quad = \quad 2 \iint\limits_{\Omega} \mu(\alpha,\ \beta) d\alpha d\beta. \tag{4.14}$$

Likewise, for monotonically decreasing $u(t)$ from t_1 to t_2, we have

$$v(t_2) - v(t_1) \quad = \quad -2 \iint\limits_{\Omega} \mu(\alpha,\ \beta) d\alpha d\beta. \tag{4.15}$$

$\blacksquare$

The congruency property is explained by making use of Proposition 1. Consider two inputs $u_1(t)$ and $u_2(t)$, such that at time t_0 both inputs have achieved the same value, *i.e.*, $u_1(t_0) = u_2(t_0) = u_a$. Both inputs prior to time t_0 can have different past input histories. Suppose after time t_0 the inputs $u_1(t)$ and $u_2(t)$ experience a monotonic increase to u_b and then decrease back down to u_a. The resulting change for both inputs is $\Delta u_1 = \Delta u_2 = \Delta u$. As a result of this change, the area $\boldsymbol{\Omega}$ is swept out in the Preisach plane. From Proposition 1, we conclude that

$$\Delta v_1 \quad = \quad 2 \iint\limits_{\Omega} \mu(\alpha, \beta) d\alpha d\beta, \tag{4.16}$$

$$\Delta v_2 \quad = \quad 2 \iint\limits_{\Omega} \mu(\alpha, \beta) d\alpha d\beta, \tag{4.17}$$
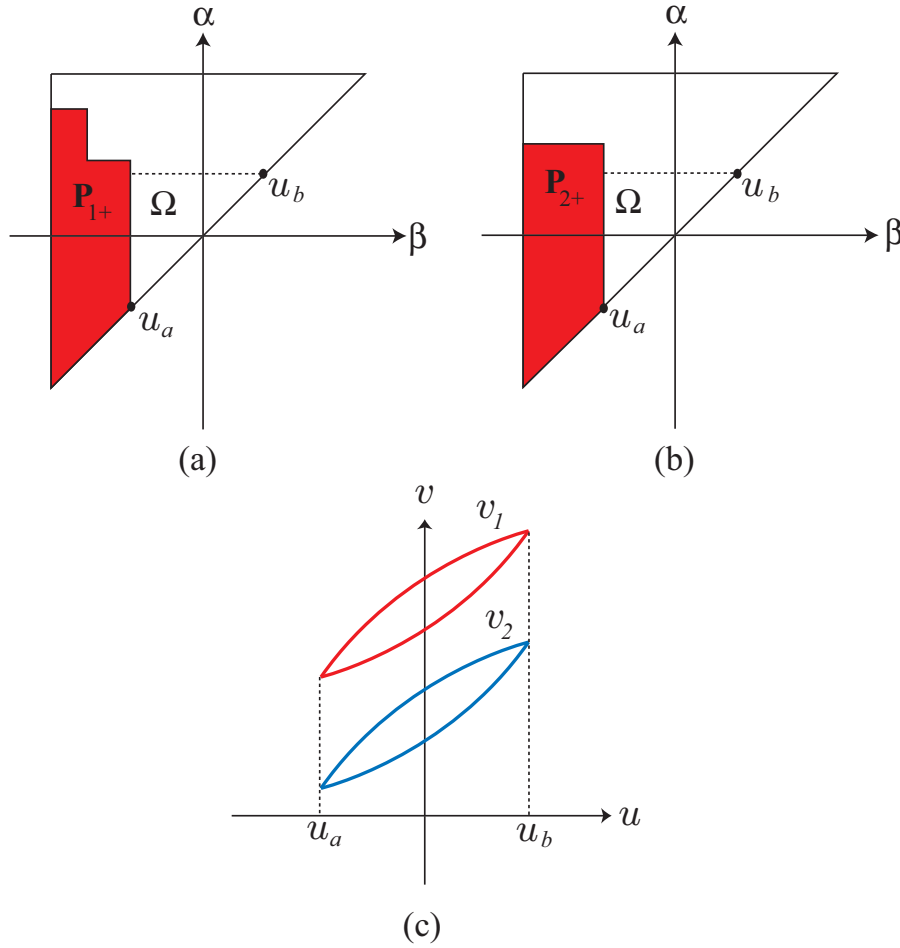
Figure 4.6: The congruency property. The output variation of minor hysteresis loops are the same for two consecutive inputs that vary between $[u_a, u_b]$.

which implies that $\Delta v_1 = \Delta v_2$ and this is illustrated in Fig. 4.6. In the figure, the output variation associated with inputs u_1 and u_2 are the same because the same area $\boldsymbol{\Omega}$ is swept. The congruency property is stated precisely as follows:

Property 2 (The Congruency Property) *All minor hysteresis loops corresponding to back-and-forth variations of inputs between the same two consecutive extremum values $[u_a, u_b] \in [\underline{u}, \bar{u}]$ are congruent.*

4.3.3 Nonlocal Memory

It is interesting to note that the elementary relay $\mathcal{R}$ operator exhibits local memory[3]; however, the Preisach model exhibits nonlocal memory, that is, the current output at time t_0 along with the current and future input $u(t)$ for $t \geq t_0$ does not provide enough information to determine uniquely the output $v(t)$ for $t > t_0$. The reason is the Preisach model captures the effect of past input history and this is reflected in the partitioning of the plane by the interface $L(t)$. It is quite possible that two outputs coincide at time t_0; however, the same input variation $u(t)$ for $t \geq t_0$ can produce completely different outputs $v_1(t)$ and $v_2(t)$ for $t > t_0$. This is because at time t_0, the interfaces associated with the two outputs, $L_1(t)$ and $L_2(t)$, are completely different. For this reason, the Preisach model exhibits nonlocal memory as illustrated in Fig. 4.7. In the figure, the output (point Q) for $t > t_0$ can evolve in an infinite number of paths, depending on the partition of the Preisach plane at time t_0. Therefore, knowing the output at time t_0 does not provide enough information about how the output will change for $t > t_0$. On the other hand, the output can be determined uniquely by knowing the partitioning of the Preisach plane at time t_0, $i.e.$, knowing the region $\mathbf{P}_+(t_0)$ or equivalently, the memory curve $L(t_0)$.
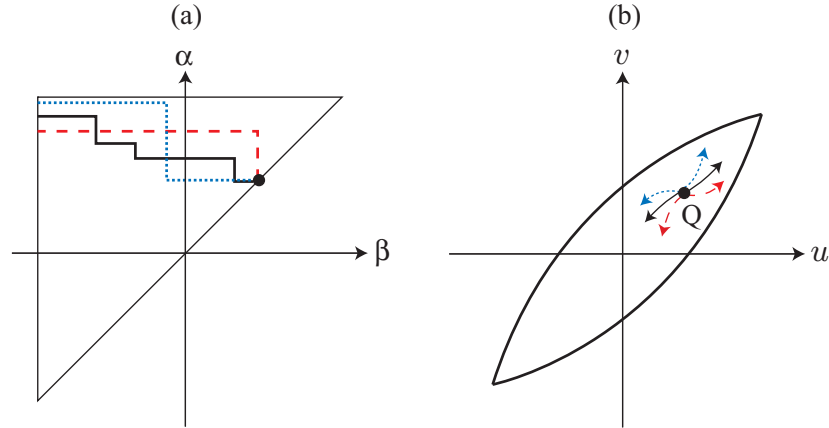
Figure 4.7: Nonlocal memory effect.

[3]Recall that a relay exhibits local memory when the output of the relay for $t \geq t_0$ can be uniquely determined by knowing the output $v(t)$ at the current time t_0 and the input $u(t)$ for $t \geq t_0$.

4.3.4   The Effects of Looping (Branching) and Loss of Directionality

Another behavior associated with Preisach-type hysteresis is shown in Fig. 4.8. In this figure, suppose the inputs u_1 and u_2 were increased monotonically such that $u_1 > u_2$ at time t_0. By the partitioning of the Preisach plane, it is clear that at time t_0, $v_1 > v_2$ as shown in Fig. 4.8(a). Next suppose that at time t_1, the input u_1 is decreased monotonically until time t_2. The decrease in input causes the vertical line associated with u_1 to swept from right to left as shown in Fig. 4.8(b). At time t_2, we have that $u_1 > u_2$ and $v_1 > v_2$. Now suppose the input u_1 continues to decrease monotonically until time t_3 such that $u_1 < u_2$ and for this situation, we still have that $v_1 > v_2$ (Fig. 4.8(c)). Essentially, this behavior is interpreted as follows: the sign of the error of the output (*i.e.*, $v_2 - v_1$) cannot be used to infer the sign of the difference in the input (*i.e.*, $u_2 - u_1$). This behavior implies a loss of *direction* information between the input and output. For example, at some time t, knowledge of the sign of the tracking error provides no useful information about the direction the input should be applied to reduce the tracking error. This notion is schematically depicted in Fig. 4.8(d) which shows a typical hysteresis curve (plot of v versus u). In the figure, for a given value v_d, there exists an uncountable set of possible desired input values u_d that achieves v_d. And depending on which branch is associated with the current input value, the direction for which the input needs to change can either be positive or negative. For example, if point Q was the output at some time t, then it is unclear if the input u should be increased or decreased to minimize the error between Q and v_d, unless, however, we know which hysteresis branch point Q belongs. As a result, the looping or branching effects can pose a problem for showing convergence of iteration-based control schemes because of the lack of direction information, which is essential to the convergence of such schemes.

4.3.5   Preisach Model Assumptions and Relevant Definitions

We will consider the following additional properties, assumptions and definitions related to the Preisach hysteresis model. An extensive study of other mathematical properties of the Preisach model can be found in [144], for example.
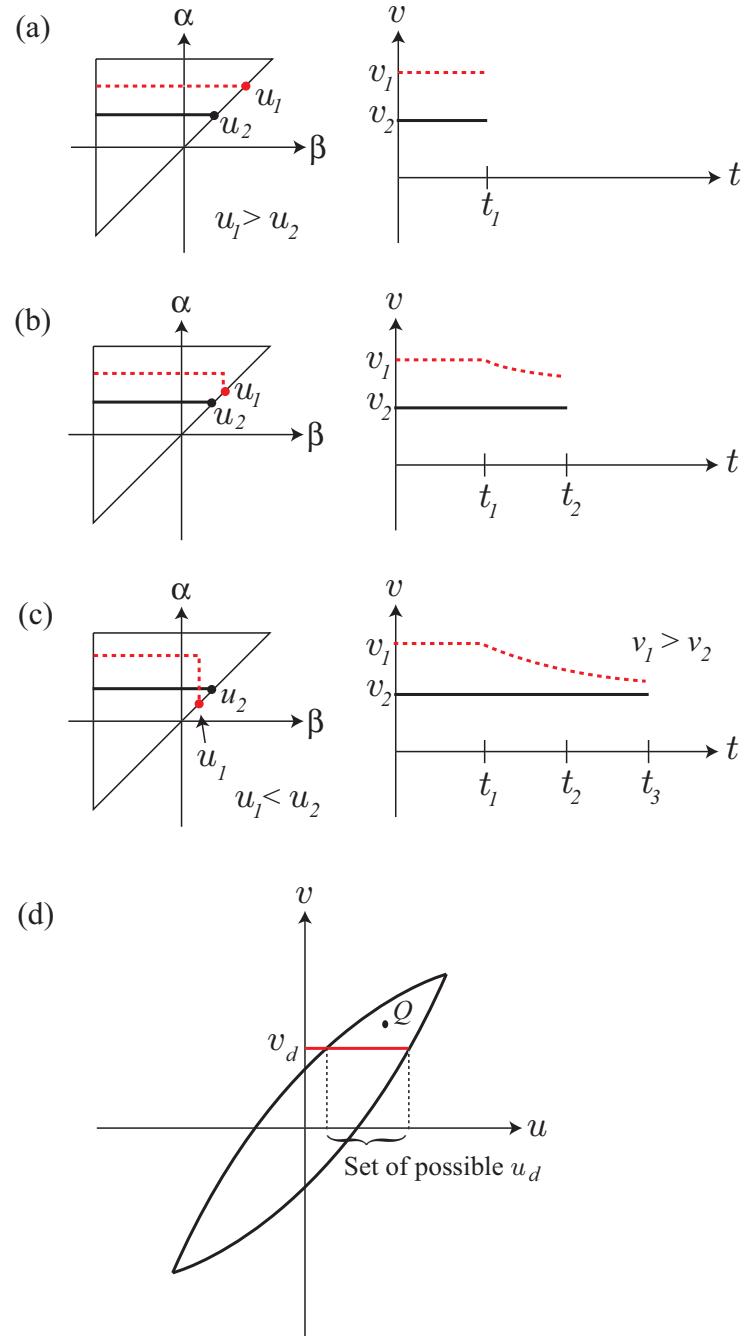
Figure 4.8: Input-output behavior of Preisach-type hysteresis. (a)-(c) Output behavior associated with two inputs. (d) Typical hysteresis curve. For a given v_d, there exists an uncountable set of possible u_d.

Definition 2 (The Initial Memory Curve) *We let L_0 denote the initial state of the Presiach operator, or otherwise known as the initial memory curve, i.e., $L_0 \triangleq L(t_0)$.*

Assumption 1 (Preisach Model Assumptions) *For the Preisach model, we assume:*

a) *The applied input $u \in [\underline{u}, \bar{u}]$.*

b) *The Preisach weighting function is bounded by $0 \leq \mu(\alpha, \beta) \leq \mu_{max} < \infty$ and piecewise continuous $\forall (\alpha, \beta) \in \mathbf{P}$, where $\mathbf{P}$ is given by Eq. (4.5) and*

$$\mu_{max} \triangleq \max_{\forall \alpha, \beta \in \mathbf{P}} \mu(\alpha, \beta). \tag{4.18}$$

c) *There exists a $\xi > 0$ such that $\mu(\alpha, \beta) \geq \underline{\mu} > 0$, $\forall (\alpha, \beta) \in \Omega_\xi$, where Ω_ξ is the region depicted in Fig. 4.9(a)[4] and*

$$\underline{\mu} = \min_{\forall (\alpha, \beta) \in \Omega_\xi} \mu(\alpha, \beta). \tag{4.19}$$

The region Ω_ξ is enclosed between the lines $\alpha = \beta$ and $\alpha = \beta + \xi$.

Let Assumption 1 hold and L_0 be the initial memory curve as defined in Definition 2, then:

Property 3 (Continuity) $\mathcal{H} : C^0(I) \to C^0(I)$ *is continuous (in the sup norm) (e.g., see reference [144], Section 3).*

Property 4 (Piecewise Monotonicity) *The output $v \in C_m^0(I)$ is strictly increasing (respectively, decreasing) if and only if $u \in C_m^0(I)$ is strictly increasing (respectively, decreasing) (e.g., see reference [144], Section 5).*

Definition 3 (Branch) *Let L_0 be an initial memory curve and $u \in C_{m+}^0(I)$ (respectively, $u \in C_{m-}^0(I)$), then we say the pair $(u, \mathcal{H}[u])$ belongs to the branch $\mathcal{B}_\uparrow[\cdot, L_0]$ (respectively, $\mathcal{B}_\downarrow[\cdot, L_0]$). By the Preisach Property 4 a branch is an increasing function of u (Examples of three different branches with initial memory curves L_0, $\tilde{L}_0$, and L_0^* are shown in Fig. 4.9(b).).*

---

[4]This assumption ensures that a nonzero change in the input will result in a nonzero change in the output.
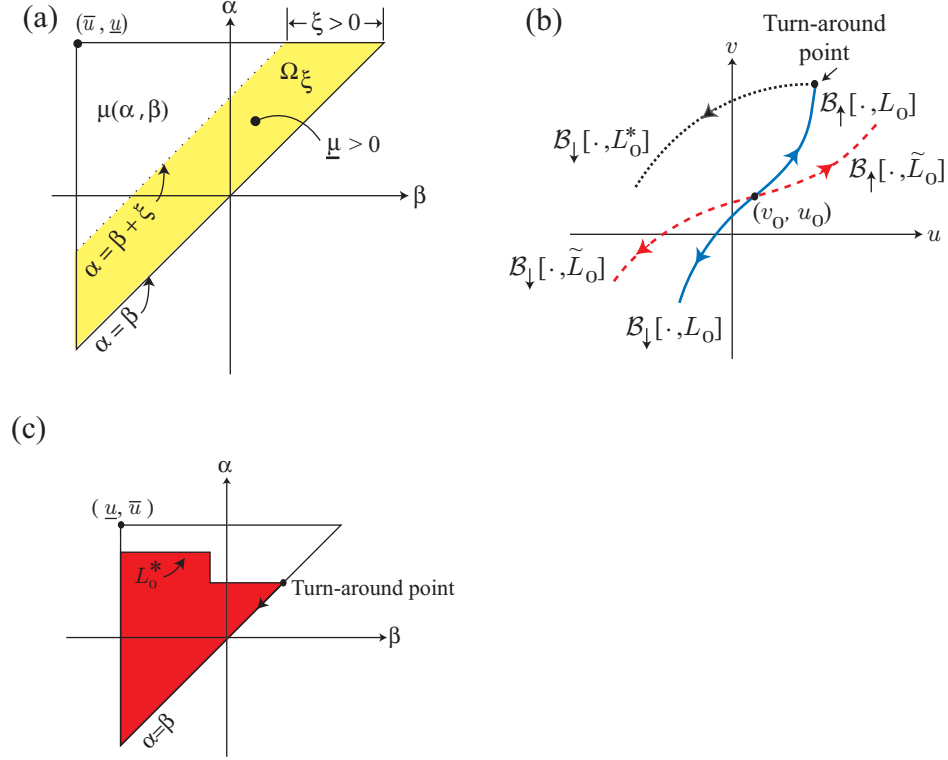
Figure 4.9: (a) Geometric representation of Assumption 1(c). (b) Branches and turn-around point. (b) Location of a turn-around point in the Preisach plane.

Definition 4 (Turn-around Point) *We call a turn-around point the location in the u-v plane where the input u changes from increasing to decreasing in time or vice versa, e.g., see Figs. 4.9(b) and (c).*

4.4 Summary

A brief introduction to the Preisach model for hysteresis was presented in this chapter. Some of the properties of the model were discussed in the context of the work in this dissertation. In the following chapters, the Preisach model will be used in the formulation and analysis of a proposed iterative learning control approach to compensate for hysteresis in piezos.

Chapter 5

ITERATIVE LEARNING CONTROL OF HYSTERESIS: THEORY

In Chapter 3, feedback and feedforward control were used to precisely control an experimental piezo positioner; feedback control was decoupled from feedforward control, where feedback control compensated for creep and hysteresis effects, and feedforward input accounted for movement-induced vibration. The results in Chapter 3 showed that the tracking error can be reduced by over an order of magnitude compared to the uncompensated case. Although the amount of improvement is a significant contribution, for applications requiring high-precision positioning over large range, say 50 μm, the residual error can be as large as a few microns. Such large positioning error is unacceptable in applications such as nanofabrication where the probe tip is required to maintain a precision of less than 100 nm. Therefore, the need to achieve high-precision control of emerging SPM-based nanotechnologies motivates the work in this chapter.

In this chapter, a method to iteratively find feedforward input to compensate for hysteresis-caused positioning error in piezo positioners is developed. In particular, iterative learning control (ILC) is used to achieve high-precision positioning and a proof of convergence for a proposed ILC algorithm is presented. In the analysis, the Preisach hysteresis model is used to characterize the nonlinear behavior of a piezo positioner. Using this model, we quantify the number of iterations required to achieve a prescribed tracking precision. Afterwards in Chapter 6, the method is applied to an experimental atomic force microscope system to demonstrate its efficacy, and results show that the positioning error can be reduced to the noise level of the sensor measurement. Contrast to the feedback and feedforward approach presented in Chapter 3, the ILC method further reduces the error due to hysteresis, and we note that higher precision can be achieve with the use of better sensors. Additionally, we note that the ILC approach can be integrated with existing feedback and feedforward schemes [3, 4, 5, 145] to further improve performance.

5.1 Introduction and Motivation

As a nanomanufacturing tool, piezo-based positioners, with their ultra-fine positioning capability, have the potential of, for example, down scaling current semiconductor devices toward the atomic regime [146]. For instance, quantum point contact (QPC) nanoelectronic devices have been fabricated using scanning probe microscopy (SPM)-based techniques [147]. The production and study of such nanoelectronic devices are needed for creating smaller, faster and cheaper semiconductor electronics to meet the continued growth of computing power [148]. Interestingly, research has shown that a QPC's conductance threshold voltage, a critical electrical characteristic, is directly related to its fabricated dimensions [147]. As a result, precise lateral (x- and y-axis) control of the SPM-based fabrication tool is needed to create high-quality nanoelectronic devices. Likewise, long-range nano-precision control of the SPM-based tool is required to enable large-scale production. Unfortunately, hysteresis effect in piezos leads to significant loss in positioning precision and it drastically affects the quality of the nanomanufacturing process, $i.e.$, large hysteresis-caused positioning error leads to part distortion, consequently affecting a part's performance [147]. Therefore, the critical need to achieve long-range nano-precision positioning motivates the effort to correct for positioning errors due to hysteresis.

Additionally, high-precision positioning is needed for emerging AFM-based high-density data storage devices [149]. The AFM-based approach was developed to address the limitations of magnetic-based storage devices. For example, consider the current areal density of 100 Gb/in^2 in magnetic media-based computer hard drives. The 100 Gb/in^2 translates to roughly 12.5 GB/in^2 areal density. Figure 5.1(a) shows the top view of a standard hard drive platter where the data is encoded on concentric rings on a magnetic platter [150, 151]. For the density of 100 Gb/in^2, ideally, a data bit occupies an area roughly 80 $nm \times$ 80 nm square. However, the industry standard calls for a bit aspect ratio of 4:1 [152] as shown in Fig. 5.1(b); therefore, the 80 $nm \times$ 80 nm square converts to a 40 $nm \times$ 160 nm rectangular area [151]. If the bits are packed closely together on each track, then their arrangement relative to the disk motion is illustrated in Fig. 5.1(c), where the track pitch width (center-to-center track distance) is 160 nm. As a rule of thumb (by industry standards [151]), the

maximum positioning error that the read/write head is allowed is 10% of the track width, which means the error in positioning the read/write head cannot deviate more than 16 nm. If we consider the standard stroke length for a piezo-based read/write positioner is 1 μm, then the 16 nm error implies that the maximum error in percent of the total stroke length is 1.6%. So, the performance of a standard hard drive these days meets these specifications to function properly. Such precision in positioning is reasonable since the performance of current feedback/feedforward control schemes can reduce the error to a few percent of the displacement range [3, 4, 5, 145].

Currently, however, the industry is now trying to achieve the density of 1 Tb/in^2 (125 GB/in^2) [153]. But due to the limitations in reducing the data bit in magnetic-data storage devices, the industry is looking at other alternatives to increase the areal density. One proposed approach is to use the AFM to physically punch holes on the surface of a material and each hole will represent a data bit, $e.g.$, see Fig. 5.2(a). At the present time, research demonstrates that holes on the order of 10 nm and even smaller can be made using an AFM [83, 149]. Such holes are substantially smaller than the achievable bit size in magnetic media. Therefore, a 1 Tb/in^2 areal density translates to a bit-area of 25 $nm \times 25$ nm square (Fig. 5.2(b)). Since holes punched by the AFM are circular in geometry, there is no need for a bit aspect ratio of 4:1 and the data bits will occupy a square area as illustrated in Fig. 5.2(b). Furthermore, if we assume that holes can be reliably produced on the order of $10-20$ nm in diameter, then data bits can be arranged as shown in Fig. 5.2(c). On the conservative side, if we assume that the holes are 20 nm in diameter and based on the precision required by current industry standards (error of 10% of the track width), the probe tip can only deviate from the center of the track position by 2.5 nm before the hole starts to encroach on the space of its neighbor. Then to achieve the 1 Tb/in^2 goal, a required 2.5 nm precision is needed for positioning the read/write. Such a precision is significantly smaller than 16 nm from the previous example. Additionally, if we use the same piezo positioner with a stroke length of 1 um, we find that the maximum error must be less than 0.25%. To this end, nano-precision positioning is important for advanced high-density data storage devices.

We note that in SPM-based applications, as much as $10-15\%$ tracking error occurs

(a)

Bit area | 80 nm

80 nm

Disk platter

(b)

4:1

160 nm

40 nm

Disk motion

(c)

Data bit

Track n+1

160 nm

Track n

Max. error = 16 nm (1.6%)

Read/write head
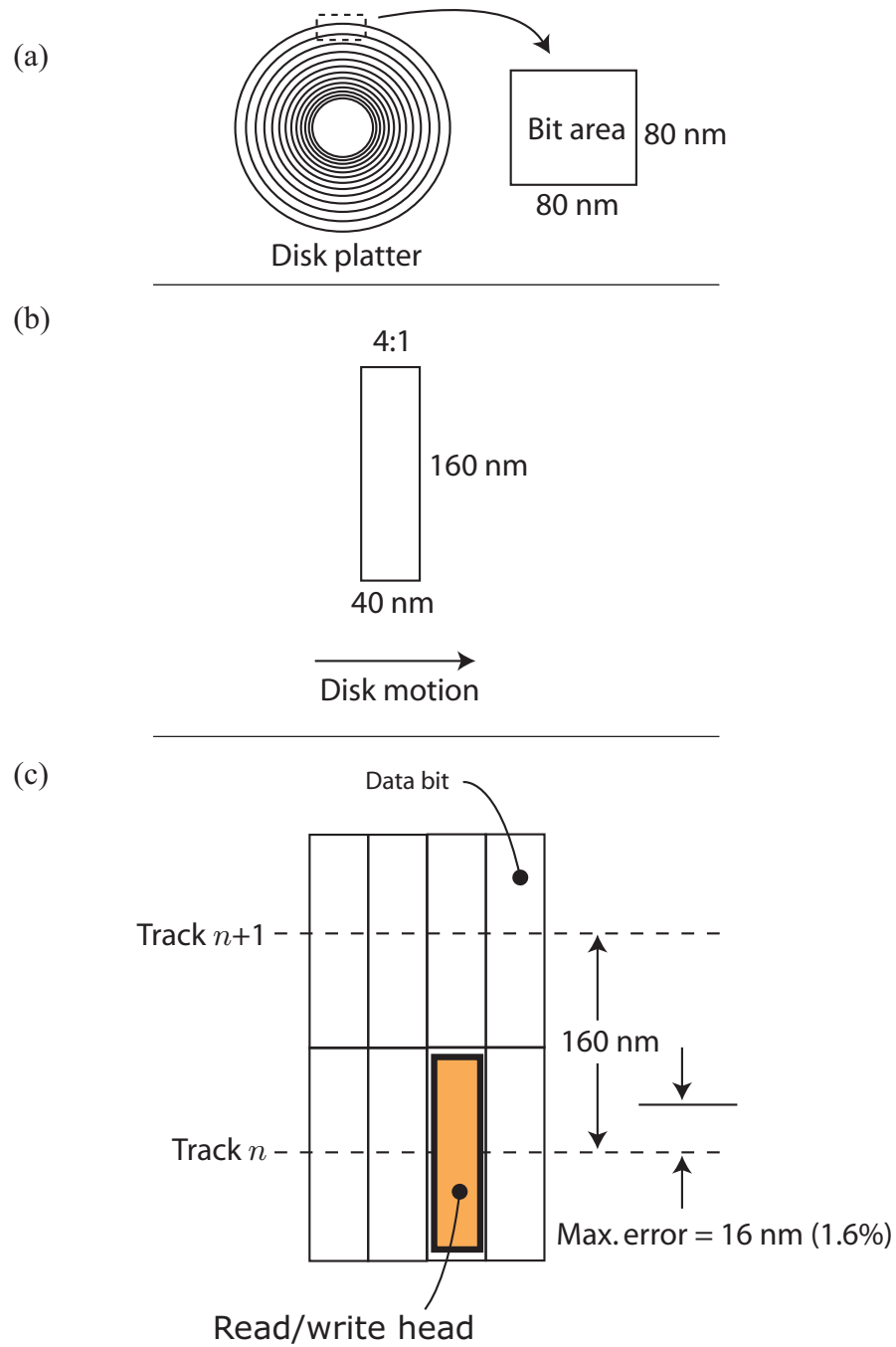
Figure 5.1: High-density data storage specification for 100 Gb/in^2 capacity [151].

(a)

Probe tip

Nano-holes

Substrate

(b)

Bit area   25 nm

25 nm

(c)

Data bit ~10-20 nm[*]

Max. error = 2.5 nm (0.25%)

Track $n+1$

25nm

Track n
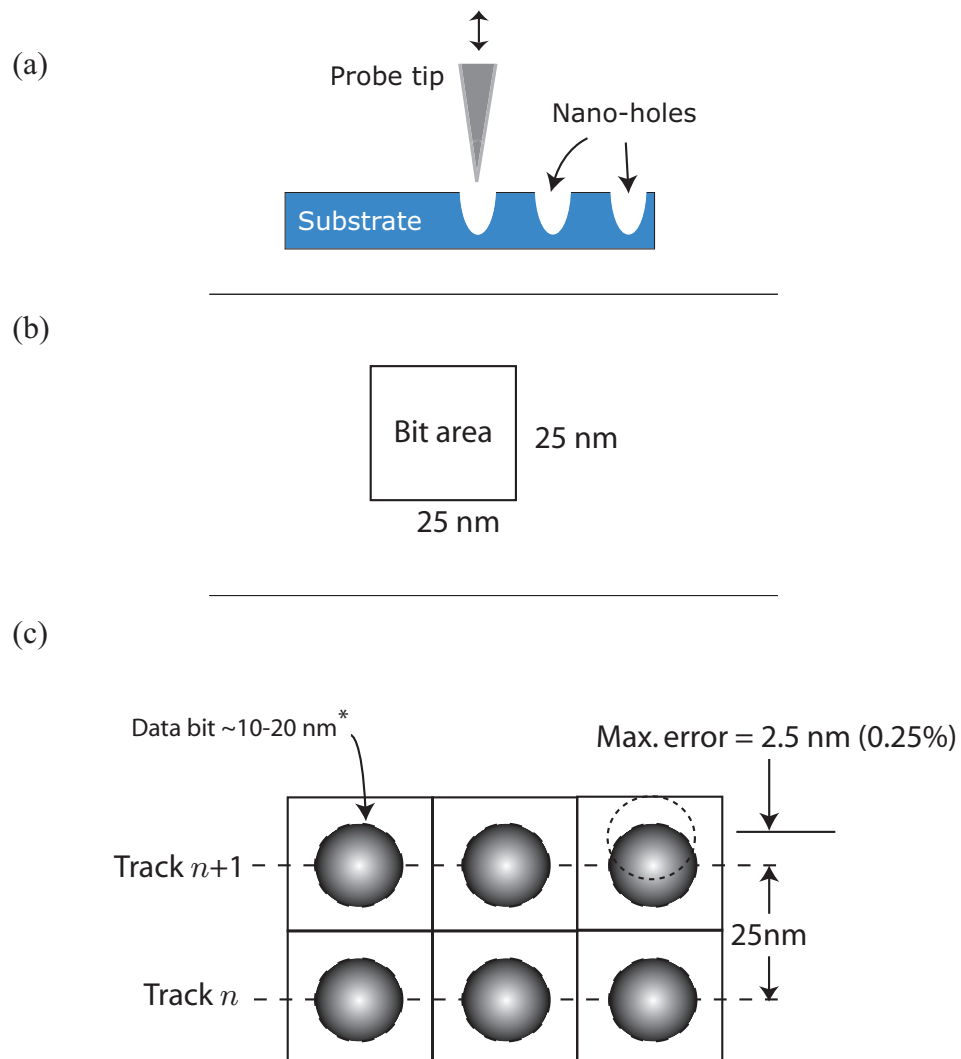
Figure 5.2: High-density data storage specification for $1\ Tb/in^2$ capacity [149].

when piezos are operated over long range [4, 5]. Compensating for hysteresis-caused positioning error is challenging and a wide variety of techniques have been proposed. For example, by using charge control (rather than voltage control), the effect of hysteresis can be minimized, but at the cost of reducing the effective displacement range of the actuator [154]. Additionally, this technique requires specially designed circuits. Also, modeling the highly nonlinear hysteresis behavior has been studied extensively, *e.g.*, [134]. A model is used to find input to compensate for hysteresis, *e.g.*, see [2]. However, the drawbacks are: (i) the approach is computationally cumbersome and (ii) it is prone to errors. On the other hand, standard feedback-based approaches [3], as well as more advanced schemes [4], have been investigated to improve positioning precision. The feedback-based approach is robust to model uncertainty and parameter variation, but closing the loop may be challenging for systems that have low gain margin; moreover, the performance of feedback-based systems is limited by the achievable gain margin [155, 145] (see Chapter 3). Notwithstanding, both feedback and model-based feedforward techniques have been relatively successful; they can reduce the positioning error to a few percent (typically between 2-5%) of the displacement range [3, 4, 5]. But even at this level of precision, unacceptably large error exists. For example, 2% tracking error over a $50\mu m$ displacement range leaves $1\mu m$ of error, which is certainly larger than the nano-precision ($< 100nm$) typically required in atomic force microscopy (AFM)-based fabrication of ultra-small semiconductor devices [147]. Alternatively, this dissertation studies ILC to compensate for hysteresis and experimental results are presented to demonstrate precision positioning beyond current feedback and feedforward techniques, *e.g.*, the tracking error reduces to the noise level of the sensor measurement. Additionally, we point out that ILC can be integrated with existing feedback/feedforward schemes (*e.g.*, the approach mentioned in Chapter 3 and in references [156, 145]) to further improve precision.

The ILC framework is based on the observation that if the system's operating conditions remain the same during each operation, then the errors in the output response repeat during each operation. The objective is to make use of the information from previous operating trials to improve the response in the next iteration; and as a result, the performance of a system can be improved through repetition. A block diagram of the control scheme is

shown in Fig. 5.3, where v_d is the desired output, and u_k and v_k are the input and output at the kth trial, respectively. Therefore, we would like to find an input for the next step, *i.e.*, u_{k+1}, such that the performance of the system is better than the previous step.

The ILC method was first proposed by Uchiyama [157][1] in the late 70's and further developed by Arimoto *et al.* [158] and Craig [159] in the mid-80's. Early contributions of modified ILC schemes were investigated by many others including Kawamura *et al.* [160], Atkeson *et al.* [161] and Bondi *et al.* [162]. Since the work of Arimoto's group, the ILC methodology has been studied for a variety of systems from linear [163] to nonlinear non-minimum phase plants [164] and a thorough treatment of the subject can be found from references [165, 166]. As a requirement, the system to be controlled must operate repetitively over a finite time interval. In practice, there are many applications for which the operation is repetitive and the ILC methodology is a convenient solution for eliminating errors. The approach has been applied to robotics [161], internal combustion engines [167] and permanent magnet motors [168], for example.

In piezo-based applications, we note that the majority of tasks, such as AFM imaging [2] and nanomanufacturing, require the piezo positioner to operate repetitively, *e.g.*, the back and forth lateral (x- and y) scanning movements. As such, ILC can be used to eliminate errors due to hysteresis (as well as the affects of vibration and creep). One advantage of ILC is it requires minimal system knowledge; therefore, it reduces the complexity of computing the feedforward input [2].
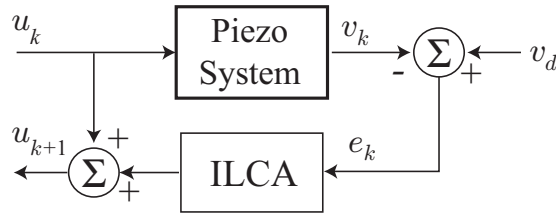
Figure 5.3: Block diagram of ILC scheme.

---

[1]The work was not well known at the time because it was written in Japanese.

The contribution of this chapter is to solving an ILC problem for hysteretic systems. Specifically, a proof of convergence for a standard iterative learning control algorithm is presented. Afterwards, a detailed discussion of implementing the ILC algorithm, which involves finding an approximate model of the hysteresis behavior, is presented in Chapter 6. The results show that the approach achieves nano-precision positioning and it is an important contribution to the design of SPM-based tools for nanotechnologies.

The outline of this chapter is as follows. First, we formulate the problem in Section 5.2 and then discuss some past work and the challenges of proving convergence of ILC for hysteretic systems. Next, we discuss in detail the convergence analysis, which is based on the properties of the Preisach model from Chapter 4. Finally, this chapter closes with concluding remarks in Section 5.4. Additionally, the ILC technique was experimentally evaluated and results are presented in Chapter 6.

5.2 Problem Formulation

5.2.1 Notation

For convenience, we define the finite time interval

$$I \triangleq [t_0, T], \tag{5.1}$$

where $t_0, T \in \mathbb{R}$ and the following order holds: $0 \leq t_0 < T \leq \infty$. Also, we denote by $C^0(I)$ the set of all continuous functions on I. Likewise, we let $C_m^0(I)$ and $C_{pm}^0(I)$ represent the set of continuous monotone and piecewise monotone functions on I, respectively. We denote by $C_{m+}^0(I)$ (respectively, $C_{m-}^0(I)$) the set of all continuous nondecreasing (respectively, nonincreasing) functions on I. Moreover, we use the notion of pointwise ordering for functions $u_1, u_2 \in C^0(I_{a,b})$, where $I_{a,b} \triangleq [t_a, t_b]$, e.g., $u_1 \leq u_2$ implies $u_1(t) \leq u_2(t)$ for any $t \in I_{a,b}$. Additionally, we will consider the standard infinity function norm $|| \cdot ||_\infty$, defined as

$$\|u(\cdot)\|_\infty \triangleq \sup_{\forall t \in I} |u(t)|. \tag{5.2}$$

We let $\mathbb{N}_0 \triangleq 0 \cup \mathbb{N}$, where $\mathbb{N}$ represents the set of all natural counting numbers, e.g., $\mathbb{N} = \{1, 2, 3, \cdots\}$.

Consider a rate-independent[2] hysteretic system of the form:

$$v(t) = \mathcal{H}[u](t), \qquad \forall t \in I, \tag{5.3}$$

where $v(t) \in \mathbb{R}$ is the output, $u(t) \in \mathbb{R}$ is the input and $\mathcal{H}$ is the Preisach hysteresis operator which we assume satisfies the Preisach model Assumption 1. Given a desired output trajectory $v_d \in C^0(I)$, the objective is to find an input $u_d \in C^0(I)$ by repetitively applying the following iterative learning control algorithm (ILCA):

$$u_{k+1}(t) = u_k(t) + \rho[v_d(t) - v_k(t)], \tag{5.4}$$

such that as the number of iterations $k \to \infty$, $u_k \to u_d$, and the input u_d satisfies

$$v_d(t) = \mathcal{H}[u_d](t), \tag{5.5}$$

for all $t \in I$. In Eq. (5.4), u_{k+1} is the input at the next $(k+1)^{th}$ trial, ρ is a constant (to be determined), and u_k and v_k are the input and output at the kth trial, respectively. Furthermore, we note that Eq. (5.4) is a typical proportional or P-type ILCA [163, 169] and a justification for choosing the control in this form is discussed in more detail in Appendix C, where the relative degree of the system is exploited in the design of the ILCA similar to the works of [163, 16].

In Chapter 4, the model of a piezo positioner was considered as a nonlinear element in series with a linear-time invariant dynamic block (refer to Fig. 4.1). In general, the hysteresis output v cannot be measured directly; however, if the response of the system is such that the dynamics effects (creep and vibration) are insignificant, then v can be measured. Therefore, in formulating our iterative learning control problem, we will only consider the hysteresis effect and operate over the range where hysteresis dominates, *i.e.*, relatively fast to avoid creep and slow enough to keep from exciting vibrational modes of the system. We note that iterative learning control has been extensively studied for LTI systems, *e.g.*, see [158, 165]. As a result, this thesis will solve an iterative learning control

---

[2]A formal definition of rate independence is discussed in reference [18], Section 2.2.

problem for hysteretic systems. Afterwards, we will address future work of combining the results of this thesis with the ILC of LTI systems, such as [164], as well as discuss other potential applications for the method.

5.2.3 Past Work and Challenges

Iterative learning control has been developed for many types of systems, from LTI [17] to a certain class of nonlinear systems with input and output disturbances [170]. More recently, the approach has been adopted to nonlinear nonminimum phase systems [171]. Few studies, however, have been done involving the ILC methodology for hysteretic systems. Particularly, the problem has been a challenge to solve due to the complexity of the hysteresis behavior. To this end, the objective of this thesis is to solve an ILC problem for hysteretic systems, and we begin by reviewing the literature and highlighting the main challenges associated with solving this problem.

In the past, few efforts to exploit the ILC methodology for hysteresis control have been presented. For instance, in 1993, Li *et al.* [172] integrated the concept of ILC into an adaptive controller. The ILC methodology was used to design a self-tuning regulator. The objective was to use information from past operating trials to improve the estimation of system parameters used by the regulator. Li *et al.* applied their technique to a piezoactuator system for which they assumed a linear third-order model to describe the dynamic behavior. (Note this approach did not explicitly address the hysteresis behavior.) In practice, their approach had several noticeable drawbacks. First, the parameters to be identified came from a linear third-order model. This model does not capture the nonlinear hysteresis behavior typical of piezo-based systems. Therefore, the performance of the control system depends on how close the estimates are to the real system parameters. As Main and Garcia [109] have shown, hysteresis can alter the characteristics of a system significantly, potentially affecting performance of the algorithm as well as its stability. Second, the initial conditions for the parameter estimator were chosen arbitrarily. Therefore, the performance of the estimator, as well as the closed-loop control system, depends on how *close* the initial guess was to the actual system parameters.

In 2001, Hu *et al.* [173] exploited the structure of ILCA Eq. (5.4) to control an electrostrictive actuator. In an electrostrictive actuator, the strain depends on the square of the applied field and such actuators exhibit a small amount of hysteresis, *i.e.*, small compared to piezoelectric actuators. They proposed a method to determine the learning gain ρ by assuming that the hysteresis effect takes on a nominal quadratic input-output relationship and then linearizing the system about an operating point similar to Newton's method [174]. Their convergence analysis, however, did not explicitly include the full nonlinear-hysteresis behavior, which includes the effect of *branching* (refer to Definition 3 in Chapter 4). Though convergence of their scheme was proved, the analysis is limited to systems that satisfy the assumptions of the approximate model, namely that the input-output relationship be a nominal quadratic (single-valued) functional. But we emphasize that if a nonlinear system exhibits an input-output behavior satisfying the assumptions of the quadratic model, then convergence is guaranteed according to Hu's group. But in general, nonlinear hysteresis behavior includes the effect of past input history, which leads to multivalued and branching effects, and it cannot be readily captured by polynomial approximations. Therefore, based on their analysis, the convergence of ILCA Eq. (5.4) for general hysteretic systems remains to be solved.

Other works include the micro-positioning of linear-piezoelectric motors based on learning nonlinear PID controller [168]. Also, a form of ILC was applied to a piezoelectric tool servo system for variable depth of cut machining [175]. Tao and Kokotovic [176] studied adaptive control for hysteretic systems. Similar to Li *et al.* and Hu *et al.*'s work, these previous studies did not explicitly deal with the full nonlinear-hysteresis behavior in the context of proving ILC convergence. Recently, Venkataraman and Krishnaprasad [177] have shown, based on the contraction mapping principle, that Eq. (5.4) converges if a nonlinear system satisfies the incrementally strictly increasing operator (ISIO) property, which is defined as:

Definition 5 (Incrementally Strictly Increasing Operators [177]) *An operator F : $C^0(I) \rightarrow C^0(I)$ is called incrementally strictly increasing if, for $u_1, u_2 \in C^0(I)$ with $u_1 \leq u_2$, there exists constants η_1 and $\eta_2 > 0$ such that*

$$\eta_1(u_2 - u_1) \leq F(u_2) - F(u_1) \leq \eta_2(u_2 - u_1). \tag{5.6}$$

A geometric interpretation of the incrementally strictly increasing property for two inputs u_1 and u_2, with $u_1 \leq u_2$ (recall our notion of pointwise ordering), is shown in Fig. 5.4. According to Venkataraman and Krishnaprasad's work, if one can show that a nonlinear system satisfies this property, then by picking $\rho = 1/\eta_2$, convergence of ILCA Eq. (5.4) is guaranteed. (For reference, the proof of Venkataraman and Krishnaprasad's work is presented in Appendix C, in expanded form.) Unfortunately, systems which exhibit hysteresis do not satisfy the ISIO property (Definition 5). For example, consider the experimental results in Fig. 5.5 measured from a piezo scanner used in a Burleigh Metris-2000NC atomic force microscope imaging system. Figure 5.5(a) shows two inputs u_1 and u_2 defined on the interval $I = [0, T] = [0, 0.8]s$, with $u_1 \leq u_2$. The first input u_1 is zero for all $t \in I$ and the second input is a triangle signal with a period of $0.8s$. The measured outputs, $\mathcal{H}[u_1]$ and $\mathcal{H}[u_2]$, as a result of these two inputs, are shown in Fig. 5.4(c). Figure 5.5(b) shows the hysteresis curve for the input-output pair $(u_2, \mathcal{H}[u_2])$ and illustrates the multivalued or looping behavior associated with hysteresis [18], *i.e.*, the ascending and descending paths in the input-output plane do not coincide. Particularly, the effect of looping (or branching) causes the following behavior: after the input u_2 achieves its maximum value and returns to its initial value at time $t = 0.8s$, the corresponding output at time $t = 0.8s$ differs by a nonzero amount from its initial value, at time $t = 0$. As a result, there does not exist
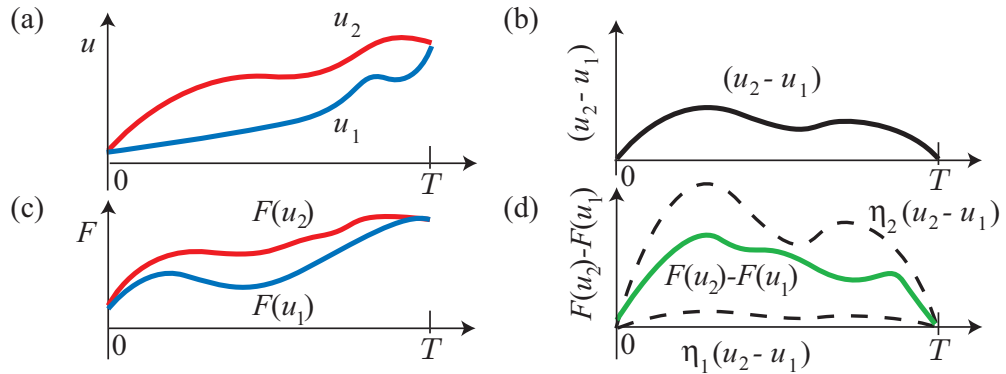
Figure 5.4: Geometrical interpretation of the incrementally strictly increasing property.
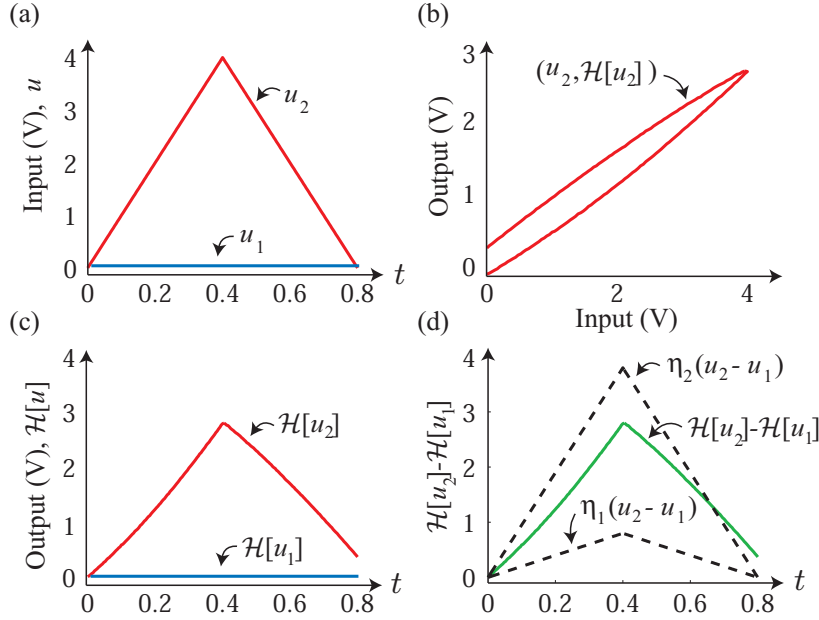
Figure 5.5: Experimental results that indicate hysteresis behavior does not satisfy the incrementally strictly increasing property.

a constant $\eta_2 > 0$ such that the product $\eta_2(u_2 - u_1)$ is the upper bound for the difference $\mathcal{H}[u_2] - \mathcal{H}[u_1]$ as indicated in Fig. 5.4(d). Therefore, the experimental results show that hysteresis does not satisfy the ISIO property, and Venkataraman and Krishnaprasad's work is not directly applicable; however, we note that their work is a significant contribution for nonlinear systems that satisfy the ISIO property, namely convergence of ILCA Eq. (5.4) is guaranteed for such systems.

In relation to the Preisach model, the failure to satisfy the ISIO property can also be explained using the geometric interpretation of the model. For example, consider a uniform Presiach weighting function $\mu(\cdot, \cdot) = 1$ and suppose that at time t_0, the Preisach plane $\mathbf{P}$ is partitioned by the initial memory curve $L(t_0)$ as shown in Fig. 5.6(a). Consequently, the output at time t_0 is related to the $\mathbf{P}_+(t_0)$ and $\mathbf{P}_-(t_0)$ regions. Next, we increase the input from u_0 to $u_1 \leq \bar{u}$, and the $\mathbf{P}_+$ regions increases as shown in Fig. 5.6(b). At this point, the output $v_1 > v_0$ because of the expansion of the $\mathbf{P}_+$ set and reduction of the $\mathbf{P}_-$ set. Now, after the input peaks at u_1, suppose the input experiences a monotonic decrease to
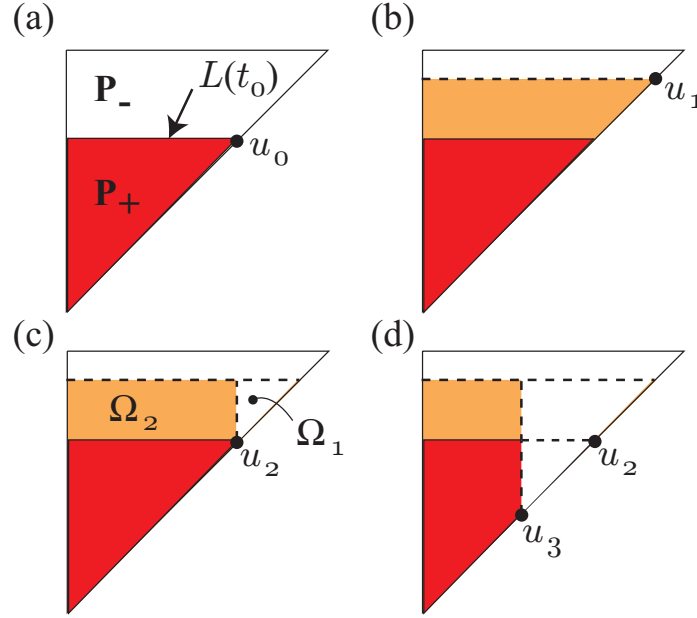
Figure 5.6: Behavior of Preisach plane.

the initial value $u_2 = u_0$, which causes the output to reduce by an amount that is related to the triangular area Ω_1 containing relays which have switched to the -1 state as indicated in Fig. 5.6(c). It is easy to see that when the input returns to u_0, the output $v_2 > v_0$ due to the additional contributions of $+1$ relays in the area Ω_2. In fact, further decrease in the input is required to achieve the initial output value of v_0, *e.g.*, compare Fig. 4.8 from the discussion of directionality in Chapter 4 and Fig. 5.6(d). As a result, the asymmetric switching of the relays associated with increasing and decreasing inputs causes branching, and the behavior in the Preisach plane clearly suggests that hysteresis behavior does not satisfy the ISIO property.

The fact that hysteresis does not satisfy Definition 5 is not astonishing because given a general desired trajectory $v_d \in C^0(I)$, for any value ρ the ILCA Eq. (5.4) does not converge as illustrated in the following example, where we make use of $\|\cdot\|_\infty$ norm. Consider the hysteresis curve shown in Fig. 5.7(a). Suppose this hysteresis curve is the desired behavior we would like the piezo positioner to achieve; therefore, the desired trajectory v_d is the
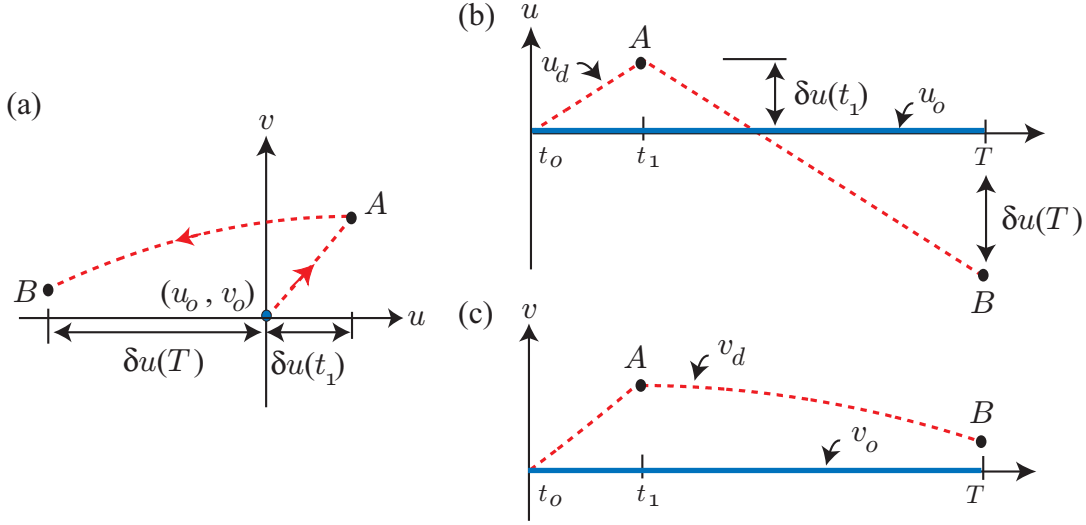
Figure 5.7: Hysteresis behavior: (a) hysteresis curve and corresponding (b) input and (c) output versus time.

dashed-line curve in Fig. 5.7(c) and the input that achieves v_d is the dashed line shown in Fig. 5.7(b) labeled u_d. Without loss of generality, assume that the initial input $u_0(t) = 0$ for all $t \in [0, T]$ (*e.g.*, the solid line in Fig. 5.7(b)). Likewise, the initial output is $v_0(t) = 0$ for all $t \in [0, T]$ (*e.g.*, the solid line in Fig. 5.7(c)). Now let $\rho < 0$, then immediately we find that the sequence of inputs generated by ILCA Eq. (5.4) diverges from the desired input u_d as $k \to \infty$ because $v_d - v_k \geq 0$ for all $k \in \mathbb{N}$, which causes $u_k \leq 0$ for all $k \in \mathbb{N}$, and $\|u_k(\cdot)\|_\infty$ increases without bound as $k \to \infty$. Now consider the case when $\rho > 0$. For this case, we also find that convergence of Eq. (5.4) is not possible over $[0, T]$ for the following reason: on the interval $[0, T]$, we find that $v_d(t) - v_0(t) \geq 0$, then for any $\rho > 0$ and $k = 1$, the term on the LHS of Eq. (5.4) is strictly greater than zero for all $t \in (0, T]$, hence $\|u_d(\cdot) - u_1(\cdot)\|_\infty \geq \|u_d(\cdot) - u_0(\cdot)\|_\infty$ implying that Eq. (5.4) fails to contract on the first step. In particular, contraction fails because the shape of the hysteresis curve is such that $|\delta u(t_1)| < |\delta u(T)|$ as shown in Figs. 5.7(a) and (b). Because of branching behavior, where the ascending and descending paths in the u versus v plane do not coincide, the error in the input fails to contract, hence converge.

One main reason why it is challenging to show contraction of ILCA Eq. (5.4) is the fact that the branching behavior leads to loss of directionality. As discussed previously in Chapter 4, Section 4.3.4, the sign of the tracking error, *i.e.*, $v_d - v_k$, does not provide enough information about the direction in which the input should be changed in order to reduce the tracking error. Because of the multivalued behavior of hysteresis, for a given output value, there exists an uncountable set of possible inputs to achieve the output value. Therefore, in general, the iterative learning control algorithm of the form Eq. (5.4) does not contract for any constant ρ due to lack of direction information. We observe, however, that if the input-output behavior was restricted to a single branch, then the sense of direction between the input and output can be achieved. For instance, on one single hysteresis branch, knowing the sign of the tracking error will provide the information needed to determine the direction the input should be changed to reduce the tracking error. This is the key observation to solving the convergence problem of ILCA Eq. (5.4). This observation also suggests that to stay on one single branch, the desired output must be monotonic (*cf.* Preisach Property 4). Therefore, the convergence of the ILCA for hysteretic systems can be readily shown for desired monotonic trajectories. An overview of the approach is presented in the following section.

5.2.4 Overview of the Approach

When the input-output behavior of a hysteretic system belongs on a single branch, the tracking error can be used to appropriately change the input to reduce the tracking error. The notion of direction is critical for the convergence of gradient-based searching algorithms. Motivated by this observation, the approach to proving convergence of the ILCA Eq. (5.4) is presented as follows. First we note that if the desired trajectory $v_d \in C^0(I)$ is monotonic, then by the Preisach Property 4, the input that achieves v_d is also monotonic, and of the same sign. This suggests that the input-output pair (u_d, v_d) traces out a single branch in the $u - v$ plane. Now, if the ILCA Eq. (5.4) generates input-output points $(u_k, \mathcal{H}[u_k])$ that belong on the same single branch, then over the course of the iteration process, the direction to change the input to reduce the tracking error is known. By exploiting the properties of the

Preisach hysteresis behavior on a branch, we find a solution to our ILC convergence problem. Again, the key requirement is that the desired trajectory be monotonic on the interval I so that the input-output behavior belongs on a single branch. As a result, convergence is proved for monotonic trajectories. Afterwards, we propose an algorithm to show convergence of general trajectories with more than one monotonic section by partitioned the desired output trajectory into N^* monotonic sections as shown in Fig. 5.8, and apply the results of the monotonic section to each individual section. In practice, the desired trajectory will contain a finite number of monotonic partitions and this thesis shows that convergence occurs branch-by-branch. In the end, we quantify the required number of iterations to realize a prescribed tracking precision. Finally, the theoretical developments are applied to an experimental atomic force microscope system to demonstrate the efficacy of the method in Chapter 6. We discuss in detail the process of implementing the iterative learning control algorithm for AFM imaging of a calibration sample. Our results show that the approach reduces hysteresis-caused positioning error by approximately an order of magnitude (roughly down to the noise level of the sensor measurement) compared to the feedback and model-based feedforward approach presented in Chapter 3. As a result, we demonstrate that the ILCA Eq. (5.4) can be employed for precision output tracking in SPM-based applications. Additionally, we note that the hysteresis-compensating feedforward input generated by this approach can be used to further improve the precision of integrated feedback/feedforward schemes, *e.g.*, [145].
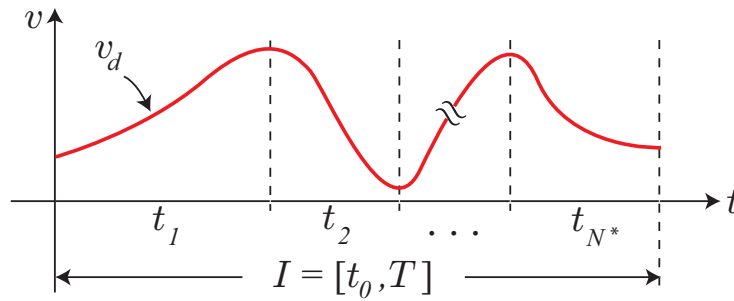
Figure 5.8: Monotonic partitioning of the desired output.

5.3 Convergence Analysis

In this section we prove convergence of the ILCA Eq. (5.4). We start by proving convergence for monotonic trajectories because the direction is known on a branch. This approach takes advantage of the property of the Preisach operator on a branch, which is presented in the following. For example, if the input-output pair $(u, \mathcal{H}[u])$ belongs on a branch, then the sign of the output error can be used to iteratively find an input that achieves a desired trajectory, hence, ILCA Eq. (5.4) converges. Afterwards, an algorithm is presented to extend the following results to general trajectories with more than one monotonic section.

5.3.1 Preisach Property on a Branch

The following property simply states that given two inputs on a single branch, the outputs associated with the two inputs are bounded above and below by functions of the difference in the inputs.

Lemma 1 (Property of a Branch) *Let Presiach model Assumption 1 hold and L_0 be an initial memory curve. Given $u_1, u_2 \in C^0_{m+}(I)$ (respectively, $u_1, u_2 \in C^0_{m-}(I)$) such that $(u_1, \mathcal{H}[u_1]), (u_2, \mathcal{H}[u_2]) \in \mathcal{B}_\uparrow[\cdot, L_0]$ (respectively, $(u_1, \mathcal{H}[u_1]), (u_2, \mathcal{H}[u_2]) \in \mathcal{B}_\downarrow[\cdot, L_0]$) and if $u_1(t_1) \le u_2(t_2)$ for any $t_1, t_2 \in I$, then*

$$\Phi\big(u_2(t_2) - u_1(t_1)\big) \le \mathcal{H}[u_2](t_2) - \mathcal{H}[u_1](t_1) \le \eta_2 \times \big(u_2(t_2) - u_1(t_1)\big), \tag{5.7}$$

where

$$\Phi\big(u_2(t_2) - u_1(t_1)\big) \;=\; \begin{cases} \underline{\mu}\big(u_2(t_2) - u_1(t_1)\big)^2 & \text{when } \big(u_2(t_2) - u_1(t_1)\big) \le \xi, \\[2mm] \underline{\mu}\Big[2\xi\big(u_2(t_2) - u_1(t_1)\big) - \xi^2\Big] & \text{when } \big(u_2(t_2) - u_1(t_1)\big) > \xi, \end{cases} \tag{5.8}$$

$$\eta_2 \;=\; 2\mu_{max}(\bar{u} - \underline{u}). \tag{5.9}$$

Proof

We first prove for the nondecreasing case, *i.e.*, $u_1, u_2 \in C^0_{m+}(I)$. Since the pairs $(u_1, \mathcal{H}[u_1])$ and $(u_2, \mathcal{H}[u_2]) \in \mathcal{B}_\uparrow[\cdot, L_0]$, then at time t_0, the memory curve L_0 associated with both inputs u_1 and u_2 are the same. Consequently, $u_1, u_2 \in C^0_{m+}(I)$ implies the inputs $u_1(t)$

and $u_2(t)$ for any $t \in I$ will have caused the last link of the memory curve associated with each input to sweep horizontally upward (recall the geometric interpretation of the Preisach model in Chapter 4). As a result, if $u_1(t_1) \leq u_2(t_2)$ for any $t_1, t_2 \in I$, then the Presiach plane is partitioned as shown in Fig. 5.9(b) where the output difference $\mathcal{H}[u_2](t_2) - \mathcal{H}[u_1](t_1)$ is related to the difference in the regions $\mathbf{P}_{2+}(t_2)$ and $\mathbf{P}_{1+}(t_1)$. Let $\hat{\Omega}$ represent the difference in these regions as shown in Fig. 5.9(b). Taking into account Eq. (4.9) for the output of the Preisach model and using the fact that $\mathbf{P}_{2+}(t_2) = \mathbf{P}_{1+}(t_1) \cup \hat{\Omega}$, we find that the largest region $\hat{\Omega}$ as illustrated in Fig. 5.9(c) yields

$$
\begin{aligned}
\mathcal{H}[u_2](t_2) - \mathcal{H}[u_1](t_1) &= 2 \iint_{\mathbf{P}_{2+}(t_2)} \mu(\alpha, \beta) d\alpha d\beta - 2 \iint_{\mathbf{P}_{1+}(t_1)} \mu(\alpha, \beta) d\alpha d\beta, \\
&= 2 \iint_{\hat{\Omega}} \mu(\alpha, \beta) d\alpha d\beta, \\
&\leq 2\mu_{max} \iint_{\hat{\Omega}} d\alpha d\beta, \\
&\leq 2\mu_{max} \left[(\bar{u} - \underline{u})(u_2(t_2) - u_1(t_1)) - \frac{1}{2}(u_2(t_2) - u_1(t_1))^2 \right], \\
&\leq 2\mu_{max} (\bar{u} - \underline{u})(u_2(t_2) - u_1(t_1)),
\end{aligned}
$$

(5.10)

for any $t_1, t_2 \in I$. Likewise, the smallest region for $\hat{\Omega}$ is a triangle where two possible cases exist when we consider the Preisach model Assumption 1:

Case 1: when $(u_2(t_2) - u_1(t_1)) \leq \xi$ (refer to Fig. 5.9(d)), $\hat{\Omega} = \hat{\Omega}_0 \cup \hat{\Omega}_+$ where $\hat{\Omega}_0 = \varnothing$, therefore

$$
\begin{aligned}
\mathcal{H}[u_2](t_2) - \mathcal{H}[u_1](t_1) &= 2 \iint_{\hat{\Omega}_+} \mu(\alpha, \beta) d\alpha d\beta, \\
&\geq 2\underline{\mu} \iint_{\hat{\Omega}} d\alpha d\beta, \\
&\geq 2\underline{\mu} \left[\frac{1}{2}(u_2(t_2) - u_1(t_1))^2 \right], \\
&\geq \underline{\mu}(u_2(t_2) - u_1(t_1))^2,
\end{aligned}
$$

(5.11)

for any $t_1, t_2 \in I$.
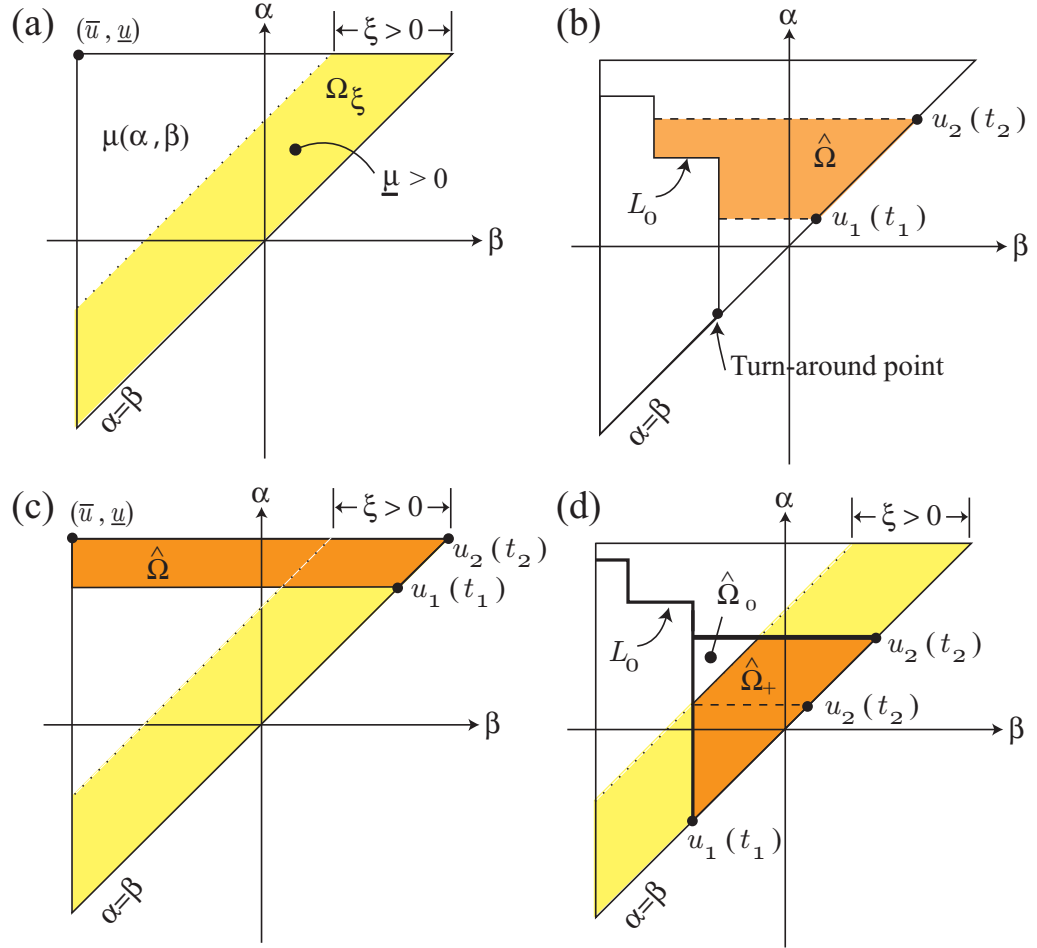
Figure 5.9: (a) Geometric representation of Assumption 1(c). (b)-(d) Behavior of memory curve with monotonic (increasing) change in the input u.

Case 2: when $\big(u_2(t_2) - u_1(t_2)\big) > \xi$ (refer to Fig. 5.9(d)),

$$
\begin{aligned}
\mathcal{H}[u_2](t_2) - \mathcal{H}[u_1](t_1) \;&=\; 2\iint\limits_{\hat{\Omega}} \mu(\alpha,\beta)d\alpha d\beta, \\[2mm]
&\geq\; 2\iint\limits_{\hat{\Omega}_0} \mu(\alpha,\beta)d\alpha d\beta + 2\underline{\mu}\iint\limits_{\hat{\Omega}_+} d\alpha d\beta. \\[2mm]
&\geq\; 2\underline{\mu}\iint\limits_{\hat{\Omega}_+} d\alpha d\beta, \\[2mm]
&\geq\; 2\underline{\mu}\left[\frac{1}{2}\big(u_2(t_2)-u_1(t_1)\big)^2 - \frac{1}{2}\Big(\big(u_2(t_2)-u_1(t_1)\big)-\xi\Big)^2\right], \\[2mm]
&\geq\; \underline{\mu}\left[2\xi\big(u_2(t_2)-u_1(t_1)\big) - \xi^2\right],
\end{aligned}
\tag{5.12}
$$

for any $t_1, t_2 \in I$.

The proof for the nonincreasing case, *i.e.*, $u_1, u_2 \in C^0_{m-}(I)$, follows directly from the above procedures; however, the difference is the inputs $u_1(t)$ and $u_2(t)$ for any $t \in I$ will have caused the last link of the memory curve associated with each input to sweep vertically from right to left (recall the geometric interpretation of the Preisach model in Chapter 4). Also, we note that if $u_1(t_1) \leq u_2(t_2)$ for any $t_1, t_2 \in I$, the output difference $\mathcal{H}[u_2](t_2) - \mathcal{H}[u_1](t_1)$ is related to the difference in the regions $\mathbf{P}_{2+}(t_2)$ and $\mathbf{P}_{1+}(t_1)$ and based on the geometry of the Preisach plane, Eqs. (5.10)–(5.12) hold, which completes the proof. ∎

5.3.2 The ILCA Generates a Sequence of Monotonic Inputs

This section shows that for a Preisach hysteretic system, using the ILCA Eq. (5.4), where the initial input is chosen to be monotonic, the resulting sequence of inputs generated by the ILCA will also be monotonic and of the same sign. For example, suppose that there is a branch $\mathcal{B}[u_d(\cdot), L_0]$ that is associated with $(u_d, \mathcal{H}[u_d])$, which originates from the point $(u(t_0), v(t_0))$. If the initial input u_0 is chosen to be nondecreasing (respectively, nonincreasing) with $u_0(t_0)$ compatible with the initial memory curve L_0, then subsequent inputs generated by the ILCA will also be nondecreasing (respectively, nonincreasing), and hence the branch $\mathcal{B}[u_k(\cdot), L_0]$ is the same as $\mathcal{B}[u_d(\cdot), L_0]$. This result implies that the pair $(u_k, \mathcal{H}[u_k])$, for all $k \in \mathbb{N}$, belongs on the same branch that is associated with the pair $(u_d, \mathcal{H}[u_d])$. And

since the pair $(u_k, \mathcal{H}[u_k])$ belongs on a single and known branch, directionality is achieved and the results of Lemma 1 applies for all $k \in \mathbb{N}$ iterations. By achieving directionality we can show that the ILCA converges for monotonic trajectories. It is important to note that each input sequence generated by the ILCA remains monotonic (and of the same sign as the desired trajectory), implying that additional branches cannot be generated. By Lemma 1, the property on a branch only applies to a single branch and it is not valid for a chain of branches. We note that generating additional branches leads to a loss in direction information, a behavior that must be avoided.

After establishing convergence for a monotonic desired trajectory v_d, then the method is extended to show convergence for a general desired trajectory $v_d \in C^0(I)$. Basically, the approach to this problem is to partition the desired trajectory into monotonic sections as illustrated in Fig. 5.8 and then develop an algorithm which incorporates the convergence proof for a single branch to prove convergence for all monotonic sections. We begin with the following initial condition requirement and then formally show that the ILCA generates a sequence of monotonic inputs.

Assumption 2 (Initial Condition Requirement) *The initial memory curves at time t_0 associated with each input sequence $u_k(t_0)$ for $k \in \mathbb{N}_0$ are the same, i.e., $L(t_0)$ is the same at the start of each iteration.*

Lemma 2 (Input Monotonicity) *Consider a hysteretic system of the form $v(t) = \mathcal{H}[u](t)$. Let the Preisach hysteresis operator $\mathcal{H} : C^0(I) \rightarrow C^0(I)$, with initial memory curve L_0, satisfy the Presiach model Assumption 1 and the initial condition Assumption 2. Given $v_d \in C_{m+}^0(I)$ (respectively, $v_d \in C_{m-}^0(I)$), pick $u_0 \in C_{m+}^0(I)$ (respectively, $u_0 \in C_{m-}^0(I)$) and if $0 < \rho \leq 1/\eta_2$, then the input sequence generated by the ILC control law Eq. (5.4) is such that $u_k \in C_{m+}^0(I)$ (respectively, $u_k \in C_{m-}^0(I)$), for all $k \in \mathbb{N}$.*

Proof

We prove by method of induction, first for the nondecreasing case, then for the nonincreasing case. First, by the Preisach Property 4, given $v_d \in C_{m+}^0(I)$ (respectively, $v_d \in C_{m-}^0(I)$) implies that $u_d \in C_{m+}^0(I)$ (respectively, $u_d \in C_{m-}^0(I)$), and so the pair $(u_d, \mathcal{H}[u_d]) \in \mathcal{B}_\uparrow[\cdot, L_0]$

(respectively, $(u_d, \mathcal{H}[u_d]) \in \mathcal{B}_\downarrow[\cdot, L_0])$, where the initial memory curve L_0 is associated with the input-output pair v_d and u_d. For the nondecreasing case (*i.e.*, $u_0, u_d, v_d \in C^0_{m+}(I)$) when $k = 0$ and by ILCA Eq. (5.4), for any $t_1 < t_2 \in I$ with $u_0, v_d \in C^0_{m+}(I)$, we have

$$
\begin{aligned}
u_1(t_2) - u_1(t_1) &= u_0(t_2) + \rho\big(\mathcal{H}[u_d](t_2) - \mathcal{H}[u_0](t_2)\big) - u_0(t_1) \\
&\quad - \rho\big(\mathcal{H}[u_d](t_1) - \mathcal{H}[u_0](t_1)\big).
\end{aligned} \tag{5.13}
$$

Substituting the terms in the above expression with the result of Lemma 1 and collecting terms, we obtain for the two cases:

Case 1: when $\big(u(t_2) - u(t_1)\big) \leq \xi$, we have

$$
\begin{aligned}
u_1(t_2) - u_1(t_1) &= \big(u_0(t_2) - u_0(t_1)\big) + \rho\big(\mathcal{H}[u_d](t_2) - \mathcal{H}[u_d](t_1)\big) \\
&\quad - \rho\big(\mathcal{H}[u_0](t_2) - \mathcal{H}[u_0](t_1)\big), \\
&\geq \big(u_0(t_2) - u_0(t_1)\big) + \rho\underline{\mu}\big(u_d(t_2) - u_d(t_1)\big)^2 \\
&\quad - \rho\eta_2\big(u_0(t_2) - u_0(t_1)\big), \\
&\geq \big(1 - \rho\eta_2\big)\big(u_0(t_2) - u_0(t_1)\big) + \rho\underline{\mu}\big(u_d(t_2) - u_d(t_1)\big)^2 \\
&\geq 0,
\end{aligned} \tag{5.14}
$$

for any $t_1 < t_2 \in I$ because $u_0, u_d \in C^0_{m+}(I)$ and

$$
0 < 2\rho\mu_{max}(\bar{u} - \underline{u}) = \rho\eta_2 \leq 1. \tag{5.15}
$$

Case 2: when $\big(u(t_2) - u(t_1)\big) > \xi$, we have

$$
\begin{aligned}
u_1(t_2) - u_1(t_1) &= \big(u_0(t_2) - u_0(t_1)\big) + \rho\big(\mathcal{H}[u_d](t_2) - \mathcal{H}[u_d](t_1)\big) \\
&\quad - \rho\big(\mathcal{H}[u_0](t_2) - \mathcal{H}[u_0](t_1)\big), \\
&\geq \big(u_0(t_2) - u_0(t_1)\big) + \rho\underline{\mu}\Big[2\xi\big(u_d(t_2) - u_d(t_1)\big) - \xi^2\Big] \\
&\quad - \rho\eta_2\big(u_0(t_2) - u_0(t_1)\big), \\
&\geq \big(1 - \rho\eta_2\big)\big(u_0(t_2) - u_0(t_1)\big) + \rho\underline{\mu}\Big[2\xi\big(u_d(t_2) - u_d(t_1)\big) - \xi^2\Big], \\
&\geq 0,
\end{aligned} \tag{5.16}
$$

for any $t_1 < t_2 \in I$ because $u_0, u_d \in C^0_{m+}(I)$ and Eq. (5.15) holds.

Therefore, we conclude that $u_1 \in C^0_{m+}(I)$. Now, suppose for k, $u_k \in C^0_{m+}(I)$, then for any $t_1, t_2 \in I$ such that $t_1 < t_2$, Eq. (5.4) gives us the following:

Case 1: when $(u(t_2) - u(t_1)) \le \xi$, we have

$$
\begin{aligned}
u_{k+1}(t_2) - u_{k+1}(t_1) \quad &= \quad (u_k(t_2) - u_k(t_1)) + \rho(\mathcal{H}[u_d](t_2) - \mathcal{H}[u_d](t_1)) \\
&\qquad -\rho(\mathcal{H}[u_k](t_2) - \mathcal{H}[u_k](t_1)), \\
&\ge \quad (1 - \rho\eta_2)(u_k(t_2) - u_k(t_1)) + \rho\underline{\mu}(u_d(t_2) - u_d(t_1))^2, \\
&\ge \quad 0, \qquad\qquad\qquad\qquad\qquad\qquad (5.17)
\end{aligned}
$$

for any $t_1 < t_2 \in I$ because $u_k, u_d \in C^0_{m+}(I)$ and Eq. (5.15) holds.

Case 2: when $(u(t_2) - u(t_1)) > \xi$, we have

$$
\begin{aligned}
u_1(t_2) - u_1(t_1) \quad &= \quad (u_k(t_2) - u_k(t_1)) + \rho(\mathcal{H}[u_d](t_2) - \mathcal{H}[u_d](t_1)) \\
&\qquad -\rho(\mathcal{H}[u_k](t_2) - \mathcal{H}[u_k](t_1)), \\
&\ge \quad (u_k(t_2) - u_k(t_1)) + \rho\underline{\mu}\left[2\xi(u_d(t_2) - u_d(t_1)) - \xi^2\right] \\
&\qquad -\rho\eta_2(u_k(t_2) - u_k(t_1)), \\
&\ge \quad (1 - \rho\eta_2)(u_k(t_2) - u_k(t_1)) + \rho\underline{\mu}\left[2\xi(u_d(t_2) - u_d(t_1)) - \xi^2\right] \\
&\ge \quad 0, \qquad\qquad\qquad\qquad\qquad\qquad (5.18)
\end{aligned}
$$

for any $t_1 < t_2 \in I$ because $u_k, u_d \in C^0_{m+}(I)$ and Eq. (5.15) holds.

As a result, we find that $u_{k+1} \in C^0_{m+}(I)$ and by induction we conclude that $u_k \in C^0_{m+}(I)$ for all $k \in \mathbb{N}$.

Now we prove the assertion for the nonincreasing case, *i.e.*, $u_0, u_d, v_d \in C^0_{m-}(I)$. The proof is the same as the previous result, except for the ordering that $u(t_1) \ge u(t_2)$ (because $u \in C^0_{m-}(I)$). For instance, when $k = 0$ and by Eq. (5.4), for any $t_1 < t_2 \in I$ with $u_0, v_d \in C^0_{m-}(I)$, we have

$$
\begin{aligned}
u_1(t_1) - u_1(t_2) \quad &= \quad u_0(t_1) + \rho(\mathcal{H}[u_d](t_1) - \mathcal{H}[u_0](t_1)) - u_0(t_2) \\
&\qquad -\rho(\mathcal{H}[u_d](t_2) - \mathcal{H}[u_0](t_2)). \qquad\qquad (5.19)
\end{aligned}
$$

Substituting the terms in the above expression with the result of Lemma 1 and collecting terms, we obtain for the two cases:

Case 1: when $\big(u(t_1) - u(t_2)\big) \leq \xi$, we have

$$
\begin{aligned}
u_1(t_1) - u_1(t_2) \;&=\; \big(u_0(t_1) - u_0(t_2)\big) + \rho\big(\mathcal{H}[u_d](t_1) - \mathcal{H}[u_d](t_2)\big) \\
&\qquad -\rho\big(\mathcal{H}[u_0](t_1) - \mathcal{H}[u_0](t_2)\big), \\
&\geq\; \big(u_0(t_1) - u_0(t_2)\big) + \rho\underline{\mu}\big(u_d(t_1) - u_d(t_2)\big)^2 \\
&\qquad -\rho\eta_2\big(u_0(t_1) - u_0(t_2)\big), \\
&\geq\; \big(1 - \rho\eta_2\big)\big(u_0(t_1) - u_0(t_2)\big) + \rho\underline{\mu}\big(u_d(t_1) - u_d(t_2)\big)^2, \\
&\geq\; 0, \hspace{6cm} (5.20)
\end{aligned}
$$

for any $t_1 < t_2 \in I$ because $u_0, u_d \in C^0_{m-}(I)$ and Eq. (5.15) holds.

Case 2: when $(u(t_1) - u(t_2)) > \xi$, we have

$$
\begin{aligned}
u_1(t_1) - u_1(t_2) \;&=\; \big(u_0(t_1) - u_0(t_2)\big) + \rho\big(\mathcal{H}[u_d](t_1) - \mathcal{H}[u_d](t_2)\big) \\
&\qquad -\rho\big(\mathcal{H}[u_0](t_1) - \mathcal{H}[u_0](t_2)\big), \\
&\geq\; \big(u_0(t_1) - u_0(t_2)\big) + \rho\underline{\mu}\Big[2\xi\big(u_d(t_1) - u_d(t_2)\big) - \xi^2\Big] \\
&\qquad -\rho\eta_2\big(u_0(t_1) - u_0(t_2)\big), \\
&\geq\; \big(1 - \rho\eta_2\big)\big(u_0(t_1) - u_0(t_2)\big) + \rho\underline{\mu}\Big[2\xi\big(u_d(t_1) - u_d(t_2)\big) - \xi^2\Big], \\
&\geq\; 0, \hspace{6cm} (5.21)
\end{aligned}
$$

for any $t_1 < t_2 \in I$ because $u_0, u_d \in C^0_{m-}(I)$ and Eq. (5.15) holds.

As a result, we conclude that $u_1 \in C^0_{m-}(I)$. Now, suppose for k, $u_k \in C^0_{m-}(I)$, then for any $t_1, t_2 \in I$ such that $t_1 < t_2$, Eq. (5.4) gives us the following:

Case 1: when $\big(u(t_1) - u(t_2)\big) \leq \xi$, we have

$$
\begin{aligned}
u_{k+1}(t_1) - u_{k+1}(t_2) \;&=\; \big(u_k(t_1) - u_k(t_2)\big) + \rho\big(\mathcal{H}[u_d](t_1) - \mathcal{H}[u_d](t_2)\big) \\
&\qquad -\rho\big(\mathcal{H}[u_k](t_1) - \mathcal{H}[u_k](t_2)\big), \\
&\geq\; \big(1 - \rho\eta_2\big)\big(u_k(t_1) - u_k(t_2)\big) + \rho\underline{\mu}\big(u_d(t_1) - u_d(t_2)\big)^2, \\
&\geq\; 0, \hspace{6cm} (5.22)
\end{aligned}
$$

for any $t_1 < t_2 \in I$ because $u_k, u_d \in C^0_{m-}(I)$ and Eq. (5.15) holds.

Case 2: when $\big(u(t_1) - u(t_2)\big) > \xi$, we have

$$
\begin{aligned}
u_{k+1}(t_1) - u_{k+1}(t_2) &= \big(u_k(t_1) - u_k(t_2)\big) + \rho\big(\mathcal{H}[u_d](t_1) - \mathcal{H}[u_d](t_2)\big) \\
&\quad -\rho\big(\mathcal{H}[u_k](t_1) - \mathcal{H}[u_k](t_2)\big), \\
&\geq \big(u_k(t_1) - u_k(t_2)\big) + \rho\underline{\mu}\Big[2\xi\big(u_d(t_1) - u_d(t_2)\big) - \xi^2\Big] \\
&\quad -\rho\eta_2\big(u_k(t_1) - u_k(t_2)\big), \\
&\geq \big(1 - \rho\eta_2\big)\big(u_k(t_1) - u_k(t_2)\big) + \rho\underline{\mu}\Big[2\xi\big(u_d(t_1) - u_d(t_2)\big) - \xi^2\Big], \\
&\geq 0, \tag{5.23}
\end{aligned}
$$

for any $t_1 < t_2 \in I$ because $u_k, u_d \in C^0_{m-}(I)$ and Eq. (5.15) holds.

As a result, we find that $u_{k+1} \in C^0_{m-}(I)$ and by induction we conclude that $u_k \in C^0_{m-}(I)$ for all $k \in \mathbb{N}$. This completes the proof. ∎

In summary, the results for the above lemma ensures that the Preisach property on a branch (Lemma 1) applies for all $k \in \mathbb{N}_0$ when the ILCA Eq. (5.4) is used. Furthermore, the results guarantee that if $0 < \rho \leq 1/\eta_2$, then the ILCA when applied to the hysteretic system does not generate any additional branches, *i.e.*, the input sequence remains monotonic and of the same sign as the desired trajectory. Now we are ready to present our main result.

5.3.3 Convergence for Monotonic Trajectories

The following theorem states that if the desired trajectory is monotonic and under certain conditions, the ILCA Eq. (5.4) converges:

Theorem 1 (Convergence for Monotonic Trajectories) *Consider a hysteretic system of the form $v(t) = \mathcal{H}[u](t)$. Let the Preisach hysteresis operator $\mathcal{H} : C^0(I) \to C^0(I)$, with initial memory curve L_0, satisfy the Presiach model Assumption 1 and the initial condition Assumption 2. Given $v_d \in C^0_{m+}(I)$ (respectively, $v_d \in C^0_{m-}(I)$), pick $u_0 \in C^0_{m+}(I)$ (respectively, $u_0 \in C^0_{m-}(I)$) and if $0 < \rho \leq 1/\eta_2$, then the iterative learning control algorithm Eq. (5.4) converges, i.e., $u_k(t) \to u_d(t)$, as $k \to \infty$ for every $t \in I$.*

Proof

Overview   For convenience, we define $\delta u_k(t) \triangleq u_d(t) - u_k(t)$. The objective is to show the terms of the sequence $\{|\delta u_k(t)|\}$ decays to zero as $k \to \infty$, for all $t \in I$. The following proof is analogous to showing a system is stable in the Lyapunov sense [178], where in this case the candidate Lyapunov function is the sequence $\{|\delta u_k(t)|\}$. The outline of the proof is as follows. **Step 1:** First, we show that the sequence $\{|\delta u_k(t)|\}$, for any $t \in I$, decreases monotonically as $k \to \infty$ and it is bounded, therefore the sequence converges [179]. **Step 2:** Second, we show that the sequence $\{|\delta u_k(t)|\}$ converges to the limit zero, the sequence's greatest lower bound, for all $t \in I$, hence $u_k(t) \to u_d(t)$ as $k \to \infty$. In the following, the proof of each step is presented and they are as follows:

Step 1:   In this step, we prove that the sequence $\{|\delta u_k(t)|\}_{k \in \mathbb{N}_0}$ decreases monotonically as $k \to \infty$ and it is bounded. We prove by method of induction. First, we immediately note that $v_d \in C_{m+}^0(I)$ (respectively, $v_d \in C_{m-}^0(I)$) implies $u_d \in C_{m+}^0(I)$ (respectively, $u_d \in C_{m-}^0(I)$) (See Preisach Property 4). Also, we assume that $v_d, u_0 \in C_{m+}^0(I)$ (nondecreasing case). For $k = 0$, suppose $u_0(t) \leq u_d(t)$ at $t \in I$. Using ILCA Eq. (5.4) and the results of Lemma 1, we find that

$$u_d(t) - u_1(t) = u_d(t) - u_0(t) - \rho\big(\mathcal{H}[u_d](t) - \mathcal{H}[u_0](t)\big) \leq u_d(t) - u_0(t), \qquad (5.24)$$

at $t \in I$. Likewise,

$$
\begin{aligned}
u_d(t) - u_1(t) &= u_d(t) - u_0(t) - \rho\big(\mathcal{H}[u_d](t) - \mathcal{H}[u_0](t)\big), \\
&\geq u_d(t) - u_0(t) - \rho\eta_2\big(u_d(t) - u_0(t)\big), \\
&\geq \big(1 - \rho\eta_2\big)\big(u_d(t) - u_0(t)\big), \\
&\geq 0, \qquad\qquad\qquad\qquad\qquad\qquad\qquad\qquad (5.25)
\end{aligned}
$$

at $t \in I$ because $0 < \rho\eta_2 \leq 1$. Consequently, Eqs. (5.24) and (5.25) give us

$$0 \leq u_d(t) - u_1(t) \leq u_d(t) - u_0(t), \quad \text{at } t \in I. \qquad (5.26)$$

Now suppose that $u_0(t) \geq u_d(t)$ at $t \in I$, then ILCA Eq. (5.4) and the results of Lemma 1 lead to

$$
\begin{aligned}
u_1(t) - u_d(t) &= u_0(t) + \rho\big(\mathcal{H}[u_d](t) - \mathcal{H}[u_0](t)\big) - u_d(t), \\
&= u_0(t) - \rho\big(\mathcal{H}[u_0](t) - \mathcal{H}[u_d](t)\big) - u_d(t), \\
&\leq u_0(t) - u_d(t),
\end{aligned}
\tag{5.27}
$$

at $t \in I$. Additionally, we find that

$$
u_1(t) - u_d(t) \geq \big(1 - \rho\eta_2\big)\big(u_0(t) - u_d(t)\big) \geq 0,
\tag{5.28}
$$

at $t \in I$ because $0 < \rho\eta_2 \leq 1$. As a result, Eqs. (5.27) and (5.28) imply

$$
u_d(t) - u_0(t) \leq u_d(t) - u_1(t) \leq 0,
\tag{5.29}
$$

and from Eqs. (5.26) and (5.29), we conclude that

$$
|u_d(t) - u_1(t)| \leq |u_d(t) - u_0(t)|,
\tag{5.30}
$$

at $t \in I$. Now, since on a branch Eq. (5.30) holds if $u_0(t) \leq u_d(t)$ at $t \in I$, or if $u_0(t) \geq u_d(t)$ at $t \in I$, and t was chosen arbitrarily, then Eq. (5.30) is satisfied for any $t \in I$.

Next, suppose for k, $u_k(t) \leq u_d(t)$ at $t \in I$. Using ILCA Eq. (5.4) and the results of Lemma 1, we can write

$$
u_d(t) - u_{k+1}(t) = u_d(t) - u_k(t) - \rho\big(\mathcal{H}[u_d](t) - \mathcal{H}[u_k](t)\big) \leq u_d(t) - u_k(t),
\tag{5.31}
$$

at $t \in I$. Similarly,

$$
\begin{aligned}
u_d(t) - u_{k+1}(t) &= u_d(t) - u_k(t) - \rho\big(\mathcal{H}[u_d](t) - \mathcal{H}[u_k](t)\big) \\
&\geq u_d(t) - u_k(t) - \rho\eta_2\big(u_d(t) - u_k(t)\big) \\
&\geq \big(1 - \rho\eta_2\big)\big(u_d(t) - u_k(t)\big) \\
&\geq 0, \qquad \text{at } t \in I,
\end{aligned}
\tag{5.32}
$$

because $0 < \rho\eta_2 \leq 1$. Consequently, Eqs. (5.31) and (5.32) give us

$$
0 \leq u_d(t) - u_{k+1}(t) \leq u_d(t) - u_k(t), \qquad \text{at } t \in I.
\tag{5.33}
$$

Now suppose that $u_k(t) \geq u_d(t)$ at $t \in I$, then ILCA Eq. (5.4) and the results of Lemma 1 lead to

$$u_{k+1}(t) - u_d(t) = u_k(t) + \rho\big(\mathcal{H}[u_d](t) - \mathcal{H}[u_k](t)\big) - u_d(t) \leq u_k(t) - u_d(t), \qquad (5.34)$$

at $t \in I$. Additionally, we find that

$$u_{k+1}(t) - u_d(t) \geq \big(1 - \rho\eta_2\big)\big(u_k(t) - u_d(t)\big) \geq 0, \qquad \text{at } t \in I. \qquad (5.35)$$

As a result, Eqs. (5.34) and (5.35) imply

$$u_d(t) - u_k(t) \leq u_d(t) - u_{k+1}(t) \leq 0, \qquad (5.36)$$

at $t \in I$ and from Eqs. (5.33) and (5.36), we conclude that

$$|u_d(t) - u_{k+1}(t)| \leq |u_d(t) - u_k(t)|, \qquad \text{at } t \in I. \qquad (5.37)$$

Now, since on a branch Eq. (5.37) holds if $u_k(t) \leq u_d(t)$ at $t \in I$, or if $u_k(t) \geq u_d(t)$ at $t \in I$, and t was chosen arbitrarily, then Eq. (5.37) is satisfied for any $t \in I$. Additionally, since k was chosen arbitrarily, we conclude by induction that Eq. (5.37) holds for $k \in \mathbb{N}_0$, implying that $\{|\delta u_k(t)|\}$ decreases monotonically in k. Furthermore, we observe that the sequence $\{|\delta u_k(t)|\}$ is bounded from above by $\|\delta u_0(\cdot)\|_\infty$, where the function norm $\|\cdot\|_\infty$ is defined by Eq. (5.2). Since $\{|\delta u_k(t)|\}$ is nonnegative and decreases monotonically in k, it is also bounded from below by zero. Therefore, the bounded sequence $\{|\delta u_k(t)|\}$ converges [179] for the nondecreasing case.

Finally, we note that Eqs. (5.24)–(5.37) also apply to the nonincreasing case, $i.e.$, $u_0, v_d \in C_{m-}^0(I)$, therefore the sequence $\{|\delta u_k(t)|\}$ decreases monotonically in k for any $t \in I$. Additionally, it is bounded from above by $\|\delta u_0(\cdot)\|_\infty$ and bounded from below by zero; therefore, we conclude that the bounded sequence $\{|\delta u_k(t)|\}$ converges for the nonincreasing case. This completes the proof of Step 1.

Step 2: In this step we show that the sequence $\{|\delta u_k(t)|\}$ converges to zero. We know from the previous step that the nonnegative sequence $\{|\delta u_k(t)|\}$ decreases monotonically and it is bounded from above by the constant $\|\delta u_0(\cdot)\|_\infty$ and bounded from below by zero

(because it is nonnegative). As a result, the sequence $\{|\delta u_k(t)|\}$ converges and its limit point is $a \geq 0$ [179]. Now we prove that the limit point of the sequence $a = 0$ by contradiction. If we consider the ILCA Eq. (5.4), then we find for the following two cases:

Case 1: $\delta u_k = \big(u_d(t) - u_k(t)\big) \leq \xi$. First, suppose that $u_0(t) \leq u_d(t)$ at $t \in I$. From Step 1, $u_0(t) \leq u_d(t)$ implies that $u_k(t) \leq u_d(t)$, for all $k \in \mathbb{N}$. Consequently, by the ILCA Eq. (5.4) and the results of Lemma 1, we find that

$$
\begin{aligned}
u_d(t) - u_{k+1}(t) &= u_d(t) - u_k(t) - \rho\big(\mathcal{H}[u_d](t) - \mathcal{H}[u_k](t)\big), \\
&\leq u_d(t) - u_k(t) - \rho\underline{\mu}\big(u_d(t) - u_k(t)\big)^2.
\end{aligned}
\tag{5.38}
$$

Furthermore, by Lemma 2 we get

$$
0 \leq u_d(t) - u_{k+1}(t) \leq u_d(t) - u_k(t) - \rho\underline{\mu}\big(u_d(t) - u_k(t)\big)^2.
\tag{5.39}
$$

Similarly, when $u_0(t) \geq u_d(t)$ at $t \in I$, from Step 1 and the results of Lemma 1, we find

$$
\begin{aligned}
u_{k+1}(t) - u_d(t) &= u_k(t) + \rho\big(\mathcal{H}[u_d](t) - \mathcal{H}[u_k](t)\big) - u_d(t), \\
&\leq u_k(t) - u_d(t) - \rho\underline{\mu}\big(u_k(t) - u_d(t)\big)^2,
\end{aligned}
\tag{5.40}
$$

and also by Lemma 2, we obtain

$$
0 \geq u_d(t) - u_{k+1}(t) \geq u_d(t) - u_k(t) + \rho\underline{\mu}\big(u_d(t) - u_k(t)\big)^2.
\tag{5.41}
$$

Then, considering the absolute value, Eqs. (5.39) and (5.41) yield

$$
\begin{aligned}
|u_d(t) - u_{k+1}(t)| &\leq |u_d(t) - u_k(t)| - \rho\underline{\mu}|u_d(t) - u_k(t)|^2, \\
|\delta u_{k+1}(t)| &\leq |\delta u_k(t)| - \rho\underline{\mu}|\delta u_k(t)|^2,
\end{aligned}
\tag{5.42}
$$

Now suppose for contradiction that the limit point for the sequence $\{|\delta u_k(t)|\}$ is $a > 0$. Subtracting $|\delta u_k(t)|$ from both sides of Eq. (5.42), taking limits of both sides and using the properties of limits, we obtain

$$
\begin{aligned}
|\delta u_{k+1}(t)| - |\delta u_k(t)| &\leq -\rho\underline{\mu}|\delta u_k(t)|^2, \\
\lim_{k\to\infty}\big\{|\delta u_{k+1}(t)| - \delta|u_k(t)|\big\} &\leq -\lim_{k\to\infty}\big\{\rho\underline{\mu}|\delta u_k(t)|^2\big\}, \\
a - a &\leq -\rho\underline{\mu}\lim_{k\to\infty}\big\{|\delta u_k(t)|^2\big\}, \\
0 &\leq -\rho\underline{\mu}a^2.
\end{aligned}
\tag{5.43}
$$

Since we have assumed that $a > 0$, and $0 < \rho \le 1/\eta_2$ and $\underline{\mu} > 0$, we arrive at a contradiction. Therefore, we conclude that the limit point $a = 0$, which implies that $\{|\delta u_k(t)|\} \to 0$ as $k \to \infty$ at $t \in I$, hence $u_k(t) \to u_d(t)$ as $k \to \infty$. Additionally, since $t \in I$ was chosen arbitrarily, we conclude that $u_k(t) \to u_d(t)$ as $k \to \infty$, for any $t \in I$.

Case 2: $\delta u_k = \big(u_d(t) - u_k(t)\big) > \xi$. First, suppose that $u_0(t) \le u_d(t)$ at $t \in I$. From Step 1, $u_0(t) \le u_d(t)$ implies that $u_k(t) \le u_d(t)$, for all $k \in \mathbb{N}$. Consequently, by the ILCA Eq. (5.4) and the results of Lemma 1, we find that

$$
\begin{aligned}
u_d(t) - u_{k+1}(t) \; &= \; u_d(t) - u_k(t) - \rho\big(v_d(t) - v_k(t)\big), \\
&\le \; u_d(t) - u_k(t) - \rho\underline{\mu}\Big[2\xi\big(u_d(t) - u_k(t)\big) - \xi^2\Big], \\
&\le \; u_d(t) - u_k(t) - \rho\underline{\mu}\xi\big(u_d(t) - u_k(t)\big).
\end{aligned}
\tag{5.44}
$$

Figure 5.10 shows a geometric representation for the upper bound in Eq. (5.44). Furthermore, by Lemma 2 we get

$$
0 \le u_d(t) - u_{k+1}(t) \le u_d(t) - u_k(t) - \rho\underline{\mu}\xi\big(u_d(t) - u_k(t)\big).
\tag{5.45}
$$
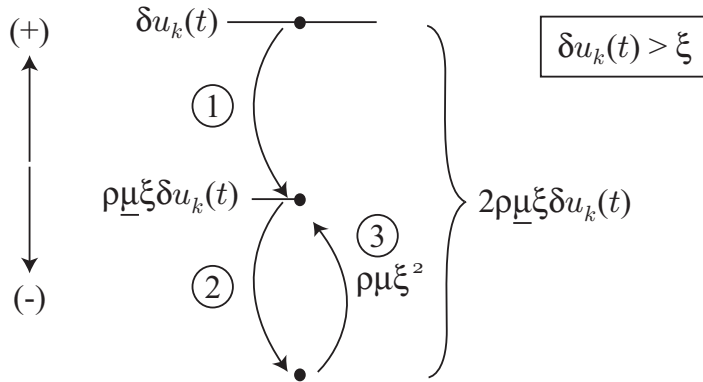
Figure 5.10: Geometric representation for the upper bound in Eq. (5.44).

Similarly, when $u_k(t) \geq u_d(t)$ at $t \in I$, we find that

$$
\begin{aligned}
u_{k+1}(t) - u_d(t) &= u_k(t) + \rho\big(v_d(t) - v_k(t)\big) - u_d(t), \\
&\leq u_k(t) - u_d(t) - \rho\underline{\mu}\Big[2\xi\big(u_k(t) - u_d(t)\big) - \xi^2\Big], \\
&\leq u_k(t) - u_d(t) - \rho\underline{\mu}\xi\big(u_k(t) - u_d(t)\big), \quad (5.46)
\end{aligned}
$$

and also by Lemma 2, we obtain

$$
0 \geq u_d(t) - u_{k+1}(t) \geq u_d(t) - u_k(t) + \rho\underline{\mu}\xi\big(u_d(t) - u_k(t)\big). \quad (5.47)
$$

Then, considering the absolute value, Eqs. (5.45) and (5.47) yield

$$
\begin{aligned}
\big|u_d(t) - u_{k+1}(t)\big| &\leq \big|u_d(t) - u_k(t)\big| - \rho\underline{\mu}\xi|u_d(t) - u_k(t)|, \\
|\delta u_{k+1}(t)| &\leq |\delta u_k(t)| - \rho\underline{\mu}\xi|\delta u_k(t)|. \quad (5.48)
\end{aligned}
$$

Now suppose for contradiction that the limit point for the sequence $\{|\delta u_k(t)|\}$ is $a > 0$. Subtracting $|\delta u_k(t)|$ from both sides of Eq. (5.48), then taking limits of both sides and using the properties of limits, we find that

$$
\begin{aligned}
|\delta u_{k+1}(t)| - |\delta u_k(t)| &\leq -\rho\underline{\mu}\xi|\delta u_k(t)|, \\
\lim_{k\to\infty}\Big\{|\delta u_{k+1}(t)| - |\delta u_k(t)|\Big\} &\leq \lim_{k\to\infty}\Big\{-\rho\underline{\mu}\xi|\delta u_k(t)|\Big\}, \\
a - a &\leq -\rho\underline{\mu}\xi \lim_{k\to\infty}\Big\{|\delta u_k(t)|\Big\}, \\
0 &\leq -\rho\underline{\mu}\xi a. \quad (5.49)
\end{aligned}
$$

Since we have assumed that $a > 0$, and $0 < \rho \leq 1/\eta_2$ and $\underline{\mu}, \xi > 0$, we arrive at a contradiction, therefore conclude that the limit point $a = 0$. Then, $\{|\delta u_k(t)|\} \to 0$ as $k \to \infty$ at $t \in I$, hence $u_k(t) \to u_d(t)$ as $k \to \infty$. Additionally, since $t \in I$ was chosen arbitrarily, we find that $\delta u_k(t) \to 0$ as $k \to \infty$, for any $t \in I$. This completes the proof of Step 2.

By Steps 1 and 2 we conclude that the ILCA Eq. (5.4) converges when $0 < \rho \leq 1/\eta_2$, and the desired trajectory and initial input are monotonic of the same sign. Moreover, the limit of the sequence $\{|\delta u_k(t)|\}$ is zero, which implies that $u_k(t) \to u_d(t)$ as $k \to \infty$, for all $t \in I$. This completes the proof. ∎

In summary, the ILCA Eq. (5.4) converges if:

1. The hysteresis behavior satisfies the Presiach model Assumption 1.

2. The initial condition is reset at each iteration, *i.e.*, $u_0(t_0) = u_k(t_0)$ for all $k \in \mathbb{N}$ (Assumption 2).

3. The constant $0 < \rho \le 1/\eta_2$ where $\eta_2 = 2\mu_{max}(\bar{u} - \underline{u})$.

4. The desired trajectory is continuous and monotonic on I, *i.e.*, $v_d \in C^0_m(I)$.

5.3.4   *Properties of Convergence*

In the following, we present the rate of convergence for the ILCA Eq. (5.4) in terms of the parameters of the Preisach model. Also, we quantify the number of iterations required to achieve a prescribed tracking precision $\varepsilon > 0$. In Chapter 6, the theoretical work will be compared with experimental results.

Theorem 2 (Rate of Convergence) *Let the conditions of Theorem 1 hold and $\varepsilon > 0$ be the desired tracking precision in the output, i.e., there exists $M \in \mathbb{N}$ such that $\|v_d(\cdot) - v_k(\cdot)\|_\infty < \varepsilon$, for all $k > M$. Then, the rates of convergence of ILCA Eq. (5.4) are:*

Case 1: *when $\varepsilon/(2\eta_2) \le \xi \Rightarrow \|u_d(\cdot) - u_k(\cdot)\|_\infty \le \xi$,*

$$\big\|v_d(\cdot) - v_{k+1}(\cdot)\big\|_\infty \le \big(1 - \rho\underline{\mu}\|v_d(\cdot) - v_0(\cdot)\|_\infty\big)\big\|v_d(\cdot) - v_k(\cdot)\big\|_\infty \le$$
$$\big(1 - \rho\underline{\mu}\|v_d(\cdot) - v_k(\cdot)\|_\infty\big)\big\|v_d(\cdot) - v_k(\cdot)\big\|_\infty \le \big(1 - \rho\underline{\mu}\varepsilon\big)\big\|v_d(\cdot) - v_k(\cdot)\big\|_\infty \quad (5.50)$$

Case 2: *when $\varepsilon/(2\eta_2) > \xi \Rightarrow \|u_d(\cdot) - u_k(\cdot)\|_\infty > \xi$,*

$$\big\|v_d(\cdot) - v_{k+1}(\cdot)\big\|_\infty \le \big\|v_d(\cdot) - v_k(\cdot)\big\|_\infty - 2\eta_2\rho\underline{\mu}\xi^2, \qquad (5.51)$$

where the norm $\|\cdot\|_\infty$ is defined in Eq. (5.2).

Proof

Case 1: when $\varepsilon/(2\eta_2) \leq \xi \Rightarrow \|u_d(\cdot) - u_k(\cdot)\|_\infty \leq \xi$. Suppose $u_k(t) \leq u_d(t)$ at $t \in I$, then by ILCA Eq. (5.4) and the results of Lemma 1 we find that

$$
\begin{aligned}
u_d(t) - u_{k+1}(t) &= u_d(t) - u_k(t) - \rho\big(v_d(t) - v_k(t)\big), \\
&\leq u_d(t) - u_k(t) - \rho\underline{\mu}\big(u_d(t) - u_k(t)\big)^2.
\end{aligned}
\tag{5.52}
$$

Furthermore, by Lemma 2, we get that

$$
0 \leq u_d(t) - u_{k+1}(t) \leq u_d(t) - u_k(t) - \rho\underline{\mu}\big(u_d(t) - u_k(t)\big)^2.
\tag{5.53}
$$

Similarly, when $u_k(t) \geq u_d(t)$ at $t \in I$, we find that

$$
\begin{aligned}
u_{k+1}(t) - u_d(t) &= u_k(t) + \rho\big(v_d(t) - v_k(t)\big) - u_d(t), \\
&\leq u_k(t) - u_d(t) - \rho\underline{\mu}\big(u_k(t) - u_d(t)\big)^2,
\end{aligned}
\tag{5.54}
$$

and also by Lemma 2, we obtain

$$
0 \geq u_d(t) - u_{k+1}(t) \geq u_d(t) - u_k(t) + \rho\underline{\mu}\big(u_d(t) - u_k(t)\big)^2.
\tag{5.55}
$$

Then, by Eqs. (5.53) and (5.55), and using the infinity norm of a function, we find that

$$
\|u_d(\cdot) - u_{k+1}(\cdot)\|_\infty \leq \|u_d(\cdot) - u_k(\cdot)\|_\infty - \rho\underline{\mu}\|u_d(\cdot) - u_k(\cdot)\|_\infty^2.
\tag{5.56}
$$

Multiplying both sides of Eq. (5.56) by $2\eta_2$ to convert to the output error and considering the bounds, we get

$$
\begin{aligned}
\big\|v_d(\cdot) - v_{k+1}(\cdot)\big\|_\infty &\leq \big(1 - \rho\underline{\mu}\|v_d(\cdot) - v_0(\cdot)\|_\infty\big)\big\|v_d(\cdot) - v_k(\cdot)\big\|_\infty \leq \\
\big(1 - \rho\underline{\mu}\|v_d(\cdot) - v_k(\cdot)\|_\infty\big)\big\|v_d(\cdot) - v_k(\cdot)\big\|_\infty &\leq \big(1 - \rho\underline{\mu}\varepsilon\big)\big\|v_d(\cdot) - v_k(\cdot)\big\|_\infty.
\end{aligned}
\tag{5.57}
$$

Case 2: when $\varepsilon/(2\eta_2) > \xi \Rightarrow \|u_d(\cdot) - u_k(\cdot)\|_\infty > \xi$. Suppose $u_k(t) \leq u_d(t)$ at $t \in I$, then by ILCA Eq. (5.4) and the results of Lemma 1 we find that

$$
\begin{aligned}
u_d(t) - u_{k+1}(t) &= u_d(t) - u_k(t) - \rho\big(v_d(t) - v_k(t)\big), \\
&\leq u_d(t) - u_k(t) - \rho\underline{\mu}\Big[2\xi\big(u_d(t) - u_k(t)\big) - \xi^2\Big], \\
&\leq u_d(t) - u_k(t) - \rho\underline{\mu}\xi^2.
\end{aligned}
\tag{5.58}
$$

Furthermore, by Lemma 2, we get that (refer to Fig. 5.10)

$$0 \leq u_d(t) - u_{k+1}(t) \leq u_d(t) - u_k(t) - \rho\underline{\mu}\xi^2. \tag{5.59}$$

Similarly, when $u_k(t) \geq u_d(t)$ at $t \in I$, we find that

$$\begin{aligned} u_{k+1}(t) - u_d(t) &= u_k(t) + \rho\big(v_d(t) - v_k(t)\big) - u_d(t), \\ &\leq u_k(t) - u_d(t) - \rho\underline{\mu}\Big[2\xi\big(u_k(t) - u_d(t)\big) - \xi^2\Big], \end{aligned} \tag{5.60}$$

and also by Lemma 2, we obtain

$$0 \geq u_d(t) - u_{k+1}(t) \geq u_d(t) - u_k(t) + \rho\underline{\mu}\xi^2. \tag{5.61}$$

Then, by Eqs. (5.59) and (5.61), and using the infinity norm of a function, we find that

$$\big\|u_d(\cdot) - u_{k+1}(\cdot)\big\|_\infty \leq \big\|u_d(\cdot) - u_k(\cdot)\big\|_\infty - \rho\underline{\mu}\xi^2. \tag{5.62}$$

Again, multiplying the above by $2\eta_2$, we find that

$$\big\|v_d(\cdot) - v_{k+1}(\cdot)\big\|_\infty \leq \big\|v_d(\cdot) - v_k(\cdot)\big\|_\infty - 2\eta_2\rho\underline{\mu}\xi^2. \tag{5.63}$$

In summary, the rate of the convergence when the tracking error is sufficiently small is linear, *i.e.*, when $\varepsilon/(2\eta_2) \leq \xi$. Otherwise, the tracking error decreases by the constant amount $2\eta_2\rho\underline{\mu}\xi^2$ from one iteration to the next. This completes the proof. ∎

Remark 2 *We note that the bounds on the rate of convergence can be tightened if a priori information about the Preisach weighting surface is available. We will show this in the experimental implementation of the ILC scheme in Chapter 6.*

Suppose a precision $\varepsilon > 0$ is specified for the output tracking error. Furthermore, assume that $\varepsilon/(2\eta_2) \leq \xi$, where $\xi > 0$ is defined in the Preisach Assumption 1. In this case, the number of iterations required to achieve the precision ε is determined as follows. By Eq. (5.56), we find that

$$\|v_d(\cdot) - v_{k+1}(\cdot)\|_\infty \leq \big(1 - \rho\underline{u}\varepsilon\big)\|v_d(\cdot) - v_k(\cdot)\|_\infty, \tag{5.64}$$

which implies that

$$\|v_d(\cdot) - v_k(\cdot)\|_\infty \leq \gamma^k \|v_d(\cdot) - v_0(\cdot)\|_\infty. \tag{5.65}$$

where $\gamma = (1 - \rho\underline{\mu}\varepsilon)$ and $0 < \rho \leq 1/\eta_2$. Solving for the required number of iterations $\mathcal{K}$ in terms of ε using Eq. (5.65), we obtain

$$k > \mathcal{K} = \frac{\ln(K_1\varepsilon)}{\ln\left(1 - K_2\varepsilon\right)}, \tag{5.66}$$

where

$$K_1 = \frac{1}{\|v_d(\cdot) - v_0(\cdot)\|_\infty}, \tag{5.67}$$

$$K_2 = \rho\underline{\mu}. \tag{5.68}$$

5.3.5   Convergence for General Trajectories

Now we discuss the extension of Theorem 1 for general desired trajectories, those with more than one monotonic partition. First, we say that $\Lambda(v) = \{t_i\}_{0\leq i\leq N}$, $t_0 = t_0 < t_1 < \cdots < t_N = T$, is a *monotonicity partition* for $v : I \rightarrow \mathbb{R}$, if v is monotone on all subintervals $[t_i, t_{i+1}] \subset I$ (*e.g.*, see reference [18], Definition 2.2.2). Second, by $N_m(\Lambda(v))$ we denote the number of monotonicity intervals in the monotonicity partition of v. Now, given $v_d \in C^0(I)$, let $N_m(v_d) \in \mathbb{N}$ be the number of monotonic partitions of the desired trajectory v_d. We assume that the number of monotonic partitions for a desired trajectory is finite, *i.e.*, $N_m(\Lambda(v)) < \infty$. In practice, this is a reasonable assumption for trajectories employed in piezo-based operations, such as AFM-based imaging [2]. Then the algorithm for showing convergence of a general desired trajectory is to apply the results of Theorem 1 to each section individually until convergence of all sections is achieved. The algorithm is explained by the following example:

First, consider an example desired trajectory $v_d \in C^0(I)$ (dashed line) defined over the interval $I = [0, T]$ as illustrated in Fig. 5.12(a1). Without loss of generality (and for simplicity), we pick an example where there are two monotonic partitions $(N_m(\Lambda(v_d)) = 2)$ as shown in the figure, *e.g.*, the monotonic partitions are $[0, t_1] \cup [t_1, T] \subset I$. Also, the

desired input u_d that achieves the example v_d is depicted in Fig. 5.12(a2)[3]. In Fig. 5.12(a1), the desired trajectory v_d is sandwiched between two curves that represent the bounds on the tracking precision, $\varepsilon > 0$. The tracking precision in the output ε is chosen by the designer. Now, the objective is to apply the ILCA Eq. (5.4) until the output error is within the bound ε for all $t \in [t_0, T]$. The following algorithm applies to the example, but it can also be generalized to trajectories that have more monotonic sections than this example. We assume that all the conditions of Theorem 1 hold. A flow chart of the algorithm is shown in Fig. 5.11 and the steps are as follows:

1. First, the desired trajectory $v_d \in C^0(I)$ is partitioned into monotonic sets where in this specific example we have $\Lambda(v_d) = \{0, t_1, T\}$ (see Fig. 5.12(a1)). This partition gives us $N_m(\Lambda(v_d)) = 2$, where the time interval partitions are as follows: $[0, t_1] \cup [t_1, T] \subset I$. Therefore, over $I_1 = [0, t_1]$, the partition $v_1 = \{v_d(t) | t \in I_1 = [0, t_1]\}$ is monotonic. In the example, $v_1 \in C^0_{m+}(I_1)$, $i.e.$, nondecreasing on I_1. Likewise, we have find that $v_2 = \{v_d(t) | t \in I_2 = [t_1, T]\} \in C^0_{m-}(I_2)$, $i.e.$, nonincreasing on I_2.

2. Next, we initialize the system as described in Assumption 2. A detailed example of this procedure can be found in the next chapter.

3. Then, starting with the first monotonic partition, the ILCA Eq. (5.4) with ρ chosen sufficiently small (see the requirements of Theorem 1), is applied to the hysteretic system.

4. Afterwards, for each iteration, we check the precision of the tracking error with respect to the desired precision $\varepsilon > 0$ (see Fig. 5.12(b1)). If the precision is within the desired value, then we proceed to the next step, otherwise, we go back to Step 2 and continue the iteration process.

---

[3]We note that the desired input u_d shown in Fig. 5.12(a2) is only an example. The actual u_d may differ from the example shown, however, by Preisach Property 4, over each monotonic partition of v_d, the input u_d is also monotonic and of the same sign in monotonicity as v_d

Start

Step 1

Partition desired
trajectory v_d

Step 2   for the nth partition

Initialize the
system

Step 3   at the kth trial

Increment k

Apply ILCA
for nth partition

Increment n

Step 6

Level
input/output

Step 4

No $\|v_d - v_k\|_\infty < \varepsilon$?

Yes

Step 5

$n = N^*$?   No

Yes

Finish
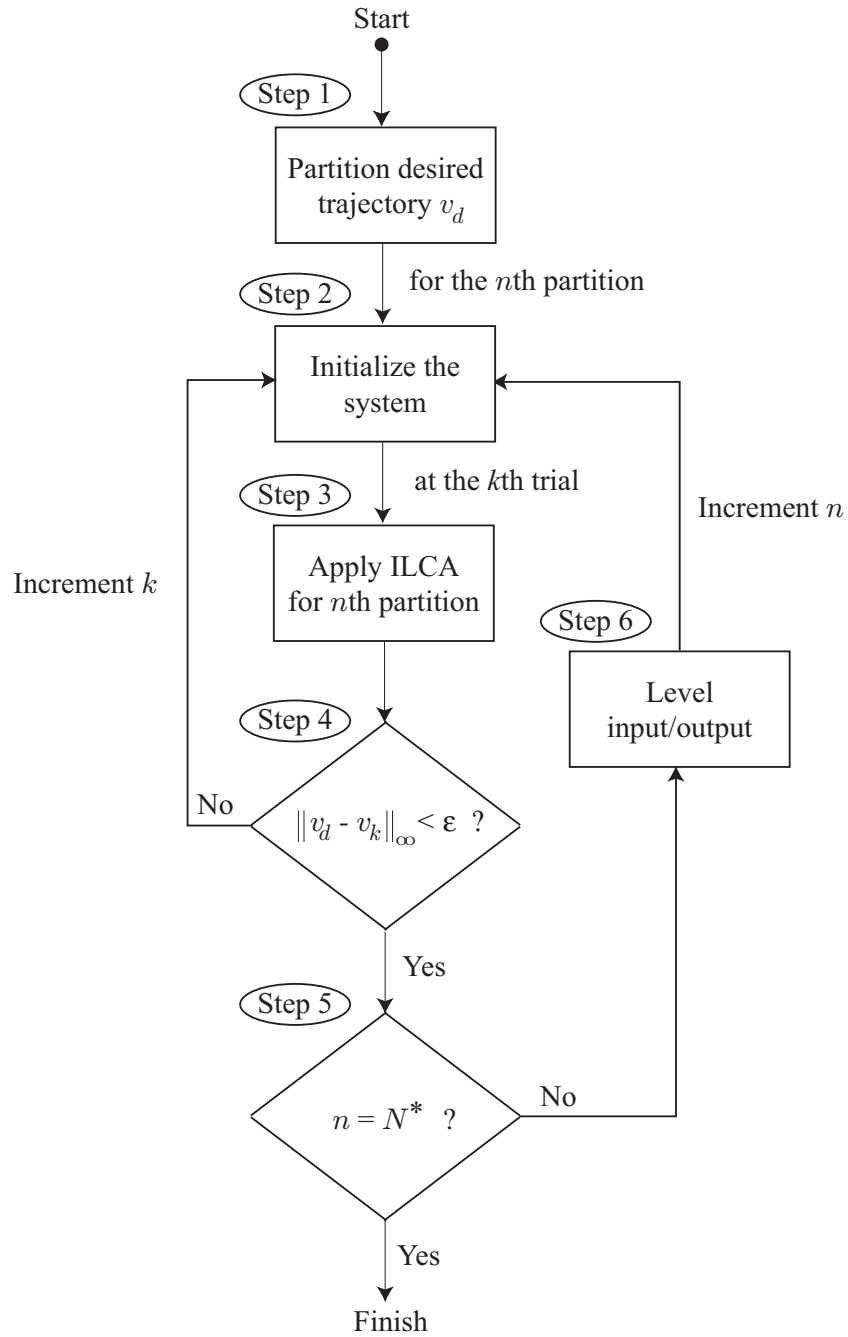
Figure 5.11: The ILC implementation flow chart.

98
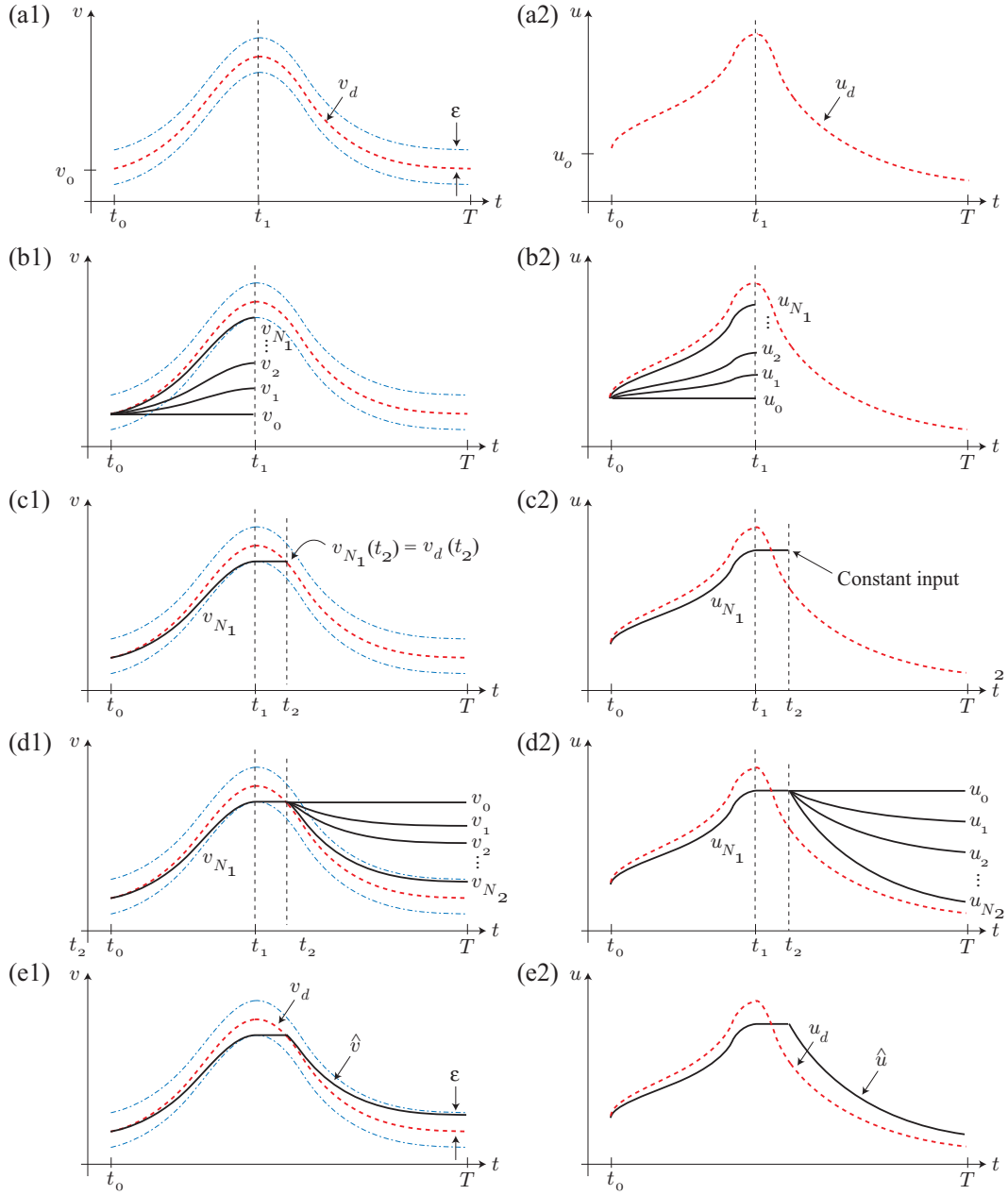
Figure 5.12: The ILC method applied to track a trajectory with two monotonic partitions.

5. Now, once a desired tracking precision is achieved, (see Fig. 5.12(b2)), we let $N_1 \in \mathbb{N}$ be the number of iterations that achieves the desired precision ε over the interval I_1. At this point we check whether precision tracking of all N^* monotonic partitions have been achieved. If it is completed, then the algorithm stops, otherwise, we continue to the next step.

6. In this step, the input is held constant until the time instant t_2 when $v_{N_1}(t_2) = v_d(t_2)$ (see Fig. 5.12(c1) and (c2)). This procedure is necessary to set up the initial conditions for applying the ILCA Eq. (5.4) to the next monotonic section defined over $[t_2, T]$. Therefore, the input $u_{N_1}(t)$ for $t \in [0, t_2]$ is combined with the input used in the initialization phase prior to time t_0 (see Assumption 2). Finally, the ILCA Eq. (5.4) is applied to the next (or second section in this example) until the tracking precision ε is achieved (see Fig. 5.12(d1) and (d2)). Let $N_2 \in \mathbb{N}$ be the number of iterations that achieves the desired precision ε over the interval $[t_2, T]$. Figures 5.12(e1) and (e2) show the resulting performance of the input $\hat{u} = u_{N_1} \cup u_{N_2}$ when it is applied to the hysteretic system. Now, for trajectories with more monotonic partitions, Steps 2 through 6 are repeated until the prescribed tracking precision is achieved for the entire trajectory.

Proposition 2 *Consider a hysteretic system of the form $v(t) = \mathcal{H}[u](t)$. Let $v_d(t) \in C^0(I)$ be given with the number of monotonicity intervals equal to $N_m(v_d) = N^* > 1$ and for a given $\varepsilon > 0$ tracking precision and using the above algorithm, the total number of iterations $\mathcal{K}^* \in \mathbb{N}$, such that $\|v_d(\cdot) - v_k(\cdot)\|_\infty < \varepsilon$ whenever $k > \mathcal{K}^*$ is*

$$\mathcal{K}^* = N^* \times \mathcal{K}, \tag{5.69}$$

where $\mathcal{K}$ is given by Eq. (5.66).

Proof

Following the steps of the propose algorithm presented above, for a given $v_d \in C^0(I)$, we form the monotonicity partition $\Lambda(v_d)$ of the desired trajectory v_d, yielding $N_m(\Lambda(v_d)) = N^*$. Given $\varepsilon > 0$, we apply Theorem 1 to the first monotonic section of v_d, and iterate

until the required tracking precision is achieve, where the number of iterations is given by Eq. (5.66). Following the above algorithm, after the first $\mathcal{K}$ number of iterations, the input $u_{\mathcal{K}}(t)$ and output $v_{\mathcal{K}}(t)$ for $t \in [t_0, t_1]$ are chosen as the desired input-output pair for the first monotonic section. At time t_1, the memory curve achieved by the input $u_{\mathcal{K}}(t)$ for $t \in [t_0, t_1]$ is chosen as the initial memory curve L_0 for the next monotonic section of v_d, *i.e.*, $v_d(t)$ for $t \in [t_1, t_2]$. Then, Theorem 1 is applied again, and we iterate another $\mathcal{K}$ number of iterations to achieve ε precision. This process is repeated N^*-times and we find that $\mathcal{K}^* = N^* \times \mathcal{K}$. ∎

5.4   Summary

In this chapter, we proved convergence of a proposed iterative learning control algorithm for hysteretic systems. The proof was based on the properties of the Presiach hysteresis model on a branch. In particular, it was shown that when the input-output behavior belongs on a single branch, then convergence for monotonic trajectories can be achieved because direction information is known between the input and output. However, the effect of branching makes it difficult to show convergence for the general case. But by using the results along a branch, an algorithm was proposed to achieve convergence for general trajectories which involves partitioning the trajectory into monotonic sections. Finally, we quantified the number of iterations required to achieve a prescribed tracking precision in terms of the parameters of the Preisach model. Next, the ILCA is applied to an experimental piezo positioning system to demonstrate its effectiveness.

Chapter 6

ITERATIVE LEARNING CONTROL OF HYSTERESIS:
EXPERIMENTAL RESULTS AND DISCUSSION

This chapter discusses the implementation of the iterative learning control method presented in the previous chapter. Experiments were performed on a commercial atomic force microscope system to demonstrate the efficacy of the method. The first section describes the experimental AFM system, followed by a discussion of the modeling of the hysteresis behavior. The modeling process involves isolating the system from the effect of creep using the inversion-based feedforward approach [2]. Afterwards, the parameters of the model are used to implement the ILCA Eq. (5.4). Finally, the remaining sections of this chapter: (i) show experimental results that demonstrate nano-precision positioning and (ii) characterize the performance of the ILC approach.

6.1 Experimental Atomic Force Microscope System

6.1.1 Overview

The experimental atomic force microscope system is a Burleigh Metris-2000NC AFM designed to image samples [67, 64, 65]. The AFM uses a sectored piezoelectric-tube (lead zirconate-titanate, PZT) positioner[1] to move a probe tip relative to a sample surface in the x-, y- and z-axis as shown in Fig. 2.5. The maximum input voltage that can be applied to the piezo-amplifier, which drives the piezo positioner, is limited to ± 5 V. Over the input range of ± 5 V, the piezo positioner has lateral, x- and y-axis, scan ranges of 95 μm and 120 μm, respectively. According to Burleigh's specifications [180], the position resolution is better than 50 angstroms in the lateral directions and 10 angstroms in the vertical (z) di-

---

[1]Long range Metris-3070 sample scanning module [180]

rection[2]. In the experiments, we apply the proposed ILC method to the lateral axes (x and y); however, the method can also be applied to the z-axis if movement leads to significant hysteresis effect.

A custom optical displacement sensor was designed to measure the lateral displacement of the piezo positioner. The level of the line noise in the sensor measurement was observed to be ± 10 mV, which corresponds to a sensor resolution of ± 140 nm in the x-axis and ± 190 nm in the y-axis. Being optical in nature, the sensor's bandwidth, in addition to the dynamic response of its signal conditioning circuitry, exceeds that of the mechanical bandwidth of the system (discussed in the next section). Therefore, the sensor adequately senses the dynamic behavior of the piezo positioner. A detailed discussion of the optical sensor, including a circuit diagram, can be found in Appendix D.

For controlling the commercial AFM system, an IBM personal computer (PC) based on an Intel 266 Mhz processor is equipped with a National Instruments Lab-PC+ data acquisition card (DAC). The DAC is used to generate command signals to control the piezo positioner. Also, the DAC measures the deflection of the AFM cantilever during operation, as well as records the output of the optical sensors (see Appendix D). A `C`-program[3] was written for the DAC for open-loop and closed-loop control. The PC-based data acquisition system can achieve 35 kHz closed-loop control (see Appendix E for sample `C`-programs).

For all imaging experiments, the AFM was operated in constant-height noncontact mode. In this mode, a reference force, based on the manufacturer's specifications [180], was chosen for imaging. During the tip-to-sample approach phase, a z-axis PID-feedback controller was engaged to initially bring the tip within close proximity to the sample surface. Once the cantilever achieved the reference force, the PID gains (proportional, derivative and integral) were reduced. The gains were reduced in such a way that during scanning, the PID controller was essentially inactive and did not vary the command signal in the z-axis. In effect, as the probe tip was scanned across sample surface, the deflection of the cantilever and probe tip corresponds to the topology of the sample surface, $i.e.$, the cantilever's deflection signal

---

[2]Based on the assumption that the command signal is properly isolated from electrical noise and mechanical vibrations.

[3]Borland Turbo C MSDOS compiler, Version 3.0. See Appendix E for sample programs.

measured by an optical sensor was proportional to the relative distance between the probe tip and sample surface. By combining the information from the cantilever's deflection and the lateral (x- and y-axis) position of the probe tip over the sample surface, an image of the sample surface can be constructed.

The raster pattern used for imaging is illustrated in Figs. 2.6 and 6.11, where the trajectory in the x-axis is a triangle wave, and a ramp signal for the y-axis trajectory. The effective scan area for the first type is rectangular. As the AFM-probe tip is scanned over the surface of a sample, the deflection of the tip is measured at a fixed time instant and this information is used to construct an image of the topology of the sample surface. Additionally, a spiral pattern was used and the results are discussed in Appendix D. In this chapter, we focus on the results of the standard (rectangular) raster pattern.

6.1.2   Frequency Response

The frequency response of the piezo positioner in the x- and y-axis are shown in Fig. 6.1. The frequency response was measured using a dynamic signal analyzer (DSA)[4]. A sinusoidal input voltage, u, generated by the DSA was applied to the piezo positioner. The resulting lateral displacement the measured by the optical sensor was fed back to the DSA to construct the frequency response curves shown in Fig. 6.1. The frequency response was measured over a displacement range of 2.00 μm, which is less than 2% of the maximum output range, where hysteresis is negligible. In addition, the frequency response was measured over a relatively high frequency range (1 Hz - 7 kHz) so that the effect of creep is small. We note that the dominating resonant peak for the x- and y-axis are 445 Hz and 454 Hz, respectively. Additionally, the bandwidth of the piezo positioner (frequency at which the magnitude response crosses the value of -3 dB below the DC-gain) in the x- and y-axis are 541 Hz and 558 Hz, respectively.

---

[4]Stanford Research Systems Model SR785
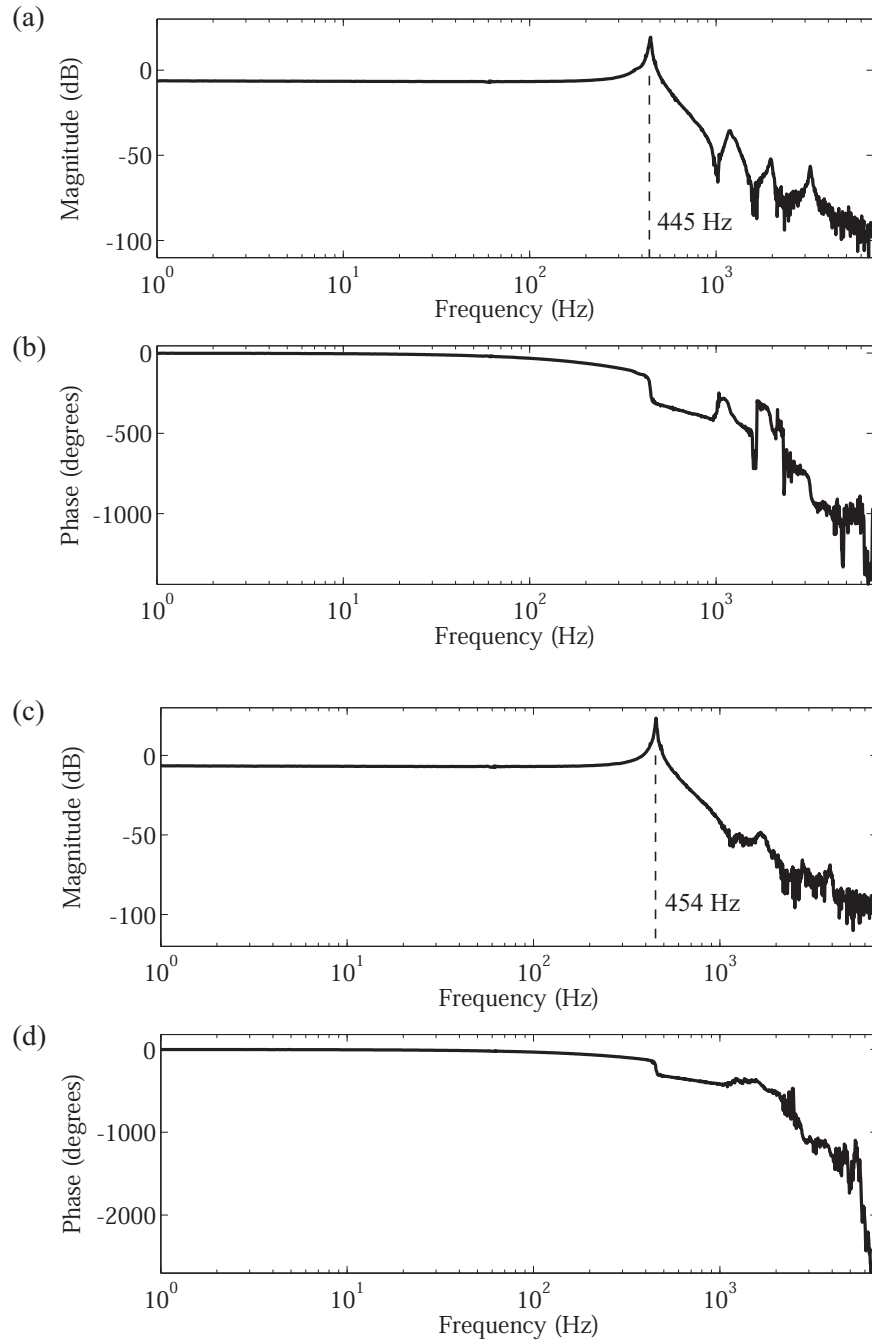
Figure 6.1: Frequency response curves for the piezo-scanner used in the Burleigh AFM-imaging system: (a) and (b) magnitude and phase versus frequency along the x-axis, respectively; (c) and (d) magnitude and phase versus frequency along the y-axis, respectively.

6.1.3 Hysteresis Effect

The measured hysteresis effect in the piezo positioner is significant. For example, in Figs. 6.2 and 6.3, the measured output hysteresis is 13.42% and 13.01% of the total displacement range for the x- and y-axis, respectively (*cf.* Figs. 6.2(c) and 6.3(c)).

6.2 Hysteresis Model Identification

An approximate model of hysteresis for an experimental system can be obtained from measured output data. Several approaches are available to determine the Preisach weighting surface $\mu(\cdot, \cdot)$, *e.g.*, see the review in reference [125] and also in reference [114]. One approach is to generate a collection of first-order descending (FOD) curves, compile the curves into a FOD surface and then differentiate the FOD surface to find the Preisach weighting surface $\mu(\cdot, \cdot)$ [143, 139]. This approach is described in more detail in Appendix C and it was applied to find the Preisach weighting surface for an experimental piezo positioner. Although the method is straightforward, the differentiation process can amplify noise in the measured output data, causing significant error. An alternative, and more favorable technique to find μ, involves discretizing the Preisach plane and using a least-squares technique to determine the values of μ at a finite number of locations in the Preisach plane $\mathbf{P}$ [181, 125]. In the following, we discuss an example to illustrate this method.

6.2.1 The Approach

Consider the Preisach plane $\mathbf{P}$ as shown in Fig. 6.4(a). The objective is to find an approximation to the weighting function $\mu(\cdot, \cdot)$ over $\mathbf{P}$ based on measured output data. To do this, we recall the output equation for the Preisach model presented earlier in Chapter 4 (Eqs. (4.3) and (4.8)):

$$
\begin{aligned}
v(t) &= \iint_{\alpha \geq \beta} \mu(\alpha, \ \beta) \mathcal{R}_{\alpha,\beta}[u](t) d\alpha d\beta, \\
&= \iint_{\mathbf{P}_+(t)} \mu(\alpha, \beta) d\alpha d\beta - \iint_{\mathbf{P}_-(t)} \mu(\alpha, \beta) d\alpha d\beta,
\end{aligned}
\tag{6.1}
$$
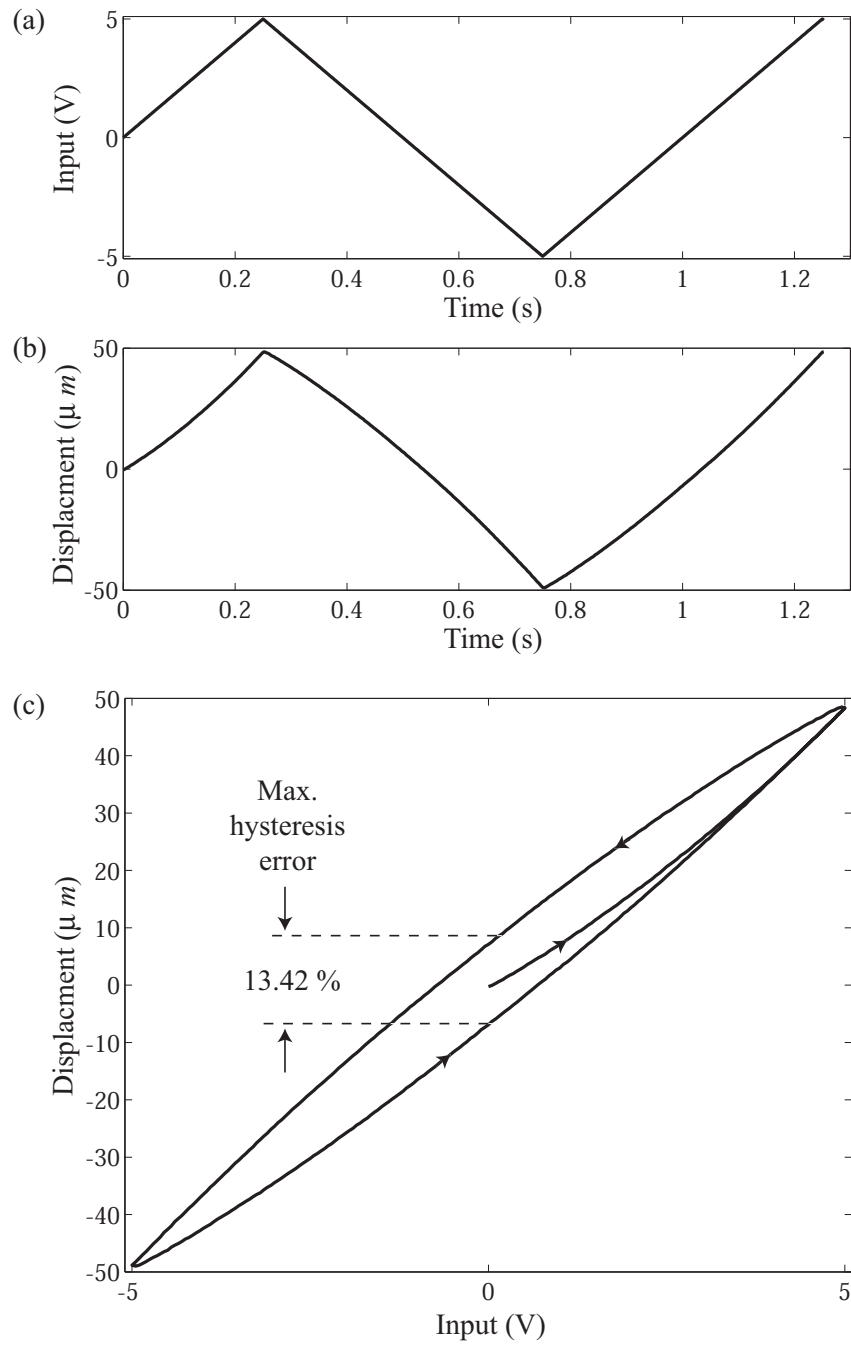
Figure 6.2: Hysteresis effect in x-axis. (a) Input versus time; (b) displacement along x-axis versus time; (c) hysteresis curve where arrows indicate ascending and descending paths.
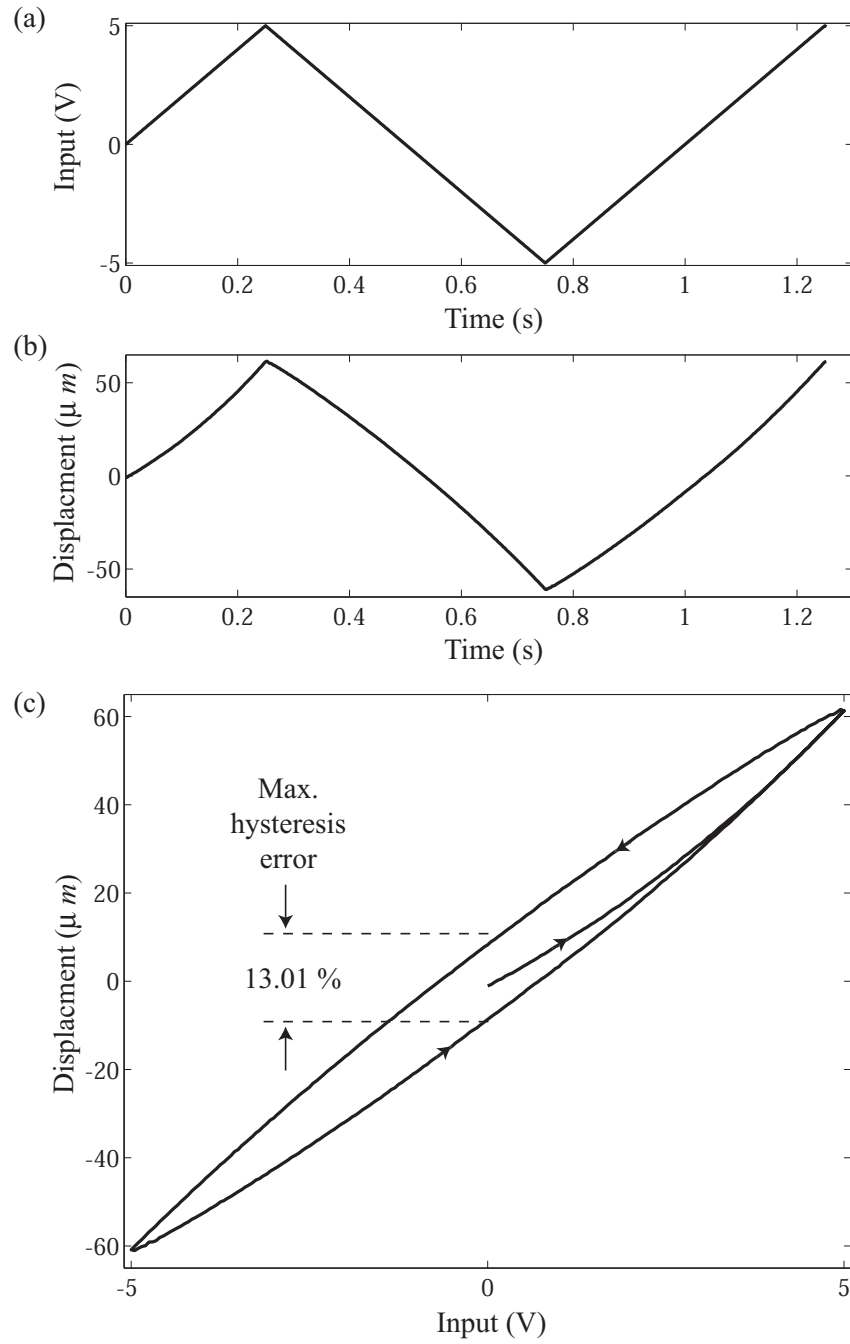
Figure 6.3: Hysteresis effect in y-axis. (a) Input versus time; (b) displacement along y-axis versus time; (c) hysteresis curve where arrows indicate ascending and descending paths.

where the sets $\mathbf{P}_+(t)$ and $\mathbf{P}_-(t)$ (defined in Eqs. (4.6) and (4.7)) represent the regions of the Preisach plane where relays have switched to the $+1$ and -1 states, respectively. Now suppose for example that $\mathbf{P}$ was discretized as shown in Fig. 6.4(a), where the α and β axes have been partitioned into four equal intervals (*i.e.*, $n = 4$). The centers of each square and triangle are labeled numerically as shown, and they are referred to as *nodes*. In this example, we have 10 nodes. Also, we note that such a coarse mesh serves to illustrate the approach and finer meshes can be used to give more accurate results. With such a discretized Preisach plane, we observe, based on the work of Banks *et al.*[182], that the output Eq. (6.1) can be approximated by

$$v(t) \approx \sum_{i=1}^{N} \mathcal{R}^* \mu_r A_r, \tag{6.2}$$

where A_i represents the area associated with the ith node, μ_i is the average value of the weighting surface over area A_i and $\mathcal{R}^*$ takes on value $+1$ or -1 depending on the state of the node, or relay at the node. In our example, $N = 10$ (see Fig. 6.4(a)). Let w denote the width of each square and triangle and let the coordinate of the ith node be (β_i, α_i) and for our example, $i = 1, 2, \cdots, N = 10$. Now consider the following algorithm for switching the relays between the $+1$ and -1 states:

Minus-to-Plus Rule $(-1 \rightarrow +1)$: For a monotonically increasing input, the ith node switches from -1 to $+1$ if $\alpha_i \leq u(t)$ and if the distance from $u(t)$ to the α_i is less than $w/2$, *i.e.*, $|u(t) - \alpha_i| < w/2$.

Plus-to-Minus Rule $(+1 \rightarrow -1)$: For a monotonically decreasing input, the ith node switches from $+1$ to -1 if the distance between $u(t)$ to β_i is less than $w/2$, *i.e.*, $\beta_i - u(t) \leq w/2$. An example `MATLAB` code that implements this algorithm in documented in Appendix E.

Suppose at time t_0, an input was applied in such a way that all the relays in the $\mathbf{P}$ were switched to the -1 state, *i.e.*, negative saturation state. Next, assume the input $u(t)$ from time t_0 increases monotonically from the negative saturation point to the maximum input value at $\bar{u}$, through a series of steps. At time t_0, taking into account the switching rules
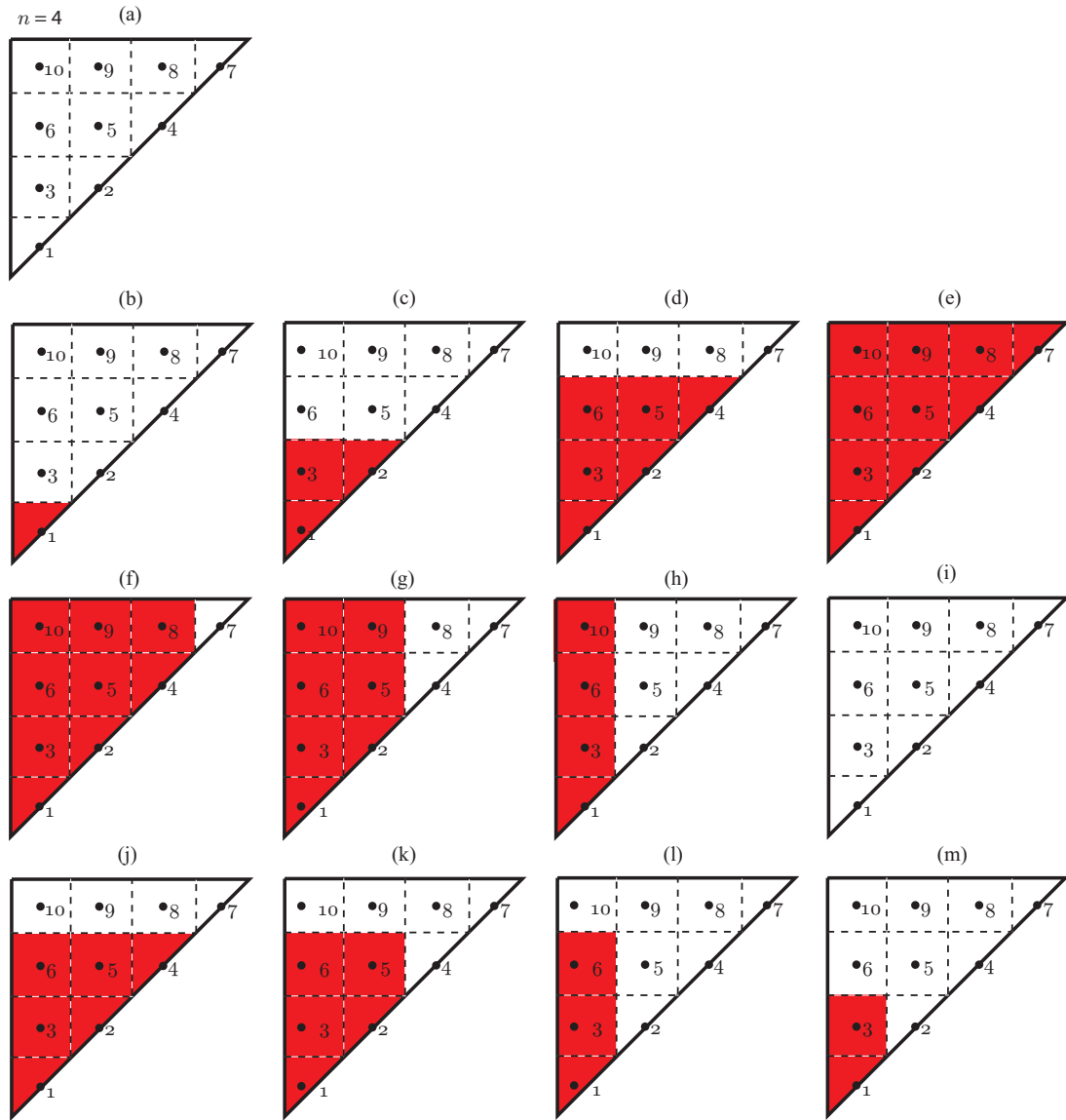
Figure 6.4: Behavior of discretized Preisach plane with input variation.

defined above, we find that for our example, node 1 switches to the $+1$ while all the relays associated with the remaining 9 nodes are at the -1 state, for example see Fig. 6.4(b), where the solid triangle indicates that the node is in the $+1$ state. Using the approximation Eq. (6.2), we can write:

$$
\begin{aligned}
v(t_0) &\approx \sum_{r=i}^{10} \mathcal{R}^* \mu_i A_i, \\
&\approx \mu_1 A_1 - \mu_2 A_2 - \mu_3 A_3 - \cdots - \mu_{10} A_{10},
\end{aligned}
\tag{6.3}
$$

where $\mathcal{R}_1^* = +1$ and $\mathcal{R}_j^* = -1$ for $j = 2, 3, \cdots, 10$. Now suppose at the next time instant $t_1 > t_0$, the input increases monotonically switching nodes 1, 2 and 3 to $+1$ state (see Fig. 6.4(c)). Then we can write the following approximation for the output:

$$
v(t_1) \approx \mu_1 A_1 + \mu_2 A_2 + \mu_3 A_3 - \mu_4 A_4 \cdots - \mu_{10} A_{10}.
\tag{6.4}
$$

Proceeding two more times until the input reaches the (maximum) value $\bar{u}$ (see Figs. 6.4(d) and (e)), we find the following expressions for the output:

$$
v(t_2) \approx \mu_1 A_1 + \cdots + \mu_6 A_6 - \mu_7 A_7 - \cdots - \mu_{10} A_{10},
\tag{6.5}
$$

$$
v(t_3) \approx \mu_1 A_1 + \mu_2 A_2 + \cdots + \mu_{10} A_{10}.
\tag{6.6}
$$

After the input peaks at $\bar{u}$, we decrease the input monotonically and consider again the switching algorithm, then we obtain the following approximations for the outputs (see Figs. 6.4(f) - (i)):

$$
v(t_4) \approx \mu_1 A_1 + \cdots + \mu_6 A_6 - \mu_7 A_7 + \mu_8 A_8 + \cdots + \mu_{10} A_{10},
\tag{6.7}
$$

$$
\begin{aligned}
v(t_5) \approx\ & \mu_1 A_1 + \mu_2 A_2 + \mu_3 A_3 - \mu_4 A_4 + \mu_5 A_5 + \mu_6 A_6 \\
& - \mu_7 A_7 + \mu_8 A_8 + \mu_9 A_9 + \mu_{10} A_{10},
\end{aligned}
\tag{6.8}
$$

$$
\begin{aligned}
v(t_6) \approx\ & \mu_1 A_1 - \mu_2 A_2 + \mu_3 A_3 - \mu_4 A_4 - \mu_5 A_5 + \mu_6 A_6 \\
& - \mu_7 A_7 - \mu_8 A_8 - \mu_9 A_9 + \mu_{10} A_{10}.
\end{aligned}
\tag{6.9}
$$

After this first cycle, the state of the relays are reset to the negative saturation state and then the input is applied once again to switch the relays as indicated in Figs. 6.4(j)-(m),

which give us the following set of equations:

$$v(t_7) \approx \mu_1 A_1 + \mu_2 A_2 + \mu_3 A_3 - \mu_4 A_4 + \mu_5 A_5 + \mu_6 A_6$$
$$-\mu_7 A_7 - \mu_8 A_8 - \mu_9 A_9 - \mu_{10} A_{10}, \tag{6.10}$$

$$v(t_8) \approx \mu_1 A_1 - \mu_2 A_2 + \mu_3 A_3 - \mu_4 A_4 - \mu_5 A_5 + \mu_6 A_6$$
$$-\mu_7 A_7 - \mu_8 A_8 - \mu_9 A_9 - \mu_{10} A_{10}, \tag{6.11}$$

$$v(t_9) \approx \mu_1 A_1 - \mu_2 A_2 - \mu_3 A_3 - \mu_4 A_4 - \mu_5 A_5 - \mu_6 A_6$$
$$-\mu_7 A_7 - \mu_8 A_8 - \mu_9 A_9 - \mu_{10} A_{10}. \tag{6.12}$$

Finally, we recognize that Eqs. (6.3)-(6.12) can be written in the following matrix form:

$$
\begin{bmatrix} v(t_0) \\ v(t_1) \\ v(t_2) \\ v(t_3) \\ v(t_4) \\ v(t_5) \\ v(t_6) \\ v(t_7) \\ v(t_8) \\ v(t_9) \end{bmatrix}
\approx
\begin{bmatrix}
1 & -1 & -1 & -1 & -1 & -1 & -1 & -1 & -1 & -1 \\
1 & 1 & 1 & -1 & -1 & -1 & -1 & -1 & -1 & -1 \\
1 & 1 & 1 & 1 & 1 & 1 & -1 & -1 & -1 & -1 \\
1 & 1 & 1 & 1 & 1 & 1 & 1 & 1 & 1 & 1 \\
1 & 1 & 1 & 1 & 1 & 1 & -1 & 1 & 1 & 1 \\
1 & 1 & 1 & -1 & 1 & 1 & -1 & -1 & 1 & 1 \\
1 & -1 & 1 & -1 & -1 & 1 & -1 & -1 & -1 & 1 \\
1 & 1 & 1 & -1 & 1 & 1 & -1 & -1 & -1 & -1 \\
1 & -1 & 1 & -1 & -1 & 1 & -1 & -1 & -1 & -1 \\
1 & -1 & 1 & -1 & -1 & -1 & -1 & -1 & -1 & -1
\end{bmatrix}
\begin{bmatrix} \mu_1 A_1 \\ \mu_2 A_2 \\ \mu_3 A_3 \\ \mu_4 A_4 \\ \mu_5 A_5 \\ \mu_6 A_6 \\ \mu_7 A_7 \\ \mu_8 A_8 \\ \mu_9 A_9 \\ \mu_{10} A_{10} \end{bmatrix},
$$
$$\begin{bmatrix} v \end{bmatrix} \approx \begin{bmatrix} \phi \end{bmatrix} \begin{bmatrix} \mu A \end{bmatrix}. \tag{6.13}$$

In Eq. (6.13), the vector $[v]$ is the measured output sampled at appropriate time instances, and the matrix $[\phi]$ consists of either $+1$'s or -1's. If a finer mesh is desired, then following the above example, an appropriate input profile can be generated such that the matrix $[\phi]$ is full rank. It is easy to see that the vector $[\mu A]$ can be solved numerically using the least-square method to find the approximate Preisach weighting function μ. For a review of other techniques to solve for the unknown parameters $[\mu A]$ in Eq. (6.13), see references [125, 183].

6.2.2   Creep Compensation

In practice, an input profile similar to the type used to obtain FOD curves discussed in Appendix C can be used generate the output vector $[v]$ and the matrix $[\phi]$ in Eq. (6.13). This is the approach taken to find the weighting function μ. However, before obtaining output data to find an approximation of the weighting function using the above approach, both the effects of creep and vibration were isolated from the hysteresis behavior. Otherwise, these effects can affect the measure output data, leading to an inaccurate model of the hysteresis behavior. (A more detailed discussion of creep compensation is discussed in Appendix C.) To avoid the effect of induced structural vibrations, the frequency of the control input was kept small, *i.e.*, the scanning frequency for all experiments were less than or equal to 1 Hz, which is significantly smaller than the dominating resonant peak of the piezo positioner at 445 Hz and 454 Hz for the x- and y-axis, respectively. Because of creep, the measured output after each input cycle slowly drifts over a period of 50 seconds as shown in Figs. 6.5(a) and (c).

The time-dependent drift in the measured displacement versus time curves no longer satisfies the rate-independent assumption of the Preisach hysteresis model [143], *i.e.*, when the input returns to the *negative saturation* point ($u = \underline{u}$) after each cycle, the Preisach model assumes the output returns to the same value, but as experiments indicate Figs. 6.5(a) and (c), the output slowly drifts.

Creep was taken into account by modeling the behavior and using the model to find an input to minimize the effect. Creep in the x- and y-axis of the piezo positioner was characterized by a second-order model consisting of series connection of dampers (c_i) and springs (k_i) [184]:

$$\frac{x(s)}{u(s)} = \frac{1}{k_0} + \sum_{i=1}^{n} \frac{1}{sc_i + k_i},$$

(6.14)

where $x(s)$ is the displacement of the piezo positioner (in the Laplace domain) and $u(s)$ is the applied input voltage. In the above equation, k_0 models the elastic behavior at low frequencies and the creep behavior is captured by selecting an appropriate model order (n), *i.e.*, number of damper-spring elements. The parameters (k_0, k_i, and c_i) of the model in
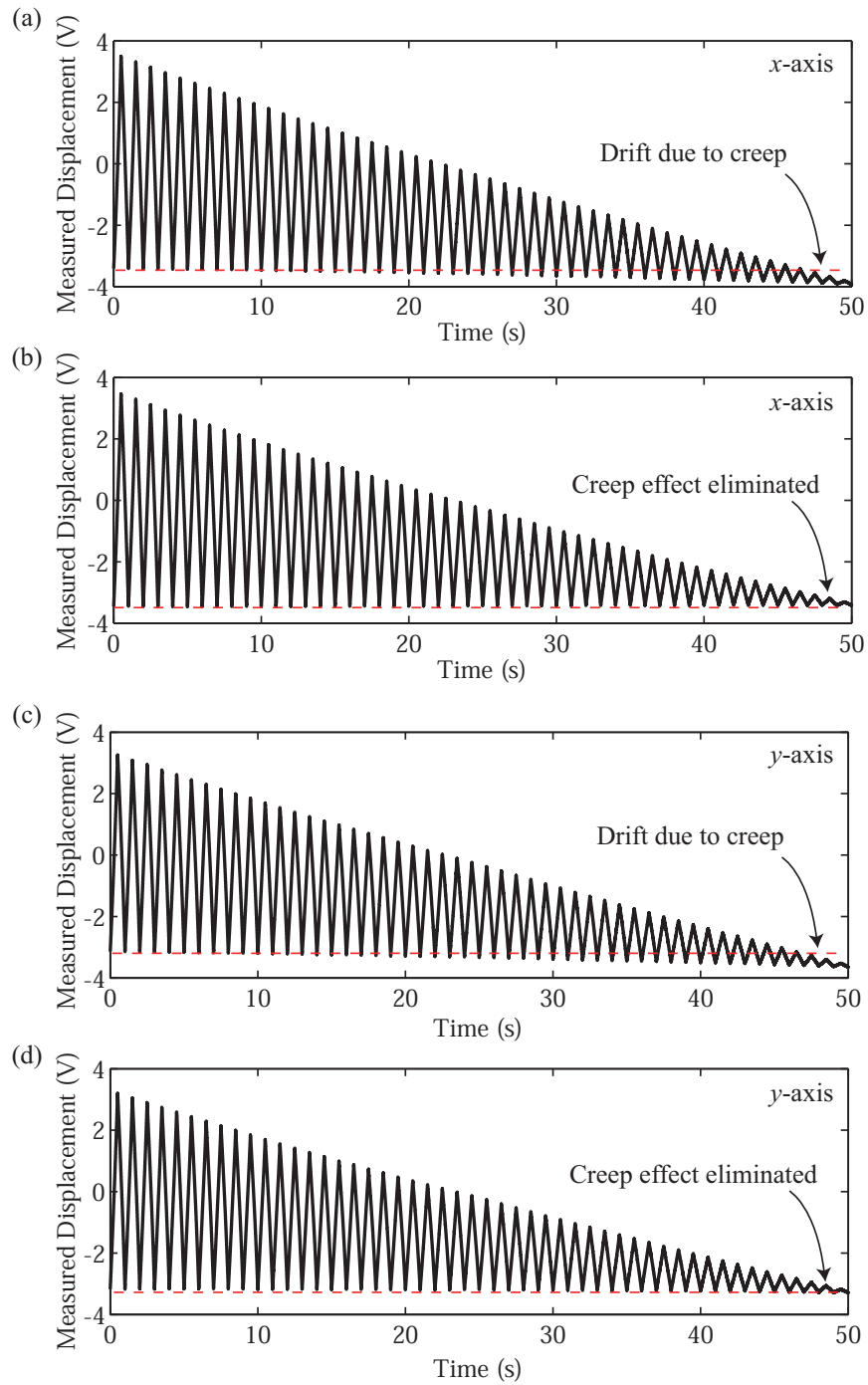
Figure 6.5: Measured output displacement versus time: (a) and (b) uncompensated and creep compensated results in x-axis; (c) and (d) uncompensated and creep compensated results in y-axis.

Eq. (6.14) were determined by curve fitting the step response of the piezo positioner [185]. For a detailed discussion of this approach, see Appendix C. The creep models for the x- and y-axis are (units V/V):

$$G_{c,x}(s) \triangleq \frac{x(s)}{u(s)} = \frac{0.4376s^2 + 9.898s + 7.494}{s^2 + 20.85s + 14.65}, \qquad (6.15)$$

$$G_{c,y}(s) \triangleq \frac{y(s)}{u(s)} = \frac{0.5428s^2 + 11.67s + 15.77}{s^2 + 20.7s + 26.09}, \qquad (6.16)$$

Figure 6.6 shows a comparison of the measured step response with creep and the linear models for both the x and y-axis. The second order model provides a good fit of the creep behavior.

Using the inversion-based approach [2] and the creep models, the resulting compensated output versus time responses are displayed in Figs. 6.5(b) and (d). The results show that creep is eliminated when compared to the uncompensated cases: Figs. 6.5(a) and (c).

(a) x-axis

(b) x-axis
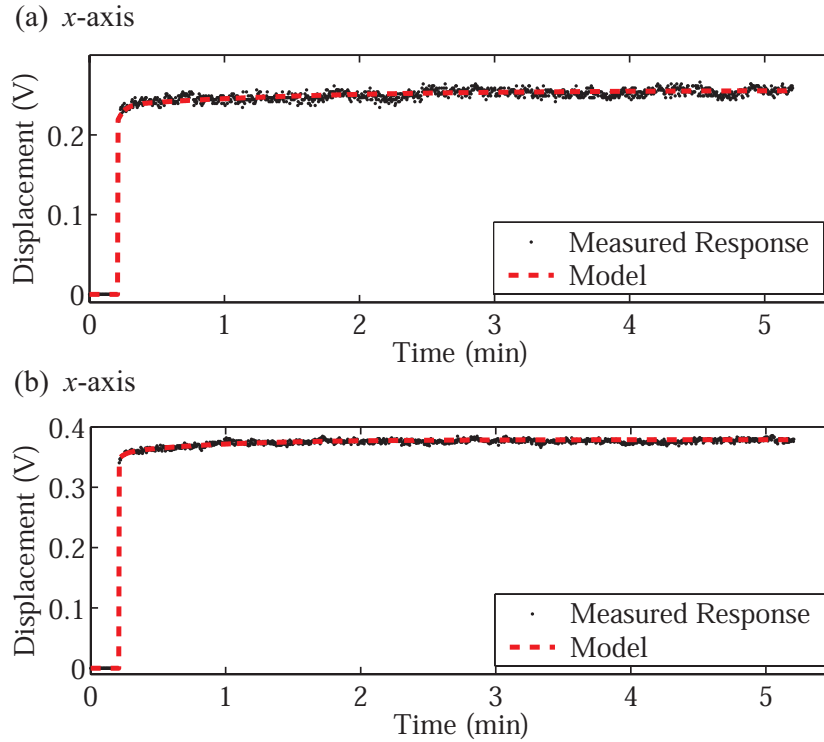
Figure 6.6: Creep models

6.2.3 Model Validation

Using the creep compensation technique and the resulting input-output data shown in Figs. 6.5(b) and (d), models of the Preisach weighting surface for in the x- and y-axis were found (see example `MATLAB` code in Appendix E). Initially, a relatively coarse mesh was used to test the algorithm. The mesh contained 26×26 nodes and the result for the x-axis hysteresis model is shown in Fig. 6.7(a). In Fig. 6.7(a), it appears that the effect of the μ weighting was concentrated along the diagonal line $\alpha = \beta$. At first, it was unclear whether the sharp ridge of the μ surface was caused by artifacts associated with noise in the measured output data. To validate the model, the following approximation was considered to test the result of the least-squares algorithm.

Based on the least-squares solution, we assumed that the Preisach weighting surface was heavily concentrated along the diagonal line $\alpha = \beta$ and the concentration spanned over the distance d as shown in Fig. 6.7(b). Therefore, the values of μ in the shaded region was assumed to be significantly larger than the values of the μ surface over the remaining portion of the Preisach plane. Then, the objective was to generate two major hysteresis loops by sweeping the entire Preisach plane **P**, one ascending branch and one descending branch, and then using the resulting branches to find an approximation of the μ surface and compare it to the least-squares result. If the result of this approximated model agreed with the least-squares result, then the least-squares results were accurate.

The approximated model based on the assumption of the behavior of μ as illustrated in Fig. 6.7(b) is presented as follows. First, the Preisach plane was put in a state of negative saturation, *i.e.*, all the relays were switched to the -1 state. Then, a monotonic input u was applied until it reached the maximum input value $\bar{u}$. During the application of this input, we measured the output change. Plotting the measure output versus input, we obtained an ascending major hysteresis loop as illustrated in Fig. 6.8. Afterwards, we applied a monotonically decreasing input until it reached the value $\underline{u}$, and again measured the output and the resulting descending major hysteresis loop is also shown in Fig. 6.8.

By assuming the Preisach weighting function is mostly concentrated along the diagonal with width d as shown in Fig. 6.7(b), we can approximate μ by curve fitting the ascending
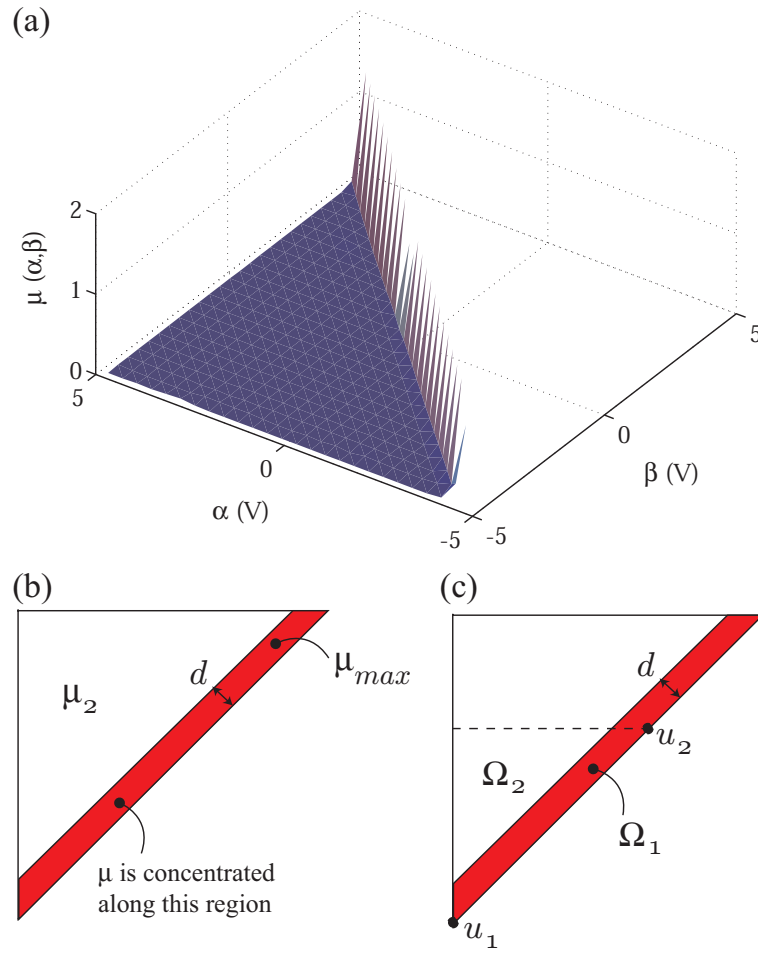
Figure 6.7: (a) Preliminary Preisach weighting surface μ in the x-axis. (b) Approximated Preisach weighting surface over the Presiach plane $\mathbf{P}$.
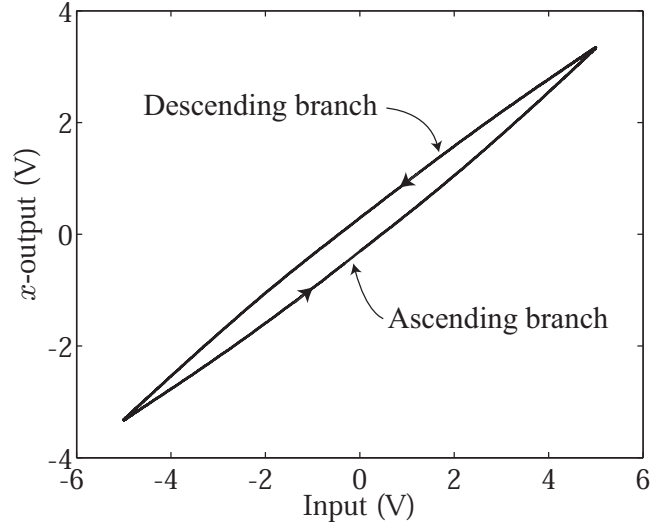
Figure 6.8: Measured major hysteresis loop for the x-axis for finding approximate hysteresis model to compare with least-squares approach.

and descending major hysteresis loops. In this case, we assume that over the region Ω_1, $\mu(\alpha, \beta) = \mu_{max} < \infty$ for all $(\alpha, \beta) \in \Omega_1$ (see Fig. 6.7(c)). Additionally, we assume that over the region Ω_2, $\mu(\alpha, \beta) = \mu_2 << \mu_{max}$ for all $(\alpha, \beta) \in \Omega_2$. This assumption is based on the result of the preliminary least-squares solution shown in Fig. 6.7(a). Then, we note that from Proposition 1, the change in output along the major hysteresis loop as the input sweeps the entire Preisach plane $\mathbf{P}$ is given by

$$\Delta v = 2 \iint_{\mathbf{P}} \mu(\alpha, \beta) d\alpha d\beta. \tag{6.17}$$

From Fig. 6.7(c), the above equation becomes

$$\Delta v = 2 \Big[\iint_{\mathbf{\Omega_1}} \mu(\alpha, \beta) d\alpha d\beta + \iint_{\mathbf{\Omega_2}} \mu(\alpha, \beta) d\alpha d\beta \Big], \tag{6.18}$$

where the regions Ω_1 and Ω_2 are shown in Fig. 6.7(c). Based on our approximation for the

weighting function and some simple geometry, we can write:

$$
\begin{aligned}
\Delta v &= 2\Big[\iint\limits_{\Omega_1} \mu(\alpha,\beta)d\alpha d\beta + \iint\limits_{\Omega_2} \mu(\alpha,\beta)d\alpha d\beta\Big], \\
&\approx 2\mu_2 \iint\limits_{\Omega_1} d\alpha d\beta + 2\mu_{max} \iint\limits_{\Omega_2} d\alpha d\beta, \\
&\approx 2\mu_2 \frac{1}{2}\Delta u^2 + 2\sqrt{2}d\mu_{max}\Delta u, \\
&\approx \mu_2\Delta u^2 + 2\sqrt{2}d\mu_{max}\Delta u,
\end{aligned}
\tag{6.19}
$$

where $d << \Delta u$. The approximation Eq. (6.19) implies that the output is a combination of a quadratic term in Δu and a linear term in Δu. Then, by curve fitting the ascending and descending major hysteresis loops in Fig. 6.8, we can find the values μ_{max}, μ_2 and d.

First, by fitting over the entire range of Δu, we find (averaged between ascending and descending branches)

$$
\Delta v = 0.0122\Delta u^2 + 0.5429\Delta u,
\tag{6.20}
$$

which gives us

$$
\begin{aligned}
\mu_2 &= 0.0122, \\
d &= \frac{0.5429}{2\sqrt{2}\mu_{max}}.
\end{aligned}
$$

Second, to find μ_{max}, we fit the curves over a relatively small range Δu because along the diagonal, μ_{max} has the greatest affect, hence we find

$$
\begin{aligned}
\Delta v &\approx \mu_{max}\Delta u^2 \\
\Delta v &= 2.1508\Delta u^2 + 0.3532\Delta u.
\end{aligned}
\tag{6.21}
$$

which implies that $\mu_{max} = 2.1508$ and $d \approx 90\ mv$. Finally, the approximated values of the μ surface where compared with the least-squares results and they were found to be in close agreement; therefore, the least-squares approach accurately models the hysteresis behavior and the approach was used to determine the Preisach weighting surface μ.

After the least-squares model was check with the approximate model and determined to yield an accurate weighting surface μ, the least-squares approach was applied to identify

the hysteresis model for the x- and y-axis. The mesh was chosen as 51×51 and the results for the weighting surfaces are shown in Figs. 6.9(a) and (b). The 51×51 model was further discretized and the measured output was compared with the model output. It was found that a mesh of 300×300 was sufficient to model the hysteresis behavior. Figures 6.9(c), (d) and (e) compares the error in model for the standard least-squares approach, the approximate model approach and a hybrid model where the solutions from the least-squares was integrated with the approximate model, respectively. In the figure, the error levels off after 300×300 nodes. The models with 300×300 mesh grid were used in the experiments and a comparison of the measured output and model output are shown in Fig. 6.10 for the x- and y-axis. The parameters of the Preisach hysteresis models for the x- and y-axis are shown in Table 6.1.
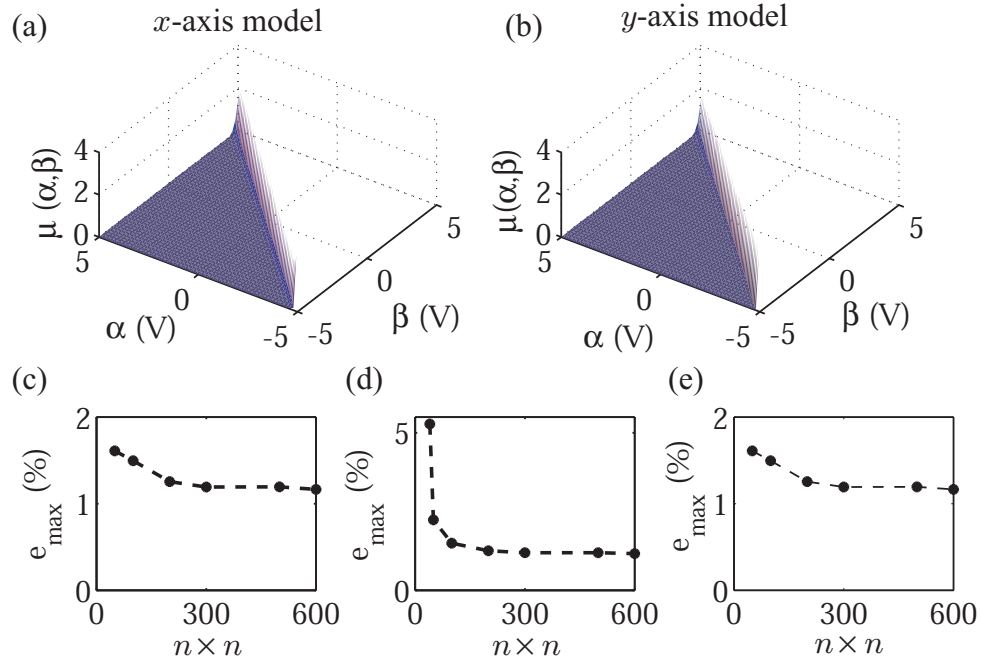
Figure 6.9: (a) x-axis μ surface. (b) y-axis μ surface. (c)-(d) Error in the model versus mesh size. No further improvement in the model is gained for meshes greater than 300×300.
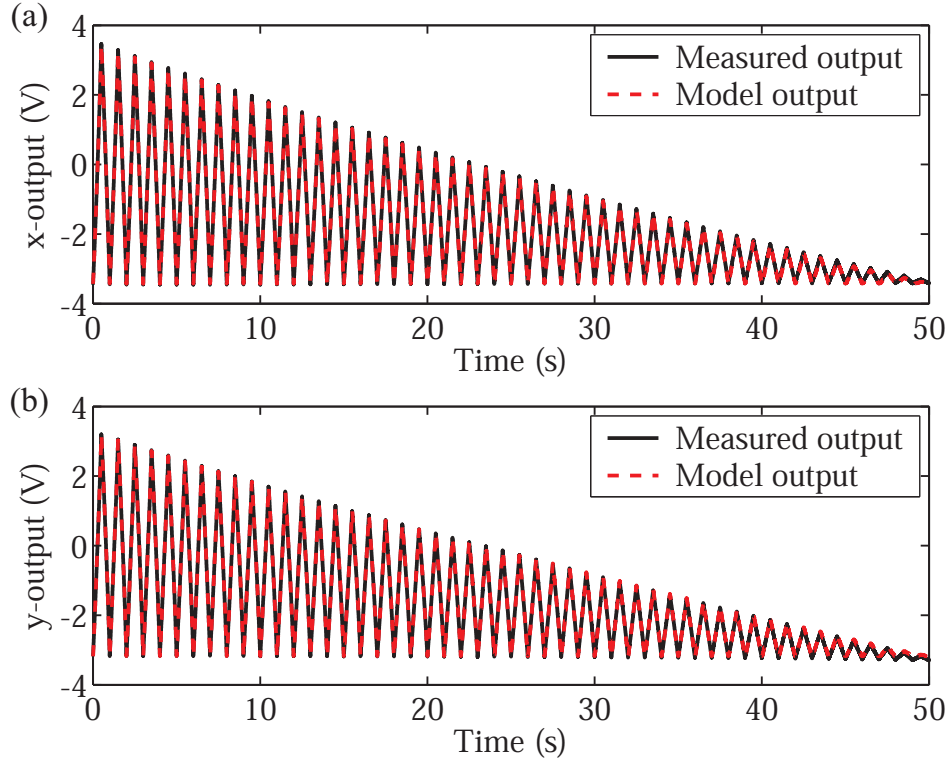
Figure 6.10: Comparing output of model: (a) x-axis; (b) y-axis.

Table 6.1: Preisach model parameters.

	x-**axis**	y-**axis**
μ_{max}	2.63	2.80
μ_{min}	0.01	0.009
$\underline{\mu}$	1.95	1.72
$d\ (mv)$	90	90
$(\bar{u} - \underline{u})\ (V)$	10	10
μ_{max} in Ω_2	0.043	0.059

6.3 Tracking of Monotonic Trajectories

The remaining sections of this chapter discusses the implementation of the ILC approach to compensate for hysteresis in an experimental atomic force microscope system. First, the ILC approach is applied to track a monotonic trajectory (demonstrating Theorem 1). Then, experimental results for an example trajectory with more than one monotonic section is described. The example trajectory is the scanning pattern used for AFM imaging. Afterwards, the ILC method is applied in AFM imaging of a calibration sample. We begin with a discussion of tracking monotonic trajectories and the steps, which follows the flow chart in Fig. 5.11, are as follows:

Step 1: Determine the Constant ρ   The ILCA (see the block diagram in Fig. 5.3) to compensate for hysteresis takes the form given by Eq. (5.4), where ρ is a constant, and $v_k(t)$ and $u_k(t)$ are the output and input for the kth operating trial, respectively. In Chapter 5 it was shown that ILCA Eq. (5.4) converges if the desired trajectory v_d is continuous and monotonic over the finite time interval $I = [t_0, T]$. Convergence of ILCA Eq. (5.4) requires a monotonic desired trajectory to overcome the difficulties associated with *multivalued* or *branching* behaviors typical of hysteresis [18]. Therefore, for a given monotonic desired trajectory $v_d(t)$ defined on I, there exists a constant ρ such that ILCA Eq. (5.4) converges; the value of ρ is chosen as

$$0 < \rho \leq \frac{1}{2\mu_{max}(\bar{u} - \underline{u})}, \tag{6.22}$$

where μ_{max} is the maximum value of the Preisach weighting surface over $\mathbf{P}$ and $(\bar{u} - \underline{u})$ is the range of the applied input voltage. Based on the parameters of the Preisach model presented in Table 6.1, we find that for the x- and y-axis:

$$\rho_x \quad \leq \quad \frac{1}{2\mu_{x,max}(\bar{u} - \underline{u})} \quad = \quad 0.019, \tag{6.23}$$

$$\rho_y \quad \leq \quad \frac{1}{2\mu_{y,max}(\bar{u} - \underline{u})} \quad = \quad 0.018. \tag{6.24}$$

Therefore, by picking the constant ρ based on the constraints given by Eqs. (6.23) and (6.24), ILCA Eq. (5.4) is guaranteed to converge. Furthermore, suppose that a tracking

precision of $\varepsilon = 15\ mv$ is required ($210\ nm$ in the x-axis and $283\ nm$ in the y-axis). Using the results of Chapter 5 (Eq. (5.66)) and the parameters of the Preisach model from Table 6.1, the total number of iterations required for x- and y-axis are:

$$\mathcal{K}_x \quad > \quad \frac{\ln(K_1\varepsilon)}{\ln(1 - K_2\varepsilon)} \quad = \quad 1.63 \times 10^5, \tag{6.25}$$

$$\mathcal{K}_y \quad > \quad \frac{\ln(K_1\varepsilon)}{\ln(1 - K_2\varepsilon)} \quad = \quad 1.79 \times 10^5, \tag{6.26}$$

where $\|x_d(\cdot) - x_0(\cdot)\|_\infty = 6.80\ V$ ($90\ \mu m$), $\|y_d(\cdot) - y_0(\cdot)\|_\infty = 6.36\ V$ ($120\ \mu m$) and $\underline{\mu}$ is replaced with μ_{min} since it is nonzero over $\mathbf{P}$. We note, however, that the required number of iterations in Eqs. (6.25) and (6.26) and the maximum allowable constant ρ determined above are extremely conservative, as with any theoretical work. Thus, the values given by Eqs. (6.25) and (6.26) serve as a guideline in design and the actual rate of convergence may be much faster than the theoretical estimates provided above.

In practice, if *a priori* knowledge about the Preisach weighting function is known, for example the shape of the weighting surface, then a *tighter* bound on the constant ρ and the number of iterations required to achieve a prescribed tracking precision can be computed. For example, based on the nature of the Preisach weighting surfaces shown in Figs. 6.9(a) and (b), by geometry (see Fig. 6.7(c)), the upper bound in Lemma 1 can be rewritten as follows:

$$
\begin{aligned}
\mathcal{H}[u_2] - \mathcal{H}[u_1] \quad &\leq \quad 2 \iint_{\Omega_1} \mu(\alpha, \beta)d\alpha d\beta + 2 \iint_{\Omega_2} \mu(\alpha, \beta)d\alpha d\beta, \\
&\leq \quad 2\sqrt{2}d\mu_{max}(\bar{u} - \underline{u}) + 2\mu_{max,2}(\bar{u} - \underline{u})^2, \\
&\leq \quad \left[2\sqrt{2}d\mu_{max} + 2\mu_{max,2}(\bar{u} - \underline{u})\right](\bar{u} - \underline{u}), \tag{6.27}
\end{aligned}
$$

where $\mu_{max,2}$ is the maximum value of μ in the region Ω_2 (see Fig. 6.7(b)). Equation 6.27 implies that the constant ρ is limited by

$$\rho \leq \frac{1}{2\mu_{max,2}(\bar{u} - \underline{u}) + 2\sqrt{2}d\mu_{max}}. \tag{6.28}$$

Substituting in the model parameters from Table 6.1 into Eq. (6.28), we find that

$$\rho_x \quad \leq \quad 0.65, \tag{6.29}$$

$$\rho_y \quad \leq \quad 0.53. \tag{6.30}$$

For the experiments, we picked $\rho_x = 0.25$ and $\rho_y = 0.25$, which satisfy the constraints given above. Furthermore, a tighter bound on the number of iterations required to achieve a tracking precision of 15 mv (case 1: when $\delta u_k \leq 255\ mv$) is given by:

$$\mathcal{K}_x = \frac{\ln(K_1\varepsilon)}{\ln(1 - K_2\varepsilon)} = 819 \tag{6.31}$$

$$\mathcal{K}_y = \frac{\ln(K_1\varepsilon)}{\ln(1 - K_2\varepsilon)} = 942 \tag{6.32}$$

where $\|x_d(\cdot) - x_0(\cdot)\|_\infty = 6.13\ V$, $\|y_d(\cdot) - y_0(\cdot)\|_\infty = 6.68\ V$. As we will see, the new estimates given by Eqs. (6.31) and (6.32) provide a more reasonable estimate, but they are also still conservative.

Step 2: Select Desired Trajectory The desired trajectory of interest was derived from an AFM imaging task. In AFM imaging, the scan trajectories for the x and y-axis are shown in Fig. 6.11. To demonstrate tracking of a monotonic trajectory, we pick the ascending path of the triangle wave, which is half of one period of the scan path shown Fig. 6.11. The scanning frequency in the x-axis is 1 Hz. We demonstrate ILC tracking in the x-axis and y-axis, where the desired trajectory in the y-axis is shown in Fig. 6.11. The range of the desired trajectories are $\pm 45\ \mu m$.

Step 3: Setting Initial Condition Requirement During the iteration process, the system is brought to the same initial starting conditions for each trial k at time t_0, *i.e.*, $L(t_0)$ is the same for all k. This process requires applying an input to put the system in the negative saturation state, followed by applying an input to bring the system to a desired starting condition compatible with the input/output objectives at time t_0, *e.g.*, $x_k(t_0) = x_d(t_0)$ and $u_k(t_0) = u_d(t_0)$ for all k.

Step 4: Apply the ILCA We applied the ILCA Eq. (5.4) with $\rho = 0.25$ to in the x- and y-axis. In the first experiment, the results of iteratively tracking the monotonically increasing trajectory in the x-axis with amplitude $45\mu m$ is presented in Fig. 6.12. Likewise, the results for the y-axis are presented in Fig. 6.13. In both experiments, the initial input $u_0(t)$ for $t \in [0.3, 0.8]\ s$ was chosen as a constant value compatible with the initial conditions

][h!]
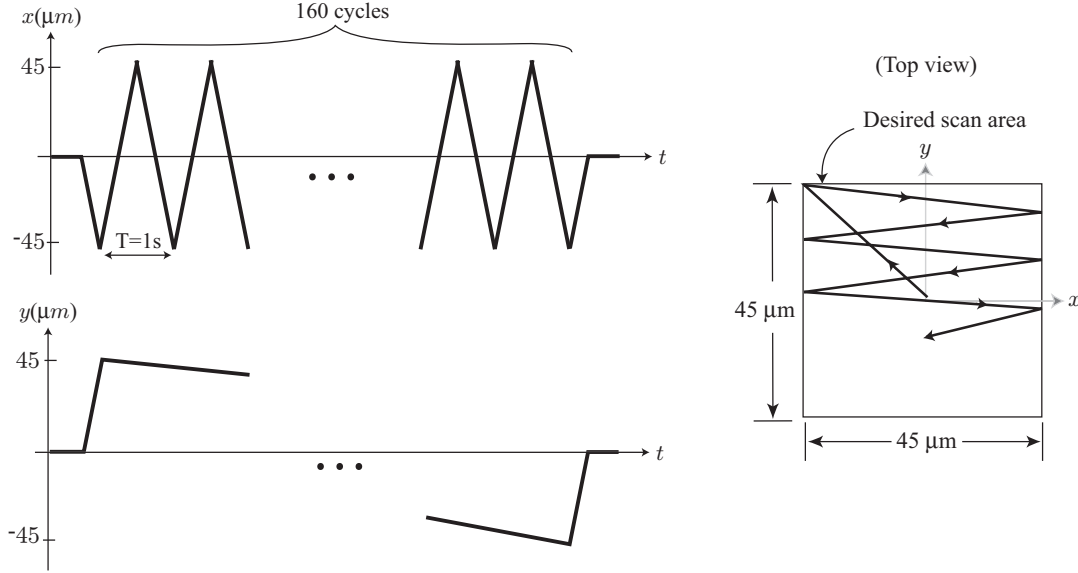
Figure 6.11: The imaging trajectory

at $t_0 = 0.3\ s$. Also, over the time interval $[0, 0.3]s$, the ILC method was not used to the track the trajectory. The input for this section was taken as the quarter of a triangle wave and the resulting output was taken as is, without applying the ILC method. Typically, over the time interval $[0, 0.3]\ s$, the AFM probe tip is moved into the starting position for imaging (at the upper left-hand corner of the imaging area, see Fig. 2.6) and there is no need to accurately track the initialization since no data is collected from the cantilever during this process.

In Figs. 6.12(c) and (d), after 50 iterations, the maximum error e_{max} and the root-mean-square error e_{rms} as a percentage of the total displacement range (90 μm), defined as,

$$e_{max} = \frac{\max |e_k(\cdot)|}{90\ \mu m} \times 100\%, \quad e_{rms} = \frac{\sqrt{\frac{1}{T} \int_{t_0}^{T} |e_k(t)|^2 dt}}{90\ \mu m} \times 100\%,$$

reduces to 0.25% and 0.11%, respectively. Also, Fig. 6.12(c) illustrates that e_{max} decays rapidly as the iteration number k increases. In terms of precision, $e_{max} = 0.25\%$ corresponds

to $\pm 14.6\ mv$ sensor output or $\pm 204\ nm$. In comparison, the amplitude of the measured sensor noise is $\pm 10\ mV$; therefore, the iterative approach achieves approximately the precision of the sensor noise level. These results suggest that high-precision positioning can be achieved using the proposed ILC approach. Additionally, we note that with higher resolution sensors, higher precision can be achieved. The results of this experiment illustrate that the ILC approach reduces the tracking error beyond existing feedback and model-based feedforward techniques, *e.g.*, the results shown in Chapter 3.

Likewise, the results of the ILC method applied to the y-axis are shown in Fig. 6.13. The desired trajectory is a ramp signal that sweeps from $+45\ \mu m$ to $-45\ \mu m$ over a period of $220\ s$. Like the results in the x-axis, the tracking error decays rapidly with the iteration number and after 50 iterations, the maximum error as a percentage of the total displacement range is 0.82%, *e.g.*, see Fig. 6.13(c).

6.4 Tracking of General Trajectories

In this experiment, we demonstrate precision tracking of a $1\ Hz$ triangle wave with a $45\ \mu m$ amplitude. The trajectory is one cycle of the x-axis AFM scanning trajectory shown in Fig. 6.11, which contains two monotonic partitions. Since the scanning process repeats, finding the input to track only one period of the entire trajectory is sufficient for the imaging process. After the input in the x-axis is found using the ILC approach, the input was then applied repetitively during the scanning process in the x-axis. The input for the y-axis movement was described in the previous section and it was used in conjunction with the x-axis input during AFM imaging. The imaging results are presented in the next section. We note that the following steps are in condensed form relative to the flow chart in Fig. 5.11 and the discussion at the end of Chapter 5.

The algorithm for applying the ILC method to a trajectory with more than one monotonic section was presented in Chapter 5, Section 5.3.5. We will follow the algorithm to demonstrate the ILC approach for tracking one period of the x-axis scan path shown in Fig. 6.11.

Step 1: Partition the desired trajectory into monotonic sections The ILC process is executed by partitioning the desired trajectory into two monotonic sections over the time intervals $T_1 = [0.3, 0.8]$ s and $T_2 = [0.8, 1.3]$ s, as shown in Fig. 6.14(a). For each section, ILCA Eq. (5.4), with $\rho = 0.25$, was applied until convergence to a desired precision was achieved.

Step 2: Apply ILC to the first section To illustrate the approach, we picked a tracking precision of ± 15 mv, roughly 1.5-times the ambient noise level. The initial input over the interval $T_1 = [0.3, 0.8]$ s was a ramp input such that the maximum output was 45 μm. Without compensation, the effect of hysteresis causes the output to distort as it reaches the maximum output of 45 μm. Over the interval T_1, 40 iterations brought the piezo response to within the ± 15 mv precision (Figs. 6.15(a) and (b)). We note that for the x-axis, the initial input u_0 was chosen as the desired trajectory scaled by a constant (DC gain) value. The initial output error was 0.46 V (6.43 μm). Recomputing the number of iterations required to achieve the tracking precision of ± 15 mv (± 210 nm), we get

$$\mathcal{K}_x = \frac{\ln(K_1 \varepsilon)}{\ln(1 - K_2 \varepsilon)} = 320 \tag{6.33}$$

where $\|x_d(\cdot) - x_0(\cdot)\|_\infty = 0.46$ V. Compared to the results of Fig. 6.15(a), the estimate is still conservative, but reasonably close to the actual performance of the piezo.

Step 3: Hold the input constant until the next section Then, after time $t \geq 0.8$ s, the input $u_{40}(t = 0.8 \ s)$ was held constant until time t_2 when $x_{40}(t_2) = x_d(t_2)$. This is required to obtain the appropriate initial condition for repeating the ILC process for the second monotonic section, defined over $[t_2, 1.3] \subset T_2$. Since the tracking error was within the noise level, the time t_2 was simply chosen as $t_2 = 0.8$ s (see Fig. 6.16).

Step 4: Apply ILC to second section and repeat if necessary Finally, the ILCA was applied to the second monotonic section defined over $[0.8, 1.3]$ s and the iteration ran for 40 trials (Figs. 6.16(a)-(c)). The tracking error as a function of the iteration number is shown in Fig. 6.17. Afterwards, the process can be repeated for additional monotonic sections, but since our example consists of only two sections, we stopped. Summing the

number of iterations for each section, we found the total to be 80 iterations to achieve a tolerance of ± 15 mv. We emphasize that in this experiment, the ± 15 mv precision was chosen as an illustrative example. Higher precision tracking can be achieved by increasing the number of iterations for each monotonic section. Additionally, with better sensors, higher precision can be achieved.

A comparison of the uncompensated response and the ILC response is shown in Fig. 6.18. Without compensation, there is significant tracking error, however, the ILC approach reduces the error down to the noise level of the sensor measurement. Figure 6.18(c) shows the hysteresis curve plotted for the uncompensated case. In the next section, the inputs found using this approach is applied in AFM imaging.

6.5 AFM Imaging Results

Using the inputs found in the previous sections, they were applied to AFM imaging. The objective was to image a calibration sample and to compare the difference between the uncompensated approach and the inputs found using the ILCA Eq. (5.4). A calibration sample consisting of parallel markings with a 16 μm pitch was imaged using the Burleigh AFM system. The input for the uncompensated case was the desired triangular trajectory scaled by a constant such that the maximum output response was 45 μm. The output response for the uncompensated case are shown in Figs. 6.18(a) for the x-axis and in Fig. 6.13(a) for the y-axis. The ILC input is shown in Fig. 6.16(c). In the figure, only one period of the input is shown, however, during imaging, the input was repeated 160-times to cover the desired area of 90 $\mu m \times 90$ μm (see Fig. 6.11).

The imaging results are shown in Fig. 6.19. Figure 6.19(a) is an image without ILC and it shows the effect of hysteresis; the features are significantly distorted due to hysteresis. Because of hysteresis, the parallel features appear curved and of varying widths. By applying the input found using the ILC approach, the distortions can be corrected as shown in Fig. 6.19(b). Reference lines, which are superimposed on the image, show the improvement in precision achieved using ILC. We note that using the ILC approach, the resulting AFM images show the true surface topology, without the distortion due to hysteresis effect.

By demonstrating the effectiveness of ILC for imaging, we emphasize that this approach has potential application in AFM-based nanomanufacturing for creating features without distortion due to hysteresis effect.

6.6 Summary

In summary, this chapter discussed the implementation of the ILC approach, which involves modeling the hysteresis behavior to determine the iteration gain ρ. Based on the experiments, we conclude that the proposed ILC algorithm can achieve high-precision positioning, down to the ambient noise level of the sensor measurement. Additionally, when compared to existing feedback and model-based feedforward approaches, the approach provides further error reduction (*cf.* Chapter 3). We have demonstrated that an ILC approach can be used in AFM-based applications, such as imaging and it also has potential use in the design of SPM-based tools for nanotechnologies.
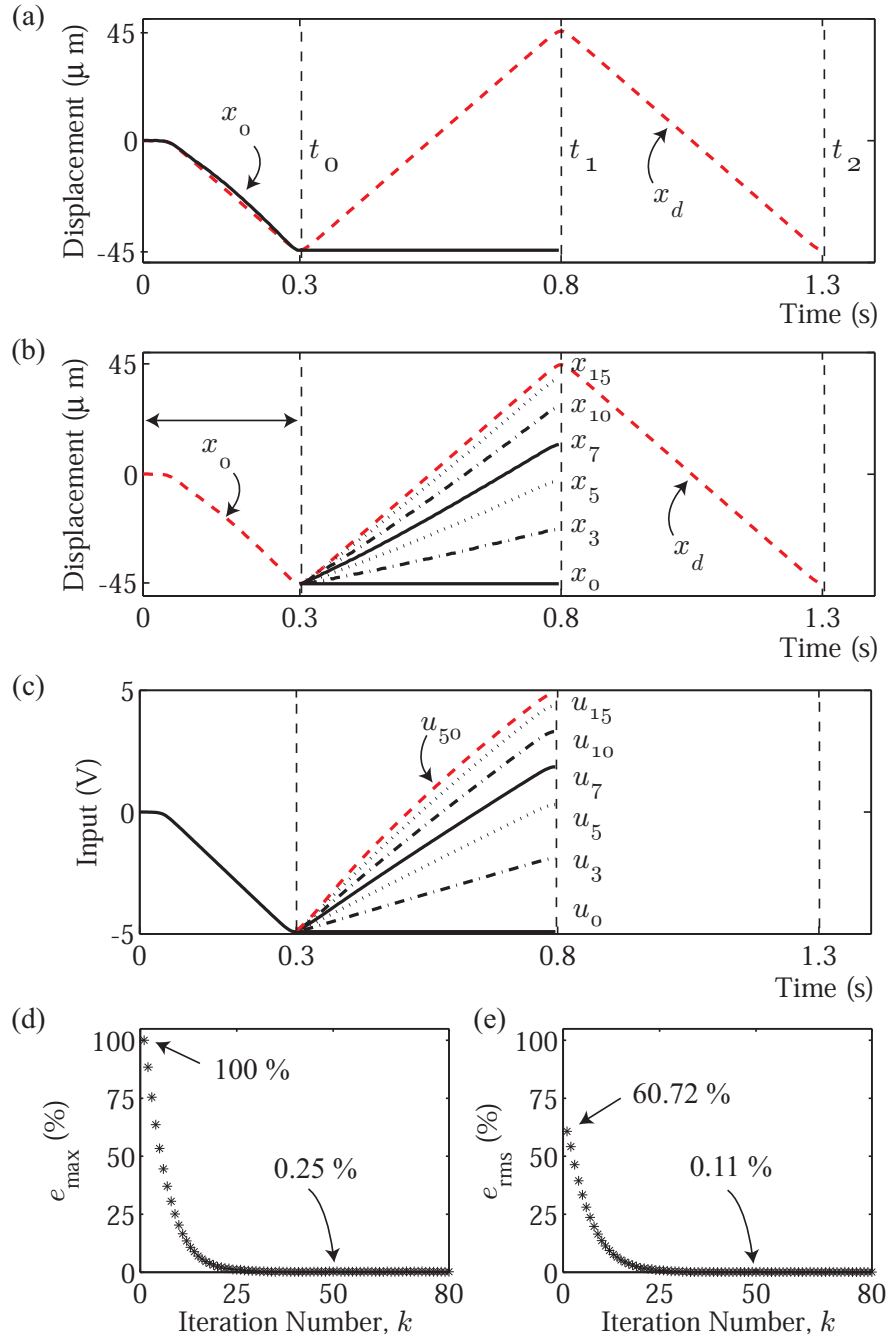
Figure 6.12: x-axis tracking results: ILC tracking of a monotonic trajectory, $\rho = 0.25$.
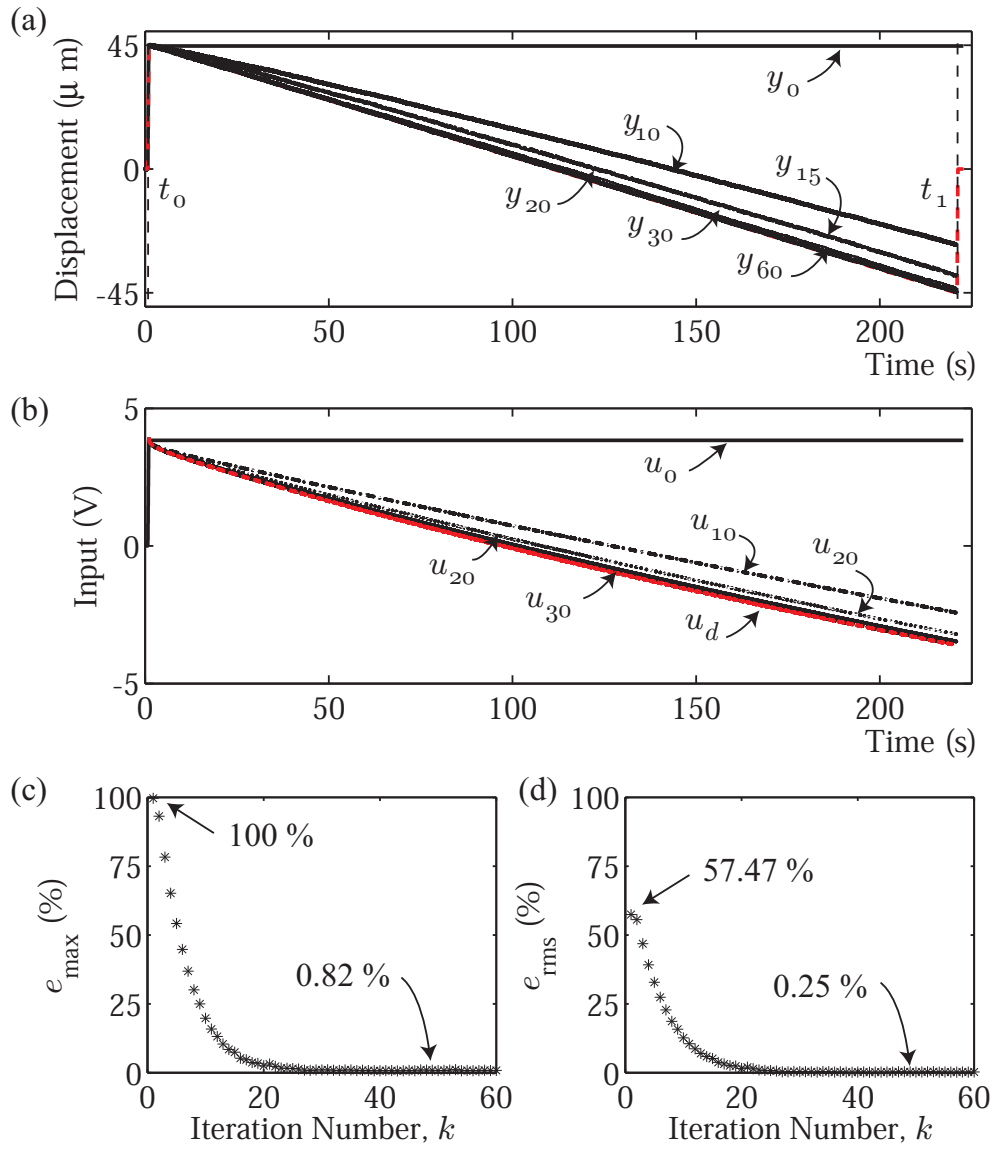
Figure 6.13: y-axis tracking results: one section of a monotonic trajectory, $\rho = 0.25$.

(a)

(b)

(c)

(d)
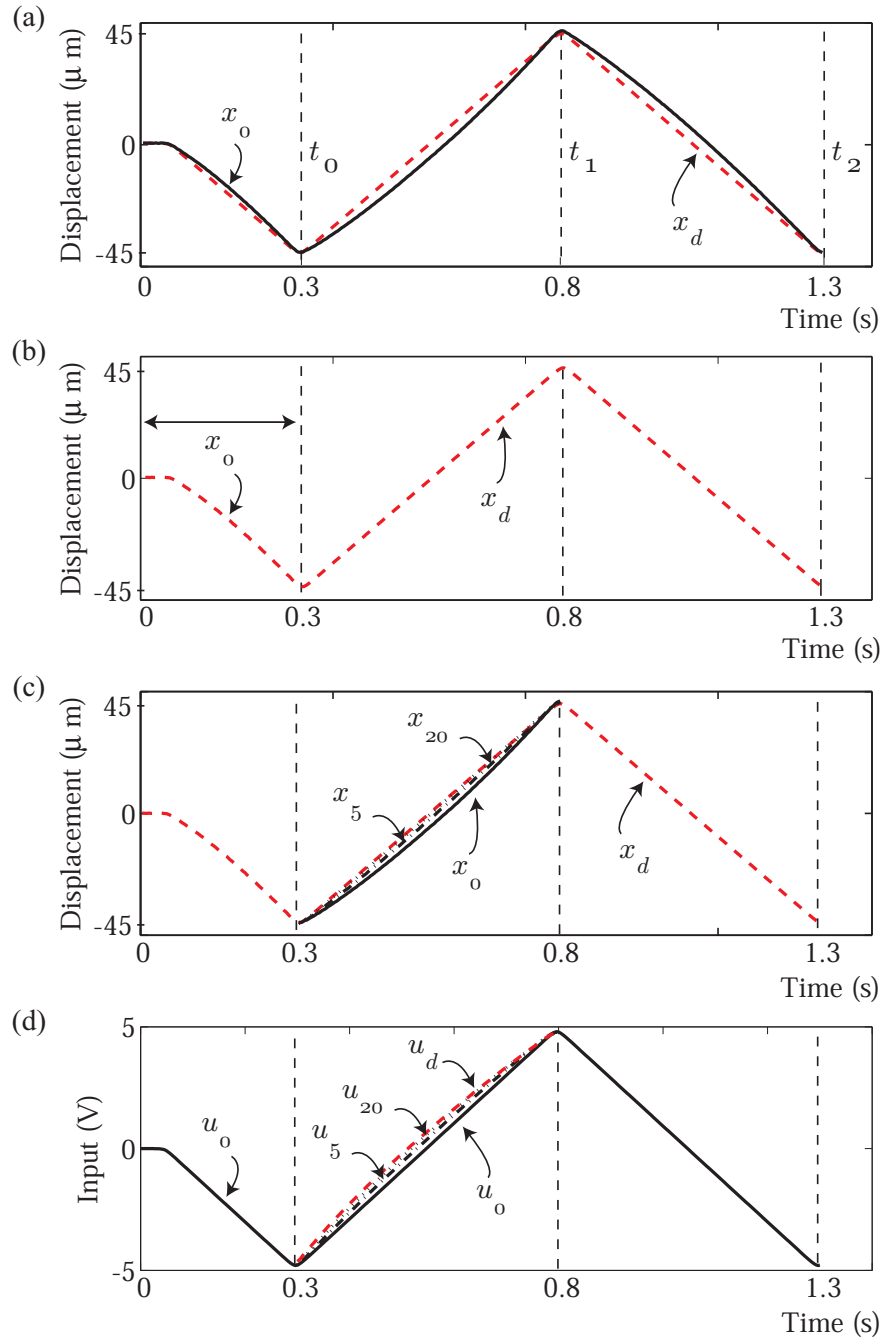
Figure 6.14: ILC tracking for the first section of a triangle trajectory where the initial input was chosen as a scalar times the desired trajectory. The constant $\rho = 0.25$.
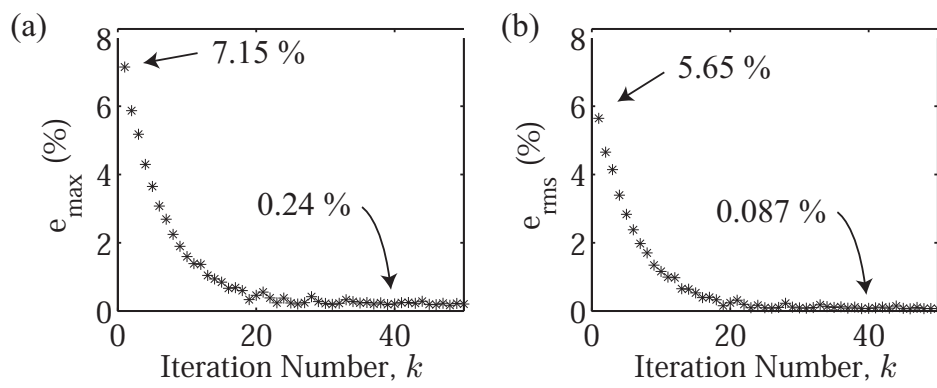
Figure 6.15: Tracking error versus number of iteration for tracking of the first monotonic section.
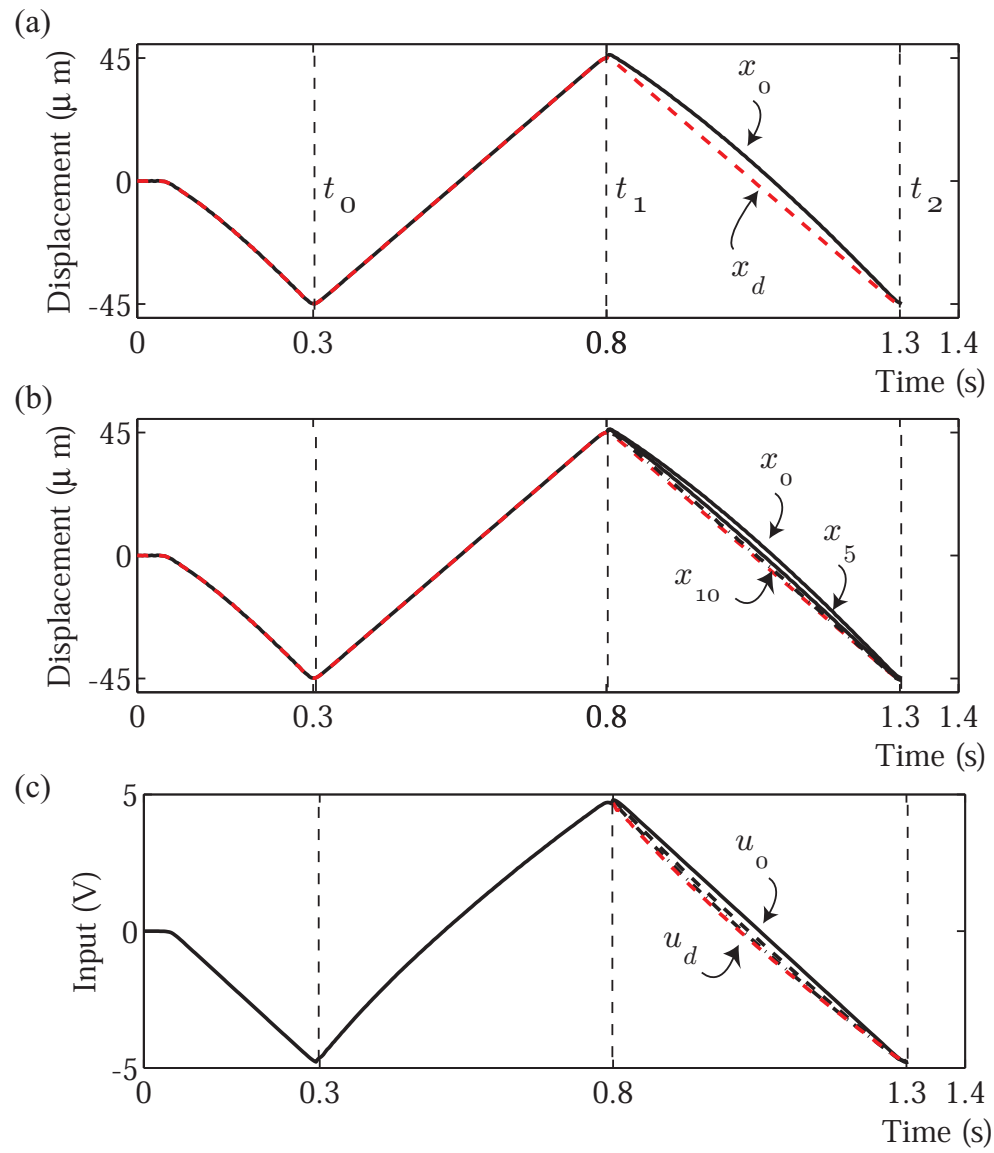
Figure 6.16: ILC results for tracking the second section of a triangle trajectory.

134
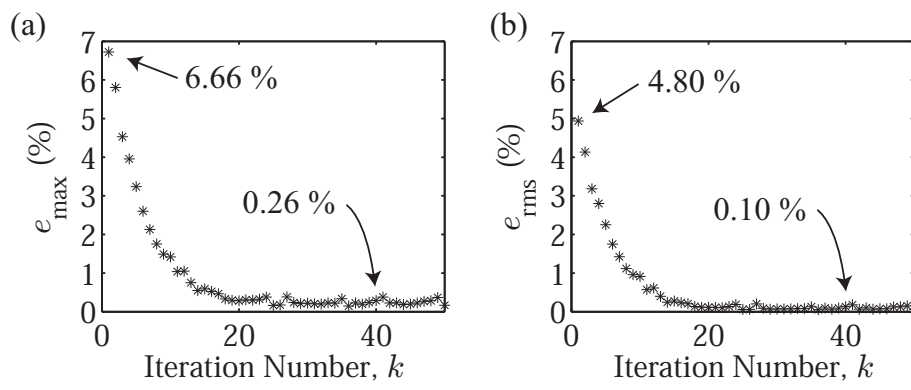
Figure 6.17: Tracking error versus number of iteration for tracking of the second monotonic section.
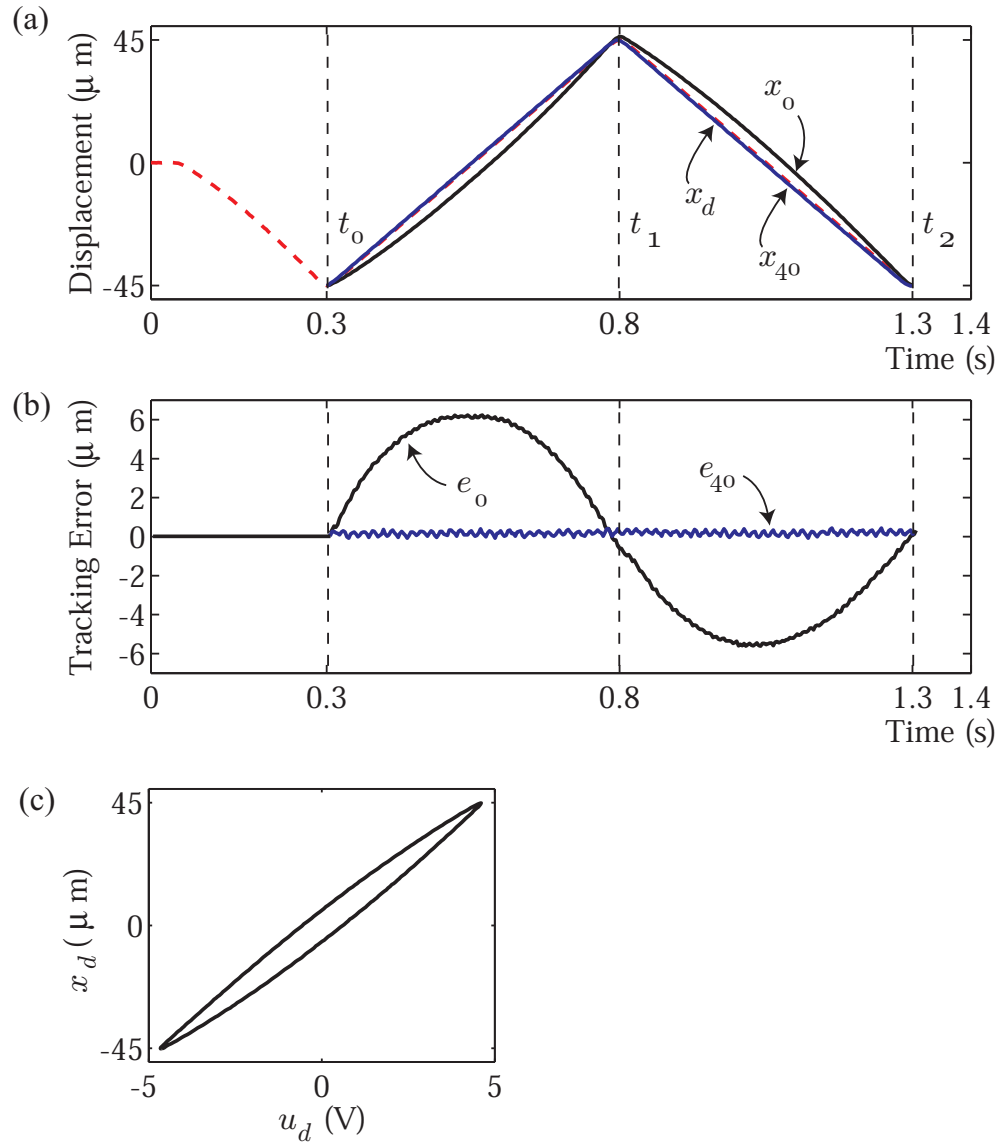
Figure 6.18: (a) and (b) Comparing the response for the uncompensated case and the ILC approach. (c) hysteresis curve for the uncompensated approach.
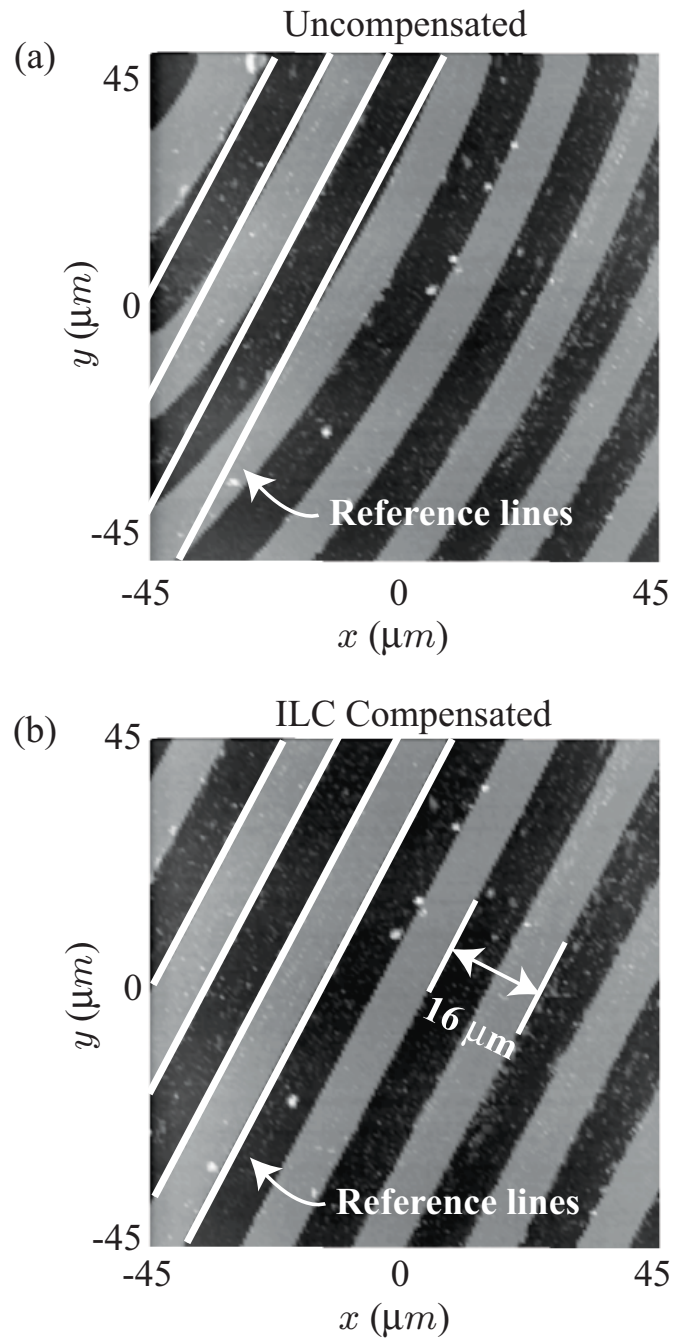
Figure 6.19: Atomic force microscope imaging results. The sample is a 16 μm-pitch encoder grating (calibration sample). (a) Uncompensated image and (b) ILC compensated image.

Chapter 7

CONCLUSIONS

In conclusion, this dissertation studied high-precision control of piezo-based systems, in particular, atomic force microscopes. First, a decoupled feedback and feedforward control approach was investigated to compensate for creep, hysteresis and vibration. Results of this method showed that an order of magnitude improvement can be achieved compared to the uncompensated case. Second, this thesis solved an ILC problem for hysteretic systems. A proof of convergence of an iterative learning control algorithm to achieve high-precision positioning was presented and the analysis was based on the Preisach hysteresis model. Because of branching effects in hysteretic systems, convergence of a proposed ILC scheme was proved by exploiting the properties of the Preisach model along a branch and convergence was shown for monotonic trajectories. Afterwards, an algorithm was proposed to demonstrate convergence for general trajectories. Finally, the proposed ILC method was applied to an experimental AFM system to demonstrate its effectiveness. The results show that the ILC method reduces the error to the noise level of the sensor measurement (0.25% of the displacement range) and with higher resolution sensors, higher precision can be achieved. Moreover, the success of this approach shows that the proposed ILC control scheme can be used to design emerging high-precision SPM-based nanotechnologies, such as AFM-based high-density data storage devices and tools for nanofabrication and nanosurgery.

Chapter 8

FUTURE WORK

This chapter discusses the extension of the ILC method developed in this dissertation to include vibration and creep effects. Additionally, some potential applications of the control method are presented.

8.1 ILC for Creep, Hysteresis and Vibration Compensation

In Chapter 4, the piezo positioner was modeled as a cascade of two subsystems: a rate-independent nonlinear element that captures the hysteresis behavior and a linear time-invariant dynamic block that represents creep and vibration effects (see Fig. 8.1(a)). In this representation, the rate-independent nonlinear element maps the input u to v and then v becomes the input to the LTI block with output y. More specifically, the complete piezo-based positioner model is given by

$$y(t) = G(v(t)); \qquad v(t) = \mathcal{H}[u](t), \tag{8.1}$$

where $\mathcal{H}$ represents the rate-independent hysteresis behavior, G is a linear mapping from v to y and u is the input to the system. This thesis solved an ILC problem for Preisach-type hysteretic systems $\mathcal{H}$. However, the ILC problem for creep, hysteresis and vibration remains to be solved.

One possible avenue to explore involves the use of the system inversion technique [14, 16, 123] and the ILC method developed in this dissertation to compensate for creep, hysteresis and vibration. First, given a desired trajectory y_d, the system inversion technique can be used to find the signal v_d that achieves y_d (see Fig. 8.1(b)). The justification for using the inversion-based approach is the LTI dynamics of the a piezo system can be easily and accurately modeled. Then, with the desired trajectory v_d computed, the ILC method developed in this dissertation can be used to find the input u_d. Of interest, of course, is
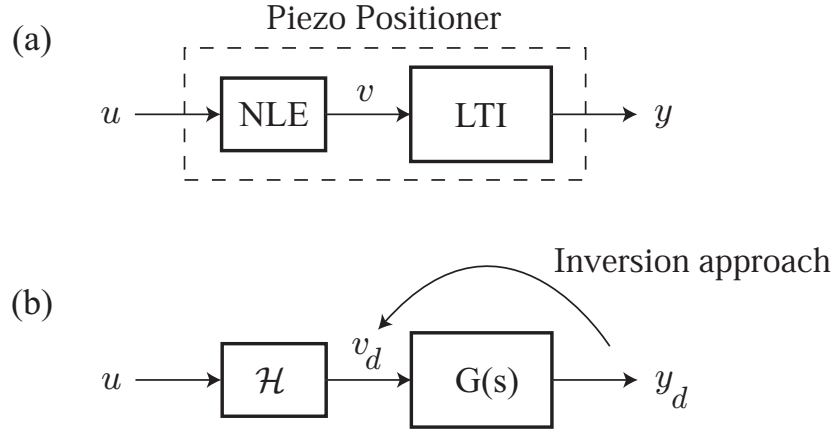
Figure 8.1: (a) The model of piezoelectric positioners. (b) Using system inversion to find v_d, then apply the ILC approach to achieve v_d.

quantifying the rate of convergence and performance of the composite system when system inversion and the ILC is applied.

Another avenue worth exploring is combining the hysteresis model and LTI system, and then pose the ILC problem for the composite system. The challenge, however, is the complexity of the model, which consists of the nonlinear-nonlocal memory behaviors of the Preisach model and dyanmics effects. The solution will require rigorous analysis to prove convergence of an ILC approach for such systems.

8.2   Potential Applications of ILC

Some of the potential applications for the ILC method developed in this dissertation include high-precision positioning in microrobotics [186, 187], for example. Complex micro-systems consisting of many parts cannot be easily produced using traditional batch fabricated tech-nqiues. Therefore, high-precision microrobotics are needed for the assembly of small and complex micro-systems that range in size from a few hundred microns to several hundred nanometers, and even smaller. The ILC method can be applied for precise control of ma-nipulators, or fabrication tools, to assemble/create parts and objects.

Likewise, piezo-based surgical tools have been developed for high-precision surgery [55].

Since hysteresis can lead to significant positioning error, precise control of the surgical tool is required in nanosurgery involving the use of piezo-based surgical tools [188]. The ILC method can be used to compensate for hysteresis and to achieve precise control of the tool for surgery applications.

Additionally, the ILC approach can be used to achieve high-precision control of piezos in the following list of applications:

- **Optics:** auto-focus systems, image stabilization

  - Wide range of motion, rapid positioning

- **Metrology:** nanometrology

  - Accurate, distortion-free measurements

- **Nanomechanics:** vibration cancellation, micro pumps, tool adjustment, needle value actuation

  - Rapid motion, precise control

- **Sensors:** Pressure sensors, force sensors, ultrasound detection, stress measurements

  - Accurate positioning, distortion-free imaging

BIBLIOGRAPHY

[1] R. Wiesendanger, *Scanning probe microscopy and spectroscopy.* Cambridge: Cambridge University Press, 1994.

[2] D. Croft, G. Shed, and S. Devasia, "Creep, hysteresis, and vibration compensation for piezoactuators: atomic force microscopy application," *ASME J. Dyn. Syst., Meas., and Control*, vol. 123, pp. 35–43, March 2001.

[3] R. C. Barrett and C. F. Quate, "Optical scan-correction system applied to atomic force microscopy," *Rev. Sci. Instrum.*, vol. 62, no. 6, pp. 1393–1399, 1991.

[4] S. Salapaka, A. Sebastin, J. P. Cleveland, and M. V. Salapaka, "High bandwidth nanopositioner: a robust control approach," *Rev. Sci. Instr.*, vol. 73, no. 9, pp. 3232–3241, 2002.

[5] M.-S. Tsai and J.-S. Chen, "Robust tracking control of a piezoactuator using a new approximate hysteresis model," *ASME J. Dyn. Syst., Meas., Control*, vol. 125, pp. 96–102, March 2003.

[6] N. S. Nise, *Control system engineering.* Redwood City, California: The Benjamin/Cummings Publishing Company, Inc., 2nd ed., 1995.

[7] A. P. Gunning, A. R. Mackie, A. R. Kirby, P. Kroon, G. Williamson, and V. J. Morris, "Motion of a cell wall polysaccharide observed by atomic force microscopy," *Macromolecules*, vol. 33, no. 15, pp. 5680–5685, 2000.

[8] G. Binnig, H. Rohrer, C. Gerber, and E. Weibel, "7×7 reconstruction on Si(111) resolved in real space," *Phys. Rev. Lett.*, vol. 50, pp. 120–123, January 1983.

[9] C. V. Nguyen, K. Chao, R. M. D. Stevens, L. Delzeit, L. Cassell, J. Han, and M. Meyyappan, "Carbon nanotube tip probes: stability and lateral resolution in scanning probe microscopy and application to surface science in semiconductors," *Nanotechnology*, vol. 12, pp. 363–367, 2001.

[10] D. J. Resnick, W. J. Dauksher, D. Mancini, K. J. Nordquist, T. C. Bailey, S. Johnson, N. Stacey, J. G. Ekerdt, C. G. Willson, S. V. Sreenivasan, and N. Schumaker, "Imprint lithography for integrated circuit fabrication," *J. Vac. Sci. Technol. B*, vol. 21, pp. 2624–2631, November/December 2003.

[11] M. Porti, X. Blasco, M. Nafria, and X. Aymerich, "Electrical characterization and fabrication of SiO_2 based metal-oxide-semiconductor nanoelectronic devices with atomic force microscopy," *Nanotechnology*, vol. 14, pp. 584–587, 2003.

[12] A. J. Lotka, *Elements of mathematical biology*. Baltimore: William and Wilkins, 1925.

[13] R. Cross, ed., *Unemployment, hysteresis, and the natural rate hypothesis*. New York: Basil Blackwell Ltd., 1988.

[14] E. Bayo, "A finite-element approach to control the end-point motion of a single-link flexible robot," *J. Robotic Systems*, vol. 4, pp. 63–75, 1987.

[15] H.-J. Lee and D. A. Saravanos, "The effects of temperature dependent material properties on the response of piezoelectric composite materials," *J. of Intelligent Material Systems and Structures*, vol. 9, pp. 503–508, July 1998.

[16] S. Devasia, D. Chen, and B. Paden, "Nonlinear inversion-based output tracking," *IEEE Trans. Autom. Control*, vol. 41, pp. 930–942, July 1996.

[17] S. Arimoto, S. Kawamura, and F. Miyazaki, "Bettering operation of dynamic systems by learning: a new control theory for servomechanism or mechatronics systems," in *Proc. American Control Conference*, pp. 1064–1069, December 1984.

[18] M. Brokate and J. Sprekels, *Hysteresis and phase transitions.* New York: Springer, 1996.

[19] A. Ballato, "Piezoelectricity: history and new thrusts," in *IEEE Ultrasonics Symposium*, pp. 575–583, IEEE, 1996.

[20] W. P. Mason, "Piezoelectricity, its history and applications," *J. Acoust. Soc. Am.*, vol. 70, pp. 1561–1566, December 1981.

[21] W. P. Mason, *Quartz crystals for electrical circuits*, ch. Quartz crystal applications, pp. 11–56. New York: D. Van Nostrand Co., Inc., 1946.

[22] W. G. Cady, *Piezoelectricity.* New York: McGraw-Hill, 1946.

[23] W. D. Callister, *Materials science and engineering: an introduction.* New York: John Wiley and Sons, Inc., 3rd ed., 1994.

[24] D. Berlincourt, "Piezoelectric ceramics: characteristics and applications," *J. Acoust. Soc. Am.*, vol. 70, pp. 1586–1595, December 1981.

[25] T. G. King, M. E. Preston, B. J. M. Murphy, and D. S. Cannell, "Piezoelectric ceramic actuators: a review of machinery applications," *Precision Engineering*, vol. 12, pp. 131–136, July 1990.

[26] K. Uchino, *Engineering Materials Handbook: Ceramics and Glass*, vol. 4, ch. Piezoelectric ceramics, pp. 1119–1123. ASM International, 1991.

[27] E. Momosaki and S. Kogure, "The application of piezoelectricity to watches," *Ferroelectrics*, vol. 40, pp. 203–216, 1982.

[28] T. Tanaka, "Piezoelectric devices in Japan," *Ferroelectrics*, vol. 40, pp. 167–187, 1982.

[29] A. V. Srinivasan and D. M. McFarland, *Smart structures: analysis and design.* New York: Cambridge University Press, 2001.

144

[30] G. Schitter, R. W. Stark, and A. Stemmer, "Sensors for closed-loop piezo control: strain gauges versus optical sensors," *Measurement Science and Technology*, vol. 13, pp. N47–N48, 2002.

[31] M. Locatelli, "Easy method to characterize a piezoelectric ceramic tube as a displacer," *Rev. Sci. Instr.*, vol. 59, no. 4, 1988.

[32] C. J. Chen, "Electromechanical deflections of piezoelectric tubes with quartered electrodes," *Appl. Phys. Lett.*, vol. 60, pp. 132–134, January 1992.

[33] C. J. Chen, "In situ testing and calibration of tube piezoelectric scanners," *Ultramicroscopy*, vol. 42-44, pp. 1653–1658, 1992.

[34] D. Damjanovic and R. E. Newnham, "Electrostrictive and piezoelectric materials for actuator applications," *J. of Intell. Mater. Syst. and Stuct.*, vol. 3, pp. 190–208, April 1992.

[35] K. Takaishi, T. Imamura, Y. Mizoshita, S. Hasegawa, T. Ueno, and T. Yamada, "Microactuator control for disk drive," *IEEE Trans. Magnetics*, vol. 32, pp. 1863–1866, May 1996.

[36] R. Oboe, A. Beghi, and B. Murari, "Modeling and control of a dual stage actuator hard disk drive with piezoelectric secondary actuator," in *Proc. 1999 IEEE/ASME Advan. Intelli. Mechatronics*, pp. 138–143, September 1999.

[37] R. B. Evans, J. S. Griesbach, and W. C. Messner, "Piezoelectric microactuator for dual stage control," *IEEE Trans. on Magnetics*, vol. 35, pp. 977–982, March 1999.

[38] H. Numasato and M. Tomizuka, "Settling control and performance of dual-actuator system for hard disk drives," in *Proc. American Control Conf.*, (Arlington, VA), pp. 2779–2785, June 25-27, 2001.

[39] Y. Okazaki, "A micro-positioning tool post using a piezoelectric actuator for diamond turning machines," *Precision Engineering*, vol. 12, pp. 151–156, July 1990.

[40] M. R. Keeling, "Ink jet printing," *Physics in Technology*, vol. 12, pp. 196–203, September 1981.

[41] D. L. White and O. R. Wood II, "Novel alignment system for imprint lithography," *J. Vac. Sci. Technol. B*, vol. 18, pp. 3552–3556, November/December 2000.

[42] J. C. Dainty, A. V. Koryabin, and A. V. Kudryashov, "Low-order adaptive deformable mirror," *Applied Optics*, vol. 37, pp. 4663–4668, July 1998.

[43] C. Radzewicz, P. Wasylczyk, and W. Wasilewski, "Piezo-driven deformable mirror for femtosecond pulse shaping," *Optics Letters*, vol. 29, pp. 177–179, January 2004.

[44] J.-Y. Shim and D.-G. Gweon, "Piezo-driven metrological multiaxis nanopositioner," *Rev. Sci. Instr.*, vol. 72, pp. 4183–4187, November 2001.

[45] G. Dai, F. Pohlenz, H.-U. Danzebrink, M. Xu, K. Hasche, and G. Wilkening, "Metrological large range scanning probe microscope," *Rev. Sci. Instr.*, vol. 75, pp. 962–969, April 2004.

[46] F. E. Scire and E. C. Teague, "Piezodriven 50-μm range stage with subnanometer resolution," *Rev. Sci. Instr.*, vol. 49, pp. 1735–1740, December 1978.

[47] F. Meli and R. Thalmann, "Long-range AFM profiler used for accurate pitch measurements," *Meas. Sci. Technol.*, vol. 9, pp. 1087–1092, 1998.

[48] M. R. Kermani, M. Moallem, and R. V. Patel, "Optimizing the performance of piezoelectric actuators for active vibration control," in *Proc. 2002 IEEE Int. Conf. Robotics and Automation*, (Washington, DC), pp. 2375–2380, May 2002.

[49] J.-H. Park, K. Yoshida, and S. Yokota, "A piezoelectric micropump using resonance drive: proposal of resonance drive and basic experiments on pump characteristics," in *Proc. of the 1997 ASME Inter. Mech. Eng. Congress and Exposition: The Fluid Power and Systems Technology Division*, vol. 4, (Dallas, TX), pp. 77–82, November 16-21, 1997.

[50] S. Stilson, A. McClellan, and S. Devasia, "High-speed solution switching using piezo-based micropositioning stages," *IEEE Trans. Biomedical Engineering*, vol. 48, pp. 806–814, July 2001.

[51] A. Haake and J. Dual, "Mico-manipulation of small particles by node position control of an ultrasonic standing wave," *Ultrasonics*, vol. 40, pp. 317–322, 2002.

[52] M. Kurosawa, M. Takahashi, and T. Higuchi, "Ultrasonic linear motor using surface acoustic waves," *IEEE Trans. on Ultrasonics, Ferroelectrics, and Frequency Control*, vol. 43, pp. 901–906, September 1996.

[53] M. Mattingly, E. A. Bailey, A. W. Dutton, B. Roemer, and S. Devasia, "Reduced-order modeling for hyperthermia: an extended balanced-realization-based approach," *IEEE Trans. Biomedical Engineering*, 1998.

[54] M. Mattingly, B. Roemer, and S. Devasia, "Exact temperature tracking for hyperthermia: a model-based approach," *IEEE Trans. Control Systems Technology*, 2000.

[55] D. J. Cappelleri and M. I. Frecker, "Optimal design of smart tools for minimally invasive surgery," in *Proc. of Optimization in Industry*, vol. 2, (Banff, Canada), pp. 139–149, June 1999.

[56] D. J. Cappelleri, M. I. Frecker, and T. W. Simpson, "Design of a PZT bimorph actuator using a metamodel-based approach," *ASME J. of Mechanical Design*, vol. 124, pp. 354–357, June 2002.

[57] J. Voigt, F. Shi, P. Hudek, I. W. Rangelow, and K. Edinger, "Progress on nanostructuring with Nanojet," *J. Vac. Sci. Technol. B*, vol. 18, pp. 3525–3529, November/December 2000.

[58] C. B. Schaffer, A. O. Jamison, and E. Mazur, "Morphology of femtosecond laser-induced structural changes in bulk transparent materials," *Applied Physics Letters*, vol. 84, pp. 1441–1443, March 2004.

[59] P. Gao, H. Tan, and Z. Yuan, "The design and characterization of a piezo-driven ultra-precision stepping positioner," *Meas. Sci. Technol.*, vol. 11, pp. N15–N19, 2000.

[60] C. Lee, T. Itoh, and T. Suga, "Micromachined piezoelectric force sensors based on PZT thin films," *IEEE Trans. Ultrasonics, Ferroelectrics, and Frequency Cont.*, vol. 43, pp. 553–559, July 1996.

[61] M. Shayegan, K. Karrai, Y. P. Shkolnikov, K. Vakili, E. P. De Poortere, and S. Manus, "Low-temperature, *in situ* tunable, uniaxial stress measurements in semiconductors using a piezoelectric actuator," *Applied Physics Letters*, vol. 83, pp. 5235–5237, December 2003.

[62] C. Z. Rosen, B. V. Hiremath, and R. Newnham, eds., *Piezoelectricity*. Key papers in the physics series, New York: American Institute of Physics, 1992.

[63] G. Binnig, H. Rohrer, C. Gerber, and E. Weibel, "Surface studies by scanning tunneling microscopy," *Phys. Rev. Lett.*, vol. 49, pp. 57–61, July 1982.

[64] G. Binnig and D. P. E. Smith, "Single-tube three-dimensional scanner for scanning tunneling microscopy," *Rev. Sci. Instr.*, vol. 57, pp. 1688–1689, August 1986.

[65] G. Binnig, "Force microscopy," *Ultramicroscopy*, vol. 42-44, pp. 7–15, 1992.

[66] C. F. Quate, "Scanning probes as a lithography tool for nanostructures," *Surface Science*, vol. 386, pp. 259–264, 1997.

[67] G. Binnig and C. F. Quate, "Atomic force microscope," *Phys. Rev. Lett.*, vol. 56, pp. 930–933, March 1986.

[68] F. Braet, R. D. Zanger, S. Kammer, and E. Wisse, "Noncontact versus contact imaging: an atomic force microscope study on hepatic endothelial cells in vitro," *Int. J. Imaging Syst. Tech.*, vol. 8, no. 2, pp. 162–167, 1997.

[69] W. Häberle, J. K. H. Hörber, R. Ohnesorge, D. P. E. Smith, and G. Binnig, "In situ investigations of single living cells infected by viruses," *Ultramicrocopy*, vol. 42-44, pp. 1161–1167, 1992.

[70] H. G. Hansma, "Atomic force microscopy of biomolecules," *J. Vac. Sci. Technol. B*, vol. 14, pp. 1390–1394, March/April 1996.

[71] S. Kasas, N. H. Thomson, B. L. Smith, P. K. Hansma, J. Miklossy, and H. G. Hansma, "Biological applications of the AFM: from single molecules to organs," *Int. J. of Imaging Syst. and Technol.*, vol. 8, no. 2, pp. 151–161, 1997.

[72] P. P. Lehenkari, G. T. Charras, A. Nykänen, and M. A. Horton, "Adapting atomic force microscopy for cell biology," *Ultramicroscopy*, vol. 82, pp. 289–295, 2000.

[73] S. A. Crawford, M. J. Higgins, P. Mulvaney, and R. Wetherbee, "Nanostructures of the diatom frustule as revealed by atomic force and scanning electron microscopy," *J. Phycol.*, vol. 37, pp. 543–554, 2001.

[74] Y. L. Lyubchenko and L. S. Shilyakhtenko, "Visualization of supercoiled DNA with atomic force microscopy *in situ*," *Prc. Natl. Acad. Sci.*, vol. 94, pp. 496–501, January 1997.

[75] L. I. Pietrasanta, D. Thrower, W. Hsieh, S. Rao, O. Stemmann, J. Lechner, and H. Hansma, "Probing the saccharomyces cerevisiae centromeric DNA (CEN DNA)-binding factor 3 (CBF3) kinetochore complex by using atomic force microscopy," *Proc. Natl. Acad. Sci.*, vol. 96, pp. 3757–3762, March 1999.

[76] C. Bustamante, M. Guthold, X. Zhu, and G. Yang, "Facilitated target location on DNA by individual escherichia coli RNA polymerase molecules observed with the scanning force microscope operating in liquid," *J. of Biological Chemistry*, vol. 274, pp. 16665–16668, June 1999.

[77] M. Radmacher, "Measuring the elastic properties of biological samples with the AFM," *IEEE Engineering in Medicine and Biology*, pp. 47–57, March/April 1997.

[78] C. Rotsch, F. Braet, E. Wisse, and M. Radmacher, "AFM imaging and elasticity measurements on living rat liver macrophages," *Cell Biology Int.*, vol. 21, no. 11, pp. 685–696, 1997.

[79] S. W. Schneider, M. E. Egan, B. P. Jena, W. B. Guggino, H. Oberleithner, and J. P. Geibel, "Continuous detection of extracellular ATP on living cells by using atomic force microscopy," *Proc. Natl. Acad. Sci.*, vol. 96, pp. 12180–12185, October 1999.

[80] G. Li, N. Xi, M. Yu, and W. K. Fung, "3-D nanomanipulation using atomic force microscopy," in *Proc. IEEE Int. Conf. on Robotics and Automation*, (Taipei, Taiwan), pp. 3642–3647, September 14-19 2003.

[81] H. J. Mamin and D. Rugar, "Thermomechanical writing with an atomic force microscope tip," *Appl. Phys. Lett.*, vol. 61, pp. 1003–1005, August 1992.

[82] B. W. Chui, T. D. Stowe, and T. W. Kenny, "Low-stiffness silicon cantilevers for thermal writing and piezoresistive readback with the atomic force microscope," *Appl. Phys. Lett.*, vol. 69, pp. 2767–2769, October 1996.

[83] S. Hosaka, A. Kikukawa, H. Koyanagi, T. Shintani, M. Miyamoto, K. Nakamura, and E. Etoh, "Spm-based data storage for ultrahigh density recording," *Nanotechnology*, vol. 8, no. 1, pp. A58–A62, 1997.

150

[84] S. Hosaka, H. Koyanagi, A. Kikukawa, M. Miyamoto, K. Nakamura, and E. Etoh, "Force modulation atomic force microscopy recording for ultrahigh density recording," *J. Vac. Sci. Technol. B*, vol. 15, no. 4, pp. 788–792, 1997.

[85] H. J. Mamin, R. P. Ried, B. D. Terris, and D. Rugar, "High-density data storage based on the atomic force microscope," *Proc. of the IEEE*, 1999.

[86] S. M. Hues, C. F. D. adn K. P. Lee, and R. J. Colton, "Effect of PZT and PMN actuator hysteresis and creep on nanoindentation measurements using force microscopy," *Rev. Sci. Instr.*, vol. 65, pp. 1561–1565, May 1994.

[87] K. R. Koops, P. M. L. O. Scholte, and W. L. de Koning, "Observation of zero creep in piezoelectric actuators," *Applied Physics A*, vol. 68, pp. 691–697, 1999.

[88] H. Jung and D.-G. Gweon, "Creep characteristics of piezoelectric actuators," *Rev. Sci. Instr.*, vol. 71, pp. 1896–1900, April 2000.

[89] G. Schitter, P. Menold, H. F. Knapp, F. Allgöwer, and A. Stemmer, "High performance feedback for fast scanning atomic force microscopes," *Rev. Sci. Instr.*, vol. 72, pp. 3320–3327, August 2001.

[90] G. Schitter and A. Stemmer, "Fast closed loop control of piezoelectric transducers," *J. Vac. Sci. Technol. B*, vol. 20, pp. 350–352, January/February 2002.

[91] H. Janocha and K. Kuhnen, "Real-time compensation of hysteresis and creep in piezoelectric actuators," *Sensors and actuators A*, vol. 79, pp. 83–89, 2000.

[92] H. Jung, J. Y. Shim, and D. Gweon, "New open-loop actuating method of piezoelectric actuators for removing hysteresis and creep," *Rev. Sci. Instr.*, vol. 71, pp. 3436–3440, September 2000.

[93] P. Krejci and K. Kuhnen, "Inverse control of systems with hysteresi and creep," *IEE Proc.-Control Theory Appl.*, vol. 148, pp. 185–192, May 2001.

[94] O. M. E. Rifai and K. Youcef-Toumi, "Creep in piezoelectric scanners of atomic force microscopes," in *Proc. of American Control Conference*, (Anchorage, AK), pp. 3777–3782, May 8-10 2002.

[95] P. Chen and S. Montgomery, "A macroscopic theory for the existence of the hysteresis and butterfly loops in ferroelectricity," *Ferroelectrics*, vol. 23, pp. 199–207, 1980.

[96] D. C. Jiles and D. L. Atherton, "Theory of ferromagnetic hysteresis," *J. Magnetism and Magnetic Materials*, vol. 61, pp. 48–60, 1986.

[97] H. Cao and A. G. Evans, "Nonlinear deformation of ferroelectric ceramics," *J. Amer. Ceram. Soc.*, vol. 76, pp. 890–896, 1993.

[98] A. E. Holman, P. M. L. O. Scholte, W. C. Heerens, and F. Tuinstra, "Analysis of piezo actuators in translation construction," *Rev. Sci. Instr.*, vol. 66, pp. 3208–3215, May 1995.

[99] D. Croft and S. Devasia, "Vibration compensation for high speed scanning tunneling microscopy," *Rev. Sci. Instr.*, vol. 70, pp. 4600–4605, December 1999.

[100] T. Ando, N. Kodera, D. Maruyama, E. Takai, K. Saito, and A. Toda, "A high-speed atomic force microscope for studying biological macromolecules in action," *Jpn. J. Appl. Phys. Part 1*, vol. 41, pp. 4851–4856, July 2002.

[101] T. Sulchek, R. Hsieh, J. D. Adams, S. C. Minne, and C. F. Quate, "High-speed atomic force microscopy in liquid," *Rev. Sci. Instr.*, vol. 71, pp. 2097–2099, May 2000.

[102] S. C. Minne, P. Flueckiger, H. T. Soh, and C. F. Quate, "Atomic force microscope lithography using amorphous silicon as a resist and advances in parallel operation," *J. Vac. Sci. Technol. B*, vol. 13, pp. 1380–1385, May/June 1995.

[103] S. R. Manalis, S. C. Minne, and C. F. Quate, "Atomic force microscopy for high speed imaging using cantilevers with an integrated actuator and sensor," *Appl. Phys. Lett.*, vol. 68, pp. 871–873, February 1996.

[104] S. R. Manalis, S. C. Minne, A. Atalar, and C. F. Quate, "High-speed atomic force microscopy using an integrated actuator and optical lever detection," *Rev. Sci. Instr.*, vol. 67, pp. 3294–3297, September 1996.

[105] S. C. Minne, G. Yaralioglu, S. R. Manalis, J. D. Adams, J. Zesch, and A. Atalar, "Automated parallel high-speed atomic force microscopy," *Appl. Phys. Lett.*, vol. 72, pp. 2340–2342, May 1998.

[106] Y.-S. Kim, H.-J. Nam, S.-M. Cho, D.-C. Kim, and J.-U. Bu, "A self-actuating PZT cantilever integrated with piezoresistor sensor for AFM with high speed parallel operation," in *Proc. IEEE Micro Electro Mechanical Systems (MEMS)*, pp. 689–692, 2002.

[107] S. Korson and A. J. Helmicki, "An H_∞ based controller for a gas turbine clearance control system," in *Proc. IEEE Conf. on Control Applications*, pp. 1154–1159, September 28-29, 1995.

[108] F. Lowrie, M. Cain, M. Stewart, and M. Gee, "Time dependent behaviour of piezoelectric materials," Tech. Rep. CMMT(A)151, National Physical Laboratory, Teddington, Middlesex, UK, 1999.

[109] J. A. Main and E. Garcia, "Piezoelectric stack actuators and control system design: strategies and pitfalls," *AIAA J. Guidance, Control, and Dynamics*, vol. 20, pp. 479–485, May–June 1997.

[110] C. Rotsch, F. Braet, E. Wisse, and M. Radmacher, "AFM imaging and elasticity measurements on living rat liver macrophages," *Cell Biology International*, vol. 21, no. 11, pp. 685–696, 1997.

[111] J. Schäfer and H. Janocha, "Compensation of hysteresis in solid-state actuators," *Sensors and Actuators A*, vol. 49, pp. 97–102, 1995.

[112] P. Ge and M. Jouaneh, "Tracking control of a piezoceramic actuator," *IEEE Trans. Contr. Syst. Tech.*, vol. 4, no. 3, pp. 209–216, 1996.

[113] S. Mittal and C.-H. Menq, "Hysteresis compensation in electromagnetic actuators through Preisach model inversion," *IEEE/ASME Transaction on Mechatronics*, vol. 5, pp. 394–409, December.

[114] S. Majima, K. Kodama, and T. Hasegawa, "Modeling of shape memory alloy actuator and tracking control system with the model," *IEEE Trans. Contr. Syst. Tech.*, vol. 9, pp. 54–59, January 2001.

[115] R. C. Smith, M. V. Salapaka, A. Hatch, J. Smith, and T. De, "Model development and inverse compensator design for high speed nanopositioning," in *Proc. 41st IEEE Conf. on Decision and Control*, (Las Vegas, NV), pp. 3652–3657, December 2002.

[116] D. Croft, D. McAllister, and S. Devasia, "High-speed scanning of piezo-probes for nano-fabrication," *ASME J. Manuf. Sci. and Eng.*, vol. 120, pp. 617–622, August 1998.

[117] S. Stilson, A. McClellan, and S. Devasia, "High-speed solution switching using piezo-based micro-positioning stages," in *Proc. American Control Conf.*, (Arlington, VA), pp. 2238–2243, June 25-27, 2001.

[118] S. Devasia, "Should model-based inverse inputs be used as feedforward under plant uncertainty?," *IEEE Trans. Autom. Contr.*, vol. 47, pp. 1865–1871, November 2002.

[119] H. Y.-F. Lam, *Analog and digital filters: design and realization.* New York: Prentice-Hall, 1979.

154

[120] R. C. Dorf and R. H. Bishop, *Modern control systems*. Upper Saddle River: Prentice-Hall, 9th ed., 2001.

[121] J. S. Dewey, K. K. Leang, and S. Devasia, "Experimental and theoretical results in output-trajectory redesign for flexible structures," *ASME J. Dyn. Syst., Meas., and Control*, vol. 120, pp. 456–461, 1998.

[122] R. Brinkerhoff and S. Devasia, "Output tracking for actuator deficient/redundant systems: multiple piezoactuator example," *AIAA J. Guid. Contr., and Dynamics*, vol. 23, no. 2, pp. 370–373, 1999.

[123] Q. Zou and S. Devasia, "Preview-based stable-inversion for output tracking," *ASME J. Dyn. Syst. Meas. Contr.*, vol. 121, pp. 625–630, December 1999.

[124] J.-T. Hsu and K. D. T. Ngo, "A Hammerstein-based dynamic model for hysteresis phenomenon," *IEEE Trans. on Power Electronics*, vol. 12, pp. 406–413, May 1997.

[125] X. Tan, R. Venkataraman, and P. S. Krishnaprasad, "Control of hysteresis: theory and experimental results," in *SPIE Modeling, Signal Processing and Control in Smart Structures*, vol. 4326, pp. 101–112, 2001.

[126] E. Eskinat, "Use of Hammerstein models in identification of nonlinear systems," *AIChE Journal*, vol. 37, pp. 255–268, February 1991.

[127] P. J. Chen and P. S. Peercy, "One dimensional dynamic electromechanical constituitive relations of ferrolectric materials," *Acta Mechanica*, vol. 31, pp. 231–241, 1979.

[128] D. C. Jiles and D. L. Atherton, "Theory of ferromagnetic hysteresis (invited)," *J. Appl. Phys.*, vol. 55, pp. 2115–2120, March 1984.

[129] O. Boser, "Statistical theory of hysteresis in ferroelectric materials," *J. Appl. Phys.*, vol. 62, pp. 1344–1348, August 1987.

[130] H. Kaizuka, "Application of capacitor insertion method to scanning tunneling microscopes," *Rev. Sci. Instr.*, vol. 60, pp. 3119–3122, October 1989.

[131] M. Goldfarb and N. Celanovic, "A lumped parameter electromechanical model for describing the nonlinear behavior of piezoelectric actuators," *ASME J. Dyn. Syst., Meas., Control*, vol. 119, pp. 478–485, September 1997.

[132] F. Vajda and E. D. Torre, "Ferenc Preisach, in memoriam," *IEEE Trans. Magnetics*, vol. MAG-31, pp. i–ii, March 1995.

[133] F. Preisach, "Uber die magnetische nachwirkung," *Zeitschrift fur Physik*, vol. 94, pp. 277–302, 1935.

[134] P. Ge and M. Jouaneh, "Modeling hysteresis in piezoceramic actuators," *Precision Engineering*, vol. 17, pp. 211–221, July 1995.

[135] H. J. M. T. A. Adriaens, W. L. de Koning, and R. Banning, "Modeling piezoelectric actuators," *IEEE/ASME Trans. Mechatronics*, vol. 5, pp. 331–341, December 2000.

[136] G. Robert, D. Damjanovic, and N. Setter, "Preisach modeling of piezoelectric nonlinearity in ferroelectric ceramics," *J. Appl. Phys.*, vol. 89, pp. 5067–5074, May 2001.

[137] H. Hu and R. B. Mrad, "On the classical Preisach model for hysteresis in piezoceramic actuators," *Mechatronics*, vol. 13, pp. 85–94, 2003.

[138] D. Hughes and J. T. Wen, "Preisach modeling of piezoceramic and shape memory alloy hysteresis," in *IEEE Conference*, pp. 1086–1091, 1995.

[139] R. B. Gorbet, D. W. L. Wang, and K. A. Morris, "Preisach model identification of a two-wire SMA actuator," in *Proc. IEEE Int. Conf. on Robotics and Automation*, (Leuven, Belgium), pp. 2161–2167, May 1998.

[140] R. Venkataraman and P. S. Krishnaprasad, "A model for a thin magnetostrictive actuator," Tech. Rep. CDCSS T.R. 98-6, Center for Dynamics and Control of Smart Structures, 1998.

[141] M. A. Krasnosel'skii and A. V. Pokrovskii, *Systems with hysteresis.* New York: Springer-Verlag, 1989.

[142] A. Visintin, ed., *Models of hysteresis.* New York: Longman Scientific and Technical, 1993.

[143] I. D. Mayergoyz, *Mathematical models of hysteresis.* New York: Springer-Verlag, 1991.

[144] M. Brokate and A. Visintin, "Properties of the Preisach model for hysteresis," *Journal fur die reine und angewandte Mathematik*, vol. 402, pp. 1–40, 1989.

[145] Q. Zou, K. K. Leang, E. Sadoun, M. J. Reed, and S. Devasia, "Control issues in high-speed AFM for biological applications: collagen imaging example," *Asian J. of Control*, 2004. To appear.

[146] J. Randall, G. Frazier, A. Seabaugh, and T. Broekaert, "Potential nanoelectronic integrated circuit technologies," *Microelectronic Engineering*, vol. 32, pp. 15–30, 1996.

[147] G. Apetrii, S. F. Fischer, U. Kunze, D. Reuter, and A. D. Wieck, "Influence of processing parameters on the transport properties of quantum point contacts fabricated with an atomic force microscope," *Semicond. Sci. Technol.*, vol. 17, pp. 735–739, 2002.

[148] S. P. Beaumont, "Nanoelectronics," *Microelectronic Engineering*, vol. 32, pp. 283–295, 1996.

[149] P. Vettiger, G. Cross, M. Despont, U. Drechsler, U. Dürig, B. Gotsmann, W. Häberle, M. A. Lantz, H. E. Rothuizen, R. Stutz, and G. K. Binnig, "The "millipede"— nanotechnology entering data storage," *IEEE Trans. on Nanotechnology*, vol. 1, pp. 39–55, March 2002.

[150] Y. Li and R. Horowitz, "Design and testing of track-following controllers for dual-stage servo systems with PZT actuated suspension," *Microsystems Technologies*, vol. 8, pp. 194–205, 2002.

[151] Y. Li, *Dual-stage servo control and active vibration compensation in magnetic hard disk drives.* PhD thesis, University of California Berkeley, Berkeley, CA, 2003.

[152] S. Yang, A. Kavčić, and W. Ryan, "Optimizing the bit aspect ratio of a recording system using an information-theoretic criterion," *IEEE Trans. on Magnetics*, vol. 39, pp. 2228–2230, September 2003.

[153] R. W. Wood, J. Miles, and T. Olson, "Recording technologies for terabit per square inch systems," *IEEE Trans. on Magnetics*, vol. 38, pp. 1711–1718, July 2002.

[154] H. Kaizuka and B. Siu, "A simple way to reduce hysteresis and creep when using piezoelectric actuators," *Jap. J. Appl. Physics*, vol. 27, pp. 773–776, May 1988.

[155] K. K. Leang and S. Devasia, "Hysteresis, creep, and vibration compensation for piezoactuators: feedback and feedforward control," in *The 2nd IFAC Conference on Mechatronic Systems*, (Berkeley, CA), pp. 283–289, December 2002.

[156] K. K. Leang and S. Devasia, "Iterative feedforward compensation of hysteresis in piezo positioners," in *IEEE 42nd Conference on Decision and Controls*, (Maui, Hawaii USA), pp. 2626 – 2631, December 2003.

[157] M. Uchiyama, "Formation of high-speed motion pattern of a mechanical arm by trial," *Trans. Society of Instrument and Control Engineers*, vol. 14, no. 6, pp. 706–712, 1978.

[158] S. Arimoto, S. Kawamura, and F. Miyazaki, "Bettering operation of robots by learning," *J. of Robotic Systems*, vol. 1, no. 2, pp. 123–140, 1984.

[159] J. J. Craig, "Adaptive control of manipulators through repeated trials," in *Proc. American Control Conference*, pp. 1566–1573, June 1984.

[160] S. Kawamura, F. Miyazaki, and S. Arimoto, "Realization of robot motion based on a learning method," *IEEE Trans. on Systems, Man, and Cybernetics*, vol. 18, pp. 126–134, January/February 1988.

[161] C. G. Atkeson and J. McIntyre, "Robot trajectory learning through practice," in *IEEE Int. Conf. on Robotics and Automation*, pp. 1737–1742, April 1986.

[162] P. Bondi, G. Casalino, and L. Gambardella, "On the iterative learning control theory for robotic manipulators," *IEEE J. Robotics and Automation*, vol. 4, pp. 14–22, February 1988.

[163] T. Sugie and T. Ono, "An iterative learning control law for dynamical systems," *Automatica*, vol. 27, no. 4, pp. 729–732, 1991.

[164] J. Ghosh and B. Paden, "Iteartive learning control for nonlinear nonminimum phase plants," *ASME J. Dyn. Syst., Meas., Control*, vol. 123, pp. 21–30, March 2001.

[165] K. L. Moore, M. Dahleh, and S. P. Bhattacharyya, "Iterative learning control: a survey and new results," *J. Robotic Systems*, vol. 9, no. 5, pp. 563–594, 1992.

[166] Y. Chen and C. Wen, *Iterative learning control: convergence, robustness and applications*. New York: Springer-Verlag, 1999.

[167] W. Hoffmann, K. Peterson, and A. G. Stefanopoulou, "Iterative learning control for soft landing of electromechanical valve actuator in camless engines," *IEEE Trans. Control Systems Technology*, vol. 11, pp. 174–184, March 2003.

[168] K. K. Tan, T. H. Lee, and H. X. Zhou, "Micro-positioning of linear-piezoelectric motors based on a learning nonlinear PID controller," *IEEE Trans. on Mechatronics*, vol. 6, pp. 428–436, December 2001.

[169] S. S. Saab, "On the P-type learning control," *IEEE Trans. Autom. Control*, vol. 39, pp. 2298–2302, November 1994.

[170] J. E. Hauser, "Learning control for a class of nonlinear systems," in *IEEE Proc. 26th Conf. on Decision and Control*, (Los Angeles, CA), pp. 859–860, December 1987.

[171] J. Ghosh and B. Paden, "A pseudoinverse-based iterative learning control," *IEEE Trans. Auto. Contr.*, vol. 47, pp. 831–837, May 2002.

[172] C. J. Li, H. S. M. Beigi, S. Li, and J. Liang, "Nonlinear piezo-actuator control by learning self-tuning regulator," *ASME J. Dyn. Syst. Meas. and Cont.*, vol. 115, pp. 720–723, December 1993.

[173] M. Hu, H. Du, and S.-F. Ling, "Motion control of an elactrostrictive actuator," in *Proc. of SPIE on Smart Structures and Devices*, vol. 4235, pp. 321–327, 2001.

[174] R. W. Hamming, *Numerical methods for scientists and engineers*. New York: McGraw-Hill, 1962.

[175] J. D. Rasmussen, T.-C. Tsao, R. D. Hanson, and S. G. Kapoor, "A piezoelectric tool servo system for variable depth of cut machining," *ASME Precision Machining: Technology and Machine Development and Improvement*, vol. 58, pp. 119–130, 1992.

[176] G. Tao and P. V. Kokotovic, "Adaptive control of plants with unknown hysteresis," *IEEE Trans. Automatic Control*, vol. 40, pp. 200–212, February 1995.

[177] R. Venkataraman and P. S. Krishnaprasad, "Approximate inversion of hysteresis: theory and numerical results," in *Proc. 39th IEEE Conf. on Decision and Control*, (Sydney, Australia), pp. 4448–4454, December 2000.

[178] R. E. Kalman and J. E. Bertram, "Control system analysis and design via the "second method" of Lyapunov: II discrete-time systems," *Trans. ASME J. Basic Engineering*, vol. 82, pp. 394–400, June 1960.

[179] M. Rosenlicht, *Introduction to analysis*. New York: Dover, 1986.

[180] Burleigh Instruments, Inc., Fishers, New York, *Burleigh Metris-2000NC atomic force microscope operating manual*, rev a ed., 1996.

[181] W. S. Galinaitis and R. C. Rogers, "Control of a hysteretic actuator using inverse hysteresis compensation," in *SPIE Conf. on Mathematics and Control in Smart Structures*, vol. 3323, pp. 267–277, March 1998.

[182] H. T. Banks, A. J. Kurdila, and G. Webb, "Identification of hysteretic confluence operators representing smart actuators: convergent approximations," Tech. Rep. CRSC-TR97-7, North Carolina State University CRSC, April 1997.

[183] M. E. Shirley and R. Venkataraman, "On the identification of preisach measures," in *Proc. SPIE Conf. Smart Structures and Materials 2003: Modeling, Signal Processing and Control in Smart Structures* (R. Smith, ed.), vol. 5349, (Bellingham, WA).

[184] L. Malvern, *Introduction to the mechanics of a continuous medium.* Prentice-Hall, 1969.

[185] G. F. Franklin, J. D. Powell, and A. Emami-Naeini, *Feedback control of dynamics systems, 3rd Edition.* New York: Addison-Wesley, 1994.

[186] S. Fatikow, J. Seyfried, S. Fahlbusch, A. Buerkle, and F. Schmoeckel, "A flexible microrobot-based microassembly station," *J. of Intelligent and Robotic Systems*, vol. 27, pp. 135–169, 2000.

[187] F. Schmoeckel and H. Wörn, "Remotely controllable mobile microrobots acting as nano positioners and intelligent tweezers in scanning electron microscopes (sems)," in *Proc. IEEE Int. Conf. on Robotics and Automation*, (Seoul, Korea), pp. 3909–3913, May 21-26 2001.

[188] J. Colombelli, S. W. Grill, and E. H. K. Stelzer, "Ultraviolet diffraction limited nanosurgery of live biological tissues," *Rev. Sci. Instr.*, vol. 75, no. 2, pp. 472–478, 2004.

[189] K. K. Leang, Q. Zou, and S. Devasia, *The CRC Mechatronics Handbook*, ch. Chapter 23: Continuous- and discrete-time state-space modeling, pp. 40–54. The CRC Press, 2002.

[190] D. Hanselman, *The Student Edition of Matlab, Version 5, User's Guide*. Upper Saddle River: Prentice-Hall, 1997.

[191] C. N. Dorny, *Understanding Dynamic Systems Approaches to Modeling, Analysis, and Design*. Englewood Cliffs: Prentice-Hall, 1993.

[192] C.-T. Chen, *Linear system theory and design*. New York: Oxford University Press, 3rd ed., 1999.

[193] B. Friedland, *Control system design: an introduction to state-space methods*. New York: McGraw-Hill, Inc., 1986.

[194] H. K. Khalil, *Nonlinear Systems*. Prentice-Hall, 2nd ed., 1996.

[195] *Discrete-time control systems*. Englewood Cliffs: Prentice Hall, 2nd ed., 1995.

[196] G. Heinzinger, D. Fenwick, B. Paden, and F. Miyazaki, "Stability of learning control with disturbances and uncertain initial conditions," *IEEE Trans. Auto. Contr.*, vol. 37, pp. 110–114, January 1992.

[197] K. K. Leang and S. Devasia, "Iterative learning control of piezo positioners for long-range spm-based nanofabrication," in *The 3rd IFAC Symposium on Mechatronic Systems*, (Manly Beach, Sydney, Australia), September 6-8 2004. Accepted.

162

Appendix A

CONTINUOUS- AND DISCRETE-TIME STATE-SPACE MODELING

This chapter[1] introduces techniques for modeling continuous- and discrete-time systems using the state-space approach. The state-space and transfer functions models obtained using the techniques described in the following were used in the modeling of the piezoactuator system described in Chapter 3. In particular, we include a discussion of determining experimentally the state-space model for a piezoactuator system by studying its measured frequency response.

A.1   Introduction

The state-space approach is a technique that uses a set of first order differential equations to represent the behavior of a system in the time-domain. The state-space approach has an advantage over frequency-domain approaches such as the transfer-function approach—it can be used to model linear, nonlinear, time-varying, and multivariable systems, whereas the transfer-function approach is suited to linear time-invariant (LTI) systems ([185], Chapter 3). In addition, models expressed in first order state-space form in the time-domain can be readily solved by a digital computer or microprocessor, which makes this approach quite useful for the design and control of modern mechatronic systems. Furthermore, there is a wide variety of available computer software, such as `MATLAB` [190], that take advantage of the state-space form for analyzing and solving design problems. Therefore, the state-space approach can be used to investigate the behavior of and facilitate in the design of both continuous- and discrete-time systems, the fundamentals of which will be the focus of this chapter.

   In the following, we begin with an example: the modeling of a piezoceramic actuator in

---

[1]This chapter is published in The CRC Mechatronics Handbook, edited by Robert Bishop, 2002 [189].

Section A.2.1 and use the example throughout the chapter. The concept of a system state is introduced in Section A.2. We explain the state-space equation for linear systems and present its solution in Section A.2.3. The linearization of nonlinear systems is the topic of Section A.2.4. The relationships between time- and frequency-domain models are discussed in Section A.3. In Section A.4, we present a procedure for obtaining a state-space model using experimental frequency-domain (frequency-response) data. Section A.5 is devoted to discrete-time state-space modeling and we conclude with a summary in Section A.6. Useful `MATLAB` commands are also included as footnotes.

A.2   *States and the State-space*

A.2.1   *An Example Piezoceramic Actuator*

We begin by modeling a piezoceramic actuator, which is an example mechatronic (electromechanical) system. When a voltage is applied to a piezoceramic material, its dimension changes. This change in dimension can be used to precisely position an object or tool (such as a sensor), thus making piezoceramics suitable actuators for a wide variety of applications. For example, due to their ability to achieve positioning with sub-nanometer level precision, piezoceramic actuators have become an ideal positioning actuator for emerging nanotechnologies. In particular, a piezo-tube actuator is used in scanning probe microscopes (SPMs, see Fig. A.1) to precisely position a probe tip for high-precision nanofabrication, surface modification, and the acquisition of images of atoms [2]. The probe tip can be positioned in the three coordinate axes (x, y, and z), with each motion controlled by an independent voltage source (V_x, V_y, and V_z). Scanning of the probe is performed parallel to the sample surface along the x- and y-axis; the z-axis movement allows motion of the probe perpendicular to the sample surface. An accurate mathematical model of the dynamics of a piezo-tube actuator is required for the analysis and design of SPM systems. A designer can exploit the known information of the system from its model to improve or optimize a design for building faster and more reliable SPMs. For example, an approach that has been successfully implemented is the inversion-based control method, which finds the inputs required to achieve exact tracking by inverting the system model [2]. This technique works best when
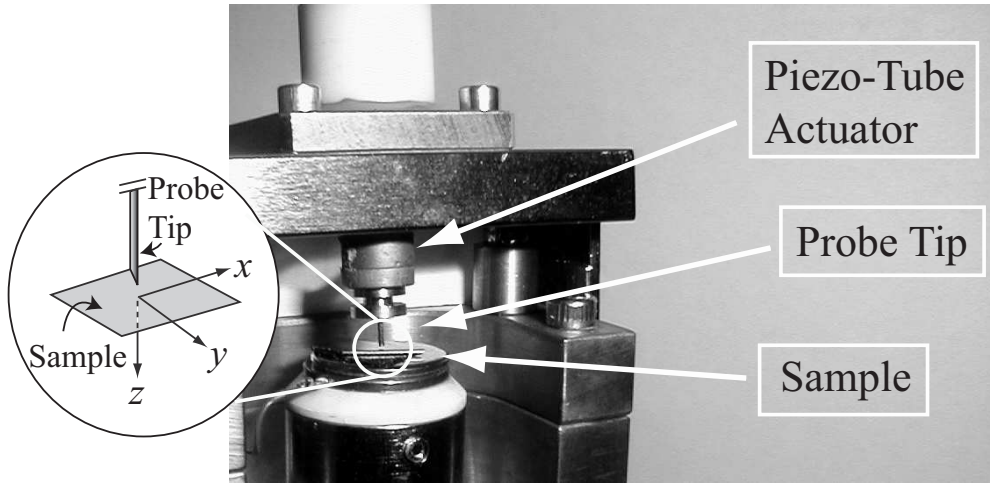
Figure A.1: The main components of a scanning probe microscope (SPM) used for surface analysis, which includes the piezo-tube actuator, the probe tip, and the sample. The configuration of the probe tip and sample with respect to the coordinate axes (x, y, and z) are shown in the magnified view.

the dynamics of the system are well characterized and understood. In general, the analysis and design of control systems also require a system model. Thus, for analysis and design, it is crucial to obtain an accurate mathematical model that describes the behavior of a system. Modeling of the example piezo-tube system is considered in the following.

Simple Model of a Piezo-Tube Actuator

We will model the dynamics of the piezo-tube actuator along the z-axis where the input $V_z(t)$ is the applied voltage and the output of the system is the displacement $z(t)$ of the probe tip. We begin the modeling by simplifying the system as an isolated mass, an ideal spring, and a damper as shown in Fig. A.2(a). The entire mass of the piezo-tube is lumped into one mass element m, the internal elastic behavior of the piezo-tube is modeled as a spring, and the structural damping in the piezo-tube is modeled as a damper or a viscous friction element (such models are referred to as *lumped models* [191]). A mathematical relationship between the applied voltage $V_z(t)$ and the displacement of the probe tip $z(t)$ can be obtained using physical laws. Using Newton's second law (the sum of all external
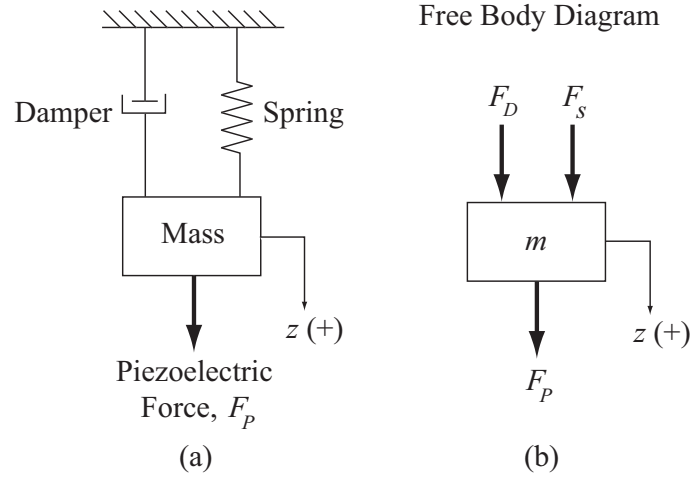
Figure A.2: (a) A simple lumped model of the piezo-tube actuator modeled along the z-axis consisting of a mass, a spring, and a damper. The positive z-direction is indicated by the arrow and the "+" sign. (b) The forces acting on the mass (free body diagram).

forces F_i acting on a body is equal the product of its mass m and acceleration $\ddot{z}(t)$) we can write the equation of motion as,

$$\sum_i F_i = m\ddot{z}(t) \tag{A.1}$$

As shown in Fig. A.2(b) (the free body diagram), there are three forces acting on the piezo-tube. First, the force exerted by the spring is assumed to be proportional to the displacement of the probe tip, $i.e.$,

$$F_s(t) = -kz(t) \tag{A.2}$$

where k is the spring constant with SI units $[N/m]$. Second, the damping force is considered to be proportional to the velocity of the probe tip $\dot{z}(t)$, $i.e.$,

$$F_d(t) = -c\dot{z}(t) \tag{A.3}$$

where c is the viscous friction or damping coefficient with SI units $[N \cdot s/m]$. Third, induced strain ϵ in the piezoceramic material is proportional to the applied voltage $V_z(t)$ [31], and by Hooke's Law, the induced stress σ is proportional to the induced strain ϵ. Hence, the

induced force $F_p(t)$ (stress σ times the cross sectional area) is proportional to the applied voltage $V_z(t)$, *i.e.*,

$$F_p(t) = bV_z(t) \tag{A.4}$$

where b is a constant with SI units $[N/V]$. Rewriting Eq. (A.1) in terms of the three forces, the equation of motion becomes,

$$
\begin{aligned}
\sum_{i=1}^{3} F_i &= m\ddot{z}(t) \\
F_s(t) + F_d(t) + F_p(t) &= m\ddot{z}(t) \\
-kz(t) - c\dot{z}(t) + bV_z(t) &= m\ddot{z}(t) \\
\Rightarrow \quad m\ddot{z}(t) + c\dot{z}(t) + kz(t) &= bV_z(t) \tag{A.5}
\end{aligned}
$$

which is called the *mass-spring-damper* model. Note that the relationship between the input voltage $V_z(t)$ and the displacement $z(t)$ of the probe tip (*i.e.*, the model of the dynamics) is a second order differential equation. The response of the probe tip (displacement of mass m) to an applied voltage $V_z(t)$ can be obtained in the frequency-domain by using the Laplace transform approach ([120], Chapter 2, Section 5); however, the state-space approach can be used to obtain the solution directly in the time-domain. In the remaining sections, the state-space approach to modeling is presented and the mass-spring-damper model of the piezo-tube actuator will be used as an example.

A.2.2 States of a System

We begin by introducing the concept of a *state*, which is the basis for the state-space approach. In general, a state can be defined as the following:

Definition 6 (The State of a System) *The state $x(t_0)$ of a dynamic system at time t_0 is a set of variables that, together with the input $u(t)$, for $t \geq 0$, determines the behavior of the system for all $t \geq t_0$ ([192], Chapter 2, Section 1.1).*

Fundamental to this definition is the notion that the state summarizes the current configuration of a system. Therefore, the memory of a dynamical system is preserved in the state variables at the current time t_0 (called initial condition), and the future behavior of

the system is determined by the initial condition $x(t_0)$ and the applied input u, for $t \geq 0$. The state of a system can be written as the set

$$\mathbf{x}(t) = \begin{bmatrix} x_1(t) \\ x_2(t) \\ x_3(t) \\ \vdots \\ x_n(t) \end{bmatrix} \tag{A.6}$$

where n is the number of states[2]. Any set of variables that satisfy the above definition can be a valid state, hence the state is not unique ([193], Chapter 2, Section 2).

Example The state variables required to describe the mass-spring-damper system can be chosen as the position $z(t)$ and velocity $\dot{z}(t)$ of the mass. We can write the state vector as

$$\mathbf{x}(t) = \begin{bmatrix} x_1(t) \\ x_2(t) \end{bmatrix} = \begin{bmatrix} z(t) \\ \dot{z}(t) \end{bmatrix} \tag{A.7}$$

where the number of states is two ($n = 2$). If the position $z(t)$ and velocity $\dot{z}(t)$ of the mass is known at time t_0, along with the applied voltage $V_z(t)$ defined for $t \geq t_0$, then the future behavior of the system (*i.e.*, the state $\mathbf{x}(t)$) can be determined by solving the differential equation (A.5).

A.2.3 The Linear State-Space Equation and its Solution

For a linear system, the evolution of the states of a system over time can be described by a set of linear first order differential equations of the form:

$$\begin{aligned} \dot{x}_1(t) &= \tfrac{dx_1(t)}{dt} &= a_{11}(t)x_1(t) + \cdots + a_{1n}(t)x_n(t) + b_{11}(t)u_1(t) + \cdots b_{1p}(t)u_p(t) \\ \dot{x}_2(t) &= \tfrac{dx_2(t)}{dt} &= a_{21}(t)x_1(t) + \cdots + a_{2n}(t)x_n(t) + b_{21}(t)u_1(t) + \cdots b_{2p}(t)u_p(t) \\ &\vdots \\ \dot{x}_n(t) &= \tfrac{dx_n(t)}{dt} &= a_{n1}(t)x_1(t) + \cdots + a_{nn}(t)x_n(t) + b_{n1}(t)u_1(t) + \cdots b_{np}(t)u_p(t) \end{aligned} \tag{A.8}$$

[2]For a discussion on the minimal set of states required to describe a system (minimal realization), see ([192], Chapter 7).

where n is the number of states (or the order of the system) and p is the number of inputs. Defining the input vector as

$$\mathbf{u}(t) \; = \; \begin{bmatrix} u_1(t) \\ u_2(t) \\ u_3(t) \\ \vdots \\ u_p(t) \end{bmatrix} \tag{A.9}$$

and the state vector $\mathbf{x}(t)$ as defined in Eq. (A.6), the set of first order differential equations given by (A.8) can be rewritten in compact matrix form as ([193], Chapter 2, section 2),

$$\begin{aligned} \dot{\mathbf{x}}(t) \; &= \; \begin{bmatrix} a_{11}(t) & a_{12}(t) & \cdots & a_{1n}(t) \\ a_{21}(t) & a_{22}(t) & \cdots & a_{2n}(t) \\ \vdots & \vdots & \ddots & \vdots \\ a_{n1}(t) & a_{n2}(t) & \cdots & a_{nn}(t) \end{bmatrix} \mathbf{x}(t) + \begin{bmatrix} b_{11}(t) & b_{12}(t) & \cdots & b_{1p}(t) \\ b_{21}(t) & b_{22}(t) & \cdots & b_{2p}(t) \\ \vdots & \vdots & \ddots & \vdots \\ b_{n1}(t) & b_{n2}(t) & \cdots & b_{np}(t) \end{bmatrix} \mathbf{u}(t) \\ &\triangleq \; A(t)\mathbf{x}(t) + B(t)\mathbf{u}(t) \end{aligned} \tag{A.10}$$

where $A(t)$ is an $n \times n$ matrix and $B(t)$ is an $n \times p$ matrix. For a system defined with q outputs $\mathbf{y}(t)$, which are assumed to be a linear combination of the state $\mathbf{x}(t)$ and input $\mathbf{u}(t)$, we can write the output equation as

$$\begin{aligned} \mathbf{y}(t) \; &= \; \begin{bmatrix} c_{11}(t) & c_{12}(t) & \cdots & c_{1n}(t) \\ c_{21}(t) & c_{22}(t) & \cdots & c_{2n}(t) \\ \vdots & \vdots & \ddots & \vdots \\ c_{q1}(t) & c_{q2}(t) & \cdots & c_{qn}(t) \end{bmatrix} \mathbf{x}(t) + \begin{bmatrix} d_{11}(t) & d_{12}(t) & \cdots & d_{1p}(t) \\ d_{21}(t) & d_{22}(t) & \cdots & d_{2p}(t) \\ \vdots & \vdots & \ddots & \vdots \\ d_{q1}(t) & d_{q2}(t) & \cdots & d_{qp}(t) \end{bmatrix} \mathbf{u}(t) \\ &\triangleq \; C(t)\mathbf{x}(t) + D(t)\mathbf{u}(t) \end{aligned} \tag{A.11}$$

where $C(t)$ is an $q \times n$ matrix and $D(t)$ is an $q \times p$ matrix. In general, the matrices $A(t)$, $B(t)$, $C(t)$, and $D(t)$ are time varying; however, in this chapter, we will only consider the time-invariant case where A, B, C, and D are constant matrices, thus

$$\dot{\mathbf{x}}(t) \; = \; A\mathbf{x}(t) + B\mathbf{u}(t) \tag{A.12}$$

$$\mathbf{y}(t) \; = \; C\mathbf{x}(t) + D\mathbf{u}(t) \tag{A.13}$$

Equations (A.12) and (A.13) are called the linear time-invariant (LTI) state and output equations, respectively[3].

The response of the system to an applied input can be quantified by the evolution of the system state $\mathbf{x}(t)$ and the output $\mathbf{y}(t)$. The state-space equation (A.12) is a set of first order differential equations in matrix form, which can be solved in time for a given initial condition $\mathbf{x}(t_0)$ as ([193], Chapter 3)

$$\mathbf{x}(t) = e^{A(t-t_0)}\mathbf{x}(t_0) + \int_{t_0}^{t} e^{A(t-\tau)}Bu(\tau)d\tau \tag{A.14}$$

Note that solution (A.14) is the sum of two terms: the first term is the effect of initial condition $\mathbf{x}(t_0)$ and the second is the effect of the applied input $\mathbf{u}(t)$ between $t_0 \leq \tau \leq t$[4]. Using the output Eq. (A.13) and the state solution given by Eq. (A.14), the output $\mathbf{y}(t)$ becomes

$$\mathbf{y}(t) = Ce^{A(t-t_0)}\mathbf{x}(t_0) + \int_{t_0}^{t} Ce^{A(t-\tau)}Bu(\tau)d\tau + D\mathbf{u}(t) \tag{A.15}$$

The system response $\mathbf{y}(t)$ to an applied input $\mathbf{u}(t)$ is characterized by the system matrices (A,B,C,D). For example, the output $\mathbf{y}(t)$ will be bounded for any bounded input if the system is stable and the system is stable if the real parts of all the eigenvalues of A are less than zero (strictly negative) ([193], Chapter 4, Section 4)[5].

Example For the mass-spring-damper example system, the state-space equation can be found by differentiating the states $\mathbf{x}(t)$ defined in Eq. (A.7) and using the equation of motion (A.5) to obtain

$$
\begin{aligned}
\dot{x}_1(t) &= \dot{z}(t) = x_2(t) \\
\dot{x}_2(t) &= \ddot{z}(t) = -\frac{k}{m}z(t) - \frac{c}{m}\dot{z}(t) + \frac{b}{m}V_z(t) = -\frac{k}{m}x_1(t) - \frac{c}{m}x_2(t) + \frac{b}{m}u(t)
\end{aligned}
\tag{A.16}
$$

---

[3]For a detailed discussion of the solution of linear time-varying equations, see [192], Chapter 4, section 5.

[4]The MATLAB command `lsim` simulates the time response of LTI models to arbitrary inputs.

[5]The MATLAB command `eig(A)` returns the eigenvalues of the system matrix A.

We choose the position of the mass $z(t)$ to be the output of the system, and write the state-space and output equation in the form given by Eqs. (A.12) and (A.13) as

$$\dot{\mathbf{x}}(t) = \begin{bmatrix} 0 & 1 \\ -(k/m) & -(c/m) \end{bmatrix} \mathbf{x}(t) + \begin{bmatrix} 0 \\ (b/m) \end{bmatrix} u(t), \tag{A.17}$$

$$y(t) = \begin{bmatrix} 1 & 0 \end{bmatrix} \mathbf{x}(t). \tag{A.18}$$

A.2.4   Linearization of Nonlinear Systems

A general form of the state-space equation (for nonlinear systems) is

$$\dot{\mathbf{x}}(t) = g(\mathbf{x}(t), \mathbf{u}(t)), \tag{A.19}$$

$$\mathbf{y}(t) = h(\mathbf{x}(t), \mathbf{u}(t)), \tag{A.20}$$

where $g(\cdot)$ and $h(\cdot)$ can be nonlinear functions. The behavior of nonlinear systems is beyond the scope of this chapter; however, a detailed discussion can be found in [194]. The behavior of a nonlinear system can be approximated by a linear model in a neighborhood of a equilibrium point. Such linearizations can simplify the analysis and design of nonlinear systems because the tools developed for linear systems can be applied under certain conditions [194]. Let $\mathbf{x}_0$ and $\mathbf{u}_0$ be the equilibrium state and input, respectively, such that ([194], Chapter 1)

$$g(\mathbf{x}_0, \mathbf{u}_0) = \mathbf{0}, \tag{A.21}$$

$$h(\mathbf{x}_0, \mathbf{u}_0) = \mathbf{y}_0. \tag{A.22}$$

Consider small perturbations in the equilibrium point $\mathbf{x}(t) = \mathbf{x}_0 + \bar{\mathbf{x}}(t)$, the input $\mathbf{u}(t) = \mathbf{u}_0 + \bar{\mathbf{u}}(t)$, and the output $\mathbf{y}(t) = \mathbf{y}_0 + \bar{\mathbf{y}}(t)$. If the perturbation $\bar{\mathbf{x}}(t)$ is small for all t, then we obtain the following by expanding (A.19) in Taylor series (neglecting higher order terms of $\bar{\mathbf{x}}(t)$ and $\bar{\mathbf{u}}(t)$),

$$\dot{\mathbf{x}}_0 + \dot{\bar{\mathbf{x}}}(t) = g(\mathbf{x}_0 + \bar{\mathbf{x}}(t), \mathbf{u}_0 + \bar{\mathbf{u}}(t)),$$

$$\dot{\bar{\mathbf{x}}}(t) = g(\mathbf{x}_0, \mathbf{u}_0) + \frac{\partial g}{\partial \mathbf{x}} \bar{\mathbf{x}}(t) + \frac{\partial g}{\partial \mathbf{u}} + \cdots . \tag{A.23}$$

Recognizing that $g(\mathbf{x}_0, \mathbf{u}_0) = \mathbf{0}$, we obtain

$$\dot{\bar{\mathbf{x}}} = \bar{A}\bar{\mathbf{x}}(t) + \bar{B}\bar{\mathbf{u}}(t), \tag{A.24}$$

where

$$\bar{A} = \left. \frac{\partial g}{\partial \mathbf{x}} \right|_{\mathbf{x}_0, \mathbf{u}_0} \quad \text{and} \quad \bar{B} = \left. \frac{\partial g}{\partial \mathbf{u}} \right|_{\mathbf{x}_0, \mathbf{u}_0}. \tag{A.25}$$

The matrices $\bar{A}$ and $\bar{B}$ are the Jacobians evaluated at $\mathbf{x}_0$ and $\mathbf{u}_0$. Equation (A.24) is a linear state equation and is valid for small perturbations about $\mathbf{x}_0$ and $\mathbf{u}_0$. A similar result can be obtained for the change $\bar{\mathbf{y}}(t)$ in the output from the equilibrium value $\mathbf{y}_0$ as

$$\dot{\bar{\mathbf{y}}} = \bar{C}\bar{\mathbf{x}}(t) + \bar{D}\bar{\mathbf{u}}(t), \tag{A.26}$$

where

$$\bar{C} = \left. \frac{\partial h}{\partial \mathbf{x}} \right|_{\mathbf{x}_0, \mathbf{u}_0} \quad \text{and} \quad \bar{D} = \left. \frac{\partial h}{\partial \mathbf{u}} \right|_{\mathbf{x}_0, \mathbf{u}_0}. \tag{A.27}$$

A.3 Relationship Between State Equations and Transfer-functions

A.3.1 State-space to Transfer-function

The input-to-output relationship of a dynamic system in the frequency-domain is represented by a transfer-function, which can be obtained by taking the Laplace transform of Eq. (A.12) and Eq. (A.13) with zero initial conditions as follows ([193], Chapter 3, Section 5)

$$sX(s) = AX(s) + BU(s), \tag{A.28}$$

$$Y(s) = CX(s) + DU(s), \tag{A.29}$$

where s is the Laplace variable. Solving Eq. (A.28) for $X(s)$ and substituting into Eq. (A.29), the ratio of the output $Y(s)$ to input $U(s)$ for a single-input single-output system (SISO) can be found as,

$$\begin{aligned} G(s) &= \frac{Y(s)}{U(s)} = C(s\mathbf{I} - A)^{-1}B + D \\ &= \frac{N(s)}{D(s)}, \end{aligned} \tag{A.30}$$

where $\mathbf{I}$ is an $n \times n$ identity matrix. In Eq. (A.30), $N(s)$ and $D(s)$ are referred to as the numerator and denominator polynomial of $G(s)$, respectively[6].

---

[6]The MATLAB command `ss2tf` can be used to convert a state-space realization to a transfer function

Analogous to the state-space equation, the boundedness of the output response $y(t)$ to a bounded input $u(t)$ is characterized by the roots of the denominator polynomial $D(s)$, *i.e.*, the values of s for which $D(s) = 0$. In particular, the output $y(t)$ will be bounded for any bounded input, *i.e.*, system is stable, if the real parts of all the roots of $D(s)$ are less than zero (strictly negative)[7]. Alternatively, a convenient method to determine stability without having to find the roots of $D(s)$ explicitly is the Routh-Hurwitz Stability Criterion ([120], Chapter 6).

Example With the state-space description of the mass-spring-damper system defined in equations Eq. (A.17) and Eq. (A.18), the transfer-function realization using Eq. (A.30) becomes

$$G(s) = \frac{Y(s)}{U(s)} = \begin{bmatrix} 1 & 0 \end{bmatrix} \left(s \begin{bmatrix} 1 & 0 \\ 0 & 1 \end{bmatrix} - \begin{bmatrix} 0 & 1 \\ -(k/m) & -(c/m) \end{bmatrix} \right)^{-1} \begin{bmatrix} 0 \\ b/m \end{bmatrix} + [0]$$

$$= \frac{b/m}{s^2 + (c/m)s + k/m}. \tag{A.31}$$

The input to the system is the applied voltage $V_z(t)$ and the output is the displacement of the mass $z(t)$.

A.3.2 Frequency-response Using Transfer-functions

Consider a linear single-input single-output (SISO) stable system with transfer-function description $G(s)$. When the system $G(s)$ is excited by a sinusoidal input of the form

$$u(t) = P \sin(\omega t) \tag{A.32}$$

with amplitude P and frequency ω, the output response (after the transients decay) will also be a sinusoid of the form

$$y(t) = MP \sin(\omega t + \phi) \tag{A.33}$$

with the same frequency ω and a phase shift ϕ ([120], Chapter 8). The output amplitude is the input amplitude scaled by M, the magnitude gain. The magnitude gain M is found

---

[7]The `MATLAB` command `roots(den)` can be used to find the roots of `den`, where `den` is the coefficients of $D(s)$

by taking the magnitude of $G(s)$ evaluated at $s = j\omega$, *i.e.*,

$$M = |G(s)|_{s=j\omega}. \tag{A.34}$$

Usually, the magnitude gain M is expressed in units of Decibels (dB), *i.e.*, $M[dB] = 20 \log M$. The phase shift ϕ is the angle of $G(s)$ evaluated at $s = j\omega$, *i.e.*,

$$\phi = \angle G(s)|_{s=j\omega}, \tag{A.35}$$

with units of degrees. The plot of the magnitude gain M and the phase shift ϕ versus the frequency ω gives a graphical representation of the frequency-response (Bode plots) of the system[8]. These plots can be obtained experimentally by measuring the magnitude gain and phase shift between the input and output response of the system over a range of frequencies. Additionally, the system's transfer-function can be obtained from an experimental frequency-response data by using curve-fitting software. In Section A.4, we present this approach to determine a model for a system using experimental frequency-response data.

A.3.3   Transfer-function to State-space

In Section A.3.1, a transfer-function model was obtained for a system in state-space form. In the following, an approach for realizing a state-space model from a transfer-function $G(s)$ is presented. For a realizable transfer function $G(s)$ of a SISO system of the form

$$G(s) = \frac{b_0 s^n + b_1 s^{n-1} + \cdots + b_n}{s^n + a_1 s^{n-1} + \cdots + a_n}, \tag{A.36}$$

the controllable canonical state-space form written in terms of the coefficients of $G(s)$ is

$$\dot{\mathbf{x}}(t) = \begin{bmatrix} -a_1 & -a_2 & \cdots & -a_{n-1} & -a_n \\ 1 & 0 & \cdots & 0 & 0 \\ 0 & 1 & \cdots & 0 & 0 \\ \vdots & \vdots & \ddots & \vdots & \vdots \\ 0 & 0 & \cdots & 1 & 0 \end{bmatrix} \mathbf{x}(t) + \begin{bmatrix} 1 \\ 0 \\ 0 \\ \vdots \\ 0 \end{bmatrix} \mathbf{u}(t), \tag{A.37}$$

$$\mathbf{y}(t) = \begin{bmatrix} (b_1 - a_1 b_0) & (b_2 - a_2 b_0) & \cdots & (b_n - a_n b_0) \end{bmatrix} \mathbf{x}(t) + [b_0]\mathbf{u}(t), \tag{A.38}$$

---

[8]The `MATLAB` command `bode` plots the magnitude gain and phase shift versus frequency for a linear system

where number of states n is equal to the highest power of the denominator of $G(s)$. The smallest possible dimension for realizing a system, referred to as the minimum realization, is an important factor to consider in analysis and design[9]. Models of minimum order require less computational power in simulation and implementation compared to higher order models. For information about other equivalent canonical state-space forms, refer to ([192], Chapter 4, Sections 3 and 4).

A.4 Experimental Modeling Using Frequency-response

An approach to modeling using experimental frequency-response data is presented in this section. Using a dynamic signal analyzer (DSA), the frequency-response of the dynamics along the x-axis for the piezo-tube actuator was measured[10]. A sinusoidal input voltage $V_x(t)$ with frequency varying between $10\ Hz$ to $6\ kHz$ was generated by a DSA and applied to the scanning probe microscope (SPM) system as shown in Fig. A.3. Using an inductive sensor, the displacement $x_p(t)$ of the piezo-tube along the x-axis was measured and fed back to the DSA to compute the frequency-response (M and ϕ versus frequency ω plots). Figure A.4 shows the Bode plots obtained by the DSA between the applied voltage $V_x(t)$ and the output of the inductive sensor $y(t)$. An estimate of the system model from the frequency-response data was then found with the `MATLAB` software (The `MATLAB` command `invfreqs` gives real numerator and denominator coefficients of experimentally determined frequency response data.). The transfer-function between the applied input voltage $V_x(t)$ and the output of the inductive sensor $y(t)$ was found to be

$$
\begin{aligned}
G_1(s) \;&=\; \frac{Y(s)}{V_x(s)} \\[2mm]
&=\; \frac{\begin{array}{c} 5.544\times10^5 s^4 - 7.528\times10^9 s^3 + 1.476\times10^{15} s^2 \\ -4.571\times10^{18} s + 9.415\times10^{23} \end{array}}{\begin{array}{c} s^6 + 1.255\times10^4 s^5 + 1.632\times10^9 s^4 \\ +1.855\times10^{13} s^3 + 6.5\times10^{17} s^2 + 6.25\times10^{21} s + 1.378\times10^{25} \end{array}}
\end{aligned} \tag{A.39}
$$

with units of $[V/V]$. We scaled Eq. (A.39) by the inductive sensor gain ($30\ Angstroms/V$) and the transfer-function between the applied voltage $V_x(t)$ and the actual displacement of

---

[9]For a detailed discussion of minimal realizations for multi-input multi-output systems, see ([192], Chapter 7).

[10]Stanford Research Systems, model SRS785.
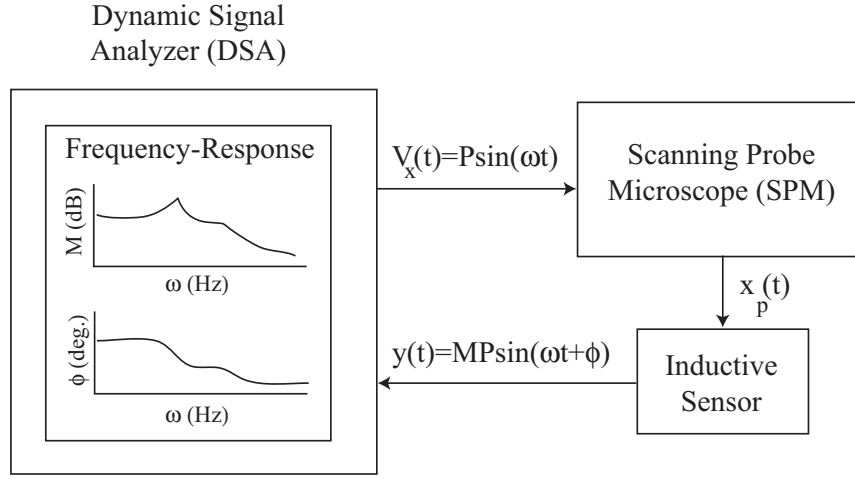
Figure A.3: A schematic of the experimental setup used to determine the frequency-response of the piezo-tube actuator. An inductive sensor measured the displacement of the actuator along the x-axis and the frequency-response data from the DSA was used to estimate the system model.

the piezo-tube $x_p(t)$ is given by

$$G_2(s) \;=\; \frac{X_p(s)}{V_x(s)}$$

$$= \frac{\begin{array}{c} 1.663\times10^7 s^4 - 2.258\times10^{11} s^3 + 4.427\times10^{16} s^2 \\ -1.371\times10^{20} s + 2.2825\times10^{25} \end{array}}{\begin{array}{c} s^6 + 1.255\times10^4 s^5 + 1.632\times10^9 s^4 \\ +1.855\times10^{13} s^3 + 6.5\times10^{17} s^2 + 6.25\times10^{21} s + 1.378\times10^{25} \end{array}} \tag{A.40}$$

with units of $[Angstroms/V]$.

A.4.1   Time Scaling of a Transfer-function Model

We present below an approach for rescaling time for $G_2(s)$ from seconds (s) to milliseconds (ms). We briefly recall the time scaling property of the Laplace transform presented in ([185], Chapter 3, Section 1.4). Let $F(s)$ be the Laplace transform of the function $f(t)$, $i.e.$,

$$f(t) \xrightarrow{\mathcal{L}} F(s), \tag{A.41}$$
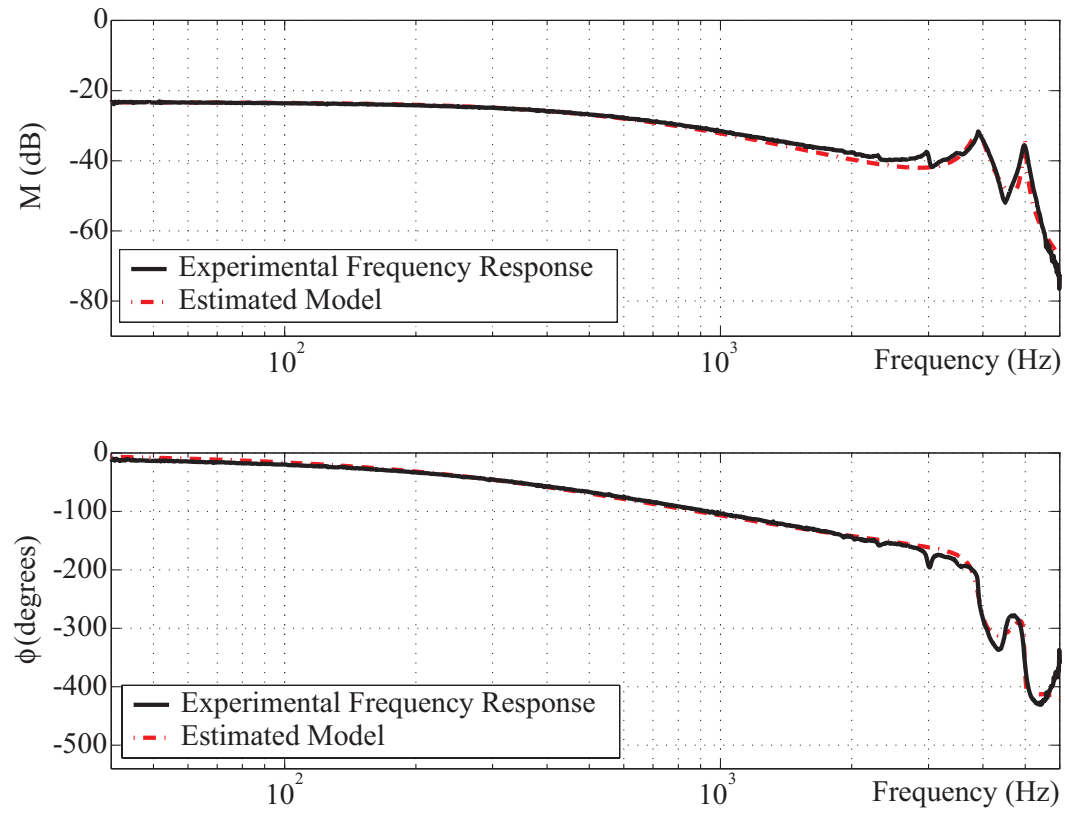
Figure A.4: The experimental magnitude gain and phase versus frequency plots for the piezo-tube actuator (x-axis). Solid line represents experimental data; dashed line represents results from estimated model.

where $\mathcal{L}$ denotes the Laplace transform operator. Now, consider a new time scale defined as $\hat{t} = at$, where a is a constant. The Laplace transform of $f(\hat{t}) = f(at)$ is given by

$$f(\hat{t}) = f(at) \xrightarrow{\mathcal{L}} \frac{1}{|a|} F\left(\frac{s}{a}\right) = \hat{F}(s). \tag{A.42}$$

Using relation (A.42), we can reduce the coefficients of $G_2(s)$ by changing the time units of both the input signal $u(t)$ and output signal $y(t)$ as follows:

$$
\begin{aligned}
\hat{G}(s) &= \frac{\hat{Y}(s)}{\hat{U}(s)} \\
&= \frac{Y(s/a)/|a|}{U(s/a)/|a|} \\
&= \frac{Y(s/a)}{U(s/a)} \\
&= G\left(\frac{s}{a}\right).
\end{aligned}
\tag{A.43}
$$

Therefore, to rescale time for $G_2(s)$ from seconds (s) to millisecond (ms), we choose $\hat{t} = at = 0.001t$ and the new rescaled transfer $\hat{G}_2(s)$ becomes,

$$
\begin{aligned}
\hat{G}_2(s) &= G_2\left(\frac{s}{a}\right)\bigg|_{a=0.001} \\
&= G_2(1000 \cdot s) \\
\hat{G}_2(s) &= \frac{1.663s^4 - 225.8s^3 + 4.427 \times 10^4 s^2 - 1.371 \times 10^5 s + 2.2825 \times 10^7}{\substack{s^6 + 12.55 \times 10^5 s^5 + 1.632 \times 10^3 s^4 + 1.855 \times 10^4 s^3 \\ + 6.5 \times 10^5 s^2 + 6.25 \times 10^6 s + 1.378 \times 10^7}} \tag{A.44}
\end{aligned}
$$

Note that the time unit of the input and output signal of $G_2(s)$ are now in milliseconds. The coefficients of the numerator and denominator polynomials are smaller and this form $(\hat{G}_2(s))$ is less prone to computational errors due to round off than the form $G_2(s)$, Eq. (A.40).

A.4.2   The State-space Model

The state-space realization for $\hat{G}_2(s)$ expressed in controllable canonical form (Eq. (A.37) and (A.38)) is given by the following:

$$\dot{\mathbf{x}}(t) = \begin{bmatrix} -12.55 & -1.632 \times 10^3 & -1.855 \times 10^4 & -6.50 \times 10^5 & -6.25 \times 10^6 & -1.378 \times 10^7 \\ 1 & 0 & 0 & 0 & 0 & 0 \\ 0 & 1 & 0 & 0 & 0 & 0 \\ 0 & 0 & 1 & 0 & 0 & 0 \\ 0 & 0 & 0 & 1 & 0 & 0 \\ 0 & 0 & 0 & 0 & 1 & 0 \end{bmatrix} \mathbf{x}(t)$$

$$+ \begin{bmatrix} 1 \\ 0 \\ 0 \\ 0 \\ 0 \\ 0 \\ 0 \end{bmatrix} \mathbf{u}(t), \tag{A.45}$$

$$y(t) = \begin{bmatrix} 0 & 16.63 & -225.8 & 4.427 \times 10^4 & -1.371 \times 10^5 & 2.825 \times 10^7 \end{bmatrix} \mathbf{x}(t). \tag{A.46}$$

The time unit for Eqs. (A.45) and (A.46) are milliseconds (ms). If the initial state at t_0 is known, along with the applied voltage defined for $t \geq t_0$, then the future behavior of the system, *i.e.*, the state $\mathbf{x}(t)$ and output $y(t)$, can be determined from Eqs. (A.45) and (A.46), respectively.

A.5   Discrete-time State-space Modeling

A.5.1   Introduction

The study of discrete-time systems is important to the analysis and the design of modern mechatronics systems where digital computers or small microprocessors are predominantly used to control systems. Digital computers and microprocessors output or acquire information at discrete time instants. For example, the input applied by a digital computer to actuate the piezo-tube changes at discrete time instants. Similarly, the displacement of the piezo-tube can only be measured at specified time instants using digital computers;
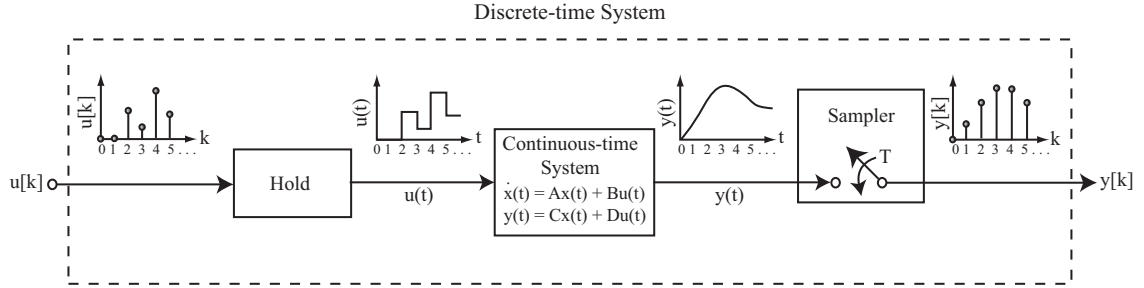
Figure A.5: A block diagram of a discrete-time system showing signals in graphic form. Note that $u[k] = u(k \cdot T)$ and $y[k] = y(k \cdot T)$, for $k = 0, 1, 2, \cdots$, and the sampling period T is assumed to be constant.

therefore in comparison to a continuous-time control system where the input signals change continuously over time, the input of a discrete-time system changes once in a while. Such discrete-time systems are studied next.

Consider a continuous-time system with continuous input $u(t)$ and output $y(t)$ as described by Eqs. (A.12) and (A.13). Let a digital computer or microprocessor be used to provide the input $u[k]$ and measure the output $y[k]$ as depicted in Fig. A.5 (such systems with continuous and discrete signals are called sampled-data systems). The input $u[k]$ and output $y[k]$ of this system are discrete with $u[k] = u(k \cdot T)$ and $y[k] = y(k \cdot T)$ for $k = 0, 1, 2, \cdots$, where T is the constant sampling period. The discrete input $u[k]$ is applied to the continuous system from a digital computer or microprocessor and is held constant during the time interval T (zero-order hold). A sampler acquires the output of the continuous system at each time instant T yielding the discrete output $y[k]$. The discrete system is between the input $u[k]$ and the output $y[k]$ ([195], Chapter 1) (We do not discuss quantizing and quantization error. See ([195], Chapter 1, Section 3) for details). The equivalent discrete-time state-space representation of the continuous-time state-space model given by Eqs. (A.12) and (A.13) is given by (the details of the formulation can be found in [195], Chapter 5, Section 5.)

$$x[k+1] \quad = \quad A_D x[k] + B_D u[k], \qquad (A.47)$$

$$y[k] \quad = \quad C_D x[k] + D_D u[k], \qquad (A.48)$$

where

$$A_D = e^{AT}, \ B_D = \left(\int_0^T e^{A\lambda} d\lambda \right) B, \ C_D = C, \text{ and } D_D = D, \tag{A.49}$$

and matrices C_D and D_D are not changed by the sampling (Given a continuous-time state space model (A,B,C,D), the MATLAB command c2d, gives the discrete time equivalent for a specified sampling period T.). This discrete model (Eqs. (A.47) and (A.48)) is the representation of the sampled-data system shown in Fig. A.5.

A.5.2   Solutions to the Discrete-time State-space Equations

The solution to the discrete model (equations (47) and (48)) is given by

$$x[k] \ = \ A_D^k x[0] + \sum_{j=0}^{k-1} A_D^{k-j-1} B_D u[j], \tag{A.50}$$

$$y[k] \ = \ CA_D^k x[0] + C \sum_{j=0}^{k-1} A_D^{k-j-1} B_D u[j] + Du[k], \tag{A.51}$$

respectively, for each sampling step k. Details of the formulation can be found in [195], Chapter 5, Section 3. The state response $x[k]$ to an applied input $u[k]$ is characterized by the system matrices (A_D,B_D,C_D,D_D). In particular, the output $y[k]$ will be bounded for any bounded input $u[k]$ if the system is stable. A system in the form given by Eq. (A.47) is stable if the magnitude of all the eigenvalues of A_D are less than unity, *i.e.*, the eigenvalues lie within the unit circle center at the origin of the z-plane ([195], Chapter 5, Section 6).

A.5.3   The Z-transform and Relationship with the State-space

The input-to-output relationship in the frequency-domain for a discrete-time system is represented by a discrete transfer-function called the z-transform, written in terms of the variable z ([185], Chapter 4). Analogous to the continuous-time case, the model of a dynamic system in discrete transfer-function form can be useful in the design and control of systems ([185], Chapter 7). If the system model is available in discrete transfer-function form, then a state-space realization can be found as follows. Given a discrete system described by the

following z-transform $G(z)$,

$$G(z) = \frac{d_0 + d_1 z^{-1} + \cdots + d_n z^{-n}}{1 + c_1 z^{-1} + \cdots + c_n z^{-n}},\tag{A.52}$$

the controllable canonical state-space realization for $G(z)$ is

$$x[k+1] = \begin{bmatrix} -c_1 & -c_2 & \cdots & -c_{n-1} & -c_n \\ 1 & 0 & \cdots & 0 & 0 \\ 0 & 1 & \cdots & 0 & 0 \\ \vdots & \vdots & \ddots & \vdots & \vdots \\ 0 & 0 & \cdots & 1 & 0 \end{bmatrix} x[k] + \begin{bmatrix} 1 & 0 & 0 & \vdots & 0 \end{bmatrix} u[k],\tag{A.53}$$

$$y[k] = \begin{bmatrix} (d_1 - c_1 d_0) & (d_2 - c_2 d_0) & \cdots & (d_n - c_n d_0) \end{bmatrix} x[k] + [d_0] u[k].\tag{A.54}$$

The number of states n is equivalent to the highest power of the denominator of $G(z)$. For information about other equivalent canonical state-space forms, refer to [195], Chapter 5, Section 2.

Example Consider the continuous-time state-space model of the piezo-tube system described by Eqs. (A.45) and (A.46). A digital computer with the sampling rate of 10 kHz ($T = 1.0 \times 10^{-4}$) is used to provide the control input $u[k]$ and measure its displacement along the x-axis (output $y[k]$). The discrete-time state-space model with (A_D, B_D, C_D, and D_D) given by Eq. (A.49) is

182

$$x[k+1] =$$

$$\begin{bmatrix}
0.999 & -0.163 & -1.85 & -65.0 & -624.5 & -1377.1 \\
9.99 \times 10^{-5} & 0.999 & -9.26 \times 10^{-5} & -3.25 \times 10^{-3} & -3.12 \times 10^{-2} & -6.69 \times 10^{-2} \\
5.00 \times 10^{-9} & 1.00 \times 10^{-4} & 1 & -1.08 \times 10^{-7} & -1.04 \times 10^{-6} & -2.30 \times 10^{-6} \\
1.67 \times 10^{-13} & 5.00 \times 10^{-9} & 1.00 \times 10^{-4} & 1 & -2.60 \times 10^{-11} & -5.74 \times 10^{-11} \\
4.17 \times 10^{-18} & 1.67 \times 10^{-13} & 5.00 \times 10^{-9} & 1.00 \times 10^{-4} & 1 & -1.15 \times 10^{-15} \\
8.33 \times 10^{-23} & 4.17 \times 10^{-18} & 1.67 \times 10^{-13} & 5.00 \times 10^{-9} & 1.00 \times 10^{-4} & 1
\end{bmatrix}$$

$$+ \begin{bmatrix}
9.99 \times 10^{-5} \\
4.99 \times 10^{-9} \\
1.67 \times 10^{-13} \\
4.17 \times 10^{-18} \\
8.33 \times 10^{-23} \\
1.39 \times 10^{-27}
\end{bmatrix} u[k], \tag{A.55}$$

$$y[k] = \begin{bmatrix} 0 & 16.63 & -225.8 & 4.427 \times 10^4 & -1.37^5 & 2.825 \times 10^7 \end{bmatrix} x[k]. \tag{A.56}$$

The realization given by Eqs. (A.55) and (A.56) was found using the `MATLAB` command
`c2d`.

A.6 Summary

We presented tools for modeling continuous- and discrete-time systems using the state-space approach in this chapter. The state-space approach to modeling is a powerful technique for the analysis and design of mechatronics and dynamic systems and can take advantage of tools available in modern digital computers and microprocessors. The discussion of the system states and the state-space was motivated by an example piezo-tube actuator system. We considered the modeling of linear systems and briefly introduced a technique for linearizing nonlinear systems. The frequency-response of a system and an approach to modeling using experimental frequency-response data was presented. Relationships between models expressed in the frequency- and time-domain for both continuous- and discrete-time systems was discussed. For additional details about the concepts mentioned in this chapter the reader is referred to the attached references.

Appendix B

CIRCUIT DIAGRAMS

This chapter describes the electronic circuits used in the experiments discussed in Chapters 3 and 6; it includes: circuit diagrams, relevant equations and component description.

B.1 The Design of Notch Filters for Improving the Gain Margin of High Quality Factor Systems

This section discusses the design of the notch filter $D(s)$ used in Chapter 3 to improve the gain margin of the piezo-positioning system (high quality factor system).

For systems with low gain margin, *i.e.*, high quality factor Q_f systems, large feedback gains tends to destabilize the system. Furthermore, such low gains do not provide significant improvement in tracking performance when feedback is used. In order to improve the performance of such feedback controlled systems, a notch filter can designed that cascades with the plant (as shown in Fig. B.1) to improve the gain margin, thereby, improving the performance of the feedback controlled system. In Fig. B.1 $C(s)$ is the feedback controller, $D(s)$ represents the notch filter to be designed, and $G(s)$ is the plant transfer function. As
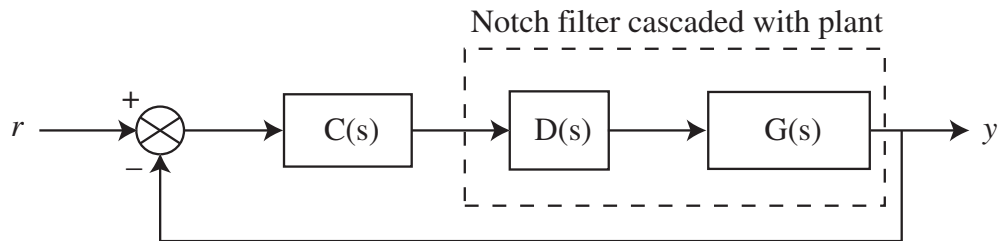
Figure B.1: A feedback controlled system with a notch filter $D(s)$ cascaded with plant $G(s)$ to improve gain margin. The feedback controller is represented by $C(s)$.

described in Chapter 3, the dynamics that make up the notch filter $D(s)$ is chosen such that its zeros cancel the effect of the sharp resonant peak of $G(s)$ (*i.e.*, dominating poles). From Chapter 3, the equation of the notch filter $D(s)$ is:

$$D(s) = k_n \frac{(s - 2\pi z_1)(s - 2\pi z_2)}{(s - 2\pi p_1)(s - 2\pi p_2)} \triangleq k_n \frac{s^2 + a_1 s + a_0}{s^2 + b_1 s + b_0}, \tag{B.1}$$

where the zeros $z_{1,2}$ were selected to coincided with the resonant poles (peaks) of $G(s)$. The poles of $D(s)$ were added to improve the low frequency gain of the notch filter and to attenuate high frequency noise. Previous work that use this technique to minimize the effect of sharp resonant peaks can be found in [39, 38]. In choosing $z_{1,2}$, one needs to pay close attention to the possibility that exact pole/zero cancelation in practice is very challenging, if not impossible. For example, small changes in the location of the resonant poles of $G(s)$ may be possible for a real system. Furthermore, realizing a notch filter such that its zeros exactly cancel the effect of the resonant poles of $G(s)$ is also very challenging, if not impossible. Because of these uncertainties, though they may be small, the best choice for $z_{1,2}$ is to place them slightly before the nominal location of the resonant poles of $G(s)$. By doing so, any small variation in the poles of $G(s)$ will not significantly alter the gain margin of the composite system (*i.e.*, gain margin of $D(s)G(s)$), and hence reduces the sensitivity of the composite system's gain margin to variations of the zeros of $D(s)$ or resonant poles of $G(s)$. Consequently, this helps to reduce the possibility of large variations in the gain margin jeopardizing the stability of the closed-loop system.

By placing the zeros of $D(s)$ before, as opposed to behind, the frequency at which the resonant peak occurs is further justified by the fact that the gain margin is determined at the -180 *degrees* crossing in the phase versus frequency plot of $G(s)$. Consider, for example, a system $G(s)$ with a sharp resonant peak located at some $\hat{\omega}$. The drop in phase in $G(s)$ around $\hat{\omega}$ happens rather quickly, say within some small neighborhood of $\hat{\omega}$. Additionally, the drop in phase (for two-poles) is -180 *degrees*, and at the -180 *degrees* crossing, the gain margin of $G(s)$ is measured below (or above) the 0 *dB* mark (*e.g.*, see [185]). Therefore, it is important to ensure that any slight variations in the frequency of the resonant pole does not significantly alter the gain margin of the composite system when $D(s)$ is added. One way to avoid this behavior is to place the zeros of $D(s)$ slightly before the frequency
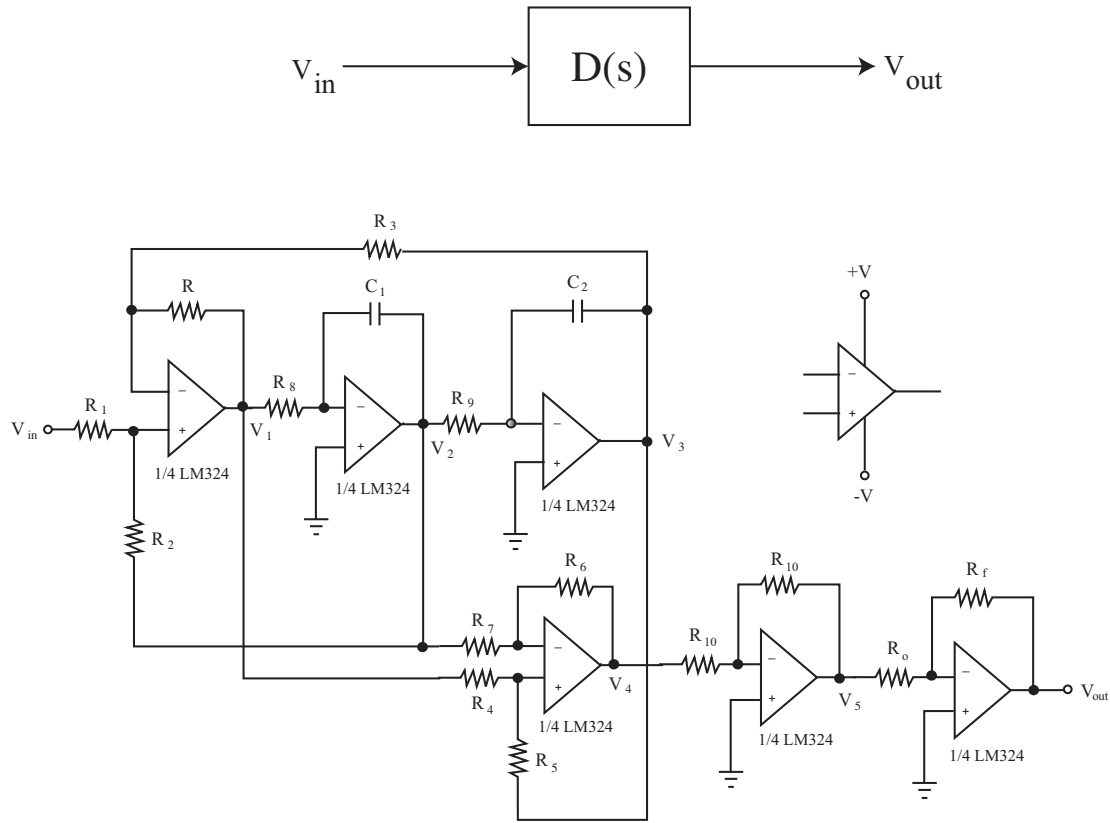
Figure B.2: Circuit diagram for notch filter. The integrated circuit component LM324 is a quad-operational amplifier chip.

where the resonant poles of $G(s)$ occur. By doing so, the zeros of $D(s)$ provides sufficient phase increase before the drop in phase caused by the resonant poles of $G(s)$, therefore postponing the -180 *degrees* crossing of the composite-system's phase higher frequencies, therefore ensuring adequate gain margin and reducing gain margin sensitivity.

The second order notch filter $D(s)$ given by Eq. (B.1) can be realized with analog op-amp circuits and a circuit diagram is shown in Fig. B.2 (or detailed description found in [119], pp. 394-399). The transfer function, in terms of resistor and capacitor component values, is obtained as follows. In the circuit diagram (Fig. B.2), the notch filter consists of basically an interconnection of five secondary building blocks—two summer, two integrator, and two amplifier circuits. Starting from left to right, the output of the first summer circuit in the

Laplace domain is

$$V_1(s) = \frac{R_2(R + R_3)V_{in}(s) + R_1(R + R_3)V_2(s) - R(R_1 + R_2)V_3(s)}{R_3(R_1 + R_2)}. \tag{B.2}$$

The output of the two integrators are:

$$V_2(s) = -\frac{1}{C_1 R_8 s}V_1(s), \tag{B.3}$$

$$V_3(s) = -\frac{1}{C_2 R_9 s}V_2(s). \tag{B.4}$$

Combining Eqs. (B.2), (B.3), and (B.4), we get the following transfer functions for three of the five secondary building blocks:

$$\frac{V_1(s)}{V_{in}(s)} = \frac{R_2(R + R_3)}{R_3(R_1 + R_2)} \frac{-C_2 R_9 s}{C_1 C_2 R_8 R_9 s^2 + \frac{R_1(R+R_3)}{R_3(R_1+R_2)}C_2 R_9 s + \frac{R}{R_3}}, \tag{B.5}$$

$$\frac{V_2(s)}{V_{in}(s)} = \frac{R_2(R + R_3)}{R_3(R_1 + R_2)} \frac{C_1 C_2 R_8 R_9 s^2}{C_1 C_2 R_8 R_9 s^2 + \frac{R_1(R+R_3)}{R_3(R_1+R_2)}C_2 R_9 s + \frac{R}{R_3}}, \tag{B.6}$$

$$\frac{V_3(s)}{V_{in}(s)} = \frac{R_2(R + R_3)}{R_3(R_1 + R_2)} \frac{1}{C_1 C_2 R_8 R_9 s^2 + \frac{R_1(R+R_3)}{R_3(R_1+R_2)}C_2 R_9 s + \frac{R}{R_3}}. \tag{B.7}$$

Finally, the two remaining amplifier circuits yield:

$$V_{out}(s) = \frac{R_f}{R_o}V_4(s). \tag{B.8}$$

Now, the output V_4 is the weighted sum of V_1, V_2, and V_3, and since V_{out} is related to V_4 by Eq. (B.8), the transfer function from the input V_{in} to the output V_{out} is given by:

$$
\begin{aligned}
\frac{V_{out}(s)}{V_{in}(s)} &= \frac{R_f}{R_o}\left[\left(\frac{R_5(R_6 + R_7)}{R_7(R_4 + R_5)}\right)\frac{V_1(s)}{V_{in}(s)} - \frac{R_6}{R_7}\frac{V_2(s)}{V_{in}(s)} + \left(\frac{R_4(R_6 + R_7)}{R_7(R_4 + R_5)}\right)\frac{V_3(s)}{V_{in}(s)}\right], \\
&= \frac{R_f}{R_o}\left[\frac{R_2 R_5(R + R_3)(R_6 + R_7)}{R_3 R_7(R_1 + R_2)(R_4 + R_5)}\right]\frac{C_1 C_2 R_8 R_9 s^2 + \frac{(R_4+R_5)}{(R_6+R_7)}\frac{R_6 R_9 C_2}{R_5}s + \frac{R_4}{R_5}}{C_1 C_2 R_8 R_9 s^2 + \frac{R_1(R+R_3)}{R_3(R_1+R_2)}C_2 R_9 s + \frac{R}{R_3}}, \\
&= \frac{R_f}{R_o}\left[\frac{R_2 R_5(R + R_3)(R_6 + R_7)}{R_3 R_7(R_1 + R_2)(R_4 + R_5)}\right]\frac{s^2 + \frac{R_6(R_4+R_5)}{C_1 R_5 R_8(R_6+R_7)}s + \frac{R_4}{C_1 C_2 R_5 R_8 R_9}}{s^2 + \frac{R_1(R+R_3)}{C_1 R_3 R_8(R_1+R_2)}s + \frac{R}{C_1 C_2 R_3 R_8 R_9}}, \\
&\triangleq K_1 K_2 \frac{s^2 + a_1 s + a_0}{s^2 + b_1 s + b_0}, \tag{B.9}
\end{aligned}
$$

where

$$a_1 = \frac{R_6(R_4 + R_5)}{C_1 R_5 R_8 (R_6 + R_7)}, \tag{B.10}$$

$$a_0 = \frac{R_4}{C_1 C_2 R_5 R_8 R_9}, \tag{B.11}$$

$$b_1 = \frac{R_1(R + R_3)}{C_1 R_3 R_8 (R_1 + R_2)}, \tag{B.12}$$

$$b_0 = \frac{R}{C_1 C_2 R_3 R_8 R_9}, \tag{B.13}$$

$$K_1 = \frac{R_f}{R_o}, \tag{B.14}$$

$$K_2 = \frac{R_2 R_5 (R + R_3)(R_6 + R_7)}{R_3 R_7 (R_1 + R_2)(R_4 + R_5)}. \tag{B.15}$$

By equating the desired $D(s)$ (Eq. (B.1)) with Eq. (B.9), the zeros, poles, and gain k_n of $D(s)$ can be related to resistor and capacitor component values (Eqs. (B.10)–(B.15)) for realizing the notch filter.

Remark 3 *If the output is V_1 (Eq. (B.5)), then the circuit behaves as a high-pass filter; if the output is V_2 (Eq. (B.6)), then we have a band-pass; and finally, if the output is V_3 (Eq. (B.5)), then the circuit is a low-pass filter.*

B.1.1   Example Notch Filter Realization

In the following, we find the capacitor and resistor component values for realizing the notch filter $D(s)$ (in Chapter 3) given by

$$D(s) = k_D \frac{(s - 2\pi z_1)(s - 2\pi z_2)}{(s - 2\pi p_1)(s - 2\pi p_2)}, \tag{B.16}$$

where $k_D = 2.22$, $z_1 = -5 + j475 \ Hz$, $z_2 = -5 - j475 \ Hz$, $p_1 = -100 \ Hz$, and $p_2 = -5000$ Hz. Substituting in values, we rewrite $D(s)$ in a more convenient form to get

$$D(s) = 2.22 \frac{s^2 + 62.83s + 8.908 \times 10^6}{s^2 + 3.204^4 s + 1.974 \times 10^7}. \tag{B.17}$$

Equating the appropriate coefficients in $D(s)$ with the Eqs. (B.10)–(B.15), we find that

$$a_1 = 62.83 = \frac{R_6(R_4 + R_5)}{C_1 R_5 R_8(R_6 + R_7)}, \tag{B.18}$$

$$a_0 = 8.908 \times 10^6 = \frac{R_4}{C_1 C_2 R_5 R_8 R_9}, \tag{B.19}$$

$$b_1 = 3.204^4 = \frac{R_1(R + R_3)}{C_1 R_3 R_8(R_1 + R_2)}, \tag{B.20}$$

$$b_0 = 1.974 \times 10^7 = \frac{R}{C_1 C_2 R_3 R_8 R_9}, \tag{B.21}$$

$$K_1 K_2 = 2.22 = \frac{R_f}{R_o} \frac{R_2 R_5(R + R_3)(R_6 + R_7)}{R_3 R_7(R_1 + R_2)(R_4 + R_5)}. \tag{B.22}$$

Picking $C_1 = 0.1~\mu F$, $C_2 = 0.1~\mu F$, $R = 10~k\Omega$, $R_2 = 10~k\Omega$, $R_4 = 2.2~k\Omega$, $R_5 = 56~k\Omega$, $R_6 = 1~k\Omega$, $R_8 = 2.2~k\Omega$, and $R_o = 4.7~k\Omega$, we solve for the remaining resistor values to get:

$$R_7 = \frac{R_6(R_4 + R_5)}{a_1 C_1 R_5 R_8} - R_6 = 356~k\Omega, \tag{B.23}$$

$$R_9 = \frac{R_4}{a_0 C_1 C_2 R_5 R_8} = 20~k\Omega, \tag{B.24}$$

$$R_3 = \frac{a_0 R R_5}{b_0 R_4} = 1.15~k\Omega, \tag{B.25}$$

$$R_1 = \frac{a_0 b_1 C_1 R_2 R_5 R_8}{b_0 R_4 + a_0 R_5 - b_1 a_0 C_1 R_5 R_8} = 26.6~k\Omega, \tag{B.26}$$

$$K_2 = \frac{R_2 R_5(R + R_3)(R_6 + R_7)}{R_3 R_7(R_1 + R_2)(R_4 + R_5)} = 0.54, \tag{B.27}$$

$$K_1 = 2.22/K_2 = 4.11, \tag{B.28}$$

$$R_f = R_o K_1 = 19.3~k\Omega, \tag{B.29}$$

Using the capacitor and resistor values, the circuit shown in Fig. B.2 can be realized for $D(s)$ (For sample MATLAB code of realizing capacitor and resistor values for $D(s)$, refer to Appendix E, Section E.1.1). The frequency response for such a circuit is shown in Chapter 3, Fig. 3.3. In the figure, the measured frequency response of the experimental piezoactuator system is depicted by the dashed line, the notch filter is shown as the dotted line, and the notch filter cascaded with the experimental system is represented by the solid line. The measured gain margin of the original system is $-17.05~dB$, whereas, the gain margin of the composite system is improved to $30.86~dB$ using the notch filter.

B.2   Analog High-gain Feedback Controller Circuit

The analog high-gain feedback controller and signal condition circuit used in Chapters 3 and 6 are shown in Figs. B.3, B.4 and B.5. Figure B.3 show the block diagram of feedback and feedforward controller. The circuit diagram for each of the blocks in this figure are shown in Figs. B.4 and B.5. The transfer function for the proportional-derivative (PD) controller is given by:

$$
\begin{aligned}
\frac{u(s)}{e(s)} &= \frac{R_p}{10\ K\Omega} + \frac{R_D}{1\ K\Omega} \cdot \frac{1}{RC} \cdot \frac{s}{(s+1/RC)^2}, \\
&\triangleq K_p + K_D \frac{s}{(s+a)^2}.
\end{aligned}
\tag{B.30}
$$
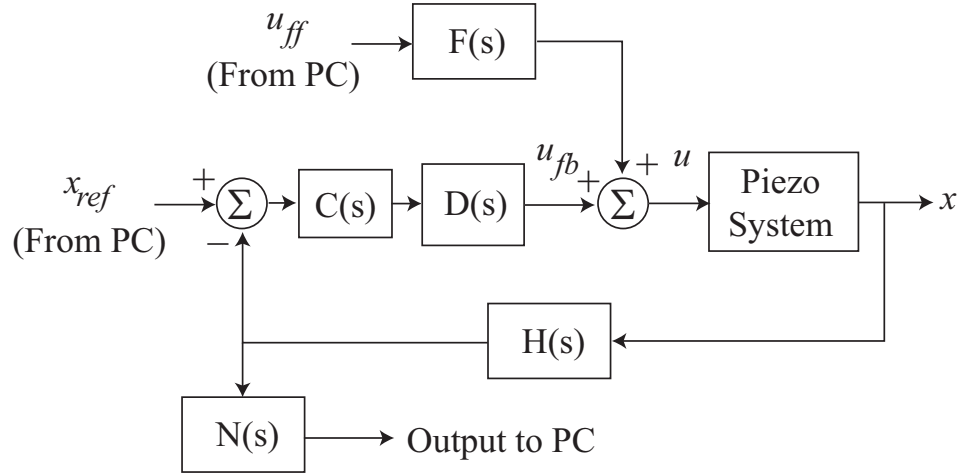
Figure B.3: Block diagram of feedback and feedforward controller.

Figure B.4: Feedback and feedforward controller circuit diagram.

Proportional controller, C(s)

Proportional-derivative controller, C(s)
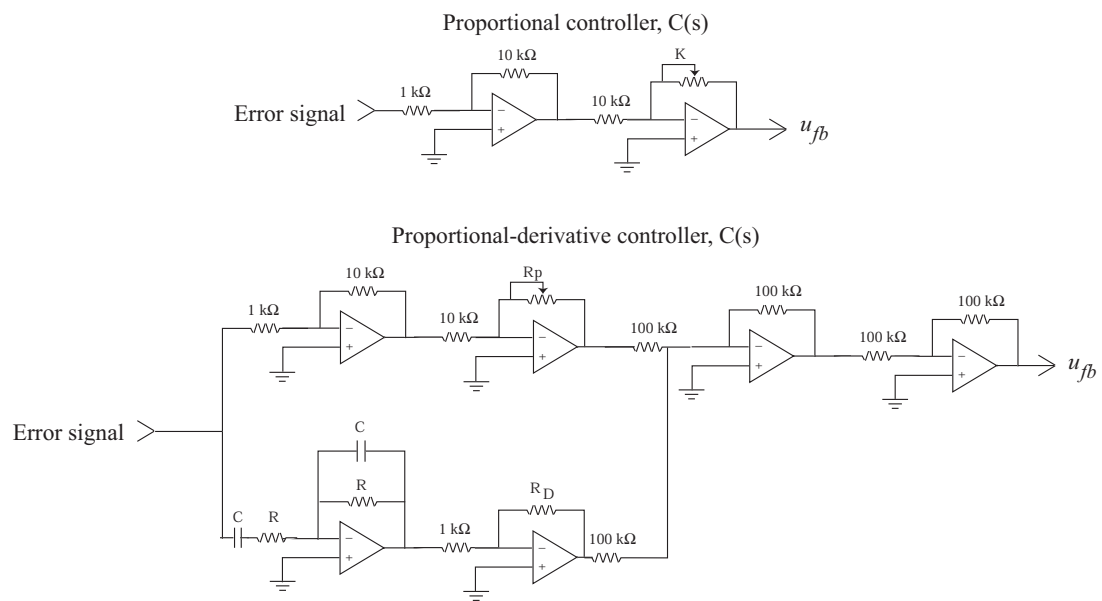
Figure B.5: Proportional and proportional-derivative controller.

Appendix C

MISCELLANEOUS ANALYSIS

C.1 Designing ILCA for Hysteretic Systems

The objective of iterative learning control is to find an input sequence $u_k(t)$, for $t \in [t_0, T]$, such that when the input sequence is successively applied to a system, the system's output converges uniformly to a desired trajectory $y_d(t)$ on $t \in [t_0, T]$. In order to design an effective ILC algorithm, the characteristics of the system must be taken into account. In this section, we describe the design of an ILCA for hysteretic systems. We start with the system inversion concept for linear systems and then discuss the generalization of Arimoto *et al.*'s [158] work on ILC. The results will be used to design a suitable ILC algorithm for hysteretic systems.

C.1.1 Review of System Inversion

Consider the linear time-invariant (LTI) single-input single-output (SISO) system with the following state-space representation:

$$\dot{\mathbf{x}}(t) = A\mathbf{x}(t) + Bu(t), \tag{C.1}$$

$$y(t) = C\mathbf{x}(t), \tag{C.2}$$

where $x \in \mathbb{R}^n$, and $u, y \in \mathbb{R}$. Differentiate the output until the input appears explicitly

$$\dot{y}(t) = C\dot{\mathbf{x}}(t)$$

$$\dot{y}(t) = CA\mathbf{x}(t) + CBu(t). \tag{C.3}$$

If $CB = 0$, then differentiate until the output appears and in general for a system with relative degree r, the input appears explicitly after differentiating the output r-times, *i.e.*,

$$y^{(r)}(t) = CA^r\mathbf{x}(t) + CA^{r-1}Bu(t). \tag{C.4}$$

Since $CA^{r-1}B \neq 0$, we can solve for the input directly to obtain

$$u(t) = [CA^{r-1}B]^{-1}(y^r(t) - CA^r\mathbf{x}(t)). \tag{C.5}$$

This approach to find an input to track a desired trajectory is known as the system inversion technique [14, 16].

C.1.2 Generalization of Arimoto et al.'s Work

We begin with some definitions. The *norm* $||\mathbf{z}||$ of a vector $\mathbf{z}$ is a real-valued function with the following properties:

   i. $||\mathbf{z}|| \geq 0$ for all $\mathbf{z} \in V$ and $||\mathbf{z}|| = 0$ if and only if $\mathbf{z} = 0$,

   ii. $||c\mathbf{z}|| = |c| \cdot ||\mathbf{z}||$ for any $\mathbf{z} \in V$ and any $c \in \mathbb{R}$, and

   iii. $||\mathbf{z} + \mathbf{w}|| \leq ||\mathbf{z}|| + ||\mathbf{w}||$ for any $\mathbf{z}$, $\mathbf{w} \in V$.

The following vector or matrix norm and function norm of the vector-valued function $\mathbf{z}(\cdot)$ defined on $[t_0, T]$ are used in the analysis of the iterative learning control process:

$$||\mathbf{z}(t)||_\infty = \max_{1 \leq i \leq q} |z_i(t)|, \tag{C.6}$$

$$||M||_\infty = \max_{1 \leq i \leq q} \left\{ \sum_{j=1}^{q} |m_{ij}| \right\}, \tag{C.7}$$

$$||\mathbf{z}(\cdot)||_\lambda = \sup_{t_0 \leq t \leq T} \left\{ e^{-\lambda t} ||\mathbf{z}(t)||_\infty \right\}, \tag{C.8}$$

where M is an $q \times q$ matrix with entries m_{ij}.

The formal definition of the λ-norm for a function $f : [t_0, T] \rightarrow \mathbb{R}^n$ is given by [17, 196]

$$||f(\cdot)||_\lambda \triangleq \sup_{t \in [t_0, T]} \left\{ e^{-\lambda t} ||f(t)||_\infty \right\}. \tag{C.9}$$

Arimoto *et al.* [17] showed that for a linear time-invariant system of the form:

$$\dot{\mathbf{x}}(t) = A\mathbf{x}(t) + B\mathbf{u}(t), \tag{C.10}$$

$$\mathbf{y}(t) = C\mathbf{x}(t), \tag{C.11}$$

which satisfies certain conditions, the iterative learning control law given by

$$u_{k+1}(t) = u_k(t) + \Gamma[\dot{y}_d(t) - \dot{y}_k(t)], \tag{C.12}$$

converges provided that

$$||I - CB\Gamma||_\infty < 1, \tag{C.13}$$

where $||\mathbf{z}||_\infty$ is the standard infinity norm of a vector $\mathbf{z}$. In the condition (C.13), a constant Γ exists that satisfies the inequality provided the matrix CB has full rank. For a relative degree one system ($CB \neq 0$), this condition is easily met. Additionally, Arimoto *et al.*'s analysis assumes that the sign of the product CB must be known, that is, for a fixed Γ, information about how the input affects the output is required in order to satisfy condition (C.13). Likewise, the work of Moore [165] concludes that for a linear system of the form $y = T_s u$, the input update law given by

$$u_{k+1} = T_u u_k + T_e(y_d - y_k), \tag{C.14}$$

where T_u and T_e are both casual operators, converges if

$$||T_u - T_e T_s||_i < 1. \tag{C.15}$$

For simplicity, assuming that $T_e = I$ and for a fixed $T_e = constant$, condition (C.15) is satisfied provided the phase of T_s is known. This can be interpreted as knowing the direction to apply the input to reduce the tracking error for the next iteration, a concept similar to Arimoto *et al.*'s assumption for the sign of the CB term. As long as the input is pointed away from the direction of increasing error, the input update law will converge. Motivated by this observation, iterative learning control for Preisach-type hysteretic systems is developed by taking advantage of the concept of *direction*. To begin, we discuss in the following the generalization of Arimoto *et al.*'s work to a linear system with r relative degree and then make connections with ILC for hysteretic systems.

Consider the linear time-invariant (LTI) single-input single-output (SISO) system with the following state-space representation:

$$\dot{x}(t) = Ax(t) + Bu(t), \tag{C.16}$$

$$y(t) = Cx(t), \tag{C.17}$$

where $x \in \mathbb{R}^n$, and $u, y \in \mathbb{R}$. We assume the following for the linear system:

1a. The linear system has a well defined relative degree r.

2a. The first $r - 1$ derivatives of the output satisfies

$$
\begin{aligned}
y_k(t_0) &= y_d(t_0), \\
\dot{y}_k(t_0) &= \dot{y}_d(t_0), \\
\vdots &= \vdots \\
y_k^{(r-2)}(t_0) &= y_d^{(r-2)}(t_0), \\
y_k^{(r-1)}(t_0) &= y_d^{(r-1)}(t_0),
\end{aligned}
$$

for $k = 0, 1, 2, \cdots$.

3a. The input $u_0 \in C^0([t_0, T])$ and $y_d \in C^{(r)}([t_0, T])$.

Consider the input update law of the form

$$
u_{k+1}(t) = u_k(t) + \rho e_k^{(r)}(t) \tag{C.18}
$$

where $e(t) \triangleq y_d(t) - y_k(t)$, and $e^{(r)}(t) \triangleq \frac{d^r}{dt^r}[e(t)]$.

Theorem 3 *Suppose the linear system satisfies Assumptions 1a, 2a, and 3a. Let $x_k(t_0) = x_d(t_0)$ for all $k \in \mathbb{N}$. If*

$$
||I - CA^{r-1}B\rho||_\infty \leq \gamma < 1, \tag{C.19}
$$

then the input update law given by Eq. (C.18) will generate a sequence of inputs, $u_k(t)$, $t \in [t_0, T]$, such that

$$
u_k(t) \to u_d(t), \tag{C.20}
$$

for all $t \in [t_0, T]$, uniformly in t. Furthermore, the sequence $y_k(t)$, $t \in [t_0, T]$, generated by these controls is such that

$$
y_k(t) \to y_d(t), \tag{C.21}
$$

for all $t \in [t_0, T]$, uniformly in t.

Proof

It follows from the definition of the error $e(t)$ that

$$e_{k+1}^{(r)}(t) = y_d^{(r)}(t) - y_{k+1}^{(r)}(t). \tag{C.22}$$

By the relative degree assumption, we have that

$$y^{(r)}(t) = CA^r x(t) + CA^{r-1} Bu(t); \quad CA^{r-1}B \neq 0, \tag{C.23}$$

and substituting this into Eq. (C.22) along with the solution to the state $x(t)$, we obtain

$$e_{k+1}^{(r)}(t) = y_d^{(r)}(t) - \left[CA^r e^{At} x_{k+1}(t_0) + \int_{t_0}^{t} CA^r e^{A(t-\tau)} Bu_{k+1}(\tau)d\tau + CA^{r-1} Bu_{k+1}(t) \right]. \tag{C.24}$$

Next, we substitute the input update law Eq. (C.18) into the above expression to obtain,

$$
\begin{aligned}
e_{k+1}^{(r)}(t) &= y_d^{(r)}(t) - \left[CA^r e^{At} x_{k+1}(t_0) + \int_{t_0}^{t} CA^r e^{A(t-\tau)} Bu_k(\tau)d\tau \right. \\
&\quad \left. + CA^{r-1} Bu_k(t) + CA^{r-1} B\rho e_k^{(r)}(t) + \int_{t_0}^{t} CA^r e^{A(t-\tau)} Be_k^{(r)}(\tau)d\tau \right], \\
&= y_d^{(r)}(t) - y_k^{(r)}(t) - CA^{r-1} B\rho e_k^{(r)}(t) - \int_{t_0}^{t} CA^r e^{A(t-\tau)} Be_k^{(r)}(\tau)d\tau, \\
&= [1 - CA^{r-1} B\rho] e_k^{(r)}(t) - \int_{t_0}^{t} CA^r e^{A(t-\tau)} Be_k^{(r)}(\tau)d\tau. \tag{C.25}
\end{aligned}
$$

Now, we take the vector ∞-norm of both sides to get

$$
\begin{aligned}
\left\| e_{k+1}^{(r)}(t) \right\|_\infty &= \left\| [1 - CA^{r-1} B\rho] e_k^{(r)}(t) - \int_{t_0}^{t} CA^r e^{A(t-\tau)} Be_k^{(r)}(\tau)d\tau \right\|_\infty, \\
&\leq \left\| [1 - CA^{r-1} B\rho] \right\|_\infty \left\| e_k^{(r)}(t) \right\|_\infty + \int_{t_0}^{t} \left\| CA^r e^{A(t-\tau)} B \right\|_\infty \left\| e_k^{(r)}(\tau) \right\|_\infty d\tau. \tag{C.26}
\end{aligned}
$$

Next, we multiply both sides by $e^{-\lambda t}$, *i.e.*,

$$
\begin{aligned}
e^{-\lambda t}\left\|e_{k+1}^{(r)}(t)\right\|_{\infty} &\leq \left\|[1-CA^{r-1}B\rho]\right\|_{\infty} e^{-\lambda t}\left\|e_{k}^{(r)}(t)\right\|_{\infty} \\
&\quad + \int_{t_0}^{t}\left\|CA^r e^{A(t-\tau)}B\right\|_{\infty} e^{-\lambda(t-\tau)}e^{-\lambda\tau}\left\|e_{k}^{(r)}(\tau)\right\|_{\infty} d\tau, \\
&\leq \left\|[1-CA^{r-1}B\rho]\right\|_{\infty} e^{-\lambda t}\left\|e_{k}^{(r)}(t)\right\|_{\infty} \\
&\quad + \sup_{t_0\leq t\leq T}\left\{\left\|CA^r e^{At}B\right\|_{\infty}\right\}\sup_{t_0\leq t\leq T}\left\{e^{-\lambda t}\left\|e_{k}^{(r)}(t)\right\|_{\infty}\right\}\int_{t_0}^{t} e^{-\lambda(t-\tau)}d\tau, \\
&\leq \left\|[1-CA^{r-1}B\rho]\right\|_{\infty} e^{-\lambda t}\left\|e_{k}^{(r)}(t)\right\|_{\infty} + h_0\left\|e_{k}^{(r)}(\cdot)\right\|_{\lambda}\int_{t_0}^{t} e^{-\lambda(t-\tau)}d\tau.
\end{aligned}
$$

$$(C.27)$$

Then we take the supremum of both sides to obtain

$$
\begin{aligned}
\sup_{t_0\leq t\leq T}\left\{e^{-\lambda t}\left\|e_{k+1}^{(r)}(t)\right\|_{\infty}\right\} &\leq \left\|[1-CA^{r-1}B\rho]\right\|_{\infty}\sup_{t_0\leq t\leq T}\left\{e^{-\lambda t}\left\|e_{k}^{(r)}(t)\right\|_{\infty}\right\} \\
&\quad + h_0\left\|e_{k}^{(r)}(\cdot)\right\|_{\lambda}\sup_{t_0\leq t\leq T}\int_{t_0}^{t} e^{-\lambda(t-\tau)}d\tau, \\
\left\|e_{k+1}^{(r)}(\cdot)\right\|_{\lambda} &\leq \left[\left\|[1-CA^{r-1}B\rho]\right\|_{\infty} + h_0\frac{1-e^{-\lambda(T-t_0)}}{\lambda}\right]\left\|e_{k}^{(r)}(\cdot)\right\|_{\lambda}, \\
&= \left[\gamma + h_0\frac{1-e^{-\lambda(T-t_0)}}{\lambda}\right]\left\|e_{k}^{(r)}(\cdot)\right\|_{\lambda}.
\end{aligned}
$$

$$(C.28)$$

Since γ is less than 1, it is possible to choose $\lambda > 0$ sufficiently large so that

$$
\eta = \gamma + h_0\frac{1-e^{-\lambda(T-t_0)}}{\lambda} < 1. \tag{C.29}
$$

Then, the sequence $e_k(t)$ is a contraction so that $\|e_k(\cdot)\|_{\lambda} \to 0$ as $k \to \infty$ and it can be easily shown that

$$
\left\|e_{k}^{(r)}(\cdot)\right\|_{\lambda} \leq \eta^k\left\|e_{0}^{(r)}(\cdot)\right\|_{\lambda} \to 0, \tag{C.30}
$$

for all $t \in [t_0, T]$ as $k \to \infty$, uniformly in t, and by Assumption 2, it follows that

$$
y_k(t) \to y_d(t), \tag{C.31}
$$

for all $t \in [t_0, T]$ as $k \rightarrow \infty$, uniformly in t. ■

Based on the above analysis and the result of Sugie and Ono [163], for a linear system with relative degree r the ILCA of the form:

$$u_{k+1}(t) = u_k(t) + \rho \frac{d^r}{dt^r}[e_k(t)], \qquad \forall t \in [t_0, T], \tag{C.32}$$

converges. For a rate-independent hysteretic system, the input affects the output directly, therefore the relative degree of the system is zero. Based on this observation and the above result, we select the ILCA for hysteretic systems of the form:

$$u_{k+1}(t) = u_k(t) + \rho[e_k(t)], \qquad \forall t \in [t_0, T], \tag{C.33}$$

where ρ is a sufficiently small constant. Another motivation for choosing this form is if full plant knowledge is available (*i.e.*, the hysteresis behavior and LTI dynamics are completely known), then exact output tracking is achieved in one iteration. For instance, the term $\rho[e_k(t)]$ in Eq. (C.33) can be replaced with the candidate function:

$$\Psi(\cdot) = \mathcal{H}^{-1} \circ G^{-1}(\cdot), \tag{C.34}$$

where $\mathcal{H}^{-1}(\cdot)$ is the inverse of the hysteresis model (assumed to exist), and $G^{-1}(\cdot)$ is the inverse of the LTI dynamics found by using the inversion-based approach [14]. Assuming the system to be minimum phase, the input update law gives one step convergence as follows (explicit time dependence is omitted for ease in notation):

$$
\begin{aligned}
u_d - u_{k+1} &= u_d - u_k - [\Psi(y_d) - \Psi(y_k)] \\
&= u_d - u_k - \left[\mathcal{H}^{-1} \circ G^{-1}(y_d) - \mathcal{H}^{-1} \circ G^{-1}(y_k)\right]
\end{aligned}
$$

Realizing that $G^{-1}(y_d) = G^{-1} \circ G \circ \mathcal{H}(u_d) = \mathcal{H}(u_d)$ and similarly for $G^{-1}(y_k)$, we obtain

$$
\begin{aligned}
u_d - u_{k+1} &= u_d - u_k - \left[\mathcal{H}^{-1} \circ \mathcal{H}(u_d) - \mathcal{H}^{-1} \circ \mathcal{H}(u_k)\right] \\
&= u_d - u_k - u_d + u_k \\
&= 0
\end{aligned}
$$

which gives one step convergence.

However, full plant knowledge may be difficult to obtain in practice, especially for systems with hysteresis. On the other hand, the LTI dynamics can be accurately modeled, *i.e.*, dynamic models can be obtained over relatively small displacement ranges where hysteresis is negligible (*e.g.*, see [99]). To this end, we consider a more practical alternative for achieving precision positioning by picking the following operator:

$$\Psi(\cdot) = \rho G^{-1}(\cdot) \tag{C.35}$$

where ρ is a positive constant and G^{-1} is the inverse of the LTI dynamics found by the inversion-based approach. In addition, by neglecting the effects of dynamics, we can rewrite the iterative learning control law in the form given by Eq. (C.33) which focuses our attention on the hysteresis effects. Now the question to ask is what value ρ will result in a convergence of the control law Eq. (C.33)? Though the above control is chosen for hysteretic systems, there is no guarantee that it will converge since the system is not linear. The proof of convergence for the above ILCA is described in Chapter 5.

C.2 Experimental Counter Example

The fact that hysteresis does not satisfy Definition 5 is not astonishing because given a general desired trajectory $v_d \in C^0(I)$, for any value ρ the ILCA Eq. (5.4) does not converge as illustrated in the following example, where we make use of $\| \cdot \|_\infty$ norm. To illustrate, consider the experimental results in Figs. C.1(a) and (b) measured from a Burleigh AFM[1] piezo scanner which shows the effect of hysteresis[2]. The solid line in Fig. C.1(a) is the input versus time profile that was applied to the piezo scanner and the solid line in Fig. 5.7(b) is the corresponding measured output response. Suppose we pick the measured output response, the solid line in Fig. C.1(b), to be the desired trajectory and label it v_d. As a result, the input that achieves v_d is the solid line shown in Fig. C.1(a), which is labeled u_d. We note that $|u_d(t_1)| = |u_d(T)|$. Now, we would like to apply the ILCA Eq. (5.4) to the piezo system and without loss of generality, we set the initial input $u_0(t)$ equal to zero for all $t \in [0, T]$

---

[1]Model Metris 2000NC

[2]The experimental results were obtained by operating the AFM at a relatively fast speed so that creep effect is small and slow enough such that vibration effect is negligible.
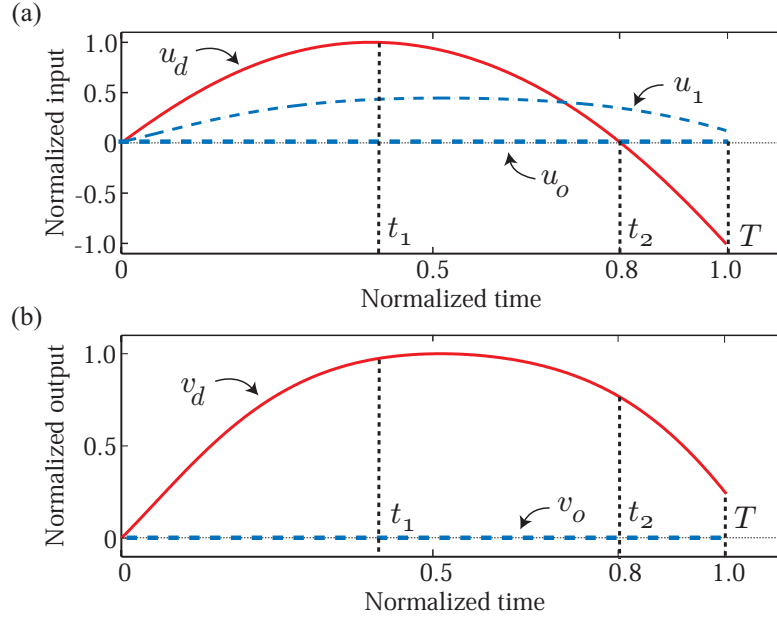
Figure C.1: Hysteresis behavior: (a) hysteresis curve and corresponding (b) input and (c) output versus time.

(dashed line in Fig. 5.7(a)). Consequently, the initial output is $v_0(t) = 0$ for all $t \in [0, T]$ (dashed line in Fig. C.1(b)). Immediately, if we apply ILCA Eq. (5.4) and pick any $\rho < 0$, the sequence of inputs generated by ILCA Eq. (5.4) does not contract to the desired input u_d as $k \to \infty$. Specifically, we conclude that $\|u_d(\cdot) - u_{k+1}(\cdot)\|_\infty \geq \|u_d(\cdot) - u_k(\cdot)\|_\infty$ for all $k \in \mathbb{N}_0$. For instance, when $k = 0$ the norm $\|u_d(\cdot) - u_0(\cdot)\|_\infty = 1$, but since $v_d(t) - v_0(t) \geq 0$ for all $t \in (0, T]$, at the first step we observe that $|u_d(t_1) - u_1(t_1)| > 1$, implying that the norm $\|u_d(\cdot) - u_1(\cdot)\|_\infty$ exceeds $\|u_d(\cdot) - u_0(\cdot)\|_\infty$. Now for $\rho > 0$, over the interval $[0, t_1]$ it is possible to show contraction of the input sequence Eq. (5.4). But over the entire interval $[0, T]$ for any $\rho > 0$, when $k = 0$ we find that $\|u_d(\cdot) - u_1(\cdot)\|_\infty \geq \|u_d(\cdot) - u_0(\cdot)\|_\infty$ because $u_1(t)$ is strictly greater than zero for all $t \in (0, T]$, implying that Eq. (5.4) fails to contract on the first step. Therefore, contraction of ILCA Eq. (5.4) in the $\|\cdot\|_\infty$ sense, in general, cannot be achieved for any constant ρ. The failure to show contraction is associated with *branching* behavior, where the ascending and descending paths in the u versus v plane do not coincide.

C.3 Convergence of ILCA for Incrementally Strictly Increasing Operators

Venkataraman and Krishnaprasd [177] have shown, based on the contraction mapping principle, that if a nonlinear operator is incrementally strictly increasing then ILCA Eq. (5.4) converges. Their result is restated in the following lemma and theorem, and a detailed discussion can be found in [177].

Assumption 3 *The incrementally strictly increasing property holds for every closed subinterval $I_{a,b} \triangleq [t_a, t_b] \subset I$.*

Lemma 3 *Let the nonlinear operator $F : C^0(I) \to C^0(I)$ be incrementally strictly increasing with constants η_1 and η_2 as defined by Definition 5, and satisfy Assumption 3. Additionally, if the constant*

$$0 < \rho \leq \frac{1}{\eta_2}, \tag{C.36}$$

then

$$\left\| \left(\frac{1}{\rho} u_2 - F(u_2) \right) - \left(\frac{1}{\rho} u_1 - F(u_1) \right) \right\|_\infty \leq \left(\frac{1}{\rho} - \eta_1 \right) \left\| u_2 - u_1 \right\|_\infty, \tag{C.37}$$

for all $u_1, u_2 \in C^0(I)$.

Proof

For $u_1, u_2 \in C^0(I)$ with $u_1 \leq u_2$, from Eq. (5.6) and (C.36), we find that

$$\eta_1(u_2 - u_1) \leq F(u_2) - F(u_1) \leq \eta_2(u_2 - u_1) \leq \frac{1}{\rho}(u_2 - u_1). \tag{C.38}$$

We rewrite Eq. (C.38) in the following form:

$$0 \leq \left(\frac{1}{\rho} u_2 - F(u_2) \right) - \left(\frac{1}{\rho} u_1 - F(u_1) \right) \leq \left(\frac{1}{\rho} - \eta_1 \right) (u_2 - u_1). \tag{C.39}$$

Likewise, for $u_1, u_2 \in C^0(I)$ with $u_2 \leq u_1$, we find that

$$0 \geq \left(\frac{1}{\rho} u_2 - F(u_2) \right) - \left(\frac{1}{\rho} u_1 - F(u_1) \right) \geq \left(\frac{1}{\rho} - \eta_1 \right) (u_2 - u_1). \tag{C.40}$$

Applying the $\| \cdot \|_\infty$ norm to Eqs. (C.39) and (C.40), we obtain

$$\left\| \left(\frac{1}{\rho} u_2 - F(u_2) \right) - \left(\frac{1}{\rho} u_1 - F(u_1) \right) \right\|_\infty \leq \left(\frac{1}{\rho} - \eta_1 \right) \left\| u_2 - u_1 \right\|_\infty, \tag{C.41}$$

therefore the assertion holds.

For general $u_1, u_2 \in C^0(I)$ with F incrementally strictly increasing and satisfying Assumption 3, we partition the interval I as follows. First, let the subinterval $D_1 = \{t \in I | u_1(t) \leq u_2(t)\}$. The set D_1 is closed. Then Eq. (C.39) holds for every $t \in D_1$ (Assumption 3). Let $\| \cdot \|_{\infty, D_1}$ be the norm on $C^0(I)$ restricted to $C_1^0(D_1) = \{u(t) | u(\cdot) \in C^0(I); t \in D_1\}$. As a result, we find that

$$\left\| \left(\frac{1}{\rho} u_2 - F(u_2) \right) - \left(\frac{1}{\rho} u_1 - F(u_1) \right) \right\|_{\infty, D_1} \leq \left(\frac{1}{\rho} - \eta_1 \right) \|u_2 - u_1\|_{\infty, D_1}. \tag{C.42}$$

Second, we let $D_2 = \{t \in I | u_2(t) \leq u_1(t)\}$. The set D_2 is also closed. Then Eq. (C.40) holds for every $t \in D_2$ (Assumption 3). Let $\| \cdot \|_{\infty, D_2}$ be the norm on $C^0(I)$ restricted to $C_2^0(D_2) = \{u(t) | u(\cdot) \in C^0(I); t \in D_2\}$. As a result, we find that

$$\left\| \left(\frac{1}{\rho} u_2 - F(u_2) \right) - \left(\frac{1}{\rho} u_1 - F(u_1) \right) \right\|_{\infty, D_2} \leq \left(\frac{1}{\rho} - \eta_1 \right) \|u_2 - u_1\|_{\infty, D_2}, \tag{C.43}$$

Now $I = D_1 \cup D_2$ and $\| \cdot \|_\infty = \max\{\| \cdot \|_{\infty, D_1}, \| \cdot \|_{\infty, D_2}\}$. Therefore, by Eqs. (C.42) and (C.43), we get Eq. (C.37) for all $u_1, u_2 \in C^0(I)$, which completes the proof. ∎

Theorem 4 *Consider a nonlinear system of the form $v(t) = F\big(u(t)\big)$ where $F : C^0(I) \to C^0(I)$ satisfies the conditions of Lemma 3. If the constant $0 < \rho \leq 1/\eta_2$, then the input sequence generated by the ILCA Eq. (5.4) converges, i.e.,*

$$\|u_d - u_k\|_\infty \leq \gamma^k \|u_d - u_0\|_\infty, \tag{C.44}$$

where $\gamma < 1$ and $u_k \to u_d$, uniformly in t, as $k \to \infty$.

Proof

To prove the assertion, we show contraction of the input sequence Eq. (5.4). Subtracting $u_{k+1}(t)$ from $u_d(t)$ and substituting $F\big(u(t)\big)$ in place of $v(t)$, we get

$$\begin{aligned} u_d(t) - u_{k+1}(t) &= u_d(t) - u_k(t) - \rho\big(v_d(t) - v_k(t)\big), \\ &= \rho \left(\frac{1}{\rho} u_d(t) - F\big(u_d(t)\big) \right) - \rho \left(\frac{1}{\rho} u_k(t) - F\big(u_k(t)\big) \right), \end{aligned} \tag{C.45}$$

for every $t \in I$. Taking the function $\| \cdot \|_\infty$ norm of Eq. (C.45), we obtain

$$\|u_d - u_{k+1}\|_\infty = \rho \left\| \left(\frac{1}{\rho} u_d - F(u_d) \right) - \left(\frac{1}{\rho} u_k - F(u_k) \right) \right\|_\infty. \tag{C.46}$$

Since the operator F is incrementally strictly increasing with constants $\eta_1 \le \eta_2$ (Definition 5) and $0 < \rho \le 1/\eta_2$, then substituting the results of Lemma 3 we obtain

$$\left\|u_d - u_{k+1}\right\|_\infty \le \rho \left(\frac{1}{\rho} - \eta_1\right) \left\|u_d - u_k\right\|_\infty \triangleq \gamma \left\|u_d - u_k\right\|_\infty, \tag{C.47}$$

where

$$\gamma = \rho \left(\frac{1}{\rho} - \eta_1\right) = 1 - \rho\eta_1 < 1, \tag{C.48}$$

because $0 < \rho\eta_1 \le 1$, and Eq. (C.47) is a contraction. Furthermore, by induction, we find that

$$\left\|u_d - u_k\right\|_\infty \le \gamma^k \left\|u_d - u_0\right\|_\infty, \tag{C.49}$$

for all $k \ge 1$, therefore the sequence $\left\|u_d - u_k\right\|_\infty \to 0$ as $k \to \infty$, hence u_k converges to u_d, uniformly in t, which completes the proof. ∎

C.4 Preisach Modeling by First Order Descending Curves [197]

This section discusses modeling the hysteresis behavior of an experimental piezo positioner, *i.e.*, finding the Preisach weighting surface μ. The modeling process involves isolating the system from the effect of creep using the inversion-based feedforward approach [2]. The parameters of the model can be used to implement the ILCA Eq. (5.4), or to find feedforward input to compensate for hysteresis, *e.g.*, see reference [2].

C.4.1 The Experimental Piezo System

The experimental piezo positioner studied in this section is a sectored piezoelectric-tube (lead zirconate-titanate, PZT) positioner common in AFM-based systems, *e.g.*, see reference [147]. Depending on how the voltage is applied to the sectors, displacement (with sub-nanometer resolution) along any of the three coordinate axes (x, y, and z) can be achieved. Figure C.2 shows a photograph of the experimental piezo positioner equipped with an optical sensor for measuring the displacement along the x-axis. In this system, a voltage amplifier drives the piezo positioner and the input voltage to the amplifier is limited to $|u| \le 5.0\ V$.
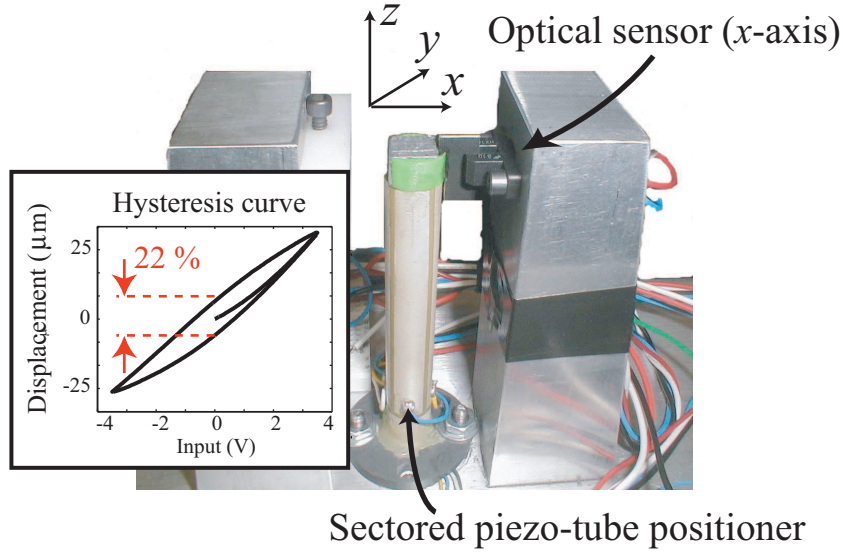
Figure C.2: The experimental piezo positioner. Inset plot shows the hysteresis behavior.

Likewise, the maximum displacement along the x-axis is approximately ± 50 μm. The amplitude of the measured sensor noise is approximately ± 10 mV, therefore the sensor can resolve the displacement of the piezo down to ± 88 nm. During the experiment, to avoid saturating the system, the piezo-amplifier input is limited to $|u| \leq 3.75$ V, hence $\underline{u} = -3.75$ V and $\bar{u} = 3.75$ V. The inset plot in Fig. C.2 shows the piezo positioner's hysteresis curve corresponding to an input range of $|u| \leq 3.75$ V, and without compensation the measured output hysteresis is 22% of the total displacement range (60.3 μm). Additionally, the dominant resonant mode of the system is at 390 Hz. In this study, we model the hysteresis behavior and apply the ILC method along the x-axis. We note that the control method can be applied to other lateral axis (y), as well as to the z-axis, if movement leads to significant hysteresis effect.

C.4.2 Modeling Procedures

One method to determine the Preisach weighting surface μ is to generate a collection of "first-order descending" (FOD) curves as described in [143, 139]. For example, suppose the

Preisach plane is in the state of negative saturation, *i.e.*, all relays are in the -1 state. Afterwards, apply a monotonically increasing input to a value $u = \alpha_1 \leq \bar{u}$, followed by a decrease to $u = \beta_1 \geq \underline{u}$. Let the measured output value corresponding to $u = \alpha_1$ be v_{α_1} and similarly, the measured output values corresponding to $u = \beta_1$ be $v_{\alpha_1\beta_1}$. When the input peaks at $u = \alpha_1$, the decrease to $u = \beta_1$ sweeps out the region Ω in the Preisach plane, which generates a descending hysteresis branch. Now define the values along the descending branch by the function $F(\alpha_1, \beta_1) = v_{\alpha_1\beta_1} - v_{\alpha_1}$; therefore, the change in output along the descending branch from $u = \alpha_1$ to $u = \beta_1$ is

$$v_{\alpha_1\beta_1} - v_{\alpha_1} \;\; = \;\; -2 \iint\limits_{\Omega} \mu(\alpha, \beta) d\alpha d\beta, \tag{C.50}$$

$$F(\alpha_1, \beta_1) \;\; = \;\; -2 \int_{\beta_1}^{\alpha_1} \int_{\beta}^{\alpha_1} \mu(\alpha, \beta) d\alpha d\beta. \tag{C.51}$$

From the above expression, the value of the Preisach weighting function $\mu(\alpha_1, \beta_1)$ at any point $(\alpha_1, \beta_1) \in \mathbf{P}$ can be determined by differentiating both sides of Eq. (C.51) twice (first with respect to β_1 and then with respect to α_1), *e.g.*,

$$\frac{\partial^2}{\partial \alpha_1 \partial \beta_1} F(\alpha_1, \beta_1) = -2\mu(\alpha_1, \beta_1). \tag{C.52}$$

As a result, by obtaining a collection of FOD curves for points in $\mathbf{P}$, we can find an approximation of the Preisach weighting surface μ. For other techniques to determine the surface μ from measured output data, see [139, 181].

To isolate and model the hysteresis effect, both creep and vibration effects must be accounted for when obtaining the FOD (output versus input) curves. Otherwise, these effects can lead to an inaccurate model of the hysteresis behavior. For instance, to avoid the effect of induced structural vibrations, the frequency of the control input used to obtain the FOD curves was kept small, *i.e.*, we chose the scanning frequency of $1Hz$, which is significantly smaller than the dominating resonant peak of the piezo positioner at $390Hz$. To account for creep effect and model hysteresis, we use the inversion-based approach as follows:

Step 1a: Model the Creep Effect In modeling the hysteresis behavior, 50 FOD curves were acquired. The control input to generate the 50 FOD curves is offset from the center of
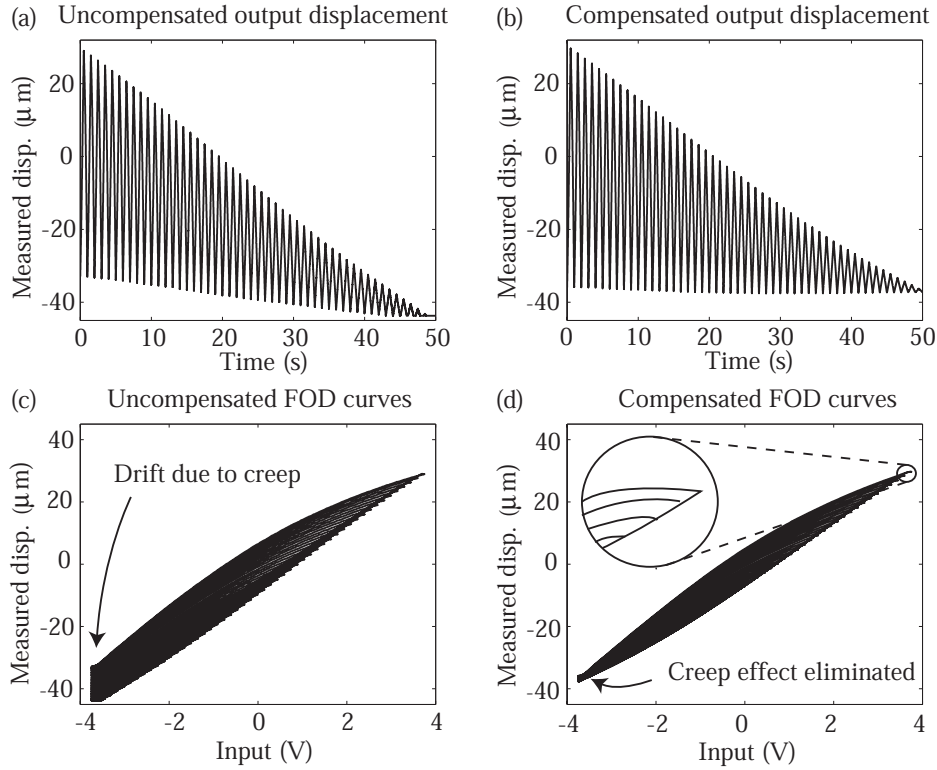
Figure C.3: (a) Uncompensated displacement versus time. (b) Compensated displacement versus time. (c) Uncompensated FOD curves. (d) Compensated FOD curves.

the piezo positioner's operating range, therefore the effect of creep in the measured output is significant. For instance, because of creep, the measured output after each input cycle slowly drifts over a period of 50 seconds as shown in Fig. C.3(a). The corresponding 50 FOD curves are shown in Fig. C.3(c). Because of creep, the time-dependent variation in the FOD curves no longer satisfies the rate-independent assumption of the Preisach hysteresis model [143], *i.e.*, when the input returns to the *negative saturation* point ($u = \underline{u}$) after each cycle, the Preisach model assumes the output returns to the same value, but experiments indicate that it creeps over time as shown in Figs. C.3(a) and (c). This effect can lead to an inaccurate model.

The creep effect, which occurs both in the mechanical and electrical domains, was mod-
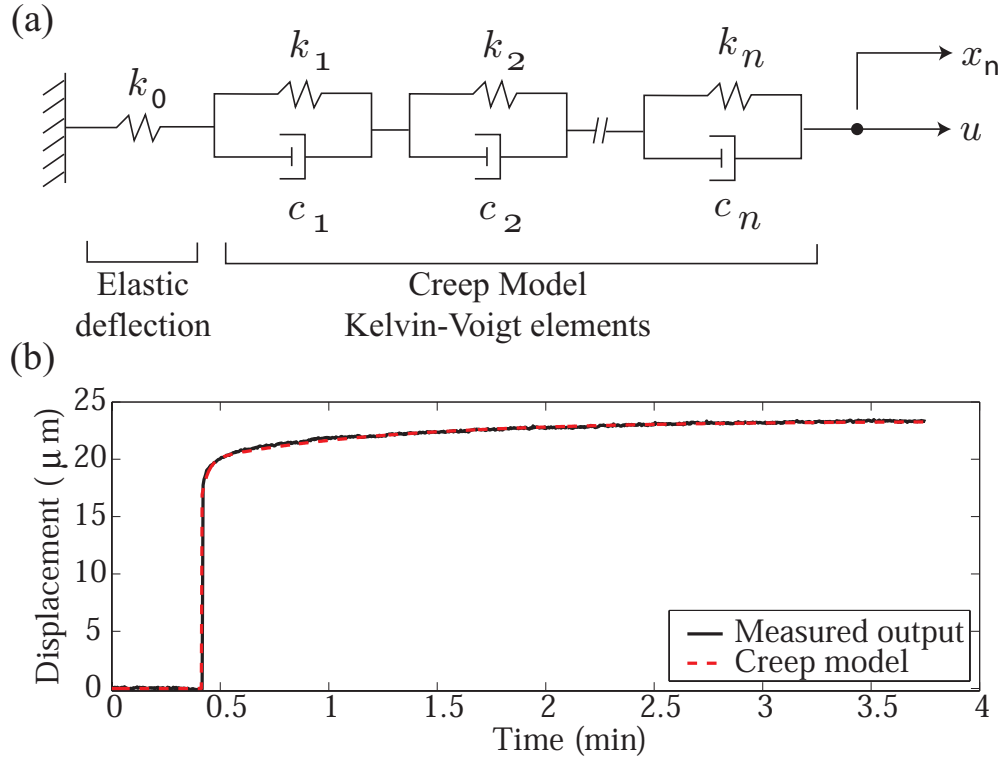
Figure C.4: Second-order creep model (dashed line) and measured piezo positioner response with creep behavior (solid line) versus time.

eled as a series connection of dampers (c_i) and springs (k_i) [184] and is described by

$$\frac{x(s)}{u(s)} = \frac{1}{k_0} + \sum_{i=1}^{n} \frac{1}{sc_i + k_i}, \tag{C.53}$$

where $x(s)$ is the displacement of the piezo positioner (in the Laplace domain) and $u(s)$ is the applied input voltage. In the above equation, k_0 models the elastic behavior at low frequencies and the creep behavior is captured by selecting an appropriate model order (n), i.e., number of damper-spring elements. The parameters $(k_0, k_i, $ and $c_i)$ of the model in Eq. (C.53) were determined by curve fitting the step response of the piezo positioner measured over a period of 3.4 minutes as shown in Fig. C.4 [185]. A good fit was obtained by selecting a second order $(n = 2)$ creep model of the following form (units V/V):

$$G_c(s) \triangleq \frac{x(s)}{u(s)} = \frac{0.968s^2 + 0.645s + 0.014}{s^2 + 0.565s + 0.0108}. \tag{C.54}$$

In Fig. C.4, the second-order creep model (dashed line) is superimposed over the measured piezo response with creep (solid line). The second-order model is a good fit of the creep behavior as indicated by the comparison.

Step 2a: Compensate for Creep: Inversion-based Approach To isolate the hysteresis behavior from creep effect, we use the creep model $G_c(s)$ and the inversion-based approach [2] to find the creep-free FOD curves. This approach finds the inverse input, which accounts for creep, to generate the FOD curves. The resulting compensated output versus time response depicted in Fig. C.3(b) shows creep is eliminated when compared to the uncompensated case: Fig. C.3(a). The corresponding FOD curves (output versus input plot) which capture only the hysteresis effect are shown in Fig. C.3(d).

Step 3a: Determine the Preisach Weighting Surface The 50 measured FOD curves shown in Fig. C.3(d) were compiled into a FOD surface over the Preisach plane $\mathbf{P}$. Differentiating this surface twice (first with respect to β and then with respect to α) produces an approximation of the Preisach weighting surface μ. However, the differentiation process can amplify the effect of noise in the measured data, which leads to an inaccurate μ surface. To minimize this effect, we use a least squares curve-fitting process. First, for each of the 50 FOD curves with constant α (*i.e.*, where β becomes the independent variable), a second order polynomial $\tilde{F}_\alpha(\alpha, \beta) = a_2\beta^2 + a_1\beta + a_0$ was fit to the data using the least squares technique. Then, the resulting FOD surface was differentiated with respect to β. Afterwards, for each of 50 the curves from the differentiated FOD curve with constant β (*i.e.*, where α becomes the independent variable), a second order polynomial $\tilde{F}_\beta(\alpha, \beta) = a_2\alpha^2 + a_1\alpha + a_0$ was fit to the data using the least squares technique. Finally, the resulting surface was differentiated with respect to α and the approximate μ surface is shown in Fig. C.5(b). From the weighting surface, we find that $\mu_{max} = 0.57$.
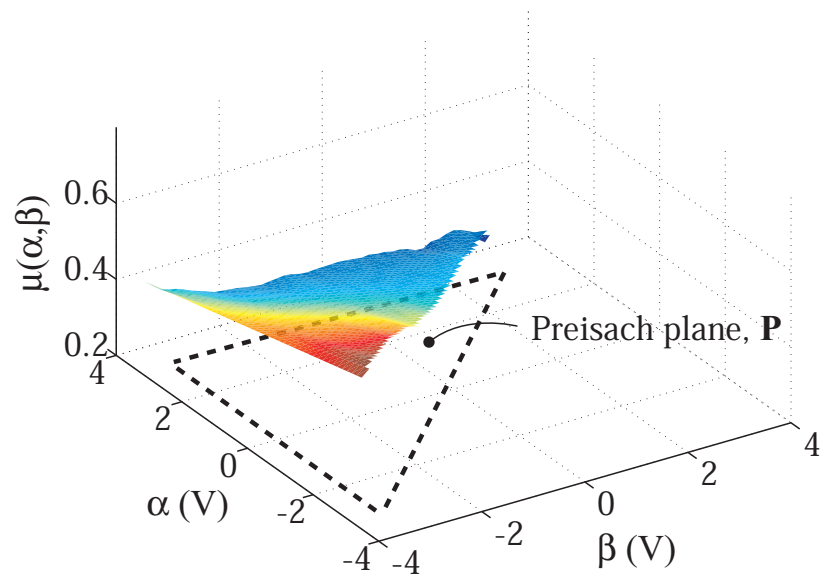
Figure C.5: The approximate $\mu(\alpha, \beta)$ surface.

Appendix D

MODIFICATIONS TO THE BURLEIGH AFM SYSTEM

This chapter discusses some modification done to the Burleigh AFM system. The information in this chapter serves as a reference.

D.1 Optical Displacement Sensor

The optical sensor to measure the displacement of the piezo positioner along the x and y axes is a phototransistor optical interrupter switch, model H21A1, manufactured by Fairchild Semiconductor. Figure D.1 shows a photograph of the sensor. The sensor is simply an optical switch configured into a displacement sensor for the piezoactuator. This configuration is used in reference [3] and a circuit diagram is shown in Fig. D.2. Other types of sensors are available, which include: linear-variable differential transformer (LVDT), optical interferometry and capacitance sensing. The choice of the optical sensor over other types is because of its simplicity and low noise. Additionally, the experimental AFM system was custom designed to house the optical sensor, and this feature was provided by the manufacturer, Burleigh Instruments.

D.2 Imaging Using Spiral Raster Pattern

A spiral raster pattern illustrated in Fig. D.3 was used for AFM imaging. To generate a spiral patter, he inputs to the x- and y-axis are sinusoidal, but phase shifted 90-degrees relative to each other to create a spiral trajectory. The effective scan area for this type is circular. One advantage of using the spiral trajectory over the standard type is the effects of creep are less noticeable in the y-axis because of a relatively fast periodic trajectory compared to the slow ramp used in the first type (*cf.* Figs. 2.6 and D.3).

DESCRIPTION

The H21A1, H21A2 and H21A3 consist of a gallium arsenide infrared emitting diode coupled with a silicon phototransistor in a plastic housing. The packaging system is designed to optimize the mechanical resolution, coupling efficiency, ambient light rejection, cost and reliability. The gap in the housing provides a means of interrupting the signal with an opaque material, switching the output from an "ON" to an "OFF" state.
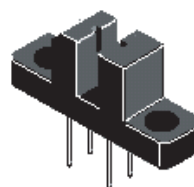
FEATURES

- Opaque housing
- Low cost
- .035" apertures
- High $I_{C(ON)}$

SCHEMATIC
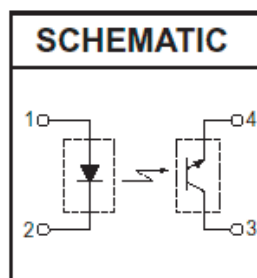
1. Derate power dissipation linearly 1.33 mW/°C above 25°C.
2. RMA flux is recommended.
3. Methanol or isopropyl alcohols are recommended as cleaning agents.
4. Soldering iron tip 1/16" (1.6mm) minimum from housing.

Figure D.1: The AFM optical-displacement sensor (compliments of Fairchild Semiconductors).
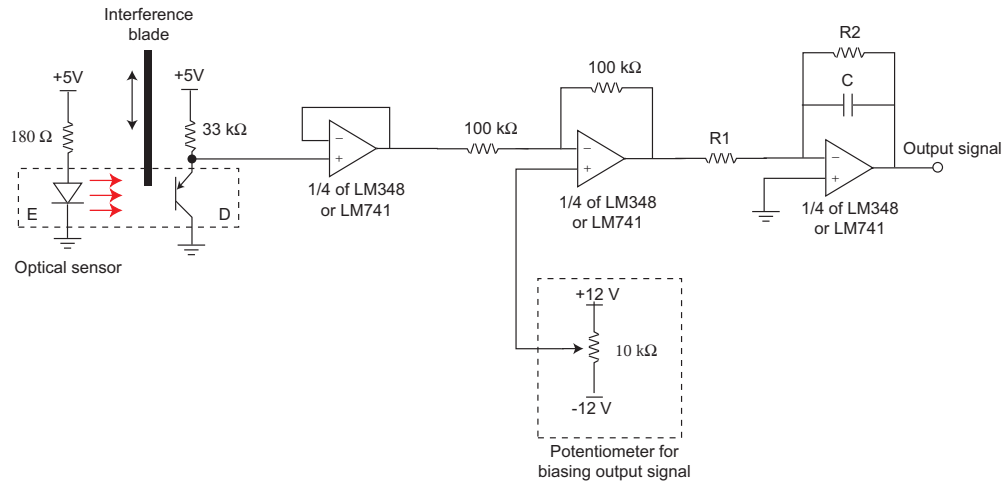
Figure D.2: The AFM optical-displacement sensor circuit diagram. The ratio $R2/R1$ determines the gain of the sensor.
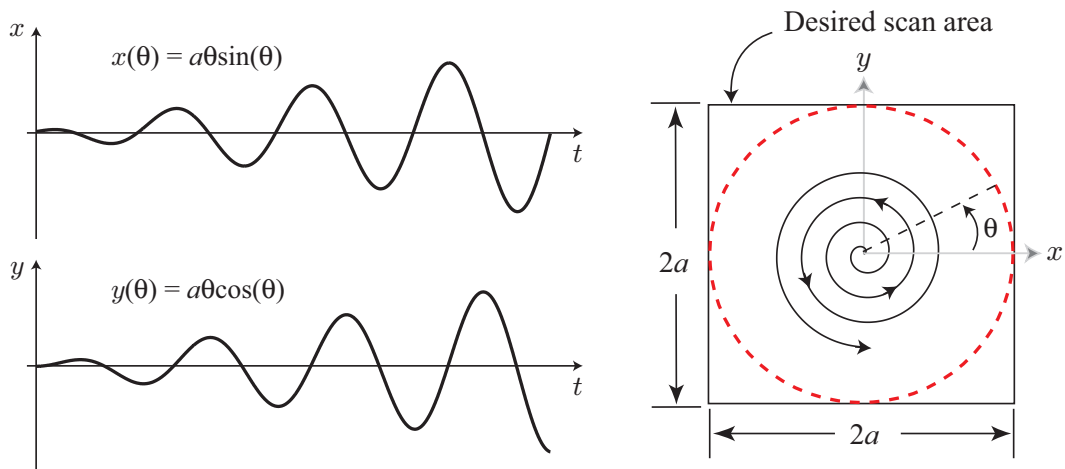
Figure D.3: Spiral trajectory for imaging.

Appendix E

SAMPLE MATLAB AND C PROGRAMS

E.1 MATLAB *Programs*

E.1.1 *Notch Filter Realization Program*

The following program complements the notch filter design discussed previously in Appendix B.1, Fig. B.2. The program computes the resistor and capacitor values. User specifies values for c_1, c_2, R, R_0, R_2, R_4, R_5, R_6, and R_8; the program returns R_1, R_3, R_7, R_9.

```
%    MATLAB Code
%    D(s) Notch Filter Design and Realization
%    Kam K. Leang 04.09.02
%
%    Notch filter D(s) has the form:
%
%                  s^2+a1s+a0
%    D(s)= K1 K2  ------------   where K = K1*K2
%                  s^2+b1s+b0
% ================================================================


clear all


% Zeros
z1   =   (-5+j*475)*2*pi;
z2   =   z1';
num  =   conv([1 -z1],[1 -z2]);
```

```
% Poles
p1  =   -100*2*pi;
p2  =   -5000*2*pi;
den =   conv([1 -p1],[1 -p2]);


% Transfer function of D(s)
Ds  =   tf(num,den);
Ds  =   Ds/(dcgain(Ds));  % scale to get DC gain = 1


% Realization
[num,den]    =   tfdata(Ds,'v');
K            =   num(1);
a1           =   num(2)/K;
a0           =   num(3)/K;
b1           =   den(2);
b0           =   den(3);


% Pick the following values
c1  =   0.1e-6; % uF
c2  =   0.1e-6; % uF
R   =   10e3;   % Ohms
R2  =   10e3;
R4  =   2.2e3;
R5  =   0.56e3;
R6  =   1e3;
R8  =   2.2e3;
Ro  =   4.7e3;


% Solve for remaing R7, R9, R3, and R1
```

```
R7  =   (R6*(R4+R5))/(a1*c1*R5*R8)-R6

R9  =   R4/(a0*c1*c2*R5*R8)

R3  =   (a0*R*R5)/(b0*R4)

R1  =   (a0*b1*c1*R2*R5*R8)/(b0*R4+a0*R5-b1*a0*c1*R5*R8)

K2  =   (R2*R5*(R+R3)*(R6+R7))/(R3*R7*(R1+R2)*(R4+R5))


% Solve for K1 such that K1*K2 = K to get feedback resistors

K1  =   K/K2;

Rf  =   K1*Ro
```

E.1.2 Least-squares Based Preisach Model Program

The following program implements the modeling of the Preisach weighting approach described in Chapter 6.

```
%   Main Program

%   Hysteresis modeling program using least-squares method

%   kam k. leang 05.20.04


clear all

% ====================================================================

% load data

% ====================================================================

no = 3151;  nf = 33151;      % starting and ending indices of data

Nc = 300;                    % number of FOD curves

load vfod5.in; vin = vfod5(no:nf);        % input voltage

% x-axis files

load xfod5cp2.out                % creep compensated fod curves

fod_data = xfod5cp2(no+2:nf+2);

% y-axis data

%load yfod5cp3.out                % creep compensated fod curves
```

```
%fod_data = yfod5cp3(no+2:nf+2);
dN = 600;                         % location of maximum peak in u
lcv = 301;
for i = 1:50
    upeak(i,1) = vin(lcv);
    lcv = lcv + dN;
end
upeak(length(upeak)+1,1) = vin(length(vin));
upeak = flipud(upeak);       % discretized input
% ascending data
ascending_u(1:301,1) = vin(1:301);
ascending_v(1:301,1) = fod_data(1:301);
lcv = 601;
for i = 1:49
    ascending_u(1:301,i+1) = vin(lcv:lcv+300);
    ascending_v(1:301,i+1) = fod_data(lcv:lcv+300);
    lcv = lcv + dN;
end
% descending data
lcv = 301;
for i = 1:50
    descending_u(1:301,i) = vin(lcv:lcv+300);
    descending_v(1:301,i) = fod_data(lcv:lcv+300);
    lcv = lcv + dN;
end
[row,col] = size(descending_v);
dec_v = descending_v; asc_v = ascending_v;
asc_u = ascending_u; dec_u = descending_u;
u = [asc_u(:,1); dec_u(2:row-1,1)];
v = [asc_v(:,1); dec_v(2:row-1,1)];
```

```
for i=2:col
    u = [u; asc_u(:,i); dec_u(2:row-1,i)];
    v = [v; asc_v(:,i); dec_v(2:row-1,i)];
end
u = [u;-5]; v = [v; v(length(v))];
% =========================================================
% find Mu using lsq method
% =========================================================
actual_u = u; actual_v = v;
[u,v,u_grid_fine] = discrete_io3(asc_u,dec_u,asc_v,dec_v);
[Bf,Af,Pf] = neg_sat(u_grid_fine);
du = u_grid_fine(2)-u_grid_fine(1);
u_grid_coarse = u_grid_fine;
[B,A,P] = neg_sat(u_grid_coarse);
phi = [];  P = relay_on4(B,A,P,u(1));
phi = comp_vect2(P);
for i = 2:length(u)
    if (u(i) >= u(i-1))
        P = relay_on4(B,A,P,u(i));
        phi = [phi; comp_vect2(P)];
    else
        P = relay_off4(B,A,P,u(i));
        phi = [phi; comp_vect2(P)];
    end
end
disp('Computing Mu surface ... please wait.');
[row,col] = size(phi);
Aeq = []; beq = [];
lb = 1e-4*ones(col,1);
ub = .1*ones(col,1);
```

```
m = lsqlin(phi,v,[],[],Aeq,beq,lb,ub);

M = extract_m(m,B,A,B);

Mu = extract_mu(m,B,A,P);

figure(1); clf;

surf(B,A,Mu); shading interp;

return


%   Routine for switching relays to +1 state

function P = relay_on4(B,A,P,u_a)

dV = (B(1,2)-B(1,1))/2;

S = length(P);

for i = 1:S

    for j=1:S

        if (A(i,j) <= u_a)

            P(i,j) = 1;

        end

    end

end

for i = 1:S

    for j = 1:S

        temp = abs(A(i,j)-u_a);

        if (temp < dV)

            P(i,j) = 1;

        end

    end

end

for i = 1:S

    for j = 1:S

        if (B(i,j)>A(i,j))

            P(i,j) = NaN;
```

```
        end

    end

end


%   Relay_on4.m

%   Routine for switching relays to +1 state

function P = relay_off4(B,A,P,u_b)

dV = abs(B(1,2)-B(1,1))/2;

S = length(P);

for i = 1:S

    for j=1:S

        if ((B(i,j)-u_b) >= dV)

            P(i,j) = -1;

        end

    end

end

for i = 1:S

    for j = 1:S

        if (B(i,j) > A(i,j))

            P(i,j) = NaN;

        end

    end

end


%   Relay_off4.m

%   resest presiach plane to -1

%   upeak = discretized input vector

%   =================================================

function [B,A,M] = neg_sat(upeak)

[B,A] = meshgrid(upeak,upeak);

M = -1*ones(size(B));
```

```
S = length(upeak);
for i = 1:S
    for j = 1:S
        if (B(i,j)>A(i,j))
            M(i,j) = NaN;
        end
    end
end

%   Compute_vect2.m
%   computes row vector
%   A1 = row vector
%   M = input matrix
%   format:
%   .  .. .. ..
%   10 9 8 7
%   6 5 4
%   3 2
%   1
%   =================================================
function [A1] = comp_vect2(M)
A1 = M(1,1);
for i = 2:length(M)
    for j = i:-1:1
        A1 = [A1, M(i,j)];
    end
end
```

E.2 C Programs

The C programs for data acquisition and real-time control are attached below. The programs
were used for the experiments in Chapters 3 and 6.

E.2.1 Feedforward Control and Data Acquisition

This program reads an input file, then sends voltage signals to the DAC channels and collects
sensor signals from the ADC channels. The measured signals are saved to an output file.
This program can be used as a template to write other A/D programs for experiments.

```
/* Scan program for AFM; scan freq=30hz, open-loop

   inverse + feedback

   Last Updated: 09.04.02

   Author: Kam Leang


   Synopsis

   input data file  [xd xopt uff], rows=664

   output data file [x  xd  xopt  uff  y], rows=1328
*/


#include <stdlib.h>

#include <stdio.h>

#include <dos.h>

#include <conio.h>

#include <malloc.h>

#include <math.h>

#include <errno.h>


#define pi 3.14159

#define board1 0x260

#define board2 0x200
```

```c
#define DAC0 0x04
#define DAC1 0x06
#define vmax 5
#define interrupt_loc 0x08


// USER MODIFIABLE VALUES *********************************************
#define N_CHAN_1 2  /* Define number of channels to acquire from   */
#define N_CHAN_2 1  /* NOTE: A/D reads in reverse starting w/ last */
                    /* w/ last CHAN first                          */
#define inSize 664    /* # points per period (Nperiod)             */
#define outSize 1328  /* 2 cycles: i.e., 2xNperiod or 2xinSize     */
#define cycleSize 1600
#define freq 20000


// User-defined routines
void user_init(int,int);    /* Init. program. Sets the frequency       */
void user_interface(void);  /* Int. task. Executed in the foreground   */
void user_task(void);       /* Periodic task. Exec in the background    */
void user_terminate(void);  /* Termtn. task. Exec after terminate()    */
void user_abort(void);      /* Abort task. Executed after ctrl-break   */
void newbreak_start(void),newtask_init(void);
void terminate(void),newbreak_stop(void),newtask_start(void);
void out(float,int,int),start_AD(int);
void write_data(void);
void read_data(void);
void cycle_system(void);
int countdown,lobyte,hibyte,doscount,done,delay_count,count;
float in(int);


// USER VARIABLES HERE ***********************************************
```

```c
float x[outSize], ucl_out[outSize], xopt_out[outSize], uff_out[outSize];
float xd[inSize], xopt[inSize], uff[inSize], cycle_data[cycleSize];
float xd_out[outSize], InputScale, InputScale_increment=.1;
int int_count, Inv, cycleloop=1;
int Ncycle=300, Nstop, Ncollect;
int Ncollect_count, traj_count, trajStop;
char outfile[80]; char cyclefile[]="cycle.in"; char infile[80];


// Main program
void main(void){
  printf("Enter INPUT file: "); gets(infile);
  printf("Enter OUTPUT file: "); gets(outfile);
  read_data();


  Nstop = outSize-1; trajStop = inSize-1;
  int_count = 0; traj_count = 0; Ncollect_count = 0;
  Ncollect = outSize/inSize;  /* number of cycles data collected */


  printf("Scanning freq: 30 Hz and Sampling freq: %d Hz\n",freq);
  printf("Number of cycles: %d\n",Ncollect);
  printf("Apply (0=xopt; 1=uff)? "); scanf("%d",&Inv); /* w/o uff  */
  printf("Input Scale: "); scanf("%f",&InputScale);   /* w/o uff   */


  user_init(board1,N_CHAN_1);
  out(0.0,board1,DAC0); out(0.0,board1,DAC1);  /* zero boards outputs */
  printf("Press any key to CYCLE system\n"); getch();
  printf("Cycling....\n"); cycle_system();
  printf("Press any key to begin SCAN\n"); getch();


  newtask_init();newbreak_start(); newtask_start();
```

```
  while(!done){
    //user_interface();
  }
  out(0.0,board1,DAC0); out(0.0,board1,DAC1);
  terminate();
  write_data();
}


// user routine.  program executes this loop when interrupt occurs
void user_task(void) {
  if(Inv == 0){ /* apply FB only */
    out(InputScale_increment*xopt[int_count],board1,DAC0);
    out(0.0,board1,DAC1);
  }
  else{        /* apply FB + FF */
    out(InputScale_increment*xopt[int_count],board1,DAC0);
    out(InputScale_increment*uff[int_count],board1,DAC1);
  }
  start_AD(board1); x[traj_count] = in(board1);            /* PIN 2 */
  start_AD(board1); ucl_out[traj_count] = in(board1);     /* PIN 1 */

  xd_out[traj_count] = InputScale_increment*xd[int_count];
  xopt_out[traj_count] = InputScale_increment*xopt[int_count];
  uff_out[traj_count] = InputScale_increment*uff[int_count];
  int_count++; traj_count++;
  if (int_count>trajStop)
    int_count = 0;
  if (traj_count > Nstop){
    Ncollect_count++; traj_count = 0;
    InputScale_increment = InputScale_increment + 0.01;
```

```c
    if (InputScale_increment > InputScale)
      InputScale_increment = InputScale;
    if (Ncollect_count > (Ncycle - 1))
      done = 1;
  }
}
void user_interface(void){
  printf("*\n");
}
void read_data(void){
  FILE *fp1;
  float temp1,temp2,temp3;
  int i;
  if((fp1=fopen(infile,"r"))==NULL){
    perror("Error opening input file!!");
    exit(EXIT_FAILURE);
  }
  for(i=0;i<(inSize);i++){
    fscanf(fp1,"%f %f %f\n",&temp1,&temp2,&temp3);
    xd[i]=temp1;
    xopt[i]=temp2;
    uff[i]=temp3;
  }
  fclose(fp1);
  printf("Acquired input data file!\n");
}
// Cycles input cycleloop times
void cycle_system(void){
  int i,j;
  float temp1;
```

```
  FILE *fp3;
  if((fp3=fopen(cyclefile,"r"))==NULL){
    perror("Error opening Cycle Data File!");
    exit(1);
  }
  else{
    for(i=0;i<cycleSize;i++){
      fscanf(fp3,"%f\n",&temp1);
      cycle_data[i]=temp1*5.0;
    }
  }
  fclose(fp3);
  for(i=0;i<cycleloop;i++){
    for(j=0;j<cycleSize;j++){
      out(cycle_data[j],board1,DAC0);
      delay(20);
      printf("Cycle x (i=%d, j=%d)\n",i,j);
    }
  }
  out(0.0,board1,DAC0);out(0.0,board1,DAC1);
}
void write_data(void){
  FILE *fp2;
  int i;
  if((fp2=fopen(outfile,"w"))==NULL)
    printf("Error opening %s!! No data saved!\n",outfile);
  else{
    for(i=0;i<outSize;i++){
      fprintf(fp2,"%f %f %f %f %f\n",x[i],xd_out[i],xopt_out[i],
              uff_out[i],ucl_out[i]);
```

```
    }
    printf("Done writing OUTPUT DATA to %s\n",outfile);
    fclose(fp2);
  }
}


// **********************************************************
// DO NOT MODIFY BELOW
// Routines to change the interrupt rate of the timer
// and to redirect the timer processing
// **********************************************************
void (interrupt *oldtask) (void);
void interrupt newtask(void) {
  user_task();
  outp(0x20,0x20);}
void newtask_init(void) {
  countdown=(int)(1193180./freq);
  hibyte=(int)(countdown/256);
  lobyte=countdown-hibyte*256;
  count=done=0;
  doscount=(int)(freq/18.2);
}
void newtask_start(void) {
  disable();
  oldtask=getvect(interrupt_loc);
  outp(0x43,0x36); outp(0x40,lobyte); outp(0x40,hibyte);
  setvect(0x08,newtask);
  enable(); }
void newtask_stop(void) {
  disable();
```

```
setvect(interrupt_loc,oldtask);

outp(0x43,0x36); outp(0x40,0); outp(0x40,0);

enable();

}


/* Routines to redirect the Ctrl-Break processing */

void (interrupt *oldbreak) ();

void interrupt newbreak(void) {

  newtask_stop(); newbreak_stop(); outp(0x20,0x20);

  user_abort(); exit(1);

}

void newbreak_start (void) {

  disable();

  oldbreak=getvect(0x23); setvect(0x23,newbreak);

  enable();

}

void newbreak_stop(void) {

  disable();

  setvect(0x23,oldbreak);

  enable();

}

void terminate(void) {

  newtask_stop(); newbreak_stop(); outp(0x20,0x20);

  user_terminate(); /*exit(1);*/

}

void user_init(int base,int no_chan_DA)  {

  outp(base+0x01,0x34);      /* Initialize Command Register 2 */

  outp(base+0x02,0x00);      /* Initialize Command Register 3 */

  outp(base+0x0F,0x00);      /* Initialize Command Register 4 */

  outp(base+0x04,0x00);      /* Initialize D/A's               */
```

```
  outp(base+0x05,0x08);
  outp(base+0x06,0x00);
  outp(base+0x07,0x08);
  outp(base,0x08+no_chan_DA-1); /* Write to command register 1 */
                                /* to set channel and gain    */
  if(no_chan_DA>1){
    outp(base,0x08+no_chan_DA-1+0x80);
  }

                                /* Start A/D conversion       */
  outp(base+0x17,0x34);         /* Select Counter A0, Mode 2  */
                                /* Force A0 high              */
  outp(base+0x08,0x00);         /* Write to A/D Clear Register */
  while(inp(base)%2){
    inp(base+0x0A);             /* Clear A/D                  */
    inp(base+0x0A);
  }
}
void user_abort(void) {
  int i;
  out(0,board1,DAC0);
  out(0,board1,DAC1);
  out(0,board2,DAC0);
  out(0,board2,DAC1);
  printf("User Abort -- End of Program\n");
  //write_data();
}
void user_terminate(void)  {
  printf("Done Collecting Data\n");
}
void out(float voltage,int base,int chan){
```

```
  long msb,lsb;

  long dacout;

  if(voltage > 4.9976) {voltage=4.9976;}

  if(voltage < -5.) {voltage=-5.;}

  dacout=(int)(voltage/vmax*2048);

  if(voltage<0) {dacout=65536+dacout;}

  msb=(int)(dacout/256);

  lsb=dacout-msb*256;

  outp(base+chan,lsb);

  outp(base+chan+0x01,msb);

}
float in(int base){

  long ADin,msb,lsb;

  float involtage;

  int status;

  status=1;

  while(status){

    if(inp(base)%2){                 /* Check status Register */

                                     /* Read A/D Conversion   */

      lsb=inp(base+0x0A);            /* Read low Byte          */

      msb=inp(base+0x0A);            /* Read high Byte         */

      ADin=msb*256+lsb;

      if(ADin>2047) {ADin=ADin-65535;}

      involtage=(float)(ADin)/2048*vmax;

      status=0;

    }

  }

  return involtage;

}
void start_AD(int base){
```

```
  outp(base+0x03,0x00);      /* Start convert register      */
}
```

E.2.2   AFM Imaging Program with Automated ILC Loop for Hysteresis Compensation

This program reads an input file and sends voltage signals to the DAC channels to control an AFM in both the x and y axes. The program also collects data from the AFM cantilever for plotting an image of the surface topology. Additionally, the program automatically runs N number of iterations, where the user provide the iteration number N. The measured data are saved to an output file after the program terminates.

```
//AFM IMAGING program
// kam leang 06.06.04
//
// User supplies an input file containing one column of data in the
// following format:
//
// ux = [1 - 57000]
// uy = [57001 - 114000]
// param = [114001 - 114010]  % parameter array
//
// Program sends ux and uy to AFM, then reads x or y optical sensors,
// and z, writes to output file in the following format:
//
// x/y = [1 - 57000]
// z   = [57001 - 114000]       % no data saved to this block
// param = [114001 - 114010]  % parameter array
//
//
// ===================================================================
```

```c
#include <stdlib.h>

#include <stdio.h>

#include <dos.h>

#include <conio.h>

#include <math.h>

#include <errno.h>

#include <alloc.h>


#define board1        0x260

#define board2        0x200

#define DAC0          0x04

#define DAC1          0x06

#define vmax          5

#define interrupt_loc 0x08


// USER MODIFIABLE VALUES *******************************************

#define N_CHAN_1  3

#define N_CHAN_2  1

#define inSize    800

#define outSize   800

#define cycleSize 1600


// USER DEFINED ROUTINES ********************************************

void user_init(int,int);

void user_interface(void);

void user_task(void);

void user_terminate(void);

void user_abort(void);

void newbreak_start(void);

void newtask_init(void);
```

```c
void terminate(void);

void newbreak_stop(void);

void newtask_start(void);

void out(float,int,int);

void start_AD(int);

void write_data(void);

void read_data(void);

void get_parameters(void);

void set_xy_scale(float,float);

void zero_outputs(void);

void get_offsets(void);

void cycle_x(int);

void cycle_y(int);

float in(int);

int countdown, delay_count;

int lobyte, hibyte;


// USER VARIABLES GOES HERE ****************************************
float huge *z;

unsigned long zSize = 114010; /* max size for memory allocation */

unsigned long ix = 0;          /* start of first block */

unsigned long iz = 57000;      /* start of third block */

unsigned long ip = 114000;     /* start of last block for storing param. */

unsigned long istop = 57000;  /* index to stop */


unsigned long int_count, k, Np;

int done, Nrev, freq;

float xScale, yScale, ux, uy, vosx, vosy;


float cycle_data[cycleSize];
```

```c
char cyclefile[]="cycle.in";
char infile[80];
char outfile[80];


// MAIN PROGRAM ****************************************
void main(void){
  /* allocate memory for z-data array using farcalloc */
  z = (float huge *)farcalloc(zSize,sizeof(float));
  if (z == NULL){
    printf("Not enough memory to store z-data\n"); exit(1);
  }
  // clear z[] vector by assigning all elements zero value
  for(k=0;k<zSize;k++){ z[k] = 0.0; }
  printf("Enter INPUT file: ");  gets(infile);
  printf("Enter OUTPUT file: "); gets(outfile);
  printf("Enter xScale:"); scanf("%f",&xScale);
  printf("Enter yScale:"); scanf("%f",&yScale);

  read_data();
  get_parameters();
  set_xy_scale(xScale,yScale);

  printf("Sampling freq: %d Hz\n",freq);

  done = 0;
  int_count = 0;

  user_init(board1,N_CHAN_1);
  //user_init(board2,N_CHAN_2);
  zero_outputs();
```

```
      printf("Press any key to CYCLE system\n"); getch();
      printf("Cycling....");
      cycle_x(1); cycle_y(1);
      printf("Cycling complete!\n");
      delay(500); get_offsets();
      newtask_init();newbreak_start(); newtask_start();
      while(!done){
        user_interface();
      }
      zero_outputs();
      terminate();
      write_data();
      zero_outputs();
}
void user_task(void) {
  ux = z[ix + int_count];
  uy = z[iz + int_count];
  out(ux,board1,DAC0);
  out(uy,board1,DAC1);
  //start_AD(board1); in(board1); /* PIN 3 */
  start_AD(board1); z[iz + int_count] = in(board1);
  /* PIN 3 */


  start_AD(board1); in(board1) - vosy;    /* PIN 2 */
  //start_AD(board1); z[ix + int_count] = in(board1) - vosy;
  /* PIN 2 */


  //start_AD(board1); in(board1) - vosx;  /* PIN 1 */
  start_AD(board1); z[ix + int_count] = in(board1) - vosx;
  /* PIN 1 */
```

```
    int_count++;
  if (int_count >= istop){
    done = 1; int_count = Np - 1;
  }
}
void user_interface(void){
  printf("%u\n", int_count);
}
void read_data(void){
  FILE *fp1;
  float temp1;
  unsigned long i;
  if((fp1=fopen(infile,"r"))==NULL){
    perror("Error opening input file!!");
    exit(EXIT_FAILURE);
  }
  for(i=0;i<zSize;i++){
    fscanf(fp1,"%f\n",&temp1);
      z[i]=temp1;
  }
  fclose(fp1);
  printf("Acquired INPUT DATA file %s!\n",infile);
}
void get_parameters(void){
  Np   = 57000;      /* total number of points */
  Nrev = 220;          /* total number of revolutions */
  freq = 220;          /* sampling frequency for 1hz scanning */
  z[ip + 2] = freq;   /* store sampling frequency */
  z[ip + 3] = xScale; /* save xScale */
  z[ip + 4] = yScale; /* save yScale */
```

```
}
void set_xy_scale(float xS, float yS){
  unsigned long i;
  for (i=0; i<57000; i++){
    z[ix + i] = xS*z[ix + i];
    z[iz + i] = yS*z[iz + i];
  }
}
void zero_outputs(void){
  out(0.0,board1,DAC0);out(0.0,board1,DAC1);
//  out(0.0,board2,DAC0);out(0.0,board2,DAC1);
}
void get_offsets(void){
  start_AD(board1); in(board1);    /* PIN 3 */
  start_AD(board1); vosy = in(board1);   /* PIN 2 */
  start_AD(board1); vosx = in(board1);   /* PIN 1 */
  printf("Offsets acquired.\n");
}
void cycle_x(int uN){
  int i,j;
  float temp1;
  FILE *fp3;
  if((fp3=fopen(cyclefile,"r"))==NULL){
    perror("Error opening Cycle Data File!");
    exit(1);
  }
  else{
    for(i=0;i<cycleSize;i++){
      fscanf(fp3,"%f\n",&temp1);
      cycle_data[i]=temp1*5.0;
```

```
    }
  }
  fclose(fp3);
  for(i=0;i<uN;i++){
    for(j=0;j<cycleSize;j++){
      out(cycle_data[j],board1,DAC0);
      delay(20);
      printf("Cycle x [%d, %d]\n",i,j);
    }
  }
  zero_outputs();
}
void cycle_y(int uN){
  int i,j;
  float temp1;
  FILE *fp4;
  if((fp4=fopen(cyclefile,"r"))==NULL){
    perror("Error opening Cycle Data File!");
    exit(1);
  }
  else{
    for(i=0;i<cycleSize;i++){
      fscanf(fp4,"%f\n",&temp1);
      cycle_data[i]=temp1*5.0;
    }
  }
  fclose(fp4);
  for(i=0;i<uN;i++){
    for(j=0;j<cycleSize;j++){
      out(cycle_data[j],board1,DAC1);
```

```
      delay(20);

      printf("Cycle y [%d, %d]\n",i,j);

    }

  }

  zero_outputs();

}

void write_data(void){

  unsigned long i;

  FILE *fp2;

  if((fp2=fopen(outfile,"w"))==NULL){

    printf("Error opening %s!! No data saved!\n",outfile);

  }

  else{

    for (i=0;i<zSize;i++){

      fprintf(fp2,"%f\n",z[i]);

    }

    printf("Done writing OUTPUT DATA to %s\n",outfile);

    fclose(fp2);

  }

}


// **************************************************

// DO NOT MODIFY BELOW

// Routines to change the interrupt rate of the timer

// and to redirect the timer processing

// **************************************************

void (interrupt *oldtask) (void);

void interrupt newtask(void) {

  user_task();

  outp(0x20,0x20);}
```

```c
void newtask_init(void) {
  countdown=(int)(1193180./freq);
  hibyte=(int)(countdown/256);
  lobyte=countdown-hibyte*256;
}
void newtask_start(void) {
  disable();
  oldtask=getvect(interrupt_loc);
  outp(0x43,0x36); outp(0x40,lobyte); outp(0x40,hibyte);
  setvect(0x08,newtask);
  enable();
}
void newtask_stop(void) {
  disable();
  setvect(interrupt_loc,oldtask);
  outp(0x43,0x36); outp(0x40,0); outp(0x40,0);
  enable();
}
/* Routines to redirect the Ctrl-Break processing */
void (interrupt *oldbreak) ();
void interrupt newbreak(void) {
  newtask_stop(); newbreak_stop(); outp(0x20,0x20);
  user_abort(); exit(1);
}
void newbreak_start (void) {
  disable();
  oldbreak=getvect(0x23); setvect(0x23,newbreak);
  enable();
}
void newbreak_stop(void) {
```

```
  disable();

  setvect(0x23,oldbreak);

  enable();

}

void terminate(void) {

  newtask_stop(); newbreak_stop(); outp(0x20,0x20);

  user_terminate(); /*exit(1);*/

}

void user_init(int base,int no_chan_DA)  {

  outp(base+0x01,0x34); /* Initialize Command Register 2 */

  outp(base+0x02,0x00); /* Initialize Command Register 3 */

  outp(base+0x0F,0x00); /* Initialize Command Register 4 */

  outp(base+0x04,0x00); /* Initialize D/A's                */

  outp(base+0x05,0x08);

  outp(base+0x06,0x00);

  outp(base+0x07,0x08);

  outp(base,0x08+no_chan_DA-1);

  /* Write to command register 1 */

  /* to set channel and gain     */

  if(no_chan_DA>1){

    outp(base,0x08+no_chan_DA-1+0x80);

  }

                       /* Start A/D conversion        */

  outp(base+0x17,0x34);  /* Select Counter A0, Mode 2   */

                       /* Force A0 high               */

  outp(base+0x08,0x00);  /* Write to A/D Clear Register */

  while(inp(base)%2){

    inp(base+0x0A);       /* Clear A/D                   */

    inp(base+0x0A);

  }
```

```
}
void user_abort(void) {
  int i;
  out(0,board1,DAC0);
  out(0,board1,DAC1);
//  out(0,board2,DAC0);
//  out(0,board2,DAC1);
  printf("User Abort -- Program Terminated.  Bye!\n");
  //write_data();
}
void user_terminate(void)  {
  printf("Done Collecting Data\n");
}
void out(float voltage,int base,int chan){
  long msb, lsb, dacout;
  if(voltage > 4.9976) {voltage=4.9976;}
  if(voltage < -5.) {voltage=-5.;}
  dacout=(int)(voltage/vmax*2048);
  if(voltage<0) {dacout=65536+dacout;}
  msb=(int)(dacout/256);
  lsb=dacout-msb*256;
  outp(base+chan,lsb);
  outp(base+chan+0x01,msb);
}
float in(int base){
  long ADin,msb,lsb;
  float involtage;
  int status;
  status=1;
  while(status){
```

```
    if(inp(base)%2){        /* Check status Register */
                            /* Read A/D Conversion    */
      lsb=inp(base+0x0A); /* Read low Byte          */

      msb=inp(base+0x0A); /* Read high Byte         */

      ADin=msb*256+lsb;

      if(ADin>2047) {ADin=ADin-65535;}

      involtage=(float)(ADin)/2048*vmax;

      status=0;

    }

  }

  return involtage;

}

void start_AD(int base){

  outp(base+0x03,0x00);/* Start convert register      */

}
```

VITA

Kam K. Leang

Education

- Ph.D., Mechanical Engineering, September 2004, Univ. of Washington, Seattle, WA, Advisor: Santosh Devasia

- M.S., Mechanical Engineering, December 1999, Univ. of Utah, Salt Lake City, UT

- Mechatronics Certificate Degree, December 1999, Univ. of Utah, Salt Lake City, UT

- B.S., Mechanical Engineering, December 1997, Univ. of Utah, Salt Lake City, UT

Research Experience

- Ph.D. Research, Department of Mechanical Engineering, Univ. of Washington, Seattle, WA, October 2000 - September 2004

- M.S. Research, Department of Mechanical Engineering, Univ. of Utah, Salt Lake City, UT, January 1997 - December 1999, Advisor: Santosh Devasia

- Undergraduate Summer Research, Department of Mechanical Engineering, Univ. of Utah, Salt Lake City, UT, June 1996 - December 1997, Advisor: Joseph C. Klewicki

Teaching Experience

- National Science Foundation GK-12 Program in Mathematics Fellow, Univ. of Washington, Kenmore junior high and Lockwood elementary school, Seattle, WA, September 2002 - June 2004

- National Science Foundation GK-12 PRIME Fellow, Univ. of Washington and Nathan Hale high school, Seattle, WA, September 2001 - June 2002

- ME 5200/6200, *Classical Controls*, Course Instructor, Department of Mechanical Engineering, Univ. of Utah, Salt Lake City, Utah, June 1999 - August 1999

- ME 3200 and 3210, *Mechatronics I and II*, Teaching Assistant, Department of Mechanical Engineering, Univ. of Utah, Salt Lake City, Utah, September 1997 - June 1999

- ME 2000, *Concurrent Engineering I: Manufacturing*, Teaching Assistant, Department of Mechanical Engineering, Univ. of Utah, Salt Lake City, Utah, March 1997 - June 1997

Publications

1. J. S. Dewey, K. K. Leang, and S. Devasia, *Experimental and theoretical results in output-trajectory redesign for flexible structures*, ASME J. Dyn. Syst., Meas., Control Vol. 120, pp. 456-461, December 1998

2. K. K. Leang, Q. Zou, and S. Devasia, *Continuous- and discrete-time state-space modeling*, Contributed chapter to the CRC Mechatronics Handbook, Edited by Robert Bishop, CRC Press, Chapter 23, pp. 40-54, 2002

3. K. K. Leang, and S. Devasia, *Hysteresis, creep, and vibration compensation*, The 2$^{\text{nd}}$ IFAC Conference on Mechatronic Systems, Berkeley, CA., 283-289, December 2002 (invited session on Smart Materials and Structures)

4. K. K. Leang, and S. Devasia, *Iterative feedforward compensation of hysteresis in piezo positioners*, IEEE 42nd Conference on Decision and Control, Maui, Hawaii USA, 2626-2631, December 2003 (invited session on Nanotechnology: Control Needs and Related Perspectives)

5. Q. Zou, K. K. Leang, E. Sadoun, M. J. Reed, and S. Devasia, *Control issues in high-speed AFM for biological applications: collagen imaging example*, Accepted for publication in the special issue on "Advances in Nanotechnology Control" in the Asian Journal of Control, June 2004

6. K. K. Leang, and S. Devasia, *Iterative control of piezo positioners for long-range SPM-based nanofabrication*, The 3rd IFAC Conference on Mechatronic Systems, Manly Beach, Sydney, Australia, September 2004

7. K. K. Leang, and S. Devasia, *Iterative learning control of hysteresis in piezo-based nano-positioners: atomic force microscopy application* (in preparation for submission to Automatica, October 2004)

Honors

- National Science Foundation and Univ. of Washington GK-12 Program in Mathematics Fellowship (2002 - present)

- National Science Foundation and Univ. of Washington GK-12 PRIME Fellowship (2001 - 2002)

- College of Engineering Outstanding Teaching Assistant Award, Univ. of Utah (1999)

- Teaching Assistant of the Year Award, Department of Mechanical Engineering, Univ. of Utah (1997-98, 1998-99)

- National Science Foundation Human and Computer Interface Intelligent Control Traineeship (1999)

- Co-President of Graduate Student Advisory Committee, Department of Mechanical Engineering, Univ. of Utah (1998-99)

- International Gas Turbine Institute Scholarship (1995)

- Clyde Christensen Scholarship (1995)

Member

- Institute of Electrical and Electronic Engineers (IEEE) (2002 - present)

- The American Society of Mechanical Engineers (ASME) (1999 - present)